FLUID DYNAMICS OF MATERIAL MICRO-DEPOSITION:

CAPILLARY-BASED DROPLET DEPOSITION AND

AEROSOL-BASED DIRECT-WRITE

A Dissertation
Submitted to the Graduate Faculty
of the
North Dakota State University
of Agriculture and Applied Science

By

Artur Lutfurakhmanov

In Partial Fulfillment of the Requirements
for the Degree of
DOCTOR OF PHILOSOPHY

Major Department:
Mechanical Engineering and Applied Mechanics

September 2012

Fargo, North Dakota

North Dakota State University
Graduate School

Title

Fluid Dynamics of Material Micro-Deposition: Capillary-Based Droplet Deposition and Aerosol-Based Direct-Write

By

Artur Lutfurakhmanov

The Supervisory Committee certifies that this ***disquisition*** complies with North Dakota State University's regulations and meets the accepted standards for the degree of

DOCTOR OF PHILOSOPHY

SUPERVISORY COMMITTEE:

Dr. Iskander Akhatov
Chair

Dr. Douglas Schulz

Dr. Yechun Wang

Dr. Orven Swenson

Approved:

10/30/12
Date

Dr. Sherman Goplen
Department Chair

ABSTRACT

With rapid development of the direct-write technology, in addition to requirement of non-destructive printing, there is a need for non-expensive, robust, and simplified techniques of micro/nano fabrication. This dissertation proposes a new technique of non-invasive lithography called Capillary-Based Droplet Deposition and suggests improvements to existing Aerosol-Jet Direct-Write method that leads to deposition of thinner lines.

A hollow capillary filled with liquid is a dispensing tool employed for the Capillary-Based Droplet Deposition method. Due to pressure applied from one side of the capillary, a liquid meniscus is formed at the opposite side of the capillary. After the meniscus touches the substrate, a liquid bridge between the capillary and substrate is formed. The capillary retraction causes the bridge rupturing and liquid droplet deposition. In the first part of this dissertation, the Capillary-Based Deposition method is considered both theoretically and experimentally. From bridge modeling, it is found that the droplet size is dependent on pressure applied, inner radius and wall thickness of the capillary, and liquid-capillary and liquid-substrate equilibrium contact angles. Three deposition scenarios are identified showing that minimum deposited droplet size is about 15% of the capillary inner diameter. Modeling results are verified in experiments with different water-glycerol solutions used as test liquid and with capillaries of wide range of inner diameters.

The second part of the dissertation is devoted to theoretical investigation of the Aerosol-Jet Direct-Write method where few micron width lines are created from aerosol droplets that move along with the gas flowing through a converging micro-nozzle. Gas velocity and density profiles inside and outside of the nozzle are obtained from

ANSYS/CFX simulation. Aerosol droplet trajectories and velocity components are calculated using all forces acting on the particles in the flow. Comparing all forces, it is found that only Stokes and Saffman forces are relevant for simulation of the gas-particle interaction. Original 1D equation for Saffman force is extended to two dimensional gas flows. For some parameter ranges, Saffman force is found to be negligibly small. Based on simulation results, two nozzle designs are proposed in order to collimate aerosol particles with diameters of 1.5-5.0 microns toward the nozzle centerline.

ACKNOWLEDGMENTS

I am very grateful to my major advisor, Dr. Iskander S. Akhatov, for his support and supervision throughout this project. This dissertation would not have been possible without the help and inspiration provided by Dr. Akhatov. I acknowledge my co-adviser, Dr. Douglas L. Schulz, for his constant guidance, motivation, and encouragement. I am very thankful to Dr. Orven Swenson, Dr. Yechun Wang, and Dr. Zakaria Mahmud for valuable discussions during my study and for advising in corrections of the dissertation.

Additionally, I am appreciative of the assistance from Gregory Loken. He helped me with most of the experiments in the capillary-based droplet deposition project. I am very thankful to Michael Robinson for his contribution in the aerosol-jet direct-write project and his willingness to share the experimental data.

Also I would like to acknowledge my colleagues for their assistance and thoughtful conversations especially regarding the experimental work. In particular, I would like to thank Andrew Gustafson, Travis Yoch, Drew Thompson, Jason Daugs, and Justin Hoey for their contributions during the project.

This work has been funded by the ND EPSCoR and the Defense Microelectronics Activity grants. I am appreciative for the support received from these sources.

Finally, I thank my parents and family for their support, love, inspiration, and understanding during my study.

TABLE OF CONTENTS

LIST OF TABLES

LIST OF FIGURES

LIST OF SYMBOLS

a ..... Particle radius

A ..... Area

A_{LV} ..... Area of the bridge's liquid-vapor interface

A_{LC} ..... Area of the bridge's liquid-capillary interface

A_{LS} ..... Area of the bridge's liquid-substrate interface

B ..... Slope parameter

c_M ..... Added mass coefficient

C_g ..... Carrier gas sonic velocity

C_D ..... Stokes force correction

C_{Sa} ..... Saffman force correction

d_2, d_3 ..... Parameters

e ..... Electron charge

$\mathbf{e}_x$ ..... Unit vector along x axis

$\mathbf{e}_y$ ..... Unit vector along y axis

$\mathbf{e}_\xi$ ..... Unit vector along ξ axis

$\mathbf{e}_\eta$ ..... Unit vector along η axis

E_Σ ..... Surface energy of the system

f_p ..... Force due to the pressure inside of the bridge

f_σ ..... Surface tension force

F ..... Functional

$\mathbf{F}_{St}$ ..... Stokes force

$\mathbf{F}_{Gr}$ ..... Gravity force

$\mathbf{F}_{Ba}$ ..... Basset force

$\mathbf{F}_{Sa}$ ..... Saffman force

$\mathbf{F}_{Ps}$ ..... Pressure gradient Force

$\mathbf{F}_{Vm}$ ..... Virtual mass Force

$\mathbf{F}_{Ma}$ ..... Magnus force

$\mathbf{g}$ ..... Gravitational acceleration vector

G..... Conductance

G..... Stokes force correction

$G_{contact}$..... Contact conductance

h ..... Distance between capillary and substrate

h ..... Plank constant

h_M..... Meniscus thickness

H..... Normalized distance between capillary and substrate

I ..... Current

k_B ..... Boltzmann constant

k..... Constant

Kn_p ..... Knudsen number

L ..... Length

L ..... Nozzle length

m..... Electron mass

m..... Particle mass

m_m..... Molar mass

M_p ..... Mach number

n_g ..... Number concentration of gas molecules per unit volume

N_A ..... Avogadro number

p ..... Applied pressure

p_0 ..... Atmospheric pressure

P ..... Normalized applied pressure

r ..... Bridge shape function

r ..... Distance from the nozzle centerline

r_C ..... Capillary inner radius

r_O ..... Capillary outer radius

r_σ ..... Radius of meniscus curvature

r_{BC} ..... Bridge's radius on the capillary

r_{BS} ..... Bridge's radius on the substrate

r_{actual} ..... Radius of the actual hydrophobized area

R ..... Distance

R ..... Resistance

R ..... Nozzle radius

R_O ..... Normalized capillary outer radius

R_{in} ..... Nozzle inlet radius

R_{out} ..... Nozzle outlet radius

R_{BS} ..... Normalized bridge's radius on the substrate

Re_p ..... Particle Reynolds number

Re_f ..... Shear Reynolds number

Re_{Ω} ..... Rotational Reynolds number

S ..... Surface area

St ..... Stokes number

t ..... Time

T ..... Temperature

u ..... Axial gas velocity

u_p ..... Axial particle velocity

$u_0^{\max}$ ..... Maximum of Poiseuelle parabolic velocity

U ..... Mean velocity of fluid

U_{in} ..... Maximum of the inlet gas velocity

v ..... Radial gas velocity

v_p ..... Radial particle velocity

$\mathbf{v}$ ..... Gas velocity vector

$\mathbf{v}_p$ ..... Particle velocity vector

V ..... Volume

V ..... Bias (voltage)

V_B ..... Liquid bridge volume

V_C ..... Volume of liquid between the piston and the capillary

W_{ext} ..... Work of external forces

x_1, x_2, x_3, x_4 .... x-coordinates of four nodes

y_1, y_2, y_3, y_4 .... y-coordinates of four nodes

z ..... Real distance

z_0 ..... Set point current distance

α..... Dimensionless shear rate

α..... Angle between vector $\tilde{\mathbf{v}} = \mathbf{v} - \mathbf{v}_p$ and x-axis

α_1..... $\arctan\left(v - v_p / u - u_p\right)$

χ..... Fluid-to-particle density ratio

δf..... Total force

δF..... Normalized total force

ε..... Ratio of the nozzle inlet radius to the nozzle length

ε..... Ratio of square root of shear Reynolds number to particle Reynolds number, $\varepsilon = \mathrm{Re}_f^{1/2} / \mathrm{Re}_p$

ε..... Dimensionless particle radius, $\varepsilon = a / L$

ε_{Gr}..... Ratio of gravity force to Stokes force

ε_{Ma}..... Ratio of Magnus force to Stokes force

ε_{Sa}..... Ratio of Saffman force to Stokes force

ε_{Ba}..... Ratio of Basset force to Stokes force

ε_{Vm}..... Ratio of virtual mass force to Stokes force

ε_{Ps}..... Ratio of pressure gradien force to Stokes force

γ..... Surface tension

γ^d..... Dispersion component of surface tension

γ^n ..... Non-dispersion component of surface tension

γ_{LS}..... Liquid-substrate tension

γ_{SV}..... Substrate-vapor tension

γ_{LV} ..... Liquid-vapor tension

γ_{LC} ..... Liquid-capillary tension

γ_{CV} ..... Capillary-vapor tension

λ ..... Mean free path

μ ..... Gas viscosity

θ_C ..... Actual liquid-capillary contact angle

θ_S ..... Actual liquid-substrate contact angle

θ_C^e ..... Liquid-capillary equilibrium contact angle

θ_S^e ..... Liquid-substrate equilibrium contact angle

θ_C^r ..... Liquid-capillary receding contact angle

θ_S^r ..... Liquid-substrate receding contact angle

θ_C^a ..... Liquid-capillary advanced contact angle

θ_S^a ..... Liquid-substrate advanced contact angle

ρ_p ..... Aerosol particle density

ρ_f ..... Carrier gas density

ρ ..... Carrier gas density

ρ_1, ρ_2, ρ_3, ρ_4 ... Gas density at four nodes

σ ..... Liquid surface tension

σ_m ..... Collision diameter of a molecule

τ_μ ..... Stokes relaxation time

$\boldsymbol{\omega}$ ..... Fluid vorticity at the particle location

ξ ..... Relative distance

ξ, η ..... Local coordinate system

$\psi_1, \psi_2, \psi_3, \psi_4$. Shape function at four nodes

Φ ..... Work function

Ψ ..... Shape function

$\Sigma\mathbf{F}$ ..... Sum of all forces

$\mathbf{\Omega}$ ..... Angular rotation rate of a particle

1. INTRODUCTION

Direct-write technology refers to the technology of direct fabrication of features on a substrate by usage of computer-controlled translational stages. The movements of these stages lead to manipulation of the substrate relative to a pattern-writing device (e.g. writing tip, ink-jet nozzle, or laser optics) which in turn causes formation of patterns with given geometry and composition.

Presently, four main categories of direct-write printing exist [1]:

- Tip-based techniques in which structures are created due to tip contact with the substrate;
- Droplet-based techniques in which structures are created due to droplet transfer on the substrate;
- Energy-based techniques in which structures are created due to transfer or subtraction of material onto/from the substrate by laser ablation;
- Flow-based techniques in which structures are created due to flow of the ink onto the substrate.

Within the tip-based direct-write category, two main sub-categories are available: dip-pen nanolithography and fountain pen nano-lithography. Details of these two techniques are discussed in sub-sections 1.1.1 and 1.1.2.

Existing droplet-based techniques (e.g. ink-jet direct-write and aerosol-jet direct-write) and their advantages and disadvantages will be considered in sub-chapter 1.2.

The energy-based category of the direct-write technology consists of the methods of creation of features based on laser or focused-ion beam usage. Focused electron beam deposition is usually material-subtractive fabrication of the patterns, while laser-based

techniques transfer or focus the material onto the substrate with high energy-beams. This category of direct-write printing is out of the scope of the current dissertation.

The flow-based category of direct write printing includes techniques of deposition based on continuous flow of ink out of the different configuration nozzles. This category can be further divided into pump and extrusion-based techniques. As in the case of the energy-based category, flow-based sections will not be considered deeply in this dissertation.

1.1. Tip-Based Direct-Write Methods

1.1.1. Dip-Pen Nano-Lithography

In 1999, Chad Mirkin developed Dip-pen nanolithography [2-6]. This method is based on the Atomic Force Microscope (AFM) where the AFM tip is employed to transfer molecules to the surface (see Figure 1). First, the AFM tip is "inked" with the material of interest. Then, the tip is brought in contact with the substrate surface, and the ink adsorbed on the tip is transferred to the substrate. The mechanism governing dip-pen nanolithography is still not fully understood. Some researchers suggest that the water meniscus plays an important role in the transport of ink to the substrate. In contrast, others believe that the meniscus is not responsible for the diffusion of molecules from the tip to substrate [4]. They claim that the diffusion rate is independent of humidity, while the deposition depends on write speed and the temperature.

Since the radius of curvature of the AFM tip is about 5-10 nm, it was experimentally proven that it is possible to make nano-features as small as 14 nm [5].

Rather et al. performed Monte Carlo simulations on meniscus condensation and found that the smallest meniscus diameter is 2.3 nm, which might be the limit of resolution in DPN [3]. Another advantage of DPN is its low-cost manufacture because there is no need of complicated stamps as in the case of photolithography or nano-imprint lithography. The DPN technique allows imaging nano-patterns right after the writing by using the same AFM tip. In addition, parallelization of DPN-patterning is feasible by using multiple tips and a suitable feedback control.

Slowness in writing is a common disadvantage of the DPN approach due to the slow flow of fluid and the necessity to re-ink and re-position the AFM cantilever if the fluid is exhausted. Multiple ink writings by using the DPN can be done only one after the other because the AFM cantilevers must be changed and the laser beams on the cantilevers must be re-aligned. One more problem with DPN is the tip wear during the deposition due to contact with the substrate.

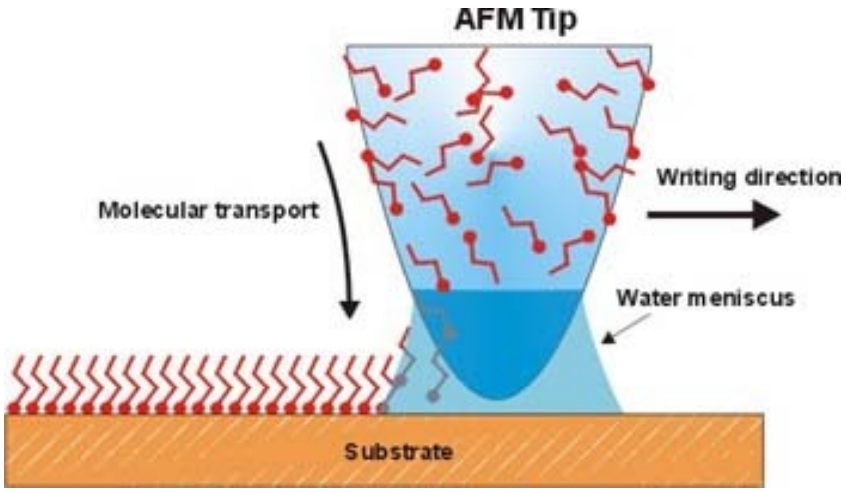

Figure 1. Schematic of the dip-pen nano-lithography, from Richard D. Piner, Jin Zhu, Feng Xu, Seunghun Hong, and Chad A. Mirkin, “”Dip-Pen” Nanolithography,” Science, Vol. 283, Copyright 1999 [6]. Reproduced with permissions from AAAS.

Various materials, such as organic compounds, bio-molecules, and polymers, have been used to fabricate nano-structures onto different substrates by using the DPN approach. The feature size in DPN depends on many parameters: "ink" properties, substrate roughness, relative humidity, temperature, writing speed, tip geometry, and contact force. While the details of these variables are complicated, it is generally found that ink solubility and diffusion processes are key parameters in the formation of DPN features.

1.1.2. Fountain Pen Nano-Lithography

In 2004, Horacio D. Espinosa proposed the Fountain Pen Nano-Lithography (FPN) approach [7-11]. FPN is a modified dip-pen nanolithography technology with new probe specially developed for continuous ink feed. The novel FPN probe called the volcano tip consists of the regular AFM tip along with a shell (see Figure 2a). The volcano tip is then connected to the ink reservoir by a micro-channel as shown in Figure 2b. Therefore, when ink is loaded to the ink-reservoir, the ink solution is driven toward the volcano tip via micro-channel due to action of the capillary force. So this innovative idea behind FPN allows fabrication of features on the substrate without re-dipping.

It was experimentally shown that by using the FPN approach it is possible to deposit biological materials, silver nano-particle ink, and a solution of 16-mercaptohexadecanoic acid in ethanol with high resolution. Espinosa et al. reported that features as small as 40 nm were patterned.

Since FPN is the technique based on the DPN method, all advantages and disadvantages of the DPN method are inherent to the FPN technique, except requirement of re-dipping. As in the case of dip-pen nano-lithography, the fountain pen approach allows writing and imaging with the same probe. Although re-dipping helps to save some time

during the patterning stage, the writing process is still slow due to single-probe patterning. Slowness in the FPN writing was recently resolved by multiple-tip, double-ink patterning. Linear arrays of 12 cantilevers were used to pattern single-stranded oligonucleotides.

The main drawback of the FPN method is the fabrication of the volcano probe along with micro-channel and ink reservoir. This multipart FPN probe requires many steps in manufacturing. Some channels may not be connected with volcano tips due to complexity in fabrication. Another problem associated with FPN probe is that channel sealing sometimes causes leakage of ink. The small size of the micro-channel sometimes results in clogging. Other problems associated with the volcano probe are: large tip radii (300-500 nm), low cantilever torsional stiffness, and small reflective area which poorly reflects signal to the AFM optical detectors. The problem with large tip radii was solved recently by growing W nanowires using the electron-beam-assisted deposition.

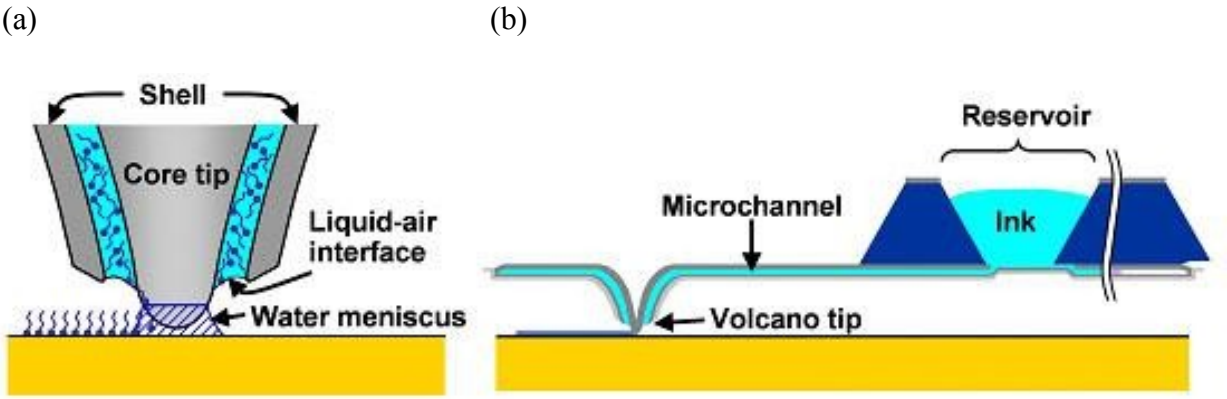

Figure 2. Fountain pen nano-lithography: (a) is volcano tip, (b) is schematics of fountain pen nano-lithography, from Keun-Ho Kim, Nicolaie Moldovan, and Horacio D. Espinosa, "A Nanofountain Probe with Sub-100 nm Molecular Writing Resolution," Small, Vol. 1(6), Copyright 2005 [10]. Reproduced with permissions from John Willey and Sons.

As mentioned before, the fabrication of the FPN probe is the most crucial and very difficult problem because the manufacturing process consists of the following sub-stages, which are expensive and time consuming:

- Si_3N_4 deposition, backside lithography, and backside KOH trench formation;
- Front-side lithography for cantilever and connection holes delineation;
- Plasma-enhanced chemical vapor deposition of SiO_2 and patterning for channel core and reservoir delineation;
- Low-pressure chemical vapor deposition of low stress nitride and patterning; resist deposition of front side and etching of protruding tips;
- Etching of SiO_2 sacrificial layer;
- PECVD of SiO_2 sealing layer on the front side and thick resist lithography on the backside of the wafer;
- Formation of reservoir wells and chips by deep RIE of Si.

1.2. Droplet-Based Direct-Write Methods

As it was mentioned above, the direct-write technology can be categorized into four major types: tip-based, droplet-based, energy-based, and flow-based. Tip-based techniques were analyzed and studied in the previous sub-chapter 1.1. This sub-chapter is devoted to the existing droplet-based techniques. Droplet-based direct-write fabrication techniques can be further divided into two sub-categories, namely, aerosol-jet direct-write and ink-jet direct-write methods. In both techniques, features are created on the substrate due to

transfer of liquid droplets onto the substrate. Similarities and dissimilarities between these methods are discussed in sub-sections 1.2.1 and 1.2.2 below.

1.2.1. Ink-Jet Direct-Write

Ink-jet direct-write is a technology which first appeared in the mid-1970s in the form of an ink-jet printer. Currently there are two modes of ink-jet technology: continuous and drop-on-demand [1, 12-13]. In both operating modes, droplets are generated out of a nozzle or orifice which is completely filled by ink. In continuous ink-jet, a constant stream of droplets is created due to break up of a liquid jet under influence of a surface tension force. Then all flying droplets are charged by the charging electrodes. Field plates are used to guide charged liquid droplets to the desired location: either the catcher (gutter) to be recycled or the substrate for deposition at the chosen place. As shown in Figure 3(a), only few droplets are used for real printing onto the substrate, while other ink droplets are recycled. Deposition in the drop-on-demand mode happens due to ejection of an individual droplet by a pressure pulse of a pressure actuator or by air bubble formation because of heat increase out of thermal actuator: the schematic of this mode is presented in Figure 3(b). The rate of the droplet generation can reach up to 25000 drops per second for single nozzle using drop-on-demand mode, and up to 1 MHz for continuous method. After the deposition of the ink droplets on the substrate, the ink material usually solidifies due to solvent evaporation, chemical changes (cross-linking), and/or cooling. Sometimes sintering of ink is necessary for certain applications. It should be mentioned that during the ink-jet deposition, the distance between the nozzle exit and substrate is fixed (it is about 1 cm). This can cause a problem if the substrate is not flat but has some variation in height.

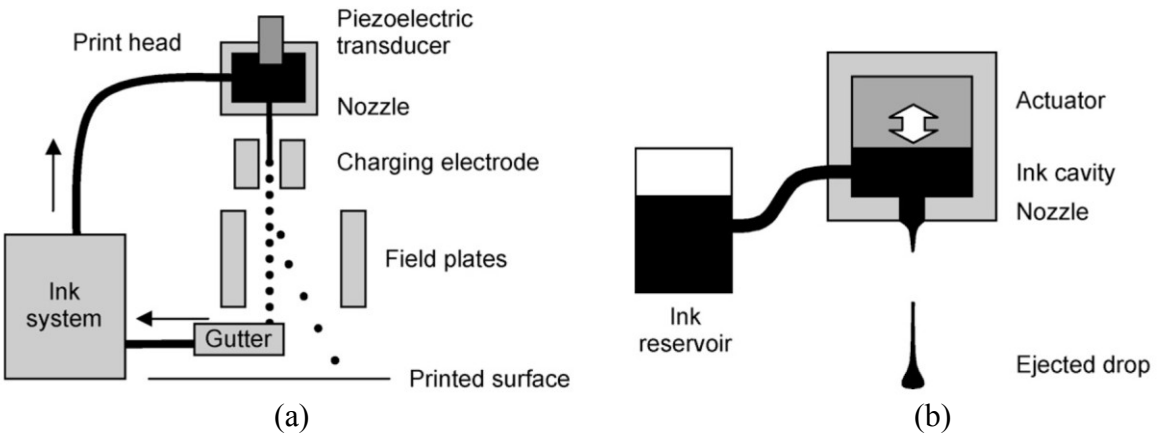

Figure 3. Schematic of the ink-jet technique: (a) is continuous ink-jet mode; (b) is drop-on-demand mode, from K.K.B. Hon et al., "Direct writing technology – Advances and developments," CIRP Annals – Manufacturing Technology, Vol. 57, Copyright 2008 [1]. Reproduced with permission from Elsevier.

The following advantages of the ink-jet direct-write can be noted:

- high resolution, which is about 20 micron currently;
- scalability to large area manufacturing which can be done by introducing several nozzles;
- low cost because there is no need to use an expensive mask with concomitant reduction in waste given the additive nature of the direct-write technique;
- non-invasive deposition; and
- computer-controlled patterning.

Disadvantages of this technology lie mostly in the formulation of proper ink. First, the colloidal ink should contain small particles without a tendency to agglomerate; otherwise the ink-jet nozzle can be easily clogged. Second, inks used for continuous ink-jet printing have to have low viscosity in the range of 2-10 cP. This requirement should be met to easily extract the liquid droplet out of the nozzle or orifice. Inks for the drop-on-demand mode should have viscosity in the range of 10-100 cP. Another restriction for the ink

formulation is surface tension of the ink, because the droplet generation process is governed by the surface tension force. Also ink wettability on the substrate plays a significant role in final feature size: low surface tension inks can lead to droplet spreading. The range of ink fluids and suspensions which is deposited in ink-jet direct-write can be extended by heating, cooling, stirring, wiping, purging, pre-oscillating, diluting, and other methods [12]. However, this extension is difficult when orifice diameter decreases, frequency increases, and number of jet in array increases. Not only must fluid restrictions be satisfied for the ink, but also it is very important to have good electrical and mechanical properties of the ink being deposited on the substrate. First, the ink has to have good adhesion to the substrate; and second, printed lines must exhibit good electrical conductance for many applications.

1.2.2. Aerosol-Jet Direct-Write

Aerosol-jet (formerly Maskless Mesoscale Material Deposition or M^3D) is another droplet-based method of the direct-write fabrication developed by Optomec Inc. [14]. In contrast with ink-jet printing, in aerosol-jet direct-write the liquid droplets are produced via the aerosol generator by some actuator (pneumatic or ultrasonic) and then moved through a nozzle due to the motion of the carrier gas. Another difference is that the aerosol particles before entering the nozzle inlet are already pre-focused because of usage of sheath gas. At the same time, the sheath gas is employed to prevent ink clogging inside of the deposition head. Final focusing of aerosol flow is done by the micro-nozzle attached to the deposition head (see Figure 4 below). Convergent micro-nozzles are also used here to accelerate aerosol particles to high velocity of about 50 m/s. This high speed of the particles allows variation of the distance between the nozzle outlet and the substrate from 1 to 5 cm, which

in turn leads to deposition of patterns on substrates with little dependency on the substrate morphology. At any time, the deposition head is fixed, but due to the substrate movements in x, y, and/or z-directions, lines of any configurations can be printed on the substrate.

Droplets used in the aerosol-jet technique are much smaller than in the case of the ink-jet printers: their sizes are about 1-5 microns, while droplet generated in ink-jet printers are about 10-150 microns. It should be noted that here most of ink droplets have no contact with the nozzle wall due to the initial pre-focusing; therefore, there is no viscosity limits for the ink formulation. Researchers claim that the viscosity of inks used in the aerosol-jet method can be from 0.7 cP to 2500 cP, while the ink viscosity in the ink-jet printing is less than 100 cP. Also since aerosol droplets have no contact with the nozzle wall, this helps to resolve the problem of the nozzle clogging. Another advantage of the aerosol-jet method is that ink does not have many requirements in terms of surface tension.

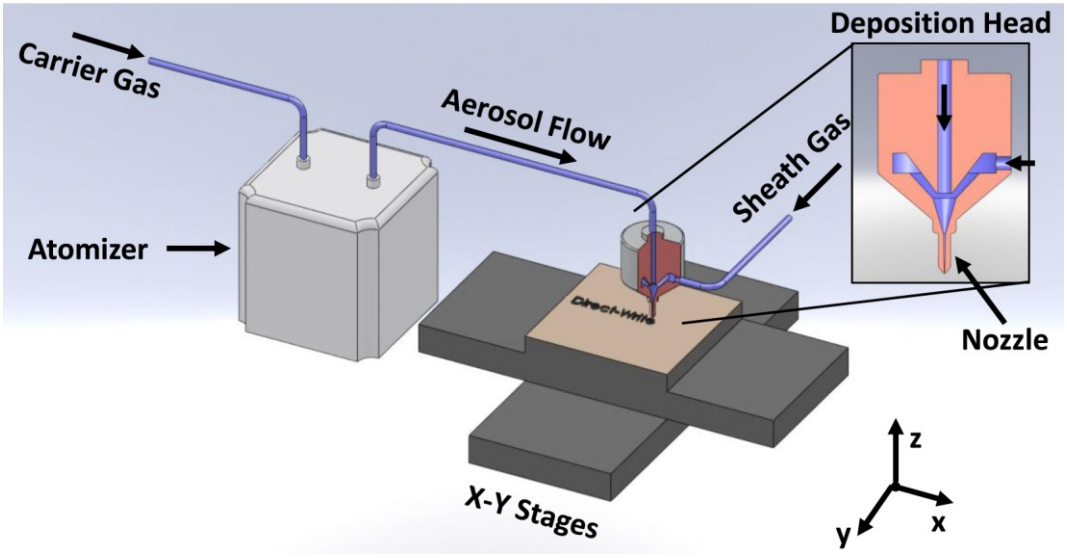

Figure 4. Schematic of the aerosol-jet technique, from Justin M. Hoey et al., "A Review on Aerosol-Based Direct-Write and Its Applications for Microelectronics," Journal of Nanotechnology, Vol. 2012, Copyright 2012 [15]. Reproduced with permission from Hindawi Publishing Corporation.

In comparison with ink-jet printing technology, the aerosol-jet method has higher resolution of 10 microns. Sub-category of the aerosol-jet method called collimated aerosol beam direct-write (CAB-DW) can produce lines with the line widths of 5 microns [16, 17]. This can be done by using a set of three nozzles (convergent-divergent-convergent) attached to each other. An example of silver lines printed by the CAB-DW system is presented in Figure 5, while a line printed by regular aerosol-jet method is shown in Figure 6. Based on Figure 6, we see that the line width is about 25 microns and the ink overspray is detected. So there is a need to design a nozzle which allows better particle focusing and collimation.

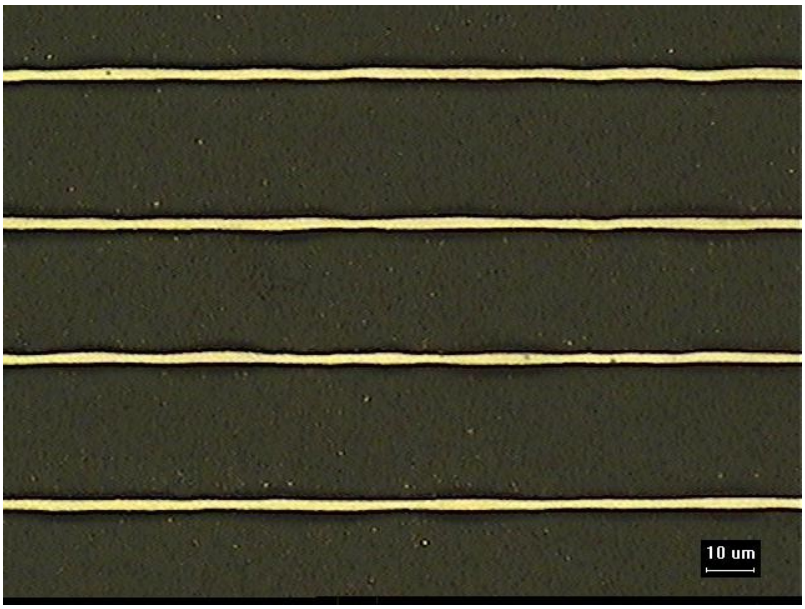

Figure 5. Silver lines printed by the CAB-DW technique.

It was shown that a wide variety of materials can be deposited via aerosol-jet direct-write method, namely, nano-particle metal suspensions, polymers, adhesives, etchants, ceramics, paste-like fluids, and bio-related materials. All of these materials may be printed

on different rigid and flexible substrates including silicon, polyimide, glass, FR-4, and aluminum oxide. This makes the aerosol-jet technique attractive for the fabrication of flexible displays, electronics, sensors, high efficiency solar cells, antennas, RFIDs, etc.

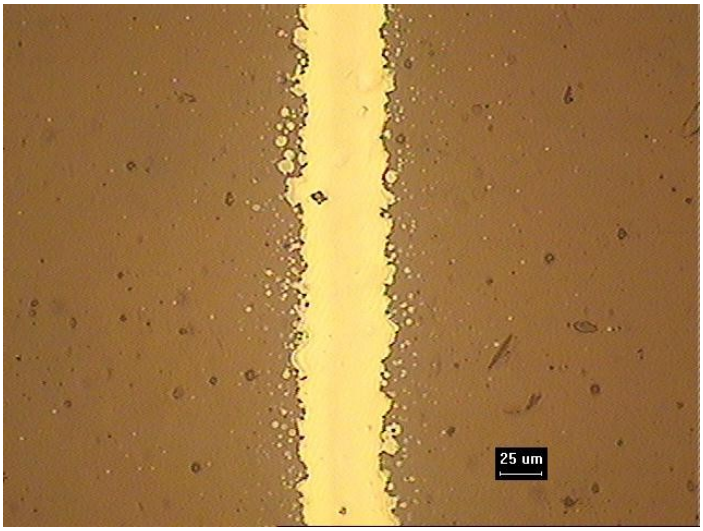

Figure 6. Line printed by the aerosol-jet technique.

1.3. Dissertation Outline

Summarizing sub-chapter 1.1, it can be concluded that problems associated with current tip-based direct-write methods include minimization of printed features as well as non-modification of the tip and the substrate during the material deposition. Therefore, a new capillary-based technique is proposed for deposition of tiny liquid droplets on substrates. Reviewing the droplet-based direct-write methods (sub-chapter 1.2), it is shown that the main drawbacks consist of the line width minimization and the ink overspray. Thus, the goal of this research is twofold.

The first part of the dissertation is devoted to development of a new method of lithography that generates features on a substrate without any modification of the substrate by using micro/nano-capillary. Theoretical modeling reveals regimes where micro/nano-droplet deposition can be achieved using a micro/nano-capillary as a deposition tool. Smaller liquid dots can be printed because the deposition mechanism is theoretically investigated so that the size of deposited dots can be controlled. It is found in this study that there are five major parameters responsible for deposition of smaller droplets: inner radius and wall thickness of the capillary, applied pressure, liquid-capillary and liquid-substrate equilibrium contact angles. The model is verified and validated using experimental observations in the micro-deposition setup, where glycerol/water solution is employed as deposition liquid and hydrophobic glass is used as a substrate. Additionally, improvements to the current fluid delivery system are identified. To extend this method for the case of nano-scale, a Scanning Tunneling Microscope is modified. A gold-coated nano-capillary is used both as the STM tip and as the fluid delivery system. It is shown in this study that it is possible to deposit liquid dots with radii as small as 3 microns.

The second part of the dissertation is dedicated to modeling the aerosol flow through a micro-nozzle, where the Eulerian-Lagrangian approach is employed. Therefore, the gas motion through the micro-nozzle is simulated separately from the particle motion by using ANSYS CFX. Then, gas flow field data is imported into the Matlab code to calculate the particles' trajectories and velocities. The developed model of the aerosol flow is compared with experiments using the shadowgraphy system. Based on this comparison, it is concluded that only Stokes and Saffman forces should be enough to describe the gas-particle interaction. Other forces, e.g. Magnus force, Buoyancy force, Pressure Gradient

force, Basset force, Virtual Mass force, are found to be not important for the gas-particle interaction. Using verified aerosol flow model, a new nozzle design is proposed to collimate aerosol particles toward the nozzle centerline. Furthermore, it is found that higher density particles and higher flow rate can enhance the particle collimation. So, lines printed out of the proposed nozzle will have smaller line-width and there will be no over spray of the material out of lines.

2. CAPILLARY-BASED LITHOGRAPHY

2.1. Proposed Capillary-Based Droplet Deposition Concept

Two tip-based methods of direct write technology are widely used nowadays: dip-pen nanolithography and nano-fountain pen lithography. In both techniques, a tip of the atomic force microscope (AFM) is employed to create nano-structures on the substrate. Since the AFM tip radius curvature is about 5 nm, it is possible to form features on the substrate as small as 10-15 nm. The main disadvantage of dip-pen nanolithography is re-dipping. In order to get rid of the process of immersing the tip into the ink reservoir, in the nano-fountain lithography technique, a regular AFM tip is replaced by a volcano tip. This modified volcano tip consists of two parts: a regular AFM tip in the core and a shell around the tip in order to have a micro-channel between the tip and shell. By connecting the volcano tip with the ink reservoir, the problem of re-dipping is solved due to continuous fluid delivery supply towards the deposition area. However, in both current tip-based methods (dip-pen nano-lithography and nano-fountain pen lithography), tips are in contact with substrate, so the tip wearing happens during the deposition. To eliminate the problem of invasive deposition, we propose to employ a new method: capillary-based deposition [18, 19]. The concept of capillary-based liquid droplet deposition is simply outlined as follows: (i) the capillary is filled with the liquid to be deposited on the substrate; (ii) the liquid meniscus protruding from the capillary tip forms due to the pressure applied from the other end of the capillary (see Figure 7a); (iii) the capillary is moved toward the substrate until the liquid meniscus touches the substrate at which moment a liquid bridge connecting the capillary to the substrate forms (see Figure 7a and c); (iv) the capillary is moved away

from the substrate, causing a bridge rupture, which leaves a residual liquid droplet on the substrate (see Figure 7d). To control the process of the liquid droplet deposition, one must understand the physics of the liquid bridge under different conditions.

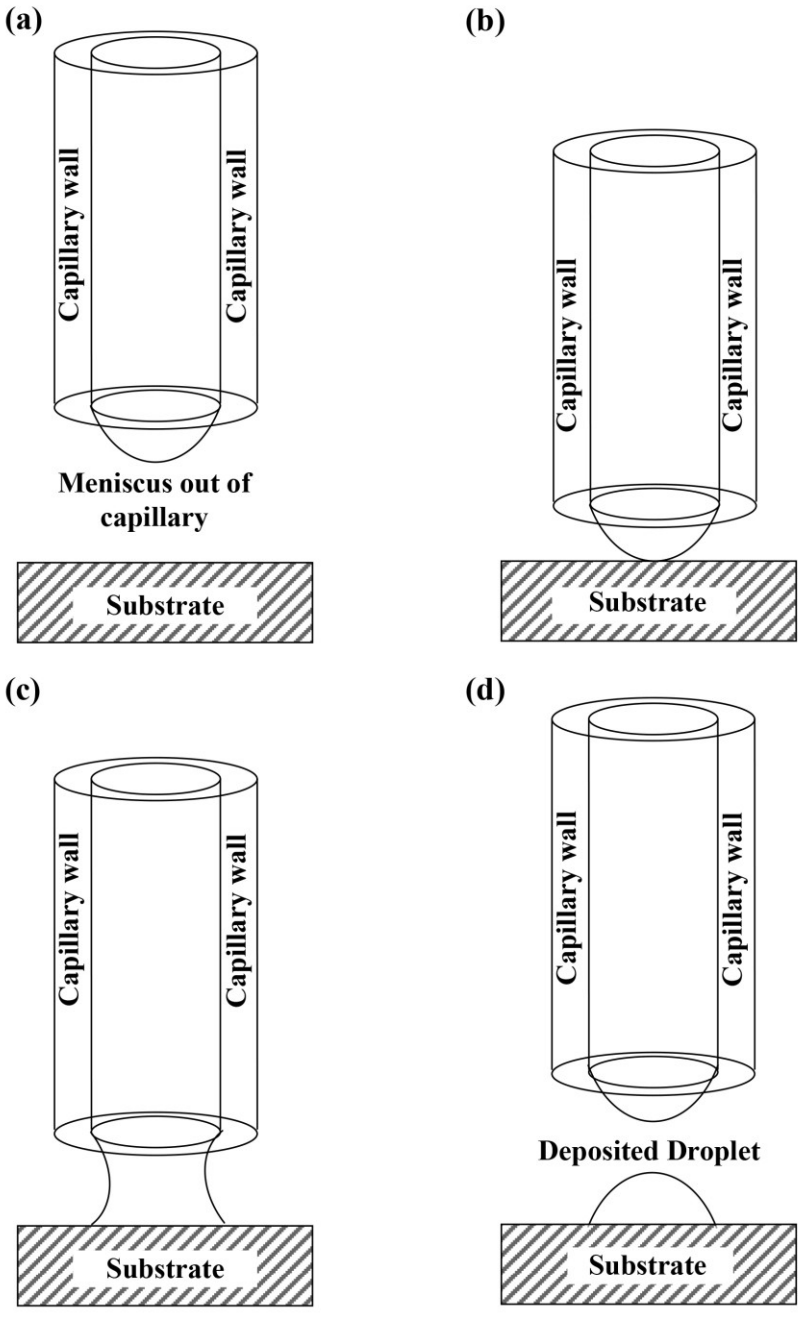

Figure 7. Proposed lithography technique.

Since the size of the nano-capillary is in the range of 100 nm, it is expected that the size of the deposited droplet may have the same order of magnitude. To implement this method, the Scanning Tunneling Microscope (STM) was modified, replacing the STM tip by the gold-coated nano-capillary.

This technique differs from others since it assumes the liquid deposition on the substrate without any modifications of the substrate. At the same time, the proposed technique employs a precise navigation of the nano-capillary, because its motion in X, Y, Z coordinates is controlled by the STM software. In order for the STM to be used, this method requires having a conductive capillary and substrate. That is why the glass nano-capillary was coated by chrome and gold. A thin layer of chrome is needed between the glass and gold to have good adhesion for the gold. The thickness of a gold layer is about 30 nm, and the thickness of chrome is 5 nm. Highly Oriented Pyrolytic Graphite (HOPG) was chosen as a conductive substrate due to high conductivity and low roughness of the substrate.

In order to implement this method, the following tasks had to be resolved:

- Theoretical modeling of the meniscus formation
- Theoretical development of the static bridge theory
- Theoretical consideration of different deposition scenarios to understand the best regime of micro/nano-droplet printing
- Understanding of dependency of all parameters on the size of the deposited droplet
- Force analysis of bridge (theoretical modeling of liquid bridge-substrate interaction)

- Experimental estimation of the interfacial energies of interaction between the liquid and different substrates in order to evaluate substrate-liquid and capillary-liquid interaction forces
- Experiments in micro-scale in order to verify the deposition theory
- Producing and characterizing of the nano-capillary
- Liquid treatment and insertion into nano-capillary
- Integration of the nano-capillary in the STM
- Tip-substrate distance evaluation in order to control the distance between the meniscus and substrate.

The following sub-chapters present how these tasks have been resolved.

2.2. Capillary-Based Liquid Droplet Deposition

2.2.1. General Overview

During the process of the deposition, the liquid out of the capillary can form two different structures: the meniscus and the bridge. For the simplicity, these two forms are considered separately below. In the modeling of the meniscus and the bridge, the following assumptions and simplifications were implemented:

1. The substrate roughness in nano-scale is neglected. Since the inner radius of the nano-capillary used is about 100 nm and the substrate roughness is about 5 nm for an area of 5 by 5 micron, the substrate roughness can be ignored.

2. The contact angle between substrate and liquid measured in micro-scale is applicable for nano-scale consideration, because it is impossible to measure the contact angle between nano-droplet and substrate.
3. The capillaries with small inner diameter are considered, thus the surface force is a dominant force during the deposition. Therefore the gravity force is ignored. The inner diameter of capillaries can vary from 200 nm to 500 micron.
4. It is assumed that the outer surface and the bottom edge of the capillary are hydrophobic to the deposition liquid.
5. Because the meniscus and the bridge can be presented by rotating the 2-D figure around the axis of symmetry, the shapes of the meniscus and the bridge are shown as a 2-D plot.

2.2.2. Meniscus

The meniscus size depends on the applied pressure: the higher the applied pressure, the higher the size of the meniscus. Another crucial parameter is the contact angle between liquid and capillary:

- If the liquid-capillary equilibrium contact angle, θ_C^e, is less than 90°, this capillary will be called “wettable” nano-capillary,
- If the liquid-capillary equilibrium contact angle, θ_C^e, is more than 90°, this capillary will be called “non-wettable” capillary.

In the case of a wettable nano-capillary, when pressure is applied to the free nano-capillary end, the meniscus shape changes as shown in Figure 8. First, the meniscus

reaches the liquid-capillary equilibrium contact angle. Then, it moves along the bottom edge of the nano-capillary, keeping this angle constant.

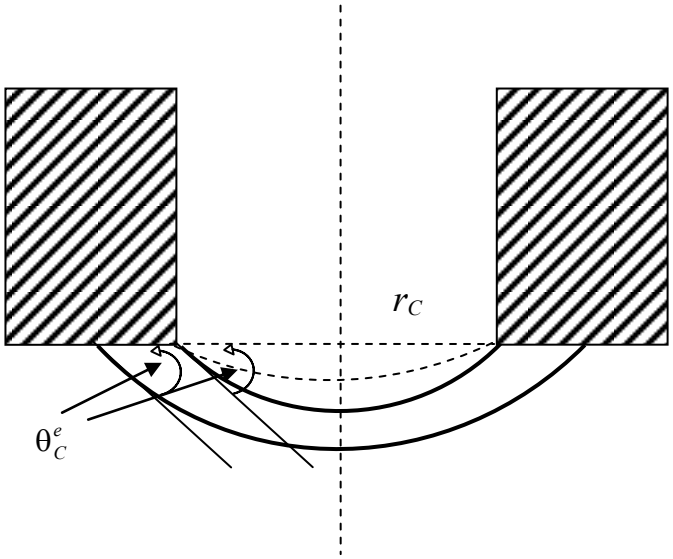

Figure 8. Meniscus changes in the case of wettable capillary.

In the case of a non-wettable capillary, one can divide the meniscus growth in three stages: the meniscus until the curvature radius is equal to the capillary radius (critical state), the meniscus from the critical state until it reaches the contact angle, and the meniscus when it starts to spread over the bottom edge of the capillary. The volume and area of the meniscus in the first stage are as follows:

$$V = \pi h_M^2 \left(r_\sigma - \frac{1}{3} h_M \right), \; A = 2\pi r_\sigma h_M \tag{1}$$

where r_σ and h_M are the curvature radius and meniscus thickness, respectively (for details see Figure 9). The thickness of the meniscus is related to the curvature radius by: $h_M = r_\sigma - \sqrt{r_\sigma^2 - r_C^2}$. The curvature radius depends on the applied pressure: $r_\sigma = \frac{2\sigma}{p}$.

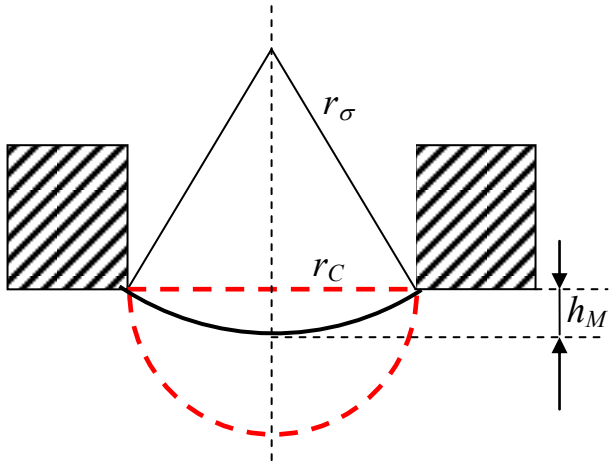

Figure 9. First stage of meniscus growth (non-wettable capillary).

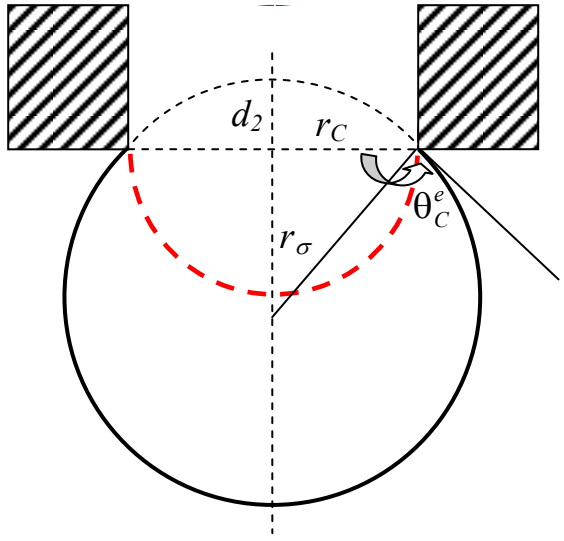

Figure 10. Second stage of meniscus growth (non-wettable capillary).

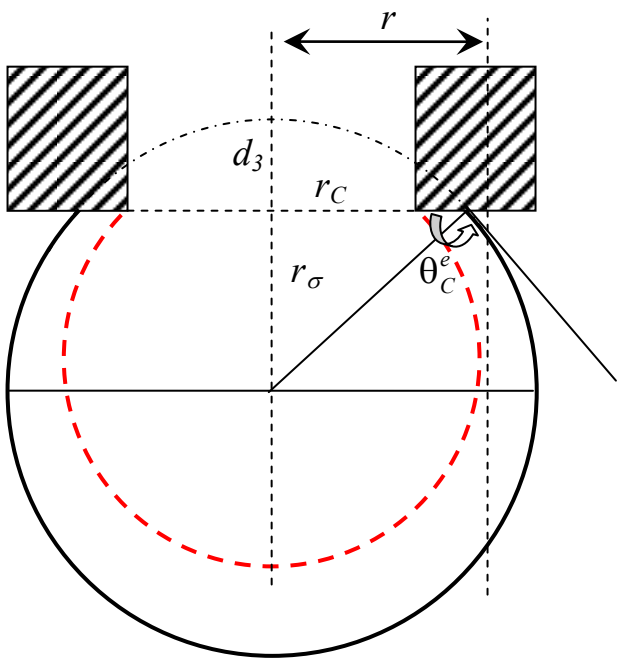

Figure 11. Third stage of meniscus growth (non-wettable capillary).

The volume and area of the meniscus in the second stage are defined as follows:

$$V = \frac{4}{3}\pi r_\sigma^3 - \pi d_2^2\left(r_\sigma - \frac{1}{3}d_2\right),\ A = 4\pi r_\sigma^2 - 2\pi r_\sigma d_2 \qquad \textbf{(2)}$$

where parameter d_2 is equal to $d_2 = r_\sigma - \sqrt{r_\sigma^2 - r_C^2}$ (see Figure 10).

The volume and area of the meniscus in the third stage can be calculated as follows:

$$V = \frac{4}{3}\pi r_\sigma^3 - \pi d_3^2\left(r_\sigma - \frac{1}{3}d_3\right),\ A = 4\pi r_\sigma^2 - 2\pi r_\sigma d_3 \quad \textbf{(3)}$$

where parameter d_3 is equal to $d_3 = r_\sigma - \sqrt{r_\sigma^2 - r^2}$ and $r_\sigma = \frac{r}{\cos\left(\theta_C^e - 90\right)}$. Angle θ_C^e is the equilibrium contact angle between capillary and liquid (non-wettable capillary, $\theta_C^e > 90°$, see Figure 11).

2.2.3. Bridge Theory

Liquid bridges are used to form a range of materials in processes such as float zone crystal growth [20, 21] and microfluidic biochemical reactors [22]. The fluid dynamics of liquid bridge formation is also employed in areas such as metallurgy, soil properties, particle sedimentation, and oil recovery from porous media [23, 24]. Bridge formation inside the human lung alveoli was recently considered experimentally [25] and modeled theoretically [26] and these results provide some insight regarding airway closure in the lungs with the theoretical analysis giving an estimate for the timescales associated inside alveoli. Liquid bridges and droplets also play an important role in the design of fuel tanks for spacecraft where, under micro-gravity conditions, the shape of the liquid surface is dependent on both the shape of the container and the surface property of the container material [27].

The first study related to the stability of liquid bridges was reported in 1863 by Plateau who considered the breakup of a liquid jet [28]. The force of interaction in an ideal soil was experimentally investigated by Haines who studied the liquid bridge forming between two physically-contacted identical spheres (i.e., soil particles) [29]. This data was later

theoretically analyzed by Fisher who estimated the cohesive forces in ideal soil and calculated the fluid neck radius of the bridge [30]. Another approach was taken by Mason and Clark who developed an experimental method for the measurement of the forces exerted on two spheres by liquid bridges [31]. Orr et al. explored a more general case, e.g. liquid bridges between a sphere and a flat substrate [32]. They analyzed the influence of different contact angles at the sphere and the plate to the bridge structures. It should be noticed that most liquid bridge studies were devoted to axisymmetric bridges between two solid bodies: two equal spheres [29, 30], sphere and horizontal plane [32], and two equal and non-equal disks [33-36]. Influence of non-axisymmetric perturbation was studied by Slobozhanin et al. in [37]. A case of non-axisymmetric liquid bridge between two parallel disks was investigated by Meseguer et al. [38]. In all of the studies mentioned above, see references [29-38], only liquid bridges of constant mass were considered, but the mass of the bridge between the liquid filled capillary and the substrate is changeable, and the pressure in the bridge is fixed. The liquid bridge dynamics between hollow capillary and substrate was considered recently in [39], but the stability of the liquid bridge was not studied.

The main objective of this chapter is to define the parameter range where stable liquid bridges form between a hollow liquid-filled capillary and a flat substrate. Therefore the chapter is organized as follows. The first part of the chapter is devoted to discussing the development of a static theory for liquid bridge formation that is based upon four main parameters: capillary-substrate distance or height, pressure applied to the liquid inside the capillary, liquid-capillary equilibrium contact angle, and liquid-substrate equilibrium contact angle. The second part of the chapter is depicted to the experimental verification of

the theoretical model where water/glycerol mixtures of various viscosity and capillaries of varying diameters were used to probe the deposition process.

The liquid bridge plus liquid between the hypothetical piston and the capillary edge (parts marked on Figure 12a as V_B and V_C, respectively) can be considered as a closed system at constant pressure, temperature, and mass (volume). Radius of the capillary is small ($Bo << 1$) so that liquid pressure is uniform in the bridge. The steady bridge forms when the work of external forces on the system's virtual displacement, δW_{ext}, is equal to the variation of surface energy of the system, δE_Σ:

$$\delta W_{ext} = \delta E_\Sigma, \tag{4}$$

$$\delta W_{ext} = -p dV_C - p_0 dV_B = (p - p_0) dV_B, \quad dV_C = -dV_B, \tag{5}$$

$$\delta E_\Sigma = \gamma_{LV} \delta A_{LV} + (\gamma_{LS} - \gamma_{SV}) \delta A_{LS} \tag{6}$$

here p is pressure in the liquid bridge, p_0 is pressure in a surrounding atmosphere, V_C is volume of the liquid between piston and capillary edge, V_B is volume of the liquid bridge (between capillary edge and the substrate), A_{LV} is area of the liquid bridge's liquid-vapor interface, A_{LS} is area of the liquid bridge's liquid-substrate interface, and $\gamma_{LV}, \gamma_{LS}, \gamma_{SV}$ are energy of liquid-vapor, liquid-substrate, and substrate-vapor interface per unit area, respectively. Using the formulae for V_B, A_{LV}, A_{LS} (see Figure 12b for coordinate system)

$$V_B = \int_0^h \pi r^2(z)dz, \quad A_{LV} = \int_0^h 2\pi r(z)\sqrt{1+r'^2(z)}dz, \quad A_{LS} = \pi r_{BS}^2, \tag{7}$$

where $r(z), r'(z)$ are unknown shape function of the liquid bridge and its derivative, r_{BS} is the unknown radius of the bridge's base on the substrate, the condition (4) for the steady bridge can be presented in the following variational form:

$$\delta F = 0, \quad F = \int_0^h f(r,r')dz - \gamma_{LV}\pi r_{BS}^2 \cos\theta_S^e, \qquad f(r,r') = 2\pi\gamma_{LV} r(z)\sqrt{1+r'^2(z)} - (p-p_0)\pi r^2(z) \tag{8}$$

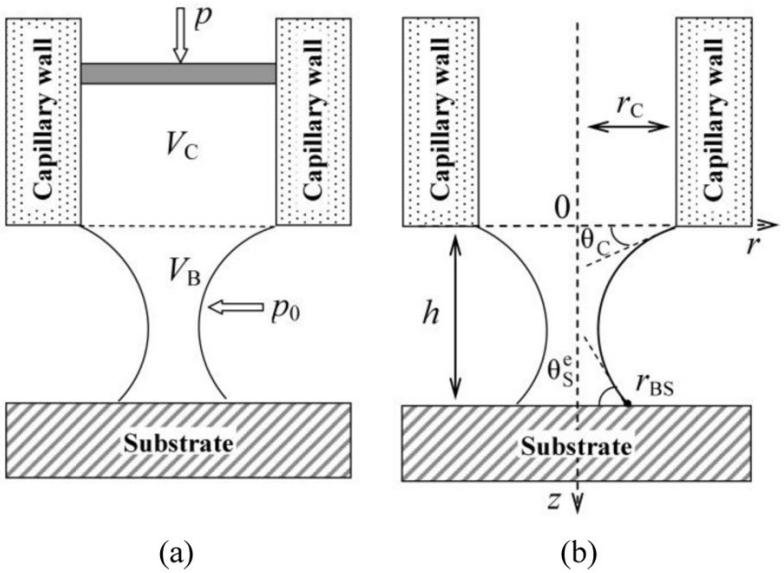

Figure 12. (a) Liquid in the bridge (zone V_B) and liquid between the (hypothetical) piston and the capillary edge (zone V_C) represent a closed system at constant pressure, temperature, and mass (volume). (b) Coordinate system used for modeling of liquid bridge shape between capillary and substrate.

Here θ_S^e is an equilibrium Young-Laplace liquid contact angle on the substrate

$$\cos\theta_S^e = \frac{\gamma_{SV} - \gamma_{LS}}{\gamma_{LV}}, \tag{9}$$

The solution of the variational problem (8) leads to the following necessary condition for the extremum of the functional F :

$$\frac{\partial f}{\partial r} - \frac{d}{dz}\left(\frac{\partial f}{\partial r'}\right) = 0, \tag{10}$$

$$\left(\frac{\partial f}{\partial r'}\delta r\right)\Big|_{z=0} = 0, \tag{11}$$

$$\left(\frac{\partial f}{\partial r'} - 2\gamma_{LV}\pi r\cos\theta_S^e\right)\Big|_{z=h} \cdot \delta r_{BS} = 0. \tag{12}$$

The Eq. (10) represents the condition that liquid pressure is uniform inside the bridge and equal to the capillary pressure

$$p - p_0 = \gamma_{LV}\left[\frac{1}{r\sqrt{1+r'^2}} - \frac{r''}{\left(1+r'^2\right)^{3/2}}\right]. \tag{13}$$

The condition (11) is satisfied with assumption that the beginning of the liquid bridge is fixed at the inner edge of the capillary

$$r(0) = r_C\,, \tag{14}$$

with the only restriction to the actual contact angle such as

$$\theta_C < \theta_C^e, \quad \cos\theta_C^e = \frac{\gamma_{CV} - \gamma_{LC}}{\gamma_{LV}}\,, \tag{15}$$

where θ_C^e is an equilibrium Young-Laplace liquid contact angle on the capillary, γ_{LC}, γ_{CV} are energy of liquid-capillary and capillary-vapor interface per unit area, respectively. The condition (12) can be rewritten as follows

$$2\pi\gamma_{LV}\left(\cos\theta_S - \cos\theta_S^e\right) r_{BS}\,\delta r_{BS} = 0\,. \tag{16}$$

Since the radius of the bridge's base is not fixed, the condition (16) is naturally satisfied when actual liquid contact angle on the substrate is equal to the equilibrium one, calculated from the Eq. (9):

$$\theta_S = \theta_S^e \text{ or } r'(h) = -\tan\left(\theta_S^e - \frac{\pi}{2}\right). \tag{17}$$

Thus, the shape of the bridge can be found as the solution of the Eq. (13) with boundary conditions (14) and (17). Systematic study of the bridge shape problem was conducted using two dimensionless parameters:

$$H = \frac{h}{r_C}, \quad P = \frac{(p - p_0) r_C}{2\gamma_{LV}}, \tag{18}$$

that along with two Young-Laplace equilibrium contact angles, θ_S^e, θ_C^e determine the solution of the problem completely.

The (H, P) diagram for the case $\theta_C^e = \theta_S^e = 95^\circ$ corresponding to the experimental parameters used in this paper is presented in Figure 13. Line 0 (bold dashed line) corresponds to capillary-substrate distance at which liquid meniscus protruded from the capillary tip first touches the substrate at given pressure:

$$H = \frac{1}{P} - \sqrt{\frac{1}{P^2} - 1}. \tag{19}$$

Shaded area shows the parameters range where steady liquid bridge is possible to form, which means the solution of the problem (13), (14), (17) exists and the condition (15) is satisfied. There are three distinct parameter ranges associated with three different deposition scenarios.

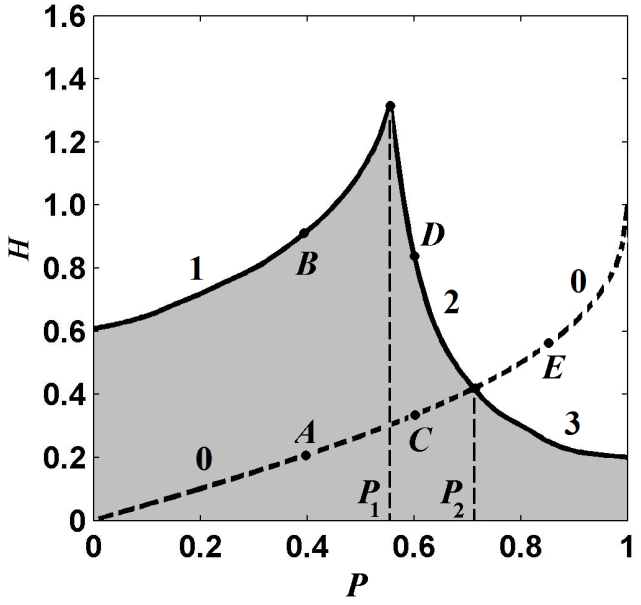

Figure 13. The (H, P) diagram for steady liquid bridge between capillary and substrate: H, P are defined in Eq. (18) and $\theta_C^e = \theta_S^e = 95^\circ$.

2.2.4. Deposition Scenarios

Range 1 ($0 < P < P_1$). Solid line 1 corresponds to the capillary-substrate distance (at given pressure) below which a stable bridge can be formed. Bridges above line 1 cannot be created as the solution of the system (13), (14), (17) does not exist due the fact that actual liquid-substrate angle cannot be equal to the equilibrium one: solution of Eq. (13) with shooting method leads to the fact that the actual liquid-substrate angle is less than the equilibrium one, θ_S^e, for any liquid-capillary contact angle. Therefore, if normalized liquid pressure is somewhere in the range $0 < P < P_1$ (see Figure 13), for example $P = 0.4$, the following scenario of liquid deposition is expected. The capillary with liquid meniscus protruding from the capillary tip moves towards the substrate until the liquid meniscus touches the substrate (point A at the intersection of line $P = 0.4$ with dashed line associated

with the Eq. (19)). At that moment the steady liquid bridge connecting the capillary with the substrate forms. If the capillary is moving up away from the substrate, then the capillary-substrate distance increases. At some point, when this height rises above line 1 (point B at the intersection of line $P = 0.4$ with line 1), it is expected that bridge will rupture naturally (even at zero retraction speed) leaving a micro-droplet on the substrate.

Range 2 ($P_1 < P < P_2$). Solid lines 2 and 3 correspond to the capillary-substrate distance (at given pressure) at which liquid-capillary contact angle is equal to the equilibrium one, $\theta_C = \theta_C^e$, and the condition (15) is no longer satisfied. When the capillary-substrate distance rises above lines 2 and 3, the schematic presented in Figure 12b is no longer applicable. It should be changed to the one presented in Figure 14, where the beginning of the liquid bridge is not fixed at the inner edge of the capillary, but instead can be shifted along the capillary edge. Then the equation (6) for the variation of surface energy of the system, δE_Σ, has to be reformulated as such:

$$\delta E_\Sigma = \gamma_{LV}\delta A_{LV} + (\gamma_{LS} - \gamma_{SV})\delta A_{LS} + (\gamma_{LC} - \gamma_{CV})\delta A_{LC}, \quad A_{LC} = \pi\left(r_{BC}^2 - r_C^2\right), \tag{20}$$

where A_{LC} is area of the bridge's liquid-capillary interface and r_{BC} is the unknown radius of the bridge's base on the capillary. The condition for the steady bridge (4), (5), (7), (20) can be presented in the following variational form (compare with (8)):

$$\delta F = 0, \quad F = \int_0^h f(r, r')dz - \gamma_{LV}\pi r_{BS}^2 \cos\theta_S^e - \gamma_{LV}\pi\left(r_{BC}^2 - r_C^2\right)\cos\theta_C^e \quad , \tag{21}$$

Here θ_C^e is an equilibrium Young-Laplace liquid contact angle on the capillary

$$\cos\theta_C^e = \frac{\gamma_{CV} - \gamma_{LC}}{\gamma_{LV}}, \tag{22}$$

The solution of the variational problem (21) gives the same equation for the shape of the bridge ((10), (13)) with the same boundary condition on the substrate ((12), (16), (17)), and with the new boundary condition on the capillary edge:

$$\left(\frac{\partial f}{\partial r'} + 2\gamma_{LV}\pi r\cos\theta_C^e\right)\Bigg|_{z=0} \cdot \delta r_{BC} = 0. \tag{23}$$

The condition (23) can be rewritten as following

$$2\pi\gamma_{LV}\left(\cos\theta_C - \cos\theta_C^e\right) r_{BC}\delta r_{BC} = 0. \tag{24}$$

Since the radius of the bridge's base on the capillary, r_{BC}, is not fixed, the condition (24) is naturally satisfied only when actual liquid contact angle on the capillary is equal to the equilibrium one, calculated from the Eq. (22):

$$\theta_C = \theta_C^e \text{ or } r'(0) = \tan\left(\theta_C^e - \frac{\pi}{2}\right) \tag{25}$$

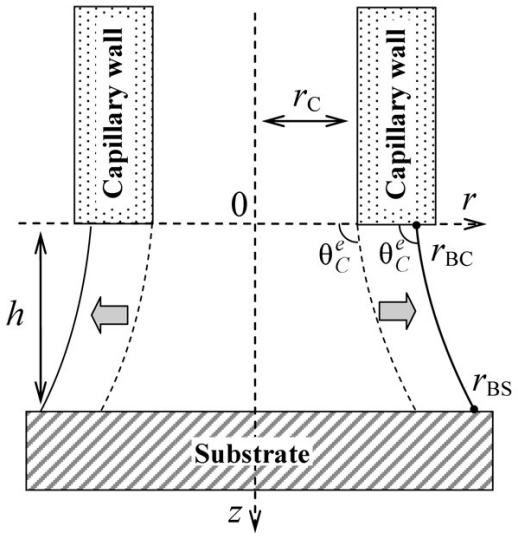

Figure 14. Liquid bridge schematic when $\theta_C = \theta_C^e$ and the beginning of the liquid bridge is not fixed at the inner edge of the capillary, but instead can be shifted along the capillary edge.

Thus, when the capillary-substrate distance rises above lines 2 and 3 (Figure 13) the shape of the bridge is the solution of the Eq. (13) with boundary conditions (17) and (25). But such solution does not exist; therefore, it is impossible to form stable bridges above of lines 2 and 3. This leads to the fact that the bridge will be spreading along the bottom edge of the capillary. At some point, the bridge will reach outer diameter of the capillary, and the capillary boundary condition (25) will be changed to:

$$r(0) = r_O\,, \tag{26}$$

where r_O is outer capillary radius. The condition (26) assumes that the beginning of the liquid bridge is fixed at the outer edge of the capillary. Note that there is no restriction to

the actual capillary contact angle, θ_C. To find the steady bridge shape formed at outer capillary diameter, one has to solve Eq. (13) with boundary conditions (17) and (26).

Therefore, if liquid pressure is somewhere in the range $P_1 < P < P_2$ (see Figure 13), for example $P = 0.6$, the following scenario of liquid deposition is envisioned. The capillary with liquid meniscus protruding from the capillary tip moves towards the substrate until the liquid meniscus touches the substrate (point C at the intersection of line $P = 0.6$ with dashed line associated with the Eq. (19)). At that moment the steady liquid bridge connecting the capillary with the substrate forms. The capillary is moving up away from the substrate and the bridge loses its stability when liquid-capillary contact angle is getting equal to its equilibrium value (point D at the intersection of line $P = 0.6$ with line 2). After that the bridge spreads along the capillary bottom edge and no steady bridge can be formed until the bridge reaches the outer capillary diameter. At this point, the bridge shape will be steady.

Range 3 ($P_2 < P < 1$). If liquid pressure in Figure 13 is from the range $P_2 < P < 1$ (e.g., 0.9), the following scenario of liquid deposition is expected. The liquid meniscus touches the substrate at point E at the intersection of line $P = 0.9$ with dashed line associated with the Eq. (19)). At that point the steady liquid bridge connecting the capillary with the substrate does not exist and the bridge will start spreading along the capillary bottom edge right after the contact. Again, as in case of Range 2, the bridge will move until it reaches the outer capillary diameter, and then it will stop by forming steady shape.

Contour plots of the bridge-capillary angle and the base bridge radius are presented in Figure 15 and Figure 16, assuming that $\theta_C^e = \theta_S^e = 95^\circ$. We observe that the base bridge radius and the bridge-capillary angle decrease as they approach line **1**. In contrast, if height

and pressure are close to lines **2** and **3**, then the base bridge radius and the bridge-capillary angle increase. More details are presented in Figure 17 and Figure 18, where the bridge-capillary angle and the base bridge radius are calculated along the lines **1**, **2**, and **3**. Figure 19 shows the dependency of the base bridge radius on the capillary-substrate height at different pressures: 0.2, 0.4, 0.6, and 0.8. If the pressure is in Range 1, then the base radius is exponentially decaying while coming to rupturing line 1. An opposite behavior can be seen, if pressures are from Range 2 and 3. First, the base bridge radius is slightly decaying with increase of the capillary-substrate height, but then it starts to grow while coming to lines 2 and 3. Based on these results, we can conclude that application of pressure within Range 1 (i.e., $P < 0.55$) is preferable to minimize the deposited droplet size.

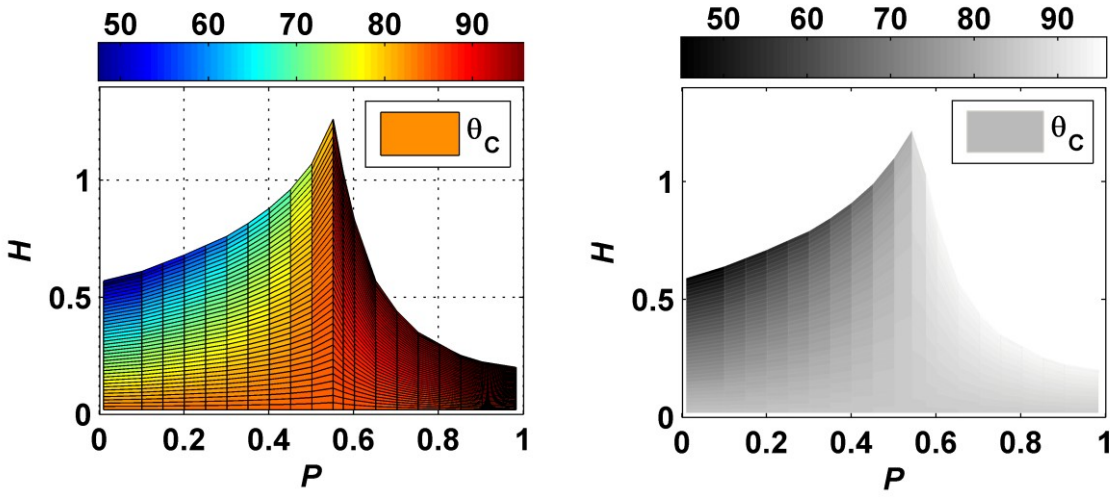

Figure 15. Contour plot of the liquid bridge-capillary angle, when $\theta_C^e = \theta_S^e = 95^\circ$.

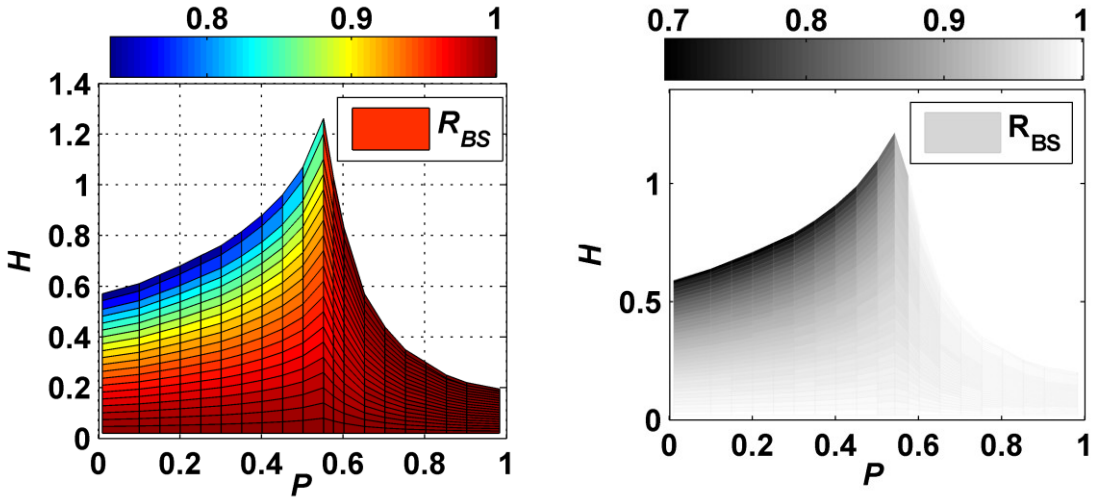

Figure 16. Contour plot of the base bridge radius, when $\theta_C^e = \theta_S^e = 95^\circ$.

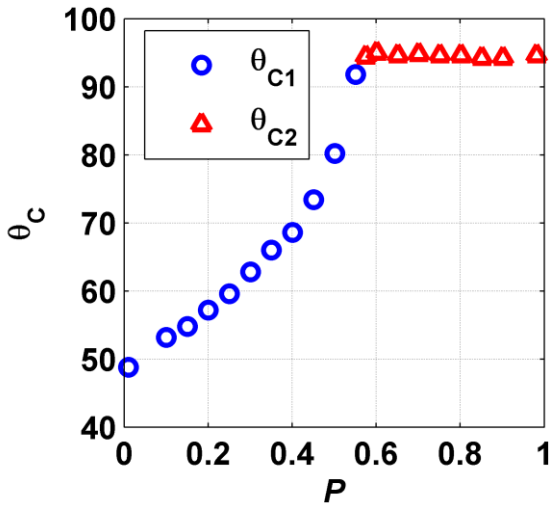

Figure 17. The liquid bridge-capillary angle as a function of pressure, when $\theta_C^e = \theta_S^e = 95^\circ$, blue circles correspond to the line 1, red triangles correspond to the lines 2 and 3. These lines are shown in Figure 13.

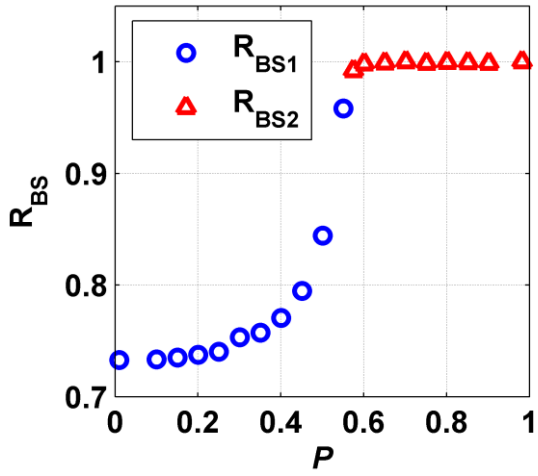

Figure 18. The base bridge radius as a function of pressure, when $\theta_C^e = \theta_S^e = 95^\circ$, blue circles correspond to the line 1, red triangles correspond to the lines 2 and 3. These lines are shown in Figure 13.

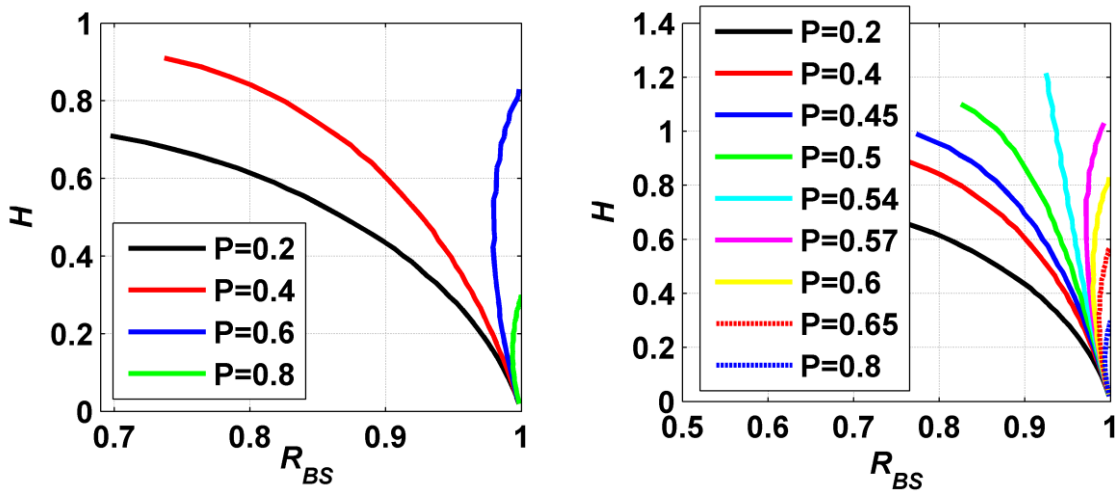

Figure 19. The base bridge radius as a function of capillary-substrate distance at different pressures.

Based on theoretical analysis of three pressure ranges, we emphasize that to produce predictable deposition, only pressures from Range 1 could be applied. If the pressure applied is from Range 2 or 3, the bridge spreading on bottom side of the capillary will lead

to larger droplet. So in the case, when $\theta_C^e = \theta_S^e = 95^\circ$, for smaller droplet deposition, one has to set pressure less than 0.55.

2.2.5. Stability Diagrams

A study for different liquid-capillary and liquid-substrate equilibrium contact angles are presented below. First, an example, when the liquid-capillary equilibrium angle is fixed ($\theta_C^e = 95^\circ$), but the liquid-substrate equilibrium angle varies, is presented in Figure 20 ($\theta_S^e = 85^\circ, 90^\circ, 95^\circ, 100^\circ, 105^\circ$). Downward pointing triangle, upward pointing triangle, square, cross, and circle markers in Figure 20 correspond to $\theta_S^e = 85^\circ, 90^\circ, 95^\circ, 100^\circ, 105^\circ$, respectively. We observe that desirable pressure Range 1 increases while liquid-substrate angle increases. For the red line with upward pointing triangles, Range 1 is bounded by $P = 0$ and $P = 0.5$. For the black line with square symbols, Range 1 is bounded by $P = 0$ and $P = 0.55$. For blue line with cross markers, Range 1 is bounded by $P = 0$ and $P = 0.6$.

Second, an example, when the liquid-substrate equilibrium angle is fixed ($\theta_S^e = 95^\circ$), but the liquid-capillary equilibrium angle varies ($\theta_C^e = 85^\circ, 90^\circ, 95^\circ, 100^\circ, 105^\circ$), is presented in Figure 21. Downward pointing triangle, upward pointing triangle, square, cross, and circle markers in Figure 21 correspond to $\theta_C^e = 85^\circ, 90^\circ, 95^\circ, 100^\circ, 105^\circ$, respectively. We see that desirable pressure Range 1 increases while liquid-capillary angle increases. For red line with upward triangles, Range 1 is from 0 to 0.52. For black line with square symbols, Range 1 is from 0 to 0.55. For blue line with cross markers, Range 1 is from 0 to 0.58.

Therefore, in order to expand Range 1, which provides predictable results for small droplets, liquids, capillaries, and substrates with higher liquid-capillary and liquid-substrate equilibrium contact angles are desired. Choosing the liquids, capillaries, and substrates with lower liquid-capillary and liquid-substrate equilibrium contact angles, will cause deposition of larger droplets.

Figure 22 and Figure 23 are devoted to the liquid bridge stability maps for different liquid-substrate and liquid-capillary equilibrium angles assuming that liquid-capillary angle is equal to liquid-substrate angle: $\theta_C^e = \theta_S^e$. We notice that there is a bifurcation of lines 2 and 3 when equilibrium contact angles reach 89°: these lines 2 and 3 move from right side to the left side. This result leads to the fact that there will be no stable bridge at high pressure (more than 0.5) for any heights, when equilibrium contact angles are equal or less than 89°. At the same time, further decreasing of equilibrium contact angles will cause shrinkage of the stable area.

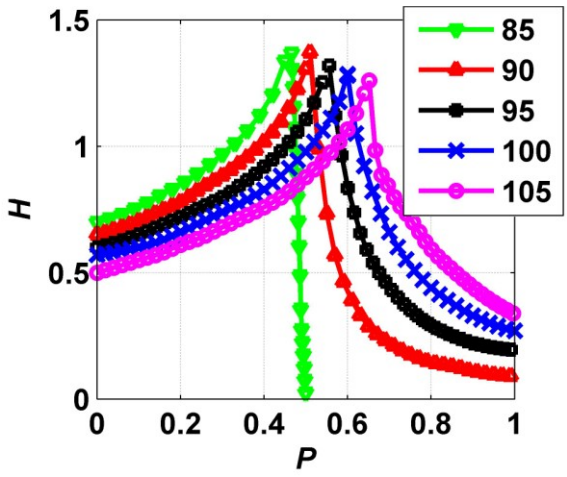

Figure 20. The (H, P) diagram for steady liquid bridge between capillary and substrate: H, P are defined in Eq. (18), $\theta_C^e = 95^\circ$; Downward pointing triangle, upward pointing triangle, square, cross, and circle markers correspond to $\theta_S^e = 85^\circ, 90^\circ, 95^\circ, 100^\circ, 105^\circ$, respectively.

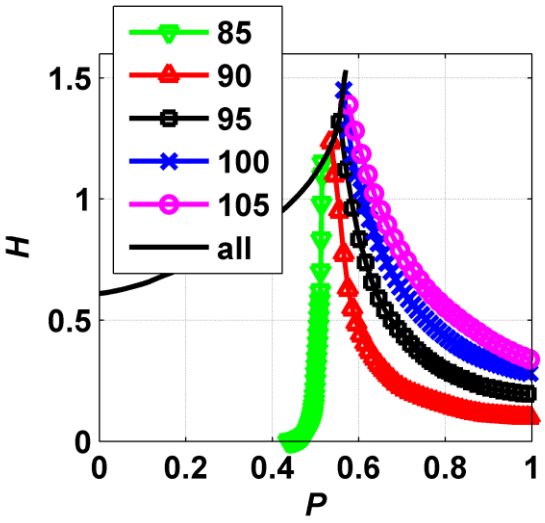

Figure 21. The (H, P) diagram for steady liquid bridge between capillary and substrate: H, P are defined in Eq. (18), $\theta_S^e = 95^\circ$; Downward pointing triangle, upward pointing triangle, square, cross, and circle markers correspond to $\theta_C^e = 85^\circ, 90^\circ, 95^\circ, 100^\circ, 105^\circ$, respectively.

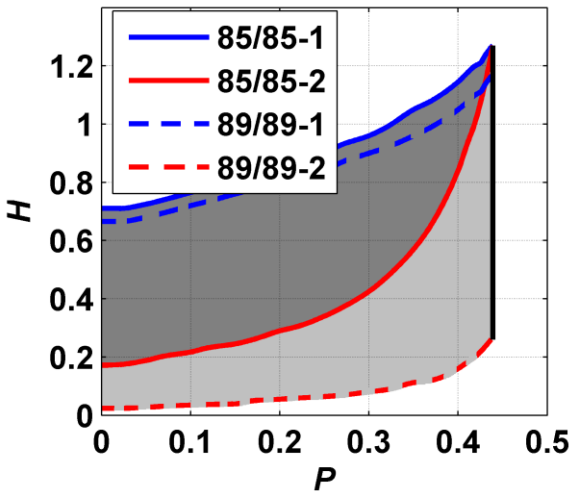

Figure 22. The (H, P) diagram for steady liquid bridge between capillary and substrate: H, P are defined in Eq. (18), Solid blue and red lines correspond to the case when $\theta_C^e = \theta_S^e = 85^\circ$, dashed blue and red lines correspond to the case when $\theta_C^e = \theta_S^e = 89^\circ$.

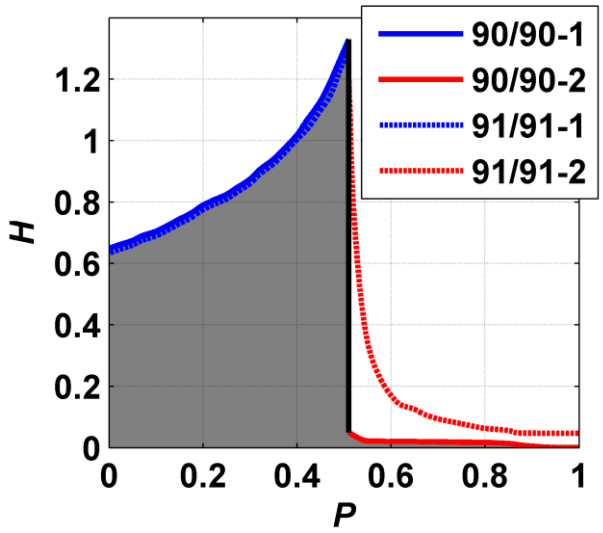

Figure 23. The (H, P) diagram for steady liquid bridge between capillary and substrate: H, P are defined in Eq. (18), Solid blue and red lines correspond to the case when $\theta_C^e = \theta_S^e = 90^\circ$, dashed blue and red lines correspond to the case when $\theta_C^e = \theta_S^e = 91^\circ$.

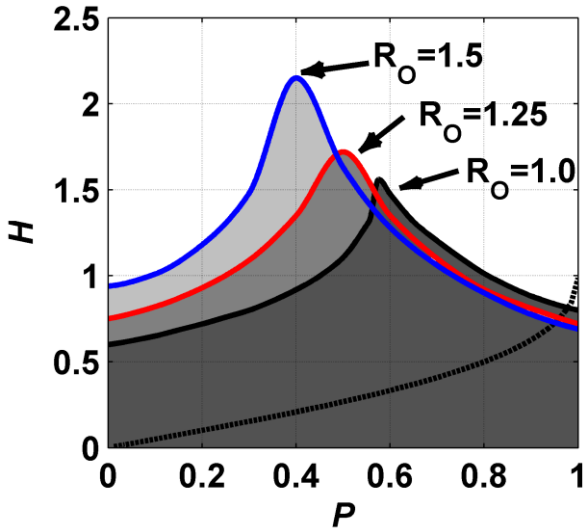

Figure 24. The (H, P) diagram for steady liquid bridge between capillary and substrate: $\theta_C^e = \theta_S^e = 95^\circ$, assuming that there is no restriction on bridge-capillary angle, see Eq. (15). OD=1; 1.25; 1.5.

The stability diagram, where there is no restriction on bridge-capillary angle (see Eq. (15)), is presented in Figure 24. The curve for $R_O = r_O / r_C = 1.0$ corresponds to the capillary without wall thickness (when outer capillary radius is equal to inner capillary radius). Line for $R_O = 1.25$ assumes that capillary wall thickness is 0.25. And line $R_O = 1.5$ assumes that capillary wall thickness is 0.5. Based on the chart we notice that preferable Range 1 decreases with increase of outer radius. Pressure Range 1 when $R_O = 1.0$ is [0, 0.58], but adding a wall thickness equal to 0.5 ($R_O = 1.5$) leads to smaller Range 1 [0, 0.4].

Note that the stability area of bridges for the case with no capillary wall thickness can be compared with the stability area of bridges between the solid rod and the substrate. Hollow capillary-substrate bridges are different from rod-substrate bridges only by the fact that the bridge mass is not constant. For the rod-substrate bridge, the pressure in the liquid is not constant, but mass is constant. If the rod-substrate height is changed, the pressure in the liquid bridges reorganizes correspondingly. Therefore for given mass or volume of bridge, one has to find the liquid pressure in the bridge in order to satisfy Eq. (13). Boundary condition for rod-substrate bridges are the same as in the case of bridges between hollow capillary with no capillary wall thickness: the bridge is fixed in outer diameter of the rod and the bridge-substrate contact angle is equal to equilibrium contact angle between the liquid and substrate. Stability diagram of the rod-substrate bridges are presented in Figure 25.

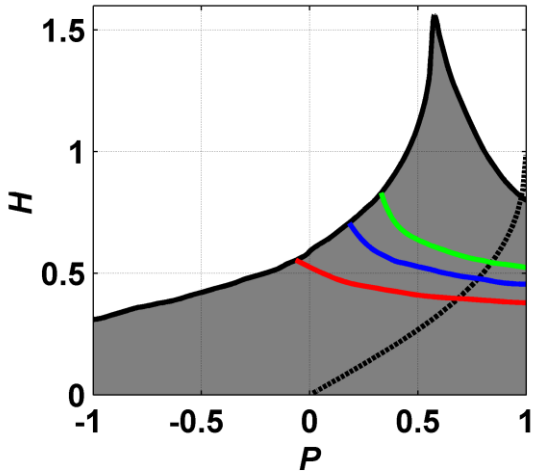

Figure 25. The (H, P) diagram for steady liquid bridge between the rod and substrate: $\theta_C^e = \theta_S^e = 95^\circ$.

Red, blue, and green lines on Figure 25 correspond to the liquid bridge masses of 0.4, 0.5, and 0.6, respectively. We notice that increasing the rod-substrate height leads to reduction of pressure in the liquid bridge. And if the rod-substrate height decreases, the pressure rises up. Another observation is that stability area of rod-substrate bridges is higher than the stability area of capillary-substrate bridges. Therefore, instead of hollow capillary it is favorable to use the rod for the droplet deposition. But this will cause a problem of re-dipping: the rod cannot be connected with fluid reservoir for continuous fluid delivery system. Detail analysis of the bridges between the rod and the flat substrate is given by B. Qian and K.S. Breuer in [40].

2.2.6. Force Analysis

While considering the bridge shapes between the capillary and substrate, notable results were obtained for force between the liquid bridge and substrate. There are two forces

acting on the substrate area due to the bridge formation (see Figure 26). First one is force due to the pressure inside of the liquid bridge:

$$f_p = (p - p_0)\pi r_{BS}^2 . \quad \textbf{(27)}$$

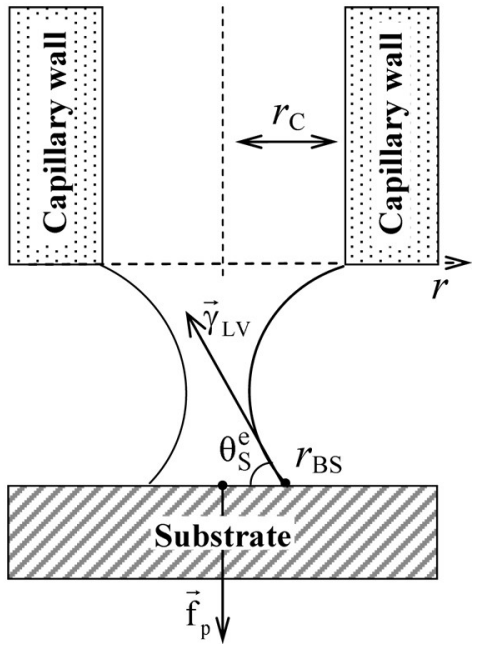

Figure 26. Forces acting on the substrate: the pressure force and the surface tension force.

Second force is the surface tension force acting in opposite direction:

$$f_\sigma = \gamma_{LV} 2\pi r_{BS} \sin\theta_S^e . \quad \textbf{(28)}$$

Therefore the total force acting on the substrate will be equal to:

$$\delta f = f_\sigma - f_p = \pi r_{BS}\left\{2\gamma_{LV}\sin\theta_S^e - (p - p_0)r_{BS}\right\}. \quad \textbf{(29)}$$

After normalization this total force will look as follows:

$$\delta F = R_{BS}\left(\sin\theta_S^e - PR_{BS}\right). \quad \textbf{(30)}$$

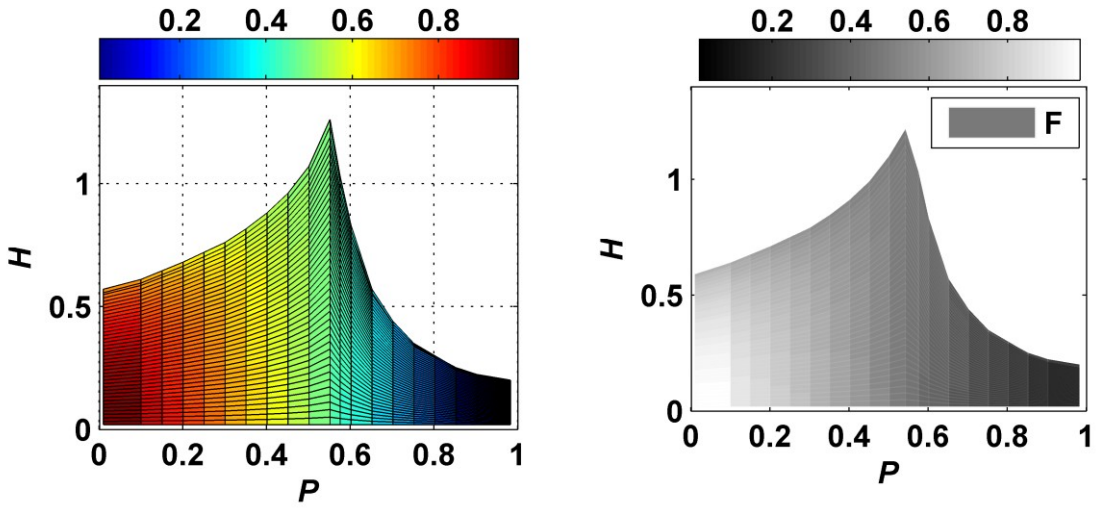

Figure 27. Contour plot of the force acting on the substrate.

The contour plot of the force acting on the substrate in the case $\theta_C^e = \theta_S^e = 95^\circ$ is shown in Figure 27. While force along the lines 1, 2 and 3 is presented in Figure 28. We find that the total bridge force is positive everywhere in the stability region. This means that surface tension force tends to pull the substrate area up with tension not exceeding the normalized force of 1.0. Note that the normalized force of 1.0 corresponds to real force of $2\pi\gamma_{LV}r_C$ (for the case of glycerol and capillary with an inner diameter of 300 μm, this force is about 60 μN). This fact can be used for manipulation with small object sitting on the substrate.

As an example, the small object (with area comparable to bridge area) can be lifted from the substrate, if the adhesion force is less than the bridge force calculated in Eq. (30). Cai and Bhushan considered not only the meniscus force, but also the viscous force for the bridges between two surfaces. They analyzed both rough and flat hydrophilic and hydrophobic surfaces. It was found that both meniscus and viscous forces decrease with increase of separation distance [41]. The same trend was observed for the bridges between hollow capillary and substrate (see Figure 27).

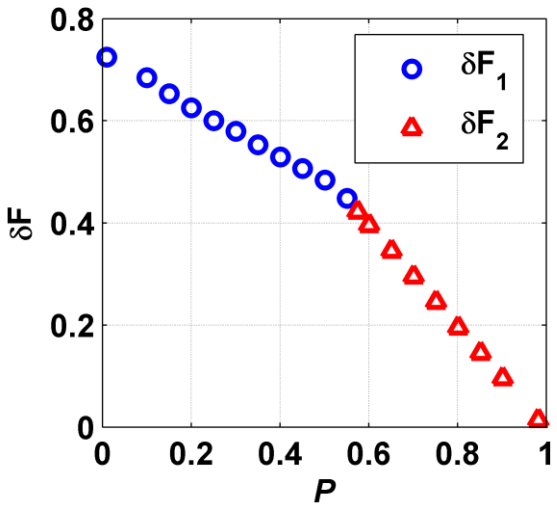

Figure 28. The force acting on the substrate along the lines 1 (blue circles), 2 and 3 (red triangles). These lines are shown in Figure 13.

2.2.7. Interfacial Energy Interaction

Knowledge about the interfacial energy of interaction is needed for understanding and modeling the process of deposition. Historically, the theory of interfacial energy started from Young's equation [42-45]:

$$\gamma_{LV}\cos\theta = \gamma_{SV} - \gamma_{SL}, \tag{31}$$

where γ_{SL} is the liquid-substrate surface tension, γ_{LV} is the liquid-vapor surface tension, γ_{SV} is the substrate-vapor surface tension, and θ is the equilibrium contact angle (see Figure 29).

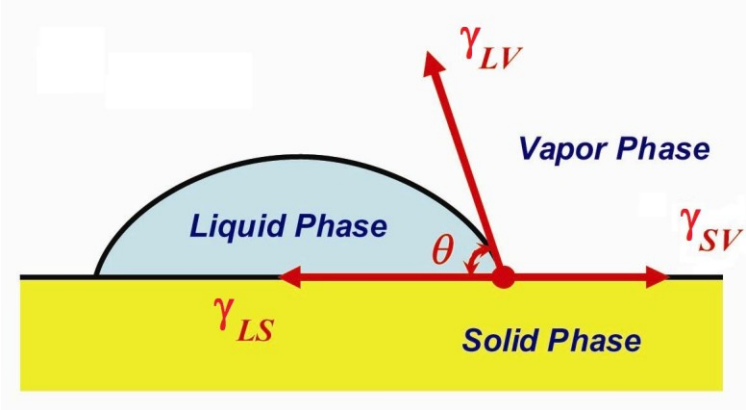

Figure 29. Sketch of the contact angle.

Based on this equation, the difference $\gamma_{SV} - \gamma_{SL}$ can be found from the experimental results of the liquid-vapor surface tension, γ_{LV}, and the contact angle, θ, but it is very important to know the values for γ_{SV} and γ_{SL} separately. There are many theories to evaluate the substrate-liquid and substrate-vapor surface tension: the Fox-Zisman approach [46], the Acid-Base Theory [47], the Harmonic-Mean technique [47], the Newmann method [48], and the Fowkes theory [47, 48]. For example, Fowkes proposed to divide the surface tension into two parts: the dispersion component and the non-dispersion component: $\gamma = \gamma^d + \gamma^n$ [43, 47]. The most common way to evaluate all components of surface tension is to use the Owens-Wendt's method. Owens and Wendt proposed that the

free energy of the adhesion between phases is equal to the Geometric Mean of two separated phases [49]:

$$\gamma_{SL} = \gamma_{SV} + \gamma_{LV} - 2\left(\gamma_{SV}^{d}\gamma_{LV}^{d}\right)^{1/2} - 2\left(\gamma_{SV}^{n}\gamma_{LV}^{n}\right)^{1/2}. \quad \textbf{(32)}$$

This equation expresses the interfacial free energy as a sum of the surface free energy of phases in contact, reduced by a geometric mean of the dispersion and non-dispersion interfacial interactions.

Combining Young's equation with Owens-Wendt's equation, one obtains the following relationship between the different components of the surface tension:

$$\gamma_{LV}\cos\theta = -\gamma_{LV} + 2\left(\gamma_{SV}^{d}\gamma_{LV}^{d}\right)^{1/2} + 2\left(\gamma_{SV}^{n}\gamma_{LV}^{n}\right)^{1/2}, \quad \textbf{(33)}$$

where $\gamma_{LV} = \gamma_{LV}^{d} + \gamma_{LV}^{n}$, and $\gamma_{SV} = \gamma_{SV}^{d} + \gamma_{SV}^{n}$.

Therefore, measuring contact angles of two liquid on one substrate allows us to find these components:

$$\begin{cases} \gamma_{LV1}\cos\theta_{L1} = -\gamma_{LV1} + 2\left(\gamma_{SV}^{d}\gamma_{LV1}^{d}\right)^{1/2} + 2\left(\gamma_{SV}^{n}\gamma_{LV1}^{n}\right)^{1/2} \\ \gamma_{LV2}\cos\theta_{L2} = -\gamma_{LV2} + 2\left(\gamma_{SV}^{d}\gamma_{LV2}^{d}\right)^{1/2} + 2\left(\gamma_{SV}^{n}\gamma_{LV2}^{n}\right)^{1/2} \end{cases}, \quad \textbf{(34)}$$

And finally:

$$\gamma_{SV}^{d}=\left[\frac{\sqrt{\gamma_{LV2}^{n}}\left(\gamma_{LV1}\cos\theta_{L1}+\gamma_{LV1}\right)-\sqrt{\gamma_{LV1}^{n}}\left(\gamma_{LV2}\cos\theta_{L2}+\gamma_{LV2}\right)}{2\left(\sqrt{\gamma_{LV1}^{d}\gamma_{LV2}^{n}}-\sqrt{\gamma_{LV2}^{d}\gamma_{LV1}^{n}}\right)}\right]^{2},$$

(35)

$$\gamma_{SV}^{n}=\left[\frac{\sqrt{\gamma_{LV2}^{d}}\left(\gamma_{LV1}\cos\theta_{L1}+\gamma_{LV1}\right)-\sqrt{\gamma_{LV1}^{d}}\left(\gamma_{LV2}\cos\theta_{L2}+\gamma_{LV2}\right)}{2\left(\sqrt{\gamma_{LV2}^{d}\gamma_{LV1}^{n}}-\sqrt{\gamma_{LV1}^{d}\gamma_{LV2}^{n}}\right)}\right]^{2}$$

The contact angles of the four liquids were measured on different substrates: glass substrate, HOPG, gold substrate, hydrophobic glass substrate, and hydrophobic gold substrate. It was done by using the FTA 136 Contact Angle Analyzer. The results are shown in Table 1. Based on these results, the best candidates for deposition are water and glycerol, because contact angles between these liquids and HOPG are more than 90 degrees after hydrophobization. Water has a higher rate of evaporation, so in the deposition experiment, the glycerol was the primary liquid.

Table 1. Contact angle, θ in degrees [18].

Substrate/Liquid	Water	Glycerol	Ethylene glycol	Diidomethane
Glass	29	31	41	39
HOPG	72	75	59	37
Gold	74	73	58	33
Glass hydrophob.	109	95	85	71
Gold hydrophob.	107	98	86	66

Table 2 depicts to the experimental values of liquid-vapor surface tension taken from literature [47, 50-52]. Table 3 shows the dispersion and non-dispersion components of the liquid-vapor surface tension found in literature [47, 50]. In order to obtain the dispersion and non-dispersion components of water, glycerol, and diidomethane, the

researchers used the same procedure as described above, but instead of substrate, they used hydrocarbon liquids [50]. In the case of hydrocarbons, their non-dispersion components are not needed (these liquids are polar). Therefore, the liquid-vapor surface tensions of hydrocarbons are equal to dispersion component of hydrocarbons, and the hydrocarbon non-dispersion components are equal to zero. Thus, by using Eq. (33), the dispersion and non-dispersion components of any liquid can be determined based on contact angle results.

Table 2. Liquid surface tension, (γ_{LV}, mN/m) [18].

	Water	Glycerol	Ethylene glycol	Diidomethane
γ_{LV}, mN/m	72.80	63.30	47.70	50.80

Table 3. Values of dispersion and non-dispersion components of liquid surface tension [18].

Liquid	γ_{LV}^{d}, mN/m	γ_{LV}^{n}, mN/m	γ_{LV}, mN/m
Water	21.80	51.00	72.80
Glycerol	33.60	29.70	63.30
Diidomethane	50.42	0.38	50.80

Based on Owens-Wendt's approach, the substrate surface tensions (Table 4) of the five substrates were calculated by using the contact angle results (Table 1). One can see that the energy of Glass and Gold substrates decrease due to the hydrophobization procedure. Since the glass capillary, coated by gold, is also hydrophobized, then it is assumed that during the deposition, the glycerol is likely to be deposited on HOPG.

Knowing the substrate surface tension of the substrates, one can calculate the substrate-liquid surface tension by using Young's equation, $\gamma_{SL} = \gamma_{SV} - \gamma_{LV}\cos\theta$, and the contact angle measurements. A summary of the results is given in Table 5.

Table 4. Substrate surface tension, (γ_{SV}, mN/m) [18].

Substrate	γ_{SV}, mN/m
Glass	61.25
HOPG	43.12
Gold	44.49
Glass hydrophob.	22.38
Gold hydrophob.	25.35

Table 5. Substrate - liquid surface tension. (γ_{SL}, mN/m) [18].

Liquid/Substrate	Glass	HOPG	Gold	Glass hydrophob.	Gold hydrophob.
Glycerol	7.15	27.36	25.96	18.45	16.46
Ethylene glycol	25.35	18.84	19.70	18.28	21.91
Alpha-terpineol	28.36	10.32	10.26		

Based on Table 5, one can see that, the Glycerol-HOPG interaction force and the Glycerol-Gold interaction force are close to each other. However, after the hydrophobization, the Glycerol-Gold interaction force decreases by 1.5 times. Therefore, if the hydrophobized gold-coated nano-capillary is used, then Glycerol can be employed as the test liquid for the liquid droplet deposition on HOPG.

2.2.8. Experiments

The presented liquid bridge theory was validated by experiments with glycerol-water solution as a deposition liquid. Three glycerol concentrations in water (by weight) were used: 100%, 85%, and 65%. Viscosity, density, and surface tension of glycerol-water mixture are shown in Table 6 [53]. The quartz micro-capillaries with inner diameters of 100, 200, and 300 μm were used in the experiments. The capillary tip was cut with automatic wafer dicing system (ADT Dicing Saw 7500) perpendicular to the capillary axis

to get sharp edge. Since the first step of the deposition procedure is the formation of the meniscus protruding out of the capillary, the outer surface of the capillary was made non-wettable to the deposited liquid using the following hydrophobization procedure. Dry capillary was immersed in 0.5 wt. % solution of octadecyltriochlosilane in toluene for 10 minutes. After that the capillary was rinsed with clean toluene. Using the hydrophobized capillary the menisci with different thicknesses $(0 < h_M < r_C)$ could be formed, with the thickness h_M controlled by applied liquid pressure in accordance with the Eq. (19). Hydrophobized quartz plate was used as a substrate. To evaluate the effectiveness of the hydrophobization procedure, the contact angles on a quartz plate (not the capillary) were measured. The pure glycerol contact angle on the quartz before hydrophobization was equal to 31º; after hydrophobization it increased to about 95º. Contact angles of glycerol-water mixtures at different concentrations on hydrophobized quartz slide are given in Table 7. The contact angle/surface tension analyzer, FTA 125, was used to measure static, advancing and receding contact angles. Equilibrium contact angles were determined by depositing sessile droplets on the substrate. The advancing angles were captured by pumping the liquid in the droplet with the syringe. The receding angles were obtained by removing the liquid from the droplet with the syringe [54]. Note that equilibrium contact angles for the glycerol-water mixtures on hydrophobic quartz slide are around 95°.

Table 6. Viscosity, density, and surface tension of glycerol-water solution.

	65% wt. glycerol in water	85% wt. glycerol in water	100% wt. glycerol in water
Viscosity, cP	15.2	109	1410
Density, kg/m^3	1204	1249	1261
Surface tension, mN/m	65.7	64	63

Table 7. Receding, equilibrium, and advancing contact angles of glycerol-water mixtures on hydrophobized quartz slide.

	65% wt. glycerol in water	85% wt. glycerol in water	100% wt. glycerol in water
Receding angle, °	84.0	85.3	83.9
Equilibrium angle, °	96.8	96.0	93.6
Advancing angle, °	100.7	98.5	98.6

After capillary hydrophobization, the micro-capillary was filled with glycerol-water solution. The meniscus was formed due to hydrostatic pressure of the glycerol column. Then the micro-capillary was connected to three Newport stages SDS65 in an XYZ assembly and the micro-capillary movement was controlled with micron resolution in all directions. The high speed camera (NanoSense Mk-III, by Dantec Dynamics) was used with the set of magnification lenses to monitor the shape of the formed bridge, the dynamics of bridge rupturing, and the size of residual droplet.

The typical deposition scenario for Range 1 is presented in Figure 30, where glycerol/water solution (glycerol concentration of 65% by wt.) was used as a deposition liquid and capillary with inner diameter of 328 microns was employed. Normalized liquid hydrostatic pressure was adjusted to $P = 0.35$, such that liquid meniscus had a thickness of $h_M = 29\,\mu\text{m}$ (Figure 30a). When liquid meniscus just touched the substrate ($H = 0.174$), a liquid bridge formed immediately (Figure 30b). Steady liquid bridge between capillary and substrate formed after less than one minute (Figure 30c). The shape of the stable bridge perfectly fit to the theoretically calculated one shown on Figure 30c with a solid line. Note that this solid line was calculated assuming that both liquid-capillary and liquid-substrate equilibrium contact angles are equal to 95°. At this capillary-substrate distance of $H = 0.174$, the capillary was kept for 25 minutes. Figure 30d shows the shape of this

bridge after waiting of 25 minutes at the capillary-substrate distance of $H = 0.174$. We see that there is no difference between Figure 30c and Figure 30d.

After that the capillary was slowly moving up from the substrate with the retraction velocity of 3μm/s until the normalized capillary-substrate distance became $H = 0.271$. Figure 30e shows the bridge structure at the stopping moment. Figure 30f represents the shape of bridge after waiting of 25 minutes with the capillary-substrate distance of $H = 0.271$. Solid lines in Figure 30e and Figure 30f illustrate the calculated shape of the steady bridge for this capillary-substrate distance. Note that the bridge-substrate contact angle and the base radius did not change during the waiting.

Then the capillary was slowly moving up with the velocity of 3μm/s until the normalized capillary-substrate distance became $H = 0.368$. Figure 30g shows the bridge structure at the moment of stopping and Figure 30h represents the bridge after 25 minutes at the capillary-substrate distance of $H = 0.368$. It is clear that in spite of very slow retraction velocity the experimental shape of the bridge is still transient showing bridge-substrate contact angle slightly lower than the equilibrium contact angle θ_S^e. Another observation is that the bridge-substrate contact angle increased during the waiting. At the same time the base radius did not change. Starting with height of 0.368, the experimental shape of the bridge does not match to the theoretically calculated one (shown with a solid line).

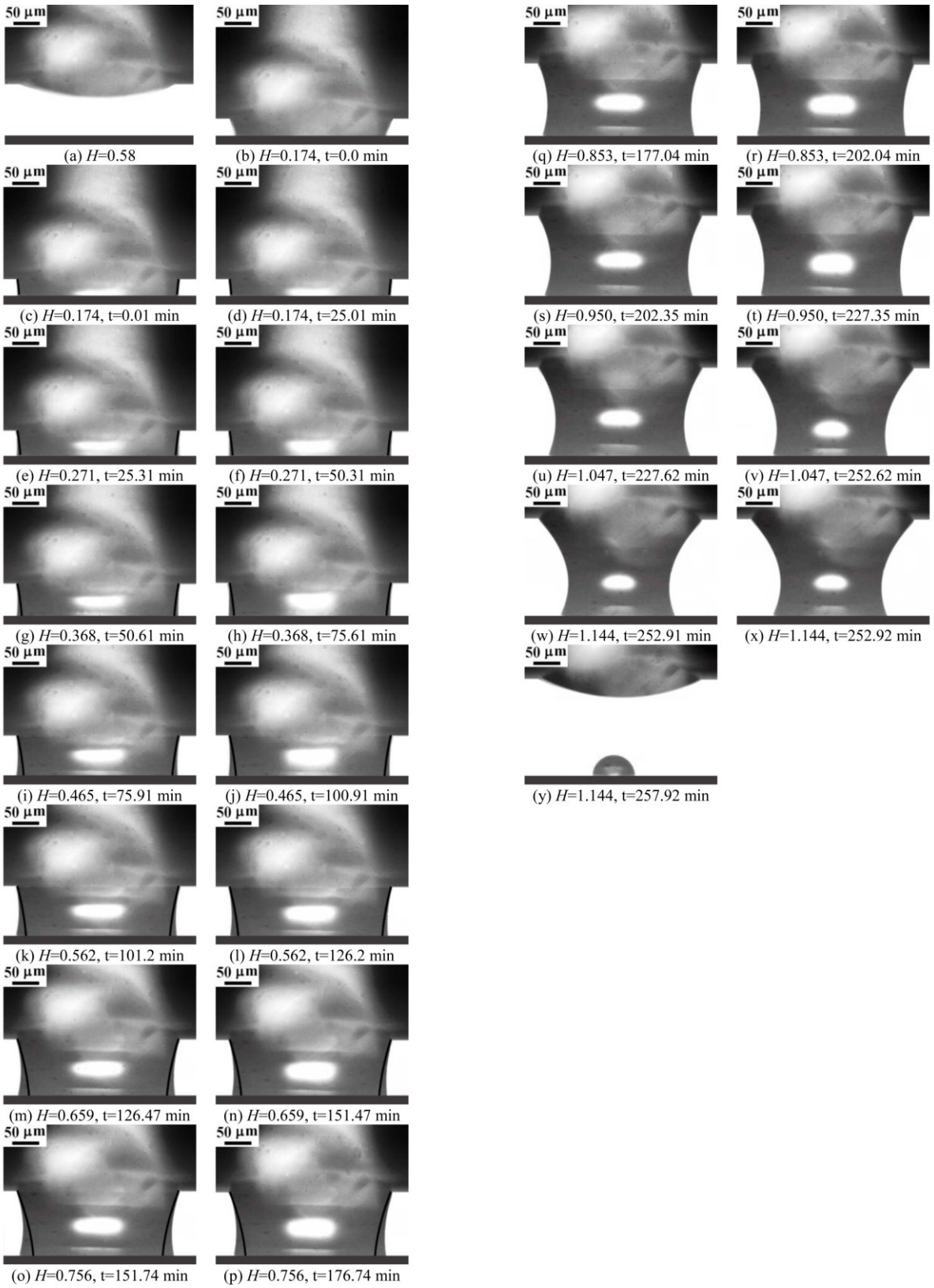

Figure 30. Typical deposition scenario for Range 1 when P=0.35.

Again, after waiting for 25 min the capillary was moving up with the retraction velocity of 3μm/s until point $H = 0.465$. Figure 30i shows the bridge structure at the moment of stopping and Figure 30j represents the bridge after waiting of 25 minutes at the capillary-substrate distance of $H = 0.465$. We observe that the bridge-substrate contact angle increased during the waiting while the base radius did not change because the current bridge-substrate contact angle is still higher than the receding contact angle of about 85°.

And again, after waiting for 25 min the capillary was moving up with the retraction velocity of 3μm/s until point $H = 0.562$. Figure 30k shows the bridge structure at the moment of stopping and Figure 30l represents the bridge after waiting of 25 minutes at the capillary-substrate distance of $H = 0.562$. Note that at this height the bridge-substrate contact angle slightly increased during the waiting while the base radius decreased. It happened because the bridge-substrate contact angle dropped below the receding contact angle. Starting from this height the bridge base radius only decreased.

Then the capillary was moving up with the retraction velocity of 3μm/s until point $H = 0.659$. Figure 30m shows the bridge structure at the moment of stopping and Figure 30n represents the bridge after waiting of 25 minutes at the capillary-substrate distance of $H = 0.659$. We notice that the bridge-substrate contact angle slightly increased during the waiting, but the base radius decreased.

The same trend was observed when the capillary was remained at the height of $H = 0.756$ (the capillary was moving up to the height $H = 0.756$ with the retraction velocity of 3μm/s). Figure 30o shows the bridge structure at the moment of stopping and Figure 30p represents the bridge after waiting of 25 minutes at the capillary-substrate

distance of $H = 0.756$. We see that the bridge-substrate contact angle slightly increased during the waiting, but the base radius decreased.

Note that the normalized capillary-substrate distance $H = 0.82$ corresponds to the theoretical line 1 on Figure 13 and therefore the bridge breakage was expected to happen somewhere around this point. After the height of $H = 0.82$, there is no stable theoretical shape to compare model with experiment.

From the height of $H = 0.756$, the capillary was moving up to the height $H = 0.853$ with the retraction velocity of 3μm/s. Figure 30q shows the bridge structure at the moment of stopping and Figure 30r represents the bridge after waiting of 25 minutes at the capillary-substrate distance of $H = 0.853$. We observe that the bridge-substrate contact angle slightly increased during the waiting, but the base radius decreased.

From the height of $H = 0.853$, the capillary was moving up to the height $H = 0.95$ with the retraction velocity of 3μm/s. Figure 30s shows the bridge structure at the moment of stopping and Figure 30t represents the bridge after waiting of 25 minutes at the capillary-substrate distance of $H = 0.95$. We find that the bridge-substrate contact angle slightly increased during the waiting, but the base radius decreased.

After the height of $H = 0.95$ the capillary was moving up to the height $H = 1.047$ with the retraction velocity of 3μm/s. Figure 30u shows the bridge structure at the moment of stopping and Figure 30v represents the bridge after waiting of 25 minutes at the capillary-substrate distance of $H = 1.047$. We see that the bridge-substrate contact angle slightly increased during the waiting, but the base radius decreased.

Finally the capillary was moving up to the height $H = 1.144$ with the retraction velocity of 3μm/s. Figure 30w shows the bridge structure at the moment of stopping and Figure 30x

represents the bridge after waiting of 6 seconds at the capillary-substrate distance of $H = 1.144$. We notice that both the bridge-substrate contact angle and the base radius decreased during the waiting time.

At this capillary-substrate distance $H = 1.144$ the bridge ruptured itself leaving the residual droplet of r_d=39 μm on the substrate (Figure 30y). The residual droplet radius was defined visually as the radius of the droplet footprint on the substrate. Since liquid-substrate contact angle is 95^0 the actual amount of the deposited liquid is approximately equal to the half of mass of liquid in the droplet of radius r_d.

Based on experiment described above we can conclude the following. First, due to retraction, initially the bridge-substrate contact angle becomes lower than the equilibrium contact angle, and then it drops below the receding contact angle. Figure 31a shows the time evolution of the bridge-substrate contact angle. After the waiting period, the bridge-substrate contact angle tends to increase to liquid-substrate equilibrium contact angle, but the time needed for that is long and depends on the capillary-substrate height.

Second, while the capillary-substrate distance is lower that "critical" height, the base radius has tendency to increase or stay the same while waiting. But as soon as the capillary-substrate distance is higher than critical one or the bridge-contact angles drops below the receding angle, the base radius starts to decrease without dependency on retraction speed (see Figure 31b).

Third observation is the following. After some height, the steady state theory for the liquid-capillary and liquid-substrate equilibrium contact angles of 95° cannot describe the experimental bridge profiles, especially when height is approaching to the rupturing point. It happens because even small retraction speed leads to changes in bridge-substrate contact

angle. Therefore the bridge-substrate contact angle in the model should be set not to the equilibrium contact angle of 95°, but to the receding liquid-substrate contact angle of 85°. In order to test this statement, the experimental bridge profile shown in Figure 30l is compared with theoretically calculated one by using the static bridge theory and assuming that the bridge-substrate contact angle is set to the receding contact angle of 85° (liquid-capillary equilibrium contact angle was kept constant of 95°). This comparison presented in Figure 32 revealed that the experimental profile is in better agreement with the theoretically calculated shape assuming that the bridge-substrate contact angle is 85°. The best representation of the experimental bridge profiles can be obtained if the bridge-substrate contact angle is set not the receding contact angle, but the actual bridge-substrate contact angle taken from experiment. But this requires performing experimental analysis first.

Another way to simulate experimental bridge profiles between the capillary and the substrate is to consider dynamic bridge problem in order to fully describe the experimental observation. Note that in addition to static bridge theory presented in the paper, a 3D spectral boundary element method was developed for the dynamics of liquid bridge between a substrate and a rising capillary. Details of this simulation was presented in [55, 56] and was not included in this paper. Bridge profiles obtained using the spectral boundary element method are compared with the static theory results and with experimental data as shown in Figure 33. In this plot, the normalized pressure was set to 0.4; the retraction speed was 300 microns/s; the capillary inner radius was 157 microns; and the deposition liquid was 65% glycerol-water mixture. We observe that initially there is no dissimilarity between the bridge profiles obtained by static analysis and those by the

boundary element method (Figure 33b), but while the capillary-substrate distance increases, the difference between static and dynamic models becomes more pronounced (Figure 33c). At the height close to bridge break up there is no bridge shape obtained by the static bridge theory, but the spectral boundary element method gives solution which is close to the experimental profile.

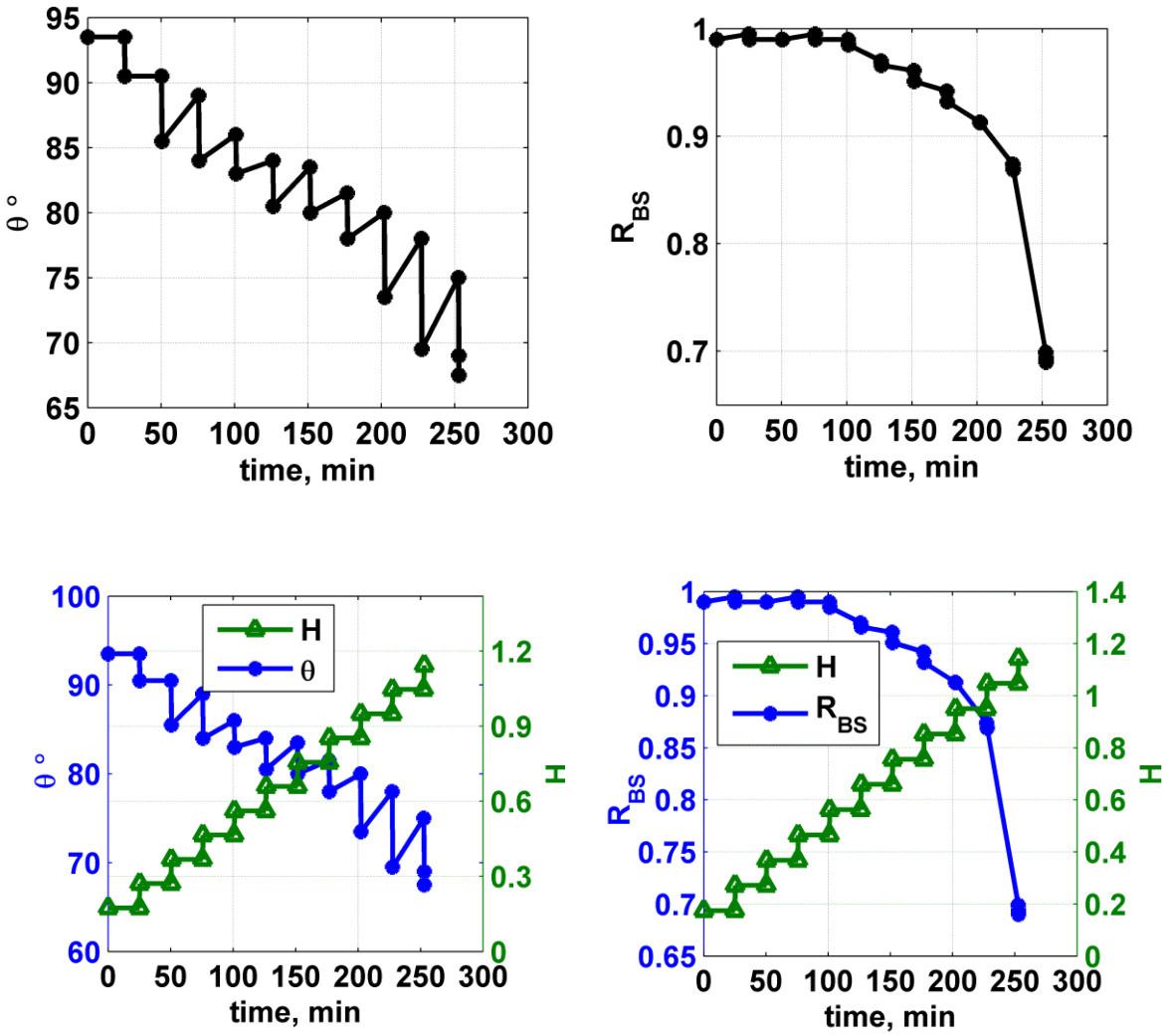

(a) (b)

Figure 31. Bridge-base radius and bridge-substrate contact angle versus time for Range 1 when P=0.35.

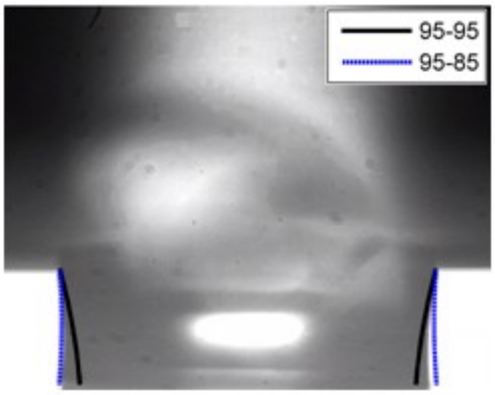

Figure 32. Experimental bridge profile compared to the theoretically calculated shapes using the steady bridge theory and assuming that a) both liquid-capillary and liquid-substrate contact angles are equal to 95° (shown as solid line), b) liquid-capillary and liquid-substrate contact angles are equal to 95° and 85°, respectively (dashed line).

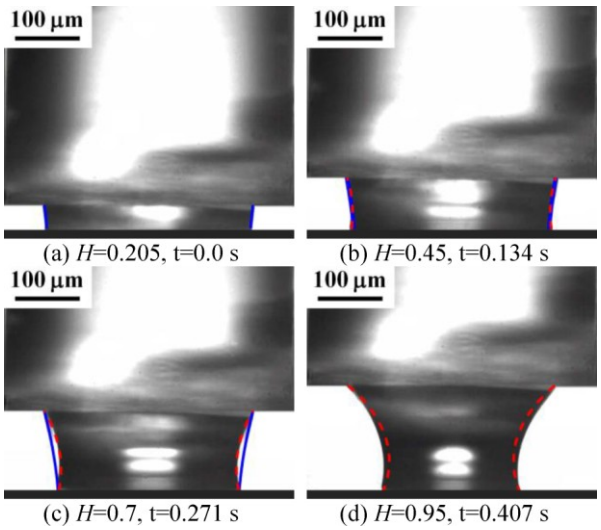

Figure 33. Spectral boundary element method bridge profiles (red dashed lines) are compared with steady theory bridges (solid blue lines) along with experimental data for normalized pressure of P=0.4 and retraction speed of 300 microns/s.

Two typical deposition scenarios for Ranges 2 and 3 are demonstrated in Figure 34. In the $P_1 < P < P_2$ case, the normalized liquid hydrostatic pressure was adjusted to $P = 0.69$, such that liquid meniscus had a thickness of $h_M = 57\,\mu\text{m}$. When liquid meniscus touches the substrate ($H = 0.38$) a steady liquid bridge between capillary and substrate formed

(Figure 34a). The shape of this bridge perfectly fit to the theoretically calculated one shown on Figure 34(a) with a solid line. The capillary was slowly moving up from the substrate with the retraction velocity of 3μm/s until the capillary-substrate distance became $H = 0.57$. Note that the normalized capillary-substrate distance $H = 0.47$ corresponds to the line 2 on Figure 13 and therefore the bridge spreading expectedly happened somewhere around this point (Figure 34b).

In the case $P_2 < P < 1$, the normalized liquid hydrostatic pressure was adjusted to $P = 0.79$, such that liquid meniscus had a thickness of $h_M = 72\,\mu\text{m}$. When liquid meniscus touches the substrate ($H = 0.48$), a spreading liquid bridge is immediately formed (Figure 34c and Figure 34d). The only way to avoid a big liquid blot on a substrate in case $P_1 < P < 1$ is to retract the capillary very fast. Recently, it was shown [39] that a wide range of the residual droplets sizes can result from the same capillary, depending strongly on the capillary retraction speed. The parameters used in the experimental and theoretical study presented in [39] fall in the range $P_2 < P < 1$.

Note that the bridge spreading along the bottom edge of the capillary for pressures from Ranges 2 and 3 happens with different speeds, chaotically. Figure 35 shows how bridge was spreading for three different experiments. It should be noticed that no trend was observed. This can be explained by imperfections of edges on the capillary and scratches on the substrate. Even cutting with dicing saw leads to some roughness of the capillary bottom edge.

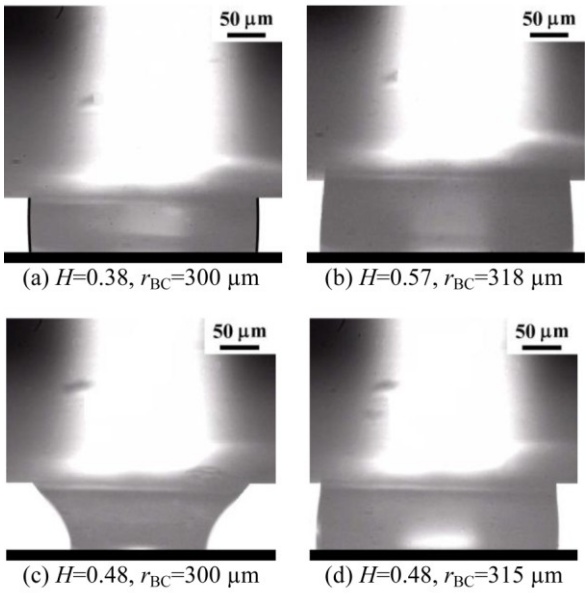

Figure 34. Typical deposition scenarios for Ranges 2 and 3 when P=0.69 and P=0.79.

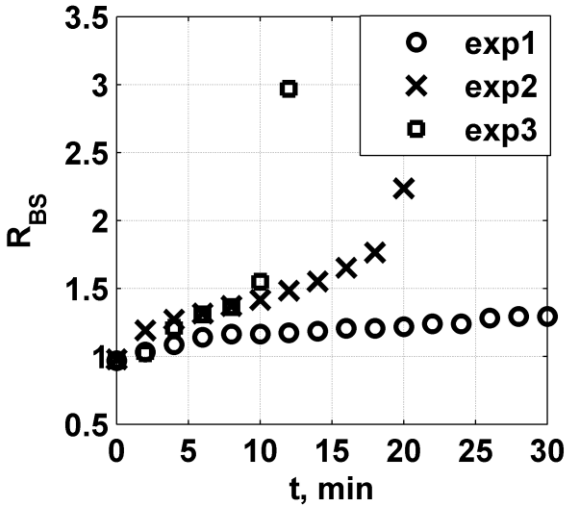

Figure 35. Spreading of bridge along the bottom capillary edge: dependency of bridge-substrate radius (R_{BS}) on time is shown for three different experiments (P=0.9).

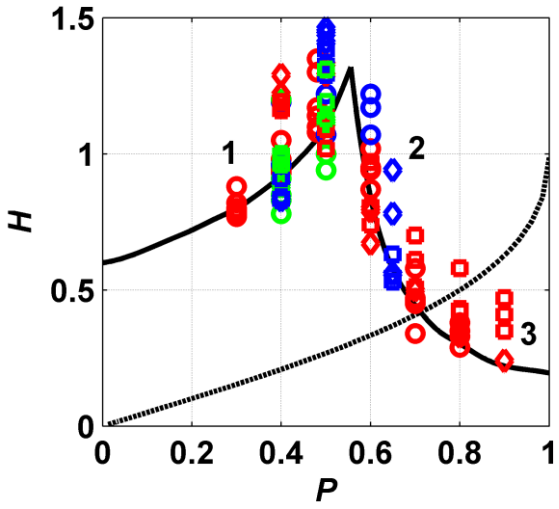

Figure 36. The normalized capillary-substrate distance at the moment of deposition (when normalized pressures are from Range 1) and at the moment of spreading (when normalized pressures are from Ranges 2 and 3). Here very low retraction speed of about 3 micron/s is applied. The experimental results conform to theoretically predicted lines 1, 2, and 3. Circle, diamond, and square marks correspond to glycerol concentration of 100, 85, and 65%, respectively. Red, blue, and green colors correspond to capillary diameters of 300, 200, and 100 micron in diameter, respectively.

Multiple experiments were conducted using a low retraction speed (about 3 micron/s) with variable normalized pressures *P*. The results are summarized in Figure 36 (Circle, diamond, and square marks correspond to glycerol concentration of 100, 85, and 65%, respectively. Red, blue, and green colors correspond to capillary diameters of 300, 200, and 100 micron in diameter, respectively). For the pressures from Range 1, the normalized capillary-substrate distances at the moment of deposition are shown. For the pressures from Ranges 2 and 3, the normalized capillary-substrate distances at the moment when spreading begins are presented. Since equilibrium contact angles for the glycerol-water mixtures on hydrophobic quartz slide are about 95°, that is why experimental results will be compared

with theoretical results corresponding to the case when $\theta_C^e = \theta_S^e = 95^\circ$. The experimental results conform to theoretically predicted lines 1, 2, and 3, when $\theta_C^e = \theta_S^e = 95^\circ$.

The residual droplet radius decrease slightly with the normalized pressure lowering as presented in Figure 37. Average size of the deposited droplet was about 20% of inner capillary radius. Note also that the higher pressure applied leads to higher scattering of experimental data for the droplet radius.

The impact of the retraction speed was also studied. Results with glycerol/water solution (glycerol concentration is 65%) and with capillary of inner diameter of 328 micron are presented in Figure 38. It was found that the smallest droplet is deposited at "zero retraction speed". Slight droplet radius increase was detected when retraction speed increased from 3 μm/s to 400 μm/s.

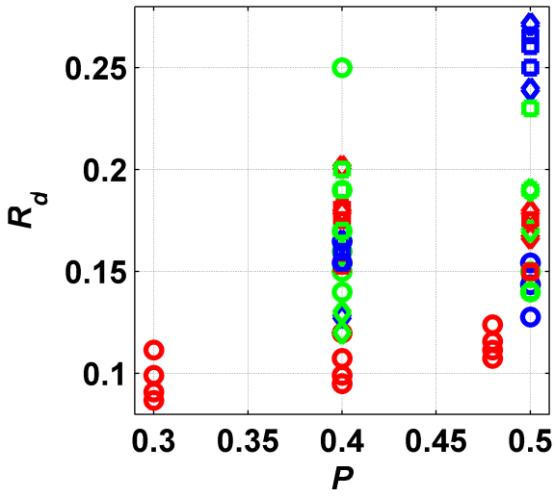

Figure 37. Residual droplet radius vs. normalized pressure from Range 1 for very low retraction speed. Circle, diamond, and square marks correspond to glycerol concentration of 100, 85, and 65%, respectively. Red, blue, and green colors correspond to capillary diameters of 300, 200, and 100 micron in diameter, respectively.

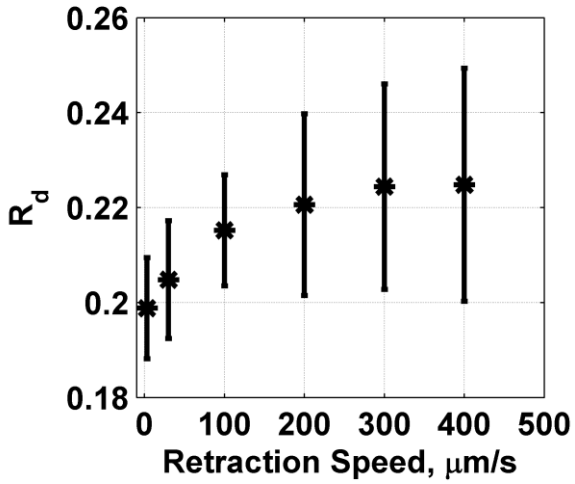

Figure 38. Residual droplet radius vs. retraction speed, when *P*=0.35. Glycerol/water solution (glycerol concentration is 65% by w.t.) was used as deposition liquid. Capillary with inner diameter of 328 micron was employed.

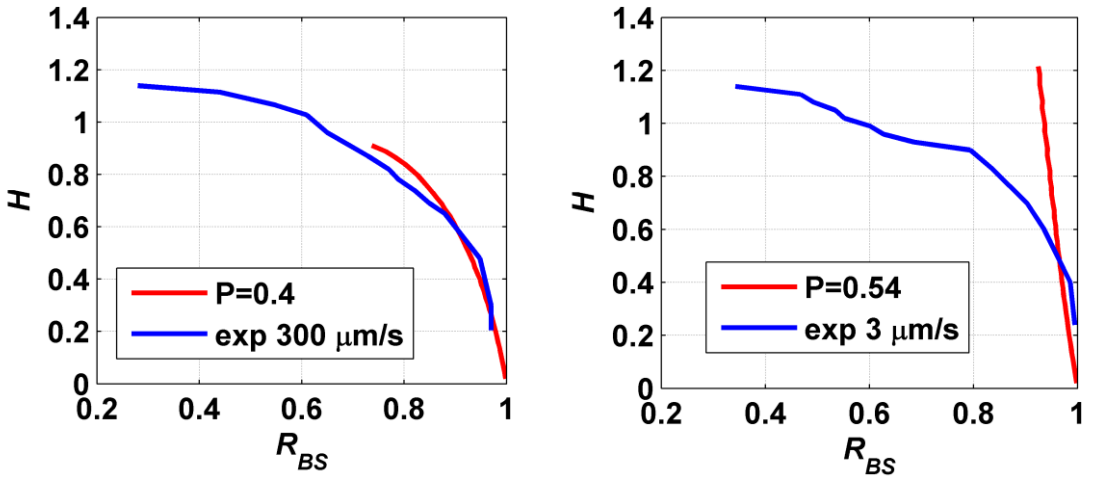

(a) (b)

Figure 39. The base bridge radius vs. capillary-substrate height at *P*=0.4 (a) and at *P*=0.54 (b) (model/experiments comparison).

Modeling/experiment comparison of the base bridge radius behavior at fixed pressure is presented at Figure 39. Two pressures, *P*=0.4 (Figure 39a) and *P*=0.54 (Figure 39b), are

considered. We see that the static bridge theory catches the trend of the dependency of bridge base radius on the capillary-substrate height, but it cannot describe the full process completely.

2.2.9. Conclusions

A capillary-based lithography method is described where the substrate is untouched by the dispensing tip. The application of the pressure from one side of capillary leads to the liquid meniscus formation at the capillary outlet. Touching the substrate with the liquid meniscus causes the liquid bridge creation between the capillary and the substrate. By withdrawing the capillary away from the substrate, the liquid bridge raptures leaving a liquid droplet on the substrate. In this paper the stability of the liquid bridges between the hollow capillary and substrate was theoretically analyzed depending on the liquid-capillary and the liquid-substrate equilibrium angles. To minimize the size of the deposited droplet, the liquid-capillary and the liquid-substrate equilibrium contact angles should be increased. Also it is desired to have capillary with smaller inner diameter and wall thickness. Based on simulation results, it was found that the liquid bridges between the capillary and substrate can be used for movements of small objects sitting on the substrate. By comparing the capillary-based deposition process with rod-based deposition scenario, we noticed that it is favorable to use rod, but the rod-based deposition requires re-dipping. Experimental study of the problem in micro-scale for a wide range of glycerol/water mixtures and different capillary radii r_C was presented as well. The size of deposited liquid droplet is in the range of 20% of inner diameter of the capillary. Comparison of theoretical results with experimental data shows good agreement [57, 58], especially at lower

capillary-substrate heights. But the static bridge theory cannot describe the experimental bridge profile for all capillary-substrate distances. The static bridge theory fails, when the capillary-substrate distance approches the rupturing heights. To catch experimental observation, the dynamic of liquid bridge must be considered. In the next sub-section, we explain how to scale this method down to nanoscale using nanocapillary navigated by Scanning Tunneling Microscope.

2.3. Attempt to Scale Down to Nano-Scale

2.3.1. Nano-Capillary Fabrication

The nano-capillaries used for the deposition are pulled from the quartz capillary manufactured by Sutter Instrument. Initially the quartz pipette has an inner diameter of about 500 microns. The Puller apparatus, P-2000 (also produced by Sutter Instrument), allows fabrication of nano-capillaries as small as 30 nm in diameter based on the apparatus parameters. It has five main parameters: the temperature, the scan length of the laser, the velocity of the carriage before the hard pull, the timing on start of the hard pull, the force of the hard pull. To fabricate the nano-capillary of 100 nm in radius, the parameters of the puller shown in Table 8 were used (note that these parameters do not have dimensions).

Table 8. Puller parameters [18].

Temperature	Scan length of laser	Velocity of carriage	Time	Force
700	4	55	132	55
750	4	50	127	55

After the pulling, the nano-capillaries were transferred into a Glove Box Evaporator (manufactured by Cooke Vacuum Products) and coated by a thin layer of chrome and gold under the pressure of 10^{-6} Torr. The Evaporator Crystal monitor detects the rate of the metal evaporation. Usually, the evaporation rate is from 1 nm/sec to 5 nm/sec. The thickness of the chrome was about 5 nm, the thickness of the gold was about 30 nm which are controlled by the Applied Evaporator Amperage. Chrome was coated first to have good adhesion between quartz and gold.

Once coated, the nano-capillaries were hydrophobized by Octadecyltriochlorosilane in order to have an non-wetting surface [59, 60] (details of this procedure was given in section 2.2.8). A side view and top-down SEM pictures of nano-capillary are shown on Figure 40.

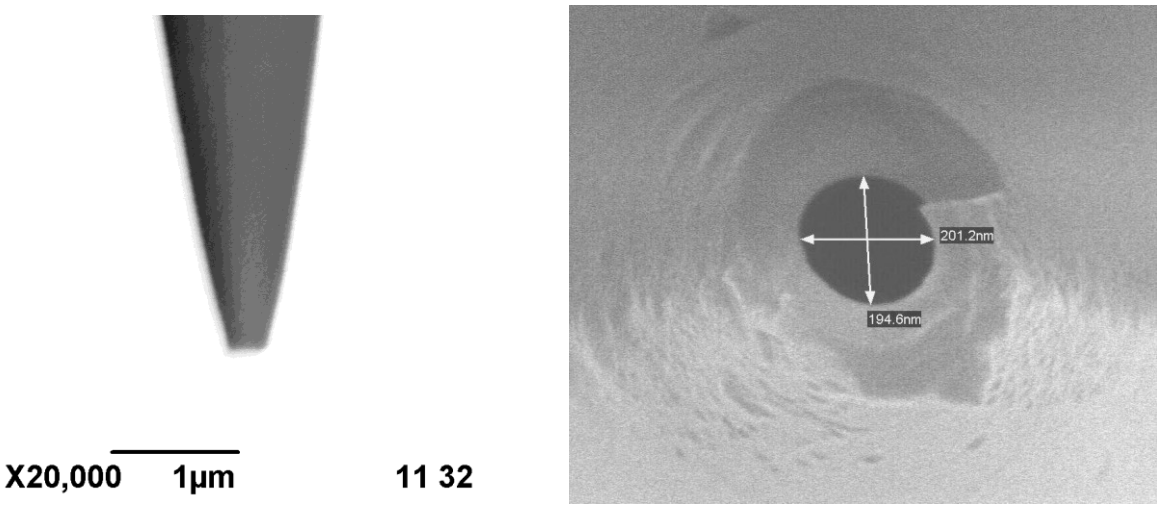

Figure 40. Side view and top-down SEM pictures of nano-capillary [18].

Based on the SEM analysis, the inner radius of the nano-capillary is defined. Another technique of inner radius determination is the Bubble Point Apparatus [61]. The idea of this apparatus is the following. The nano-capillary is connected to the nitrogen gas

tank under high pressure. The free end of the nano-capillary is inserted into a liquid reservoir. Increasing the gas pressure causes the gas bubble formation at the end of the nano-capillary. The time between the gas bubbles is measured. Based on the dependency between applied pressure and time between bubbles, the inner radius of the nano-capillary is calculated [19, 61].

The Bubble Point Apparatus error of the inner radius determination is about 10-15 percent. The SEM analysis gives the exact size of the nano-capillary inner radius. However, based on the SEM pictures, identifying if the capillary is open or clogged is impossible.

The Bubble Point Apparatus was used not only to identify the inner capillary radius, but also to test the capillary. Since the nitrogen gas is applied to the capillary, the pressurization reveals whether or not the nano-capillary is clogged after the hydrophobization.

Therefore, first, the nano-capillary inner diameter is determined based on SEM pictures, after that the nano-capillary was tested on Bubble Point Apparatus in order to compare the SEM result with the Bubble Point Apparatus result. At the same time, this Bubble Point Apparatus testing gives the information about the capillary obstruction. If the nano-capillary is not clogged, the degassed glycerol is then pulled inside of a clean syringe with a small needle. Once glycerol in the syringe, glycerol is inserted into the tested nano-capillary and the Droplet Point Test is performed in order to evaluate the actual hydrophobized area.

The Droplet Point Test is a modified Bubble Point Apparatus experiment. In the Droplet test, the nitrogen gas is used to push the glycerol through the nano-capillary to

form a droplet. Based on the pressure needed to form a glycerol droplet at the nano-capillary end, one can evaluate the actual hydrophobized area.

This test also ensures that there are no gas bubbles in the liquid glycerol and that the liquid flow is not blocked by gas bubbles.

2.3.2. Liquid Treatment and Insertion into Nano-Capillary

Before the integration of a nano-capillary inside of the Scanning Tunneling Microscope, the inverse Bubble Point Experiment (or the Droplet Point experiment) was performed. Therefore, the nano-capillary was filled by glycerol and hooked up to the gas tank of the nitrogen. After that, the pressure was gradually applied from one end of the capillary in order to visualize at what pressure the droplet of the glycerol shows up at the nano side. The droplet was watched by using an optical microscope at 100× magnification. The Inverse Bubble Point Experiment was done, since the capillary treatment involved many experimental steps, in order to check that the capillary was not clogged. At the same time, by doing this, an actual size of the hydrophobized area can be approximated by using the Laplace relation:

$$p = \frac{2\sigma}{r_{actual}} \tag{36}$$

where σ is the glycerol surface tension and r_{actual} is the radius of the actual hydrophobized circle area. Usually, it is 50 nm higher than the internal radius of the nano-capillary due to

the procedure of the nano-capillary hydrophobization: gas flow is applied while capillary is in the solution for hydrophobization.

From experimental observation it was found that glycerol bought from SigmaAlrich cannot be used right away, because after the insertion of the glycerol inside of the capillary, the gas bubbles in the liquid are formed, which can stop the liquid flow. That is why the glycerol was treated before use. An open glycerol bottle was heated to 80°C and, at the same time, sonicated in a bath sonicator (model 50 HT, VWR) for about 30 minutes. After that, it was left in a vacuum chamber for 12 hours to finally remove all the gas bubbles from the glycerol. The glycerol should be used within 5 hours after the treatment.

2.3.3. Capillary Integration in STM

Once the nano-capillary is filled with the glycerol, it is integrated in to the Scanning Tunneling Microscope, as presented in Figure 41. Rob Sailer was the first who proposed and implemented this modification of the STM replacing the standard STM tip by the nano-capillary [19]. Here, the main issue is to make sure that the nano-capillary is properly connected to the standard STM tip. Then, the performance of the integrated nano-capillary as a scanning tip is checked by scanning a 5 by 5 micron area of the HOPG. After that, a flat surface of the HOPG is chosen for the deposition, and the nano-capillary is moved there in the x, y-direction. The next step is to evaluate the distance between the nano-capillary end and the substrate; usually the distance is in the range of 2-5 nm.

Once the real distance is known, the capillary is moved in the z-direction away from the substrate for a given distance. A capillary movement in all directions is controlled by the STM software. When the capillary is far from the substrate, the meniscus is formed,

by applying the pressure from the other capillary end. Then the capillary with the meniscus is moved toward the substrate without touching the substrate. When the deposition has been completed, the capillary is moved away from the substrate, and the applied pressure is released. With one capillary, a series of 21 dots are deposited in a line by applying varying degrees of pressure at different distances between the capillary and substrate.

Figure 41. Hydrophobized gold-coated nano-capillary integrated in STM [18].

2.3.4. Tip-Substrate Distance Evaluation

2.3.4.1. Introduction

The goal of the current section is to evaluate the distance between the STM tip and the substrate. Here 3 different types of the STM tips are considered:

- 80% Pt and 20% Ir wire made by cutting at an angle. Diameter of the wire is equal to 0.2 mm,
- Electro-chemically etched STM tips produced from the same 80% Pt and 20 % Ir wire; these STM tips are commercially available.
- Gold-coated nano-capillaries.

The substrate was HOPG (highly oriented pyrolytic graphite) due to conductivity of this substrate, and because of the relatively small roughness of the HOPG substrate (5-10 nm in an area of 5 by 5 microns). Before measuring the dependency between the current and relative distance, several trials were conducted to get the best image of the substrate in order to check that the particular tip would work well.

Figure 42 shows the relative coordinate system that will be used for this paper. The following equation describes the dependency between the relative and absolute coordinate systems:

$$z = z_0 + \xi \tag{37}$$

where z_0 is the set point distance corresponding to the STM set point current and ξ is the distance relative to the set point distance. z_0 is initially unknown and to be determined from experiments.

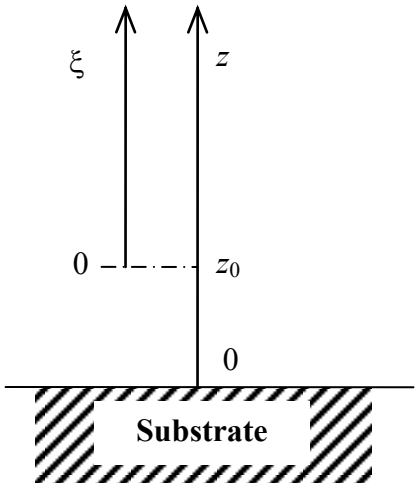

Figure 42. Relative coordinate system, ξ, and absolute coordinate system, *z* [18].

2.3.4.2. Landauer Conductance

The tunneling current *I*, can be described as [62]

$$I(z) \propto e^{-k\sqrt{2\Phi}z} \tag{38}$$

where *k* is a constant and *z* is the distance from the nucleus of the surface atom to the nucleus of the STM tip apex atom. Using the definition of conductance *G*,

$$G = \frac{1}{R} = \frac{I}{V}, \tag{39}$$

and holding the applied bias constant, a relationship for the tip-sample conductance as a function of the tip-sample distance can be determined:

$$G(z) \propto e^{-k\sqrt{2\Phi}z} \tag{40}$$

When the tip apex comes into contact with the sample surface, the tip-sample distance is equal to zero. The conductance of the point of the contact should be equal to one conductance quantum and can be written using the Landauer conductance [62, 63]

$$G(0) = G_{contact} = \frac{2e^2}{h} = 7.75 \times 10^{-5} S \tag{41}$$

From Eqs. (38), (39), and (41), it can be determined that

$$I(z) = VG_{contact} \exp(-Bz), \tag{42}$$

where $B = k\sqrt{2\Phi}$. Therefore,

$$\ln(I) = \ln(VG_{contact}) - Bz \tag{43}$$

Since

$$\frac{d\ln(I)}{d\xi} = \frac{d\ln(I)}{dz} = -B, \tag{44}$$

a trend line can be fitted to a plot of the spectroscopy data (current I vs. relative distance ξ) to find the value of B.

2.3.4.3. Simmons' Formula

Using Simmons' formula [64, 65], the tunneling current can be written as

$$I(z) = \frac{\alpha}{z}\exp(-Bz) \tag{45}$$

where $\alpha = \gamma S\sqrt{\Phi}V$, $\gamma = \frac{e\sqrt{2m}}{4\beta\pi^2\hbar^2}$, $B = A\sqrt{\Phi}$, $A = 2\beta\sqrt{\frac{2m}{\hbar^2}}$, and S is the contact area.

Using the relative coordinate system shown in Figure 42 and defined in Eq. (37), Eq. (45) can be rewritten as

$$\frac{I(z_0)}{I(z_0+\xi)} = \frac{I_0}{I} = \frac{z_0+\xi}{z_0}\frac{\exp(-Bz_0)}{\exp(-B(z_0+\xi))}. \tag{46}$$

Rearranging of Equation (46) results in:

$$\frac{I_0}{I}\exp(-B\xi) = 1 + \frac{\xi}{z_0}. \tag{47}$$

The work function between the gold nanocapillary and the HOPG substrate is not known; therefore it is necessary to find a value for B. From Eq. (45) it can be found that

$$\frac{d\ln(I)}{dz} = \frac{d\ln(I)}{d\xi} = -\frac{1}{z} - B\,. \tag{48}$$

If $z >> 1/B$, then

$$B = -\frac{d\ln(I)}{d\xi}\,. \tag{49}$$

Using the spectroscopy data (current I vs. relative distance ξ), $\frac{d\ln(I)}{d\xi}$ can be found by plotting ln(I) vs relative distance and fitting a trend line to the data. Using the value of B from Eq. (49), a plot of $\frac{I_0}{I}\exp(-B\xi)$ vs. relative distance ξ can be made and a trend line fit to the data. Thus:

$$\frac{d}{d\xi}\left[\frac{I_0}{I}\exp(-B\xi)\right] = \frac{1}{z_0}\,. \tag{50}$$

Finally, using the value of z_0 from Eq. (50), a relationship between tip-sample distance z and current I can be found

$$I(z) = \frac{I_0 z_0}{z}\exp\left[-B(z - z_0)\right] \tag{51}$$

2.3.4.4. Experimental Procedure

The experimental data was gathered by using an Agilent Technologies 5500 AFM microscope in STM imaging mode. Data was collected by using three different STM tips. The first of these was a 0.25 mm diameter 80% Pt, 20% Ir wire cut at an angle to produce a tip as sharp as possible. This tip can be seen in Figure 43.

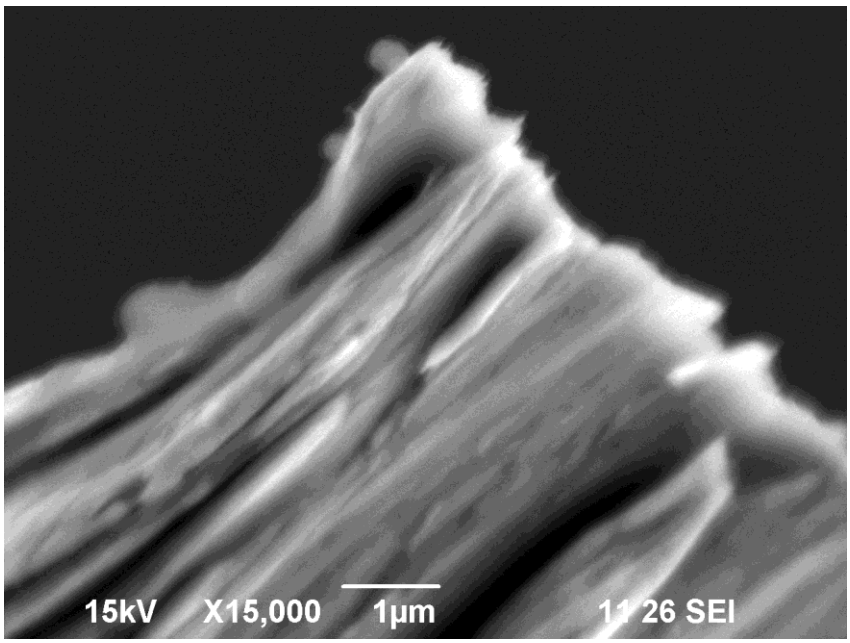

Figure 43. SEM image of Pt/Ir wire tip [18].

The second tip was an electrochemically etched 80% Pt, 20% Ir tip shown in Figure 44. The third tip was a glass nano-capillary with an opening of about 100 nm coated in gold on one side. This tip can be seen in Figure 45.

The experimental data was collected by measuring the current versus the relative distance dependency. The data gathering took about 1 second. The relative distance was changed from ~ + 4 nm to ~ -4 nm from the set point. This process was repeated three

times. The data was processed according to both Landauer and Simmon's theory. For both approaches, the current versus the relative distance plot was re-plotted in a semi-log scale shown in Figure 46. After that, the experimental data was fitted by the line, therefore the slope parameter *B* is defined.

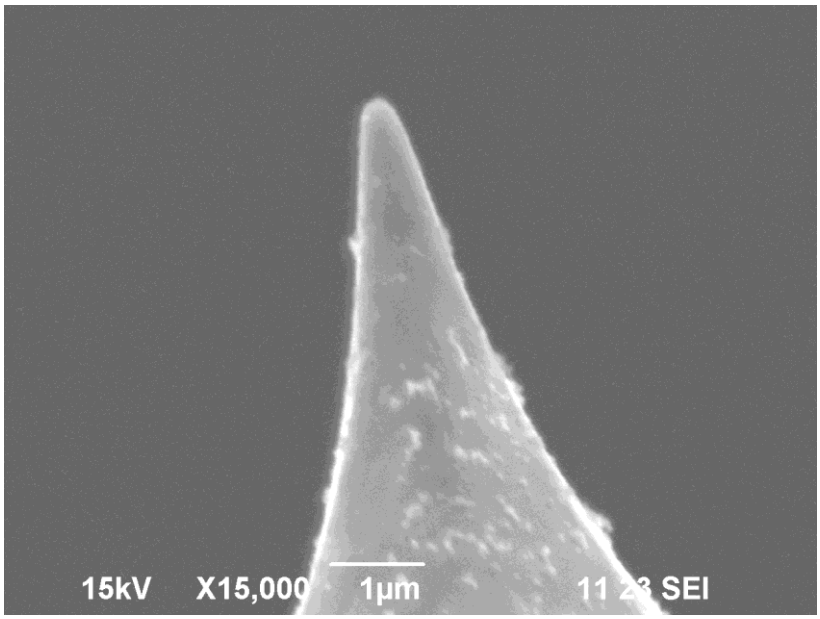

Figure 44. SEM image of electrochemically etched tip [18].

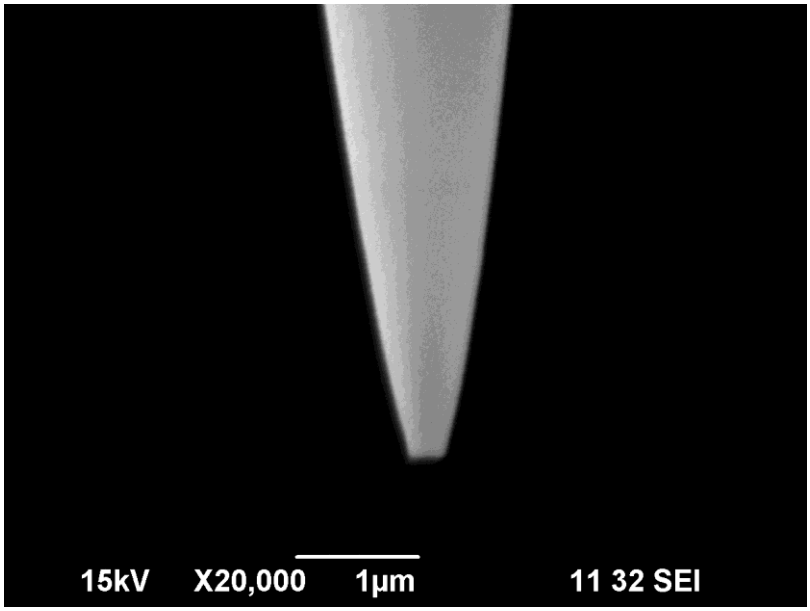

Figure 45. SEM image nano-capillary tip [18].

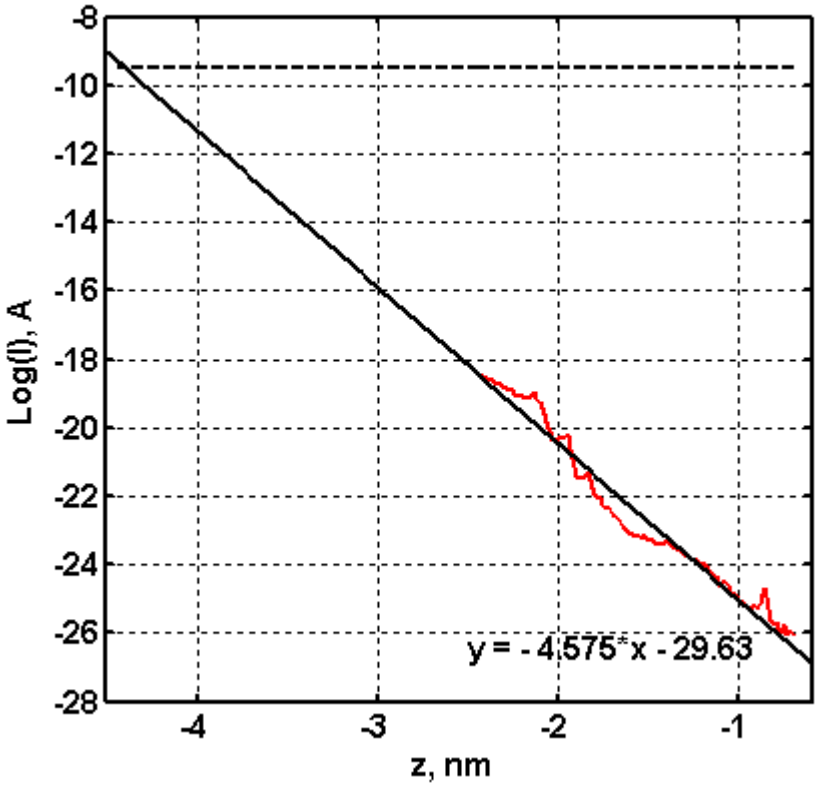

Figure 46. Experimental data (red line), Log of current vs relative distance curve, dash line means the current of contact (bias=0.1 V) [18].

Based on the Landauer theory, the intersection between the fitted line and the line of contact provides the real distance between the relative and absolute coordinate systems. For the case shown in Figure 46, the parameter B is equal to 4.58 nm^{-1}, and the distance between the relative and absolute coordinate system, z_0, is equal to 4.42 nm, so the following dependency between the current and the distance is observed:

$$I(z) = VG_{contact}\, exp(-Bz)$$

$$I(z) = 7.75\times10^{-6}\, exp(-4.58z)$$

$$I(\xi) = 7.75\times10^{-6}\, exp(-4.58(4.42+\xi)).$$

At the same time, applying the Simmon theory to experimental data does not work well: the fitted trend to the plot $\frac{I_0}{I}\exp(-B\xi)$ vs. relative distance ξ has a huge dispersion (see Figure 47). Eventually, one can conclude that Simmon's formula cannot be used to describe the process taken place in this experiment. All results shown below were obtained by using only Landauer's approach.

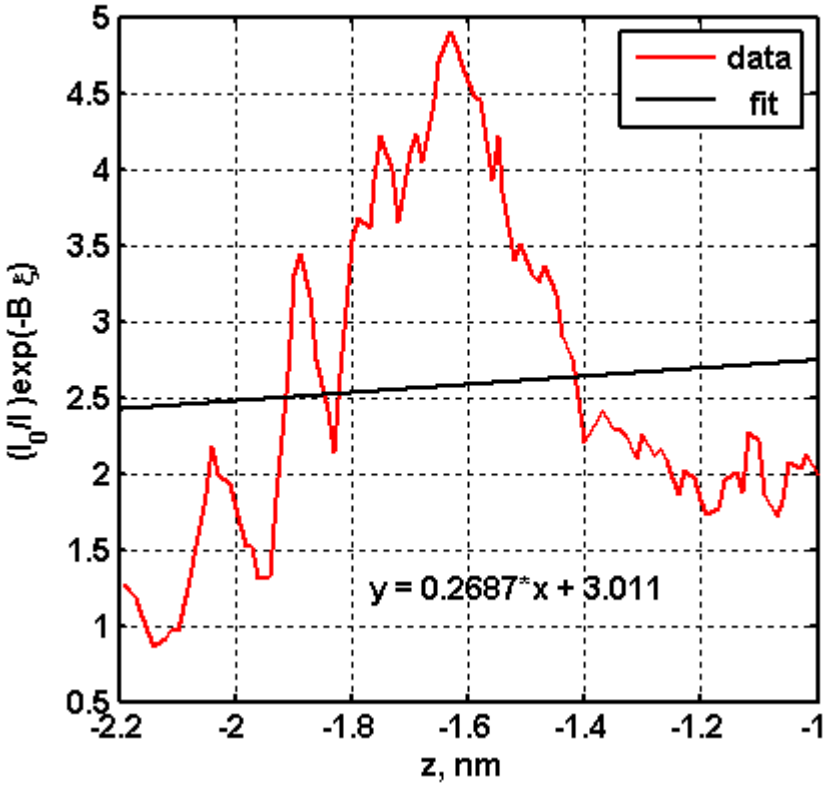

Figure 47. Simmon's fit to the experimental data [18].

2.3.4.5. Results

Below are three Tables of results for different STM tips. As one can see, there is no substantial difference between the wires, the etched tips, and the nano-capillaries. One conclusion can be obtained from the results: the higher the slope *B*, the smaller the distance

between the STM tip and substrate. Another interesting finding is that the distance between the substrate and tip is in range of 2-5 nm for any tip type.

It was observed that in most cases the scanned images of the substrate are clear and do not have any noise if the wire tips and the etched tips are used (Figure 48 and Figure 49). When the nano-capillaries were inserted into STM, sometimes, the blurred images were produced (Figure 50). Applying the high voltage helps to resolve the problem with scanning, but this procedure does not work every time. Right now, there is no plausible explanation for this phenomenon.

Table 9. Results for wire tip [18].

Tip 1	***B*, nm^{-1}**	**z_0, nm**	**Bias, V**
Trial 1	10.44	1.16	0.1
Trial 2	10.28	1.25	0.1
Trial 3	10.15	1.32	0.1
Average	**10.28**	**1.24**	**0.1**

Table 10. Results for etched tips [18].

Tip number	**Trial #**	***B*, nm^{-1}**	**z_0, nm**	**Bias, V**
1	Trial 1	5.427	3.85	1
1	Trial 2	4.546	4.42	1
1	Trial 3	5.046	4.19	1
1	**Average**	**5.006**	**4.14**	**1**
2	Trial 1	8.020	2.07	0.5
2	Trial 2	11.377	1.56	0.5
2	Trial 3	9.318	2.04	0.5
2	**Average**	**9.572**	**1.86**	**0.5**
3	Trial 1	2.544	5.44	0.1
3	Trial 2	2.652	5.44	0.1
3	Trial 3	2.498	5.29	0.1
3	**Average**	**2.565**	**5.39**	**0.1**

Table 11. Results for nano-capillaries [18].

Tip number	Trial #	B, nm^{-1}	z_0, nm	Bias, V
1	Trial 1	11.647	1.19	0.1
1	Trial 2	12.285	1.13	0.1
1	Trial 3	13.414	1.02	0.1
1	**Average**	**12.449**	**1.11**	**0.1**
2	Trial 1	10.212	1.28	0.1
2	Trial 2	10.033	1.30	0.1
2	Trial 3	9.851	1.31	0.1
2	**Average**	**10.033**	**1.30**	**0.1**
3	Trial 1	10.937	1.53	0.1
3	Trial 2	12.617	1.40	0.1
3	Trial 3	10.897	1.51	0.1
3	**Average**	**11.484**	**1.48**	**0.1**
7	Trial 1	7.16	3.03	0.1
7	Trial 2	7.81	3.96	0.1
7	Trial 3	7.39	3.03	0.1
7	**Average**	**7.45**	**3.34**	**0.1**
8	Trial 1	3.68	4.96	0.1
8	Trial 2	2.89	5.98	0.1
8	Trial 3	2.93	4.74	0.1
8	**Average**	**3.17**	**5.23**	**0.1**

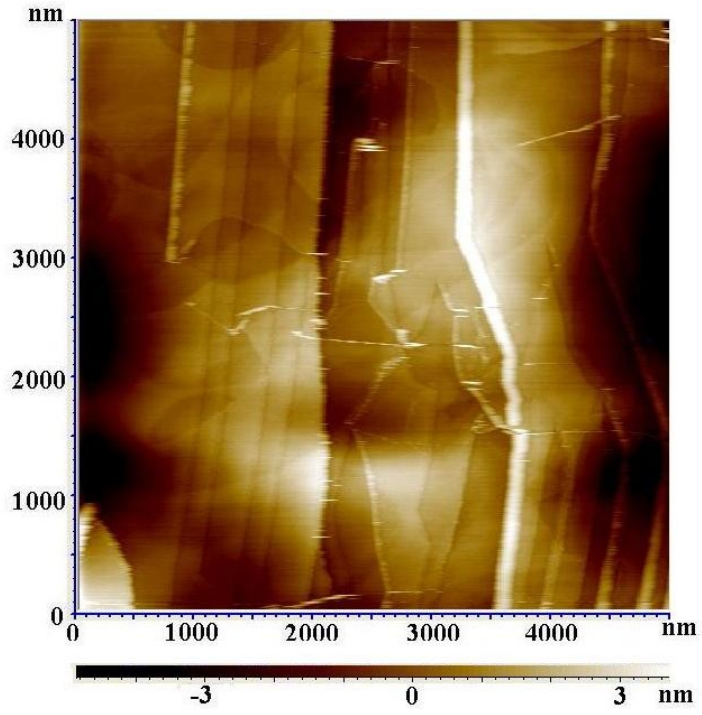

Figure 48. HOPG substrate scanned by wire cut at an angle [18].

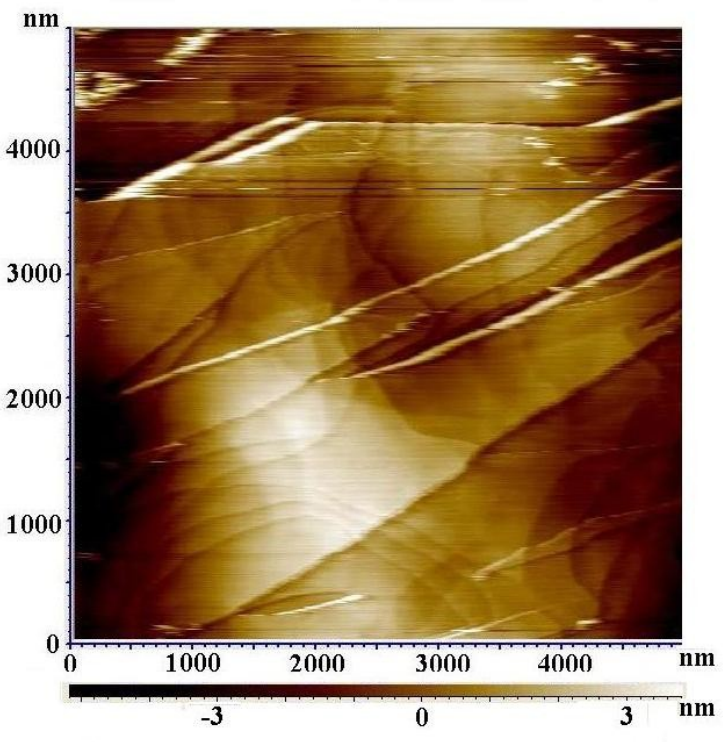

Figure 49. HOPG substrate scanned by etched STM tip [18].

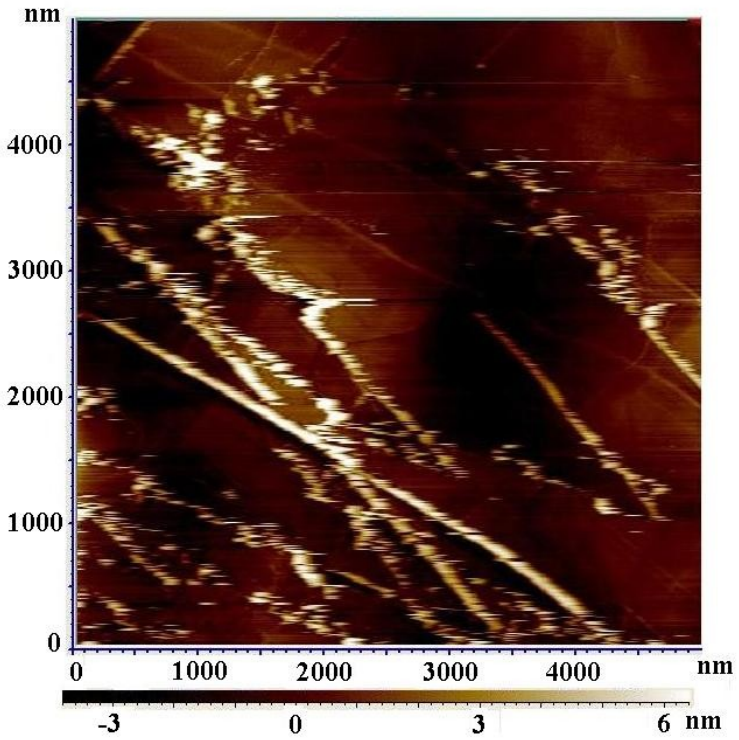

Figure 50. HOPG substrate scanned by gold nano-capillary [18].

The thickness of the gold coating at the end of the nano-capillary could be a possible source of the noise during the scanning. Applying a bias to the gold-coated nano-capillary and passing the current through the tip can cause the gold to melt. To check this assumption, the SEM with a higher resolution should be used.

2.3.5. Nano-Capillary Deposition Results

2.3.5.1. Initial Results

Once hydrophobized gold-coated nano-capillary is filled by glycerol and is integrated in the STM, it should be tested by scanning the area of 5 by 5 micron. After the successful testing, the distance between the capillary and substrate is defined. Then, the nano-capillary is moved away from the substrate at a known distance (about 1 micron), and the pressure is applied to form a given size of meniscus. Once the meniscus is formed, the capillary is moved to the substrate in order to touch the substrate with the meniscus only. The capillary is placed close to the substrate for about 1 minute to be sure that deposition happens. After that, the capillary is gradually moved from the substrate, and the applied pressure is released. To deposit one more droplet, the substrate is moved horizontally for about 150 micron, and the same procedure is applied. The deposited liquid dots are visualized by using the optical camera built in to the AFM system.

The two figures below show the surface before and after the deposition (Figure 51 was taken before deposition and Figure 52 was taken right after the deposition). The pictures were taken at the highest possible magnification and then saved in jpeg format. Several trials were performed to detect the liquid dots by switching to the non-contact

AFM mode, but the trials did not reveal any dots. The failure could have been caused by either a deposition mistake or the evaporation of the dots. The most logical reason of the failure is the evaporation, because the evaporation rate is a significant factor, when the dot dimensions approach 100 nm.

Figure 51. HOPG substrate before deposition [18].

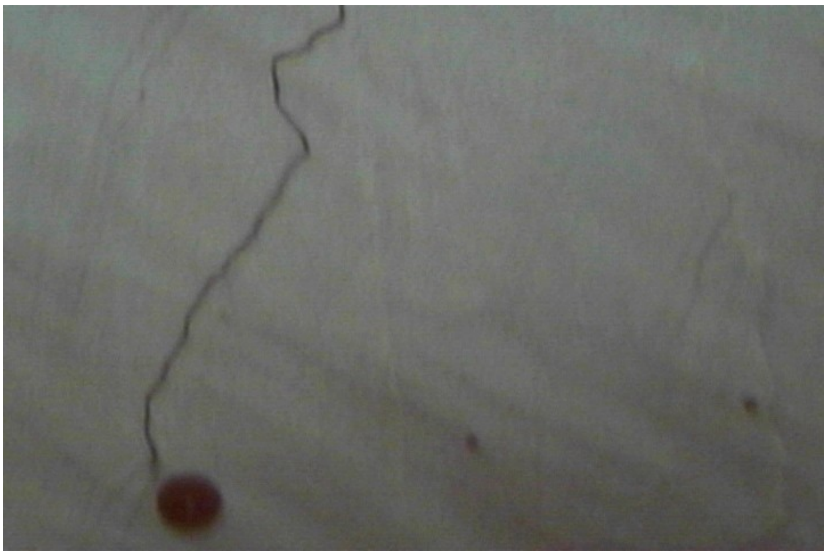

Figure 52. The same area of HOPG after deposition [18].

In order to estimate the evaporation rate, the following experiment was performed. First, a micron-size liquid dot was deposited on the substrate. Then, three photographs of the substrate were taken at 15-minute intervals to capture the change of the droplet base radius. In particular, the droplet with a 4-micron base radius decreases and after 15 minutes, its base radius equals to 2.5 microns. Based on this result, the rate of the evaporation is equal to 1.87×10^{-6} kg/(m^2 s) (see Figure 53). The known evaporation rate is applied to calculate the evaporation time for a 500-nm droplet, which is approximately 5 minutes. Therefore, if a 500-nm droplet was deposited, only 5 minutes would be available to detect this droplet. A 5-minute time interval is only enough to switch a microscope to the AFM non-contact regime, but it is insufficient to identify the droplet by AFM. One way, to solve this problem, is to deposit the liquid dots in the glycerol vapor atmosphere instead of the ambient atmosphere, because the glycerol vapor atmosphere decreases the evaporation rate.

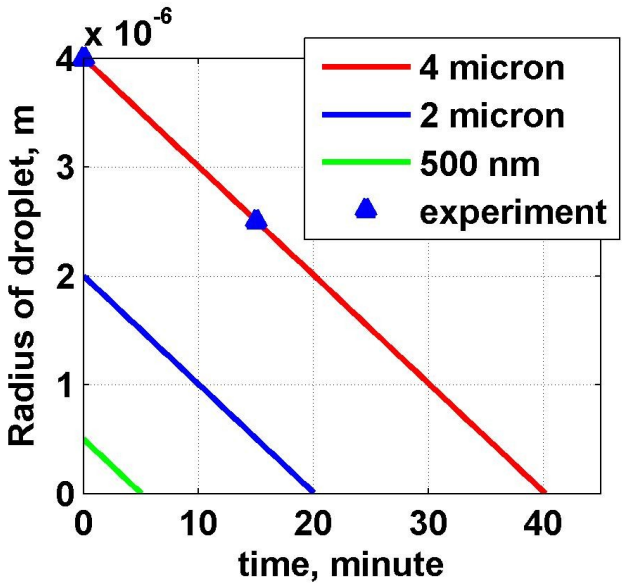

Figure 53. The change of the droplet base radius in time due to evaporation [18].

2.3.5.2. Deposition Results

During the process of the dot deposition on clean (untreated) HOPG, two parameters have been changed: the pressure applied and the distance between the capillary and substrate (see Figure 54). It was found that the change of these parameters does not change the size of deposited dots. The dot size may vary from 5 micron to 100 micron in diameter. Dependency between the pressure applied and the size of deposited dots have not been observed.

(a): P = 300 kPa (H = 70, 60, 50 nm)

(b): P = 300 kPa (H = 50, 40 nm)

(c): P = 800 kPa (H = 20 nm);
P = 200 kPa (H = 30, 20 nm)

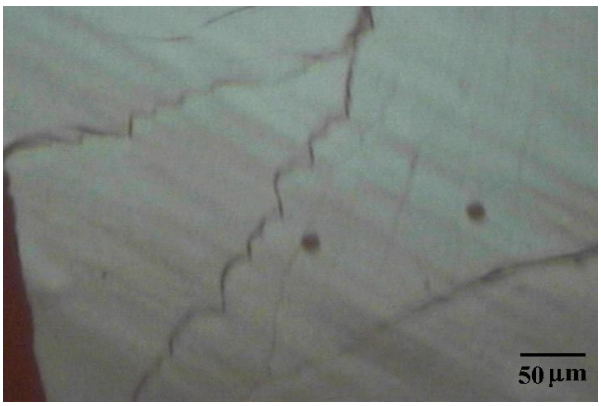

(d): P = 500 kPa (H = 20 nm);
P = 600 kPa (H = 20 nm);
P = 700 kPa (H = 20 nm)

Figure 54. Results of depositions for different pressures and capillary-substrate distances [18].

Unfortunately, the experimental contact angle between clean HOPG and glycerol is equal to 75 degrees, so no matter what pressure is used, the obtained bridge is not stable. This explains why experimentally the deposited dots have micron sizes. In order to be able to deposit nano-dots, the contact angle between Glycerol and HOPG should be increased.

Therefore, the next step was to deposit nano-droplets on hydrophobized HOPG, but these droplets were not detected by using the atomic force microscope. The reason for this fact can be explained by fast evaporation rate of the glycerol solution. To solve this problem, glycerol as a test liquid may be changed to the water solution with presence of soluble salt. By doing this, the evaporation problem will not be solved, but leftover salt can be served as signs of nano-droplet deposition. In order to check if this idea is working or not, we tried to deposit salt-water solution in micro-scale. For a salt we chose the zinc nitrate because it is soluble in water and the presence of this salt in water did not change the water contact angle with the substrate. After the deposition of salt/water solution, the water was evaporated and we observed the salt stain which can be seen in Figure 55.

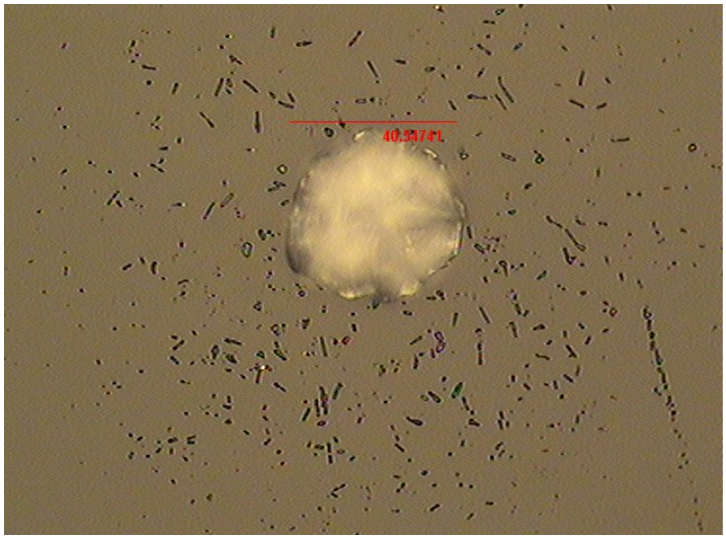

Figure 55. Zinc nitrate salt, $Zn(NO_3)_2$, is left after deposition of salted water solution.

Unfortunately deposition of salt/water solution on nano-scale was not done due to high price of experimental rent for the atomic force microscope: There was no finding available to support this activity.

2.3.6. Conclusions

Using the nano-capillary, the possibility of micro-droplets deposition with unfavorable parameter range was shown: Liquid-substrate equilibrium contact angle was 75 degree, which causes bridge spreading on the substrate. Deposition of droplets on hydrophobized substrate caused nano-droplet deposition, but these nano-droplets were not detected due to the liquid evaporation.

The problems of the proposed capillary-based technique in nano-scale (e.g. the high liquid evaporation rate and the liquid nano-dots detection) can be eliminated in the future by the deposition in a liquid vapor atmosphere and by learning how to find the liquid nano-features on a given substrate. One method of the liquid detection is freezing the liquid nano-dots and then scanning the liquid dots in a solid state by the SEM apparatus. However, this process would be a time consuming, difficult process, and out of the scope of the current work.

The deposition of water/glycerol solution mixed with salt particles will also resolve the droplet detection problem. The idea is not sophisticated: If water/glycerol evaporates, salt particle will stay. Therefore, by AFM scanning, one can define the radius of deposited droplet. By knowing the radius of the deposited droplet, it is possible to calculate the volume of the initial droplet.

Another method of solving the evaporation problem is to change the test liquid from glycerol to the non-volatile liquids. For instance, this can be done by deposition of

epoxies. Epoxies can be solidified right after deposition by applying UV light. The difficulty in this case is that the epoxies are usually designed to have low contact angles with different substrates.

3. AERSOL FLOW THROUGH MICRO-NOZZLE

3.1. Aerosol Flow Modeling

3.1.1. Introduction

Aerosol flow through micro-nozzles is a key process for many fabrication techniques such as Aerosol-Jet Direct-Write and Collimated Aerosol Beam Direct-Write. In this section, modeling of aerosol dynamics will be presented. The aim of this research work is twofold. The first goal is to develop a model which accurately describes the aerosol flow (two phase flow: gas and particle) through the nozzles based on the Eulerian-Lagrangian approach. The second objective is to design a nozzle which collimates all particles of diameters $d \geq 1$ μm to the nozzle centerline.

In order to achieve the goal, first, the gas flow through the nozzle was simulated separately from the particle motion by a commercially available package called ANSYS CFX. The continuity, momentum, and energy equations were employed to determine the gas velocity and density inside and outside the nozzle. To minimize calculation time, only a sector of five degrees was considered. Also, a plenum was added at the nozzle outlet to understand the particles' behavior flying out of the nozzle.

After that, ANSYS CFX simulation results were exported into a home-made Matlab code to calculate the particles' trajectories and velocities. Here Newton's second law was used with two forces acting on the particle due to the gas motion. These forces are Stokes force and Saffman force. Gravity, droplet condensation, and evaporation were neglected. It was also assumed that aerosol droplets have a spherical shape. Aerosol droplet collisions with the nozzle wall and with each other are not considered.

In the next step of the research, the developed model was compared and validated with experimental results using a simple convergent nozzle and a linearly-convergent nozzle attached to the straight part. Different flow rates and different particle sizes were employed. Finally, based on the verified model, a new nozzle design is proposed in order to collimate all aerosol particles toward the nozzle centerline.

3.1.2. Gas Simulation

Many methods have been considered for controlling the flow of aerosol particles. First, inertial impactors (real or virtual) can be used to sort aerosol droplets with smaller particles separated from larger particles [66-70]. Real impactors remove larger particles by causing them to impact with a coated solid plate, while virtual impactors only change the trajectories of smaller particles. Second, micro-nozzles have been incorporated into the front-end system of light-/laser-based chemical gas sensors where the aerosol particles are focused into the detection zone [71-74]. Third, aerodynamic lenses are utilized for the fabrication of nano-crystalline microstructures with line-widths of about 50 microns. Micro-nozzles have also been used for printed electronics where a single-nozzle system by Optomec [14] and a converging-diverging-converging system that we developed [16, 17] give rise to focused aerosol deposition of conductors, semiconductors, and insulators. While this field has advanced according to an empirical approach, the development of a theoretical model that describes the aerosol flow process at the micron-scale will provide additional benefits to the field of printed electronics.

Eulerian-Eulerian and Eulerian-Lagrangian (Lagrangian particle tracking) are the two main methods typically employed for simulation of aerosol particles (dispersed phase)

flowing through a gas (continuous phase). In both approaches, the Eulerian model is used for simulation of the continuous phase. But in the case of the particle tracking method, the dispersed phase is treated by the Lagrangian model. Lagrangian particle tracking is widely utilized to simulate aerosol flow because in most cases, the particle concentration is significantly lower in comparison to the gas concentration. Inter-particle interactions can be neglected for flows with low particle concentrations. Furthermore, for the aerosol flow of low particle volume fraction, the gas has an influence on the motion of aerosol particles, but the gas flow is not affected by the motion of the particles.

Both of these approaches (Eulerian-Eulerian and Eulerian-Lagrangian) are available in commercially available programs based on the finite element method such as ANSYS, Abaqus, Comsol, Nastran, etc. In our simulation of the aerosol flow we decided to use the eulerian-lagrangian approach available in ANSYS. This software was chosen because of its availability in the Mechanical Engineering department at North Dakota State University.

ANSYS CFX is a Computational Fluid Dynamics software used in modeling of fluid flows, heat transfer, combustion, etc. [75]. Any ANSYS CFX package contains four main components:

- Geometry/mesh creation module in which first, the geometry of the problem should be defined. Then, regions of fluid flow, solid regions, and surface boundary have to be named. After that, mesh settings should be set in this module.
- Setting module which is called CFX-Pre. Here the mesh files are imported from the geometry creation module. Then flow physics, fluid parameters, boundary condition, initial values, and solver parameters are specified.
- Calculation module, CFX-Solver, which solves the CFX problem.

- Post-processing module called CFX-Post. This ANSYS CFX component allows plotting simulation results graphically.

For any new nozzle design, the nozzle geometry and mesh were created by using the ANSYS package called ICEM CFD. This ANSYS product allows creation of rectangular shape elements with high aspect ratio. That is why ICEM CFD was chosen as the mesh generation software. To make a nozzle geometry, first all points should be created. After that the points should be connected with lines to create a 2D representation of the nozzle. The next step of geometry creation involves the rotation of lines along the centerline to form a 3D body. The rotation was equal to 5 degrees in order to decrease the number of nodes. Then the block that coincides with the nozzle geometry should be created. By using block setting, the number of nodes on each side of the nozzle can be set. A simple example of a linearly-convergent nozzle is presented in Figure 56 and Figure 57 in which the geometry and mesh are shown. As one can see, not only the nozzle geometry is drawn, but also the plenum part is added to the nozzle outlet in order to see how the aerosol droplets are moving out of the nozzle. The linearly-convergent nozzle considered in Figure 56 has the following dimensions: length is 17.14 mm, inlet radius is 416 μm, and outlet radius is 177 μm.

To set boundary conditions, the nozzle surface is divided into different regions: inlet, symmetry, wall, and opening. For the inlet surface, a parabolic velocity profile was implemented based on a given volumetric flow rate. By doing this, the effect of the entrance zone can be minimized. Otherwise, an inlet plenum is required. The inlet flow regime was set to subsonic. A non-slip condition was used at the wall, and atmospheric

pressure was utilized in opening. The static temperature in the inlet, opening, and wall was set to 25°C. Nitrogen ideal gas was chosen as a fluid flow. Reference pressure was 1 atm.

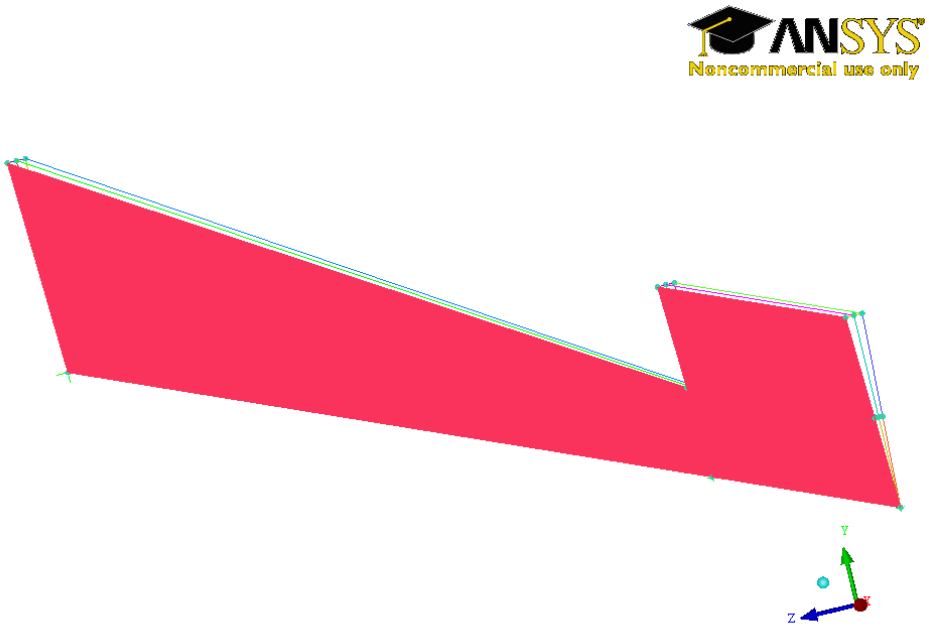

Figure 56. Schematics of geometry and meshing.

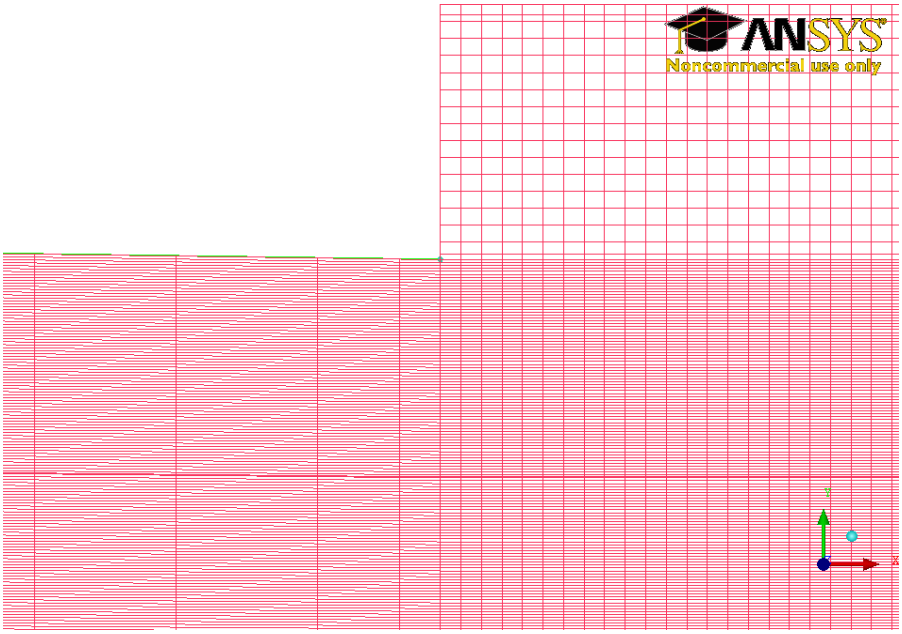

Figure 57. Zoom of meshing at outlet of the nozzle.

The complete set of parameters of CFX-Pre is shown below:

- Simulation
  - Simulation Type Option: Steady state
  - Domain Type: Fluid Domain
  - Fluid list: N2 ideal gas
  - Domain Models → Pressure → Reference Pressure: 1 [atm]
  - Domain Models → Buoyancy Option: Non Buoyant
  - Domain Models → Domain Motion Option: Stationary
  - Domain Models → Mesh Deformation Option: None
  - Fluid models → Heat Transfer Option: Total Energy
  - Fluid models → Turbulence Option: None (Laminar)
- Boundary conditions
  - Inlet → Flow Regime Option → Subsonic
  - Inlet → Mass and Momentum Option →
    - Velocity field: U=3.6787[m/s]*(1-y*y/(0.000416[m]*0.000416[m]))
    - Mass flow rate: 1.5909722×10^{-8} kg/s=10^{-6} m^3/s*1.145 kg/m^3*5°/360°
  - Inlet → Heat Transfer Option → Static temperature: 25 C
  - Open → Flow Regime Option → Subsonic
  - Open → Mass and Momentum Option → Static Pres. (Entrain): 0 Pa
  - Open → Heat Transfer Option → Static temperature: 25 C
  - Symmetry → Choose Two symmetry planes
  - Wall → Wall Influence On Flow Option: No slip
  - Wall → Heat Transfer Option → Temperature: 25 C

- Run parameters
  - Convergence criteria: 10^{-6}
  - Max iteration: 500.

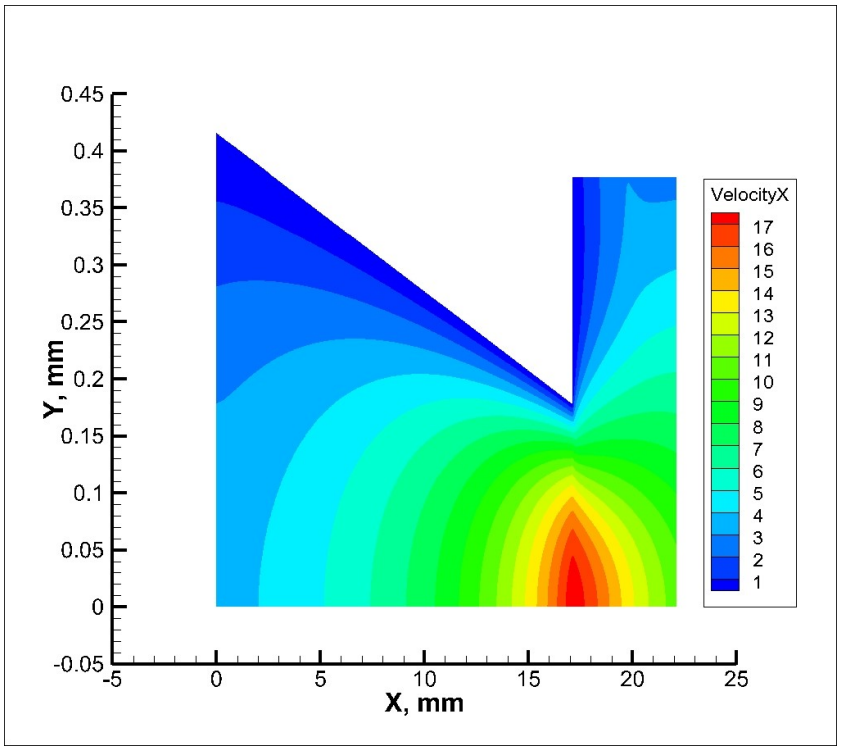

Figure 58. Velocity contour plot when Z =0.

Once ANSYS CFX finishes calculations, the gas data file is created. In this file there should be nine columns: x and y position of node, gas density in the node, x and y velocity components (u and v), and derivatives of velocity components with respect to x and y ($\partial u/\partial x$, $\partial u/\partial y$, $\partial v/\partial x$, and $\partial v/\partial y$). A detailed procedure on how to create this file is presented in Appendix.

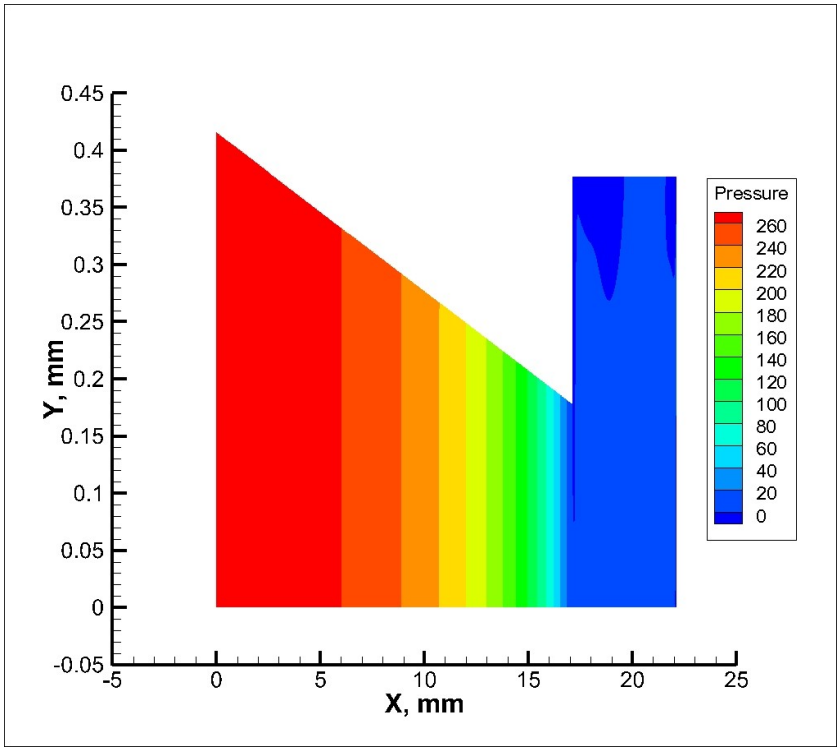

Figure 59. Pressure contour plot when Z =0.

Contour plots of gas velocity and gas pressure are presented in Figures 58 and 59. Based on the results, one can see that the gas velocity reaches its maximum value of 17.8 m/s at the nozzle outlet. Note that the experimentally measured maximum particle velocity was equal to 16 m/s. Also it was found that the ANSYS CFX pressure drop (which is equal to 262 Pa) coincides with the experimental one (measured value was equal to 205±86 Pa).

Comparison of velocity fields at different cross-sections is shown in Figures 60-67 where ANSYS CFX results are plotted against analytical solutions. Analytical results are calculated based on both Poiseuille flow and on the semi-analytical approximation given in [17]. In the case of Poiseuille flow, the x and y components of the velocity vector at any point (x,r) inside of the nozzle are:

$$\begin{cases} u(x,r) = u_{\max}\left(1-\dfrac{r^2}{R^2(x)}\right),\ u_{\max} = \dfrac{R^2(x)}{4\mu}\dfrac{\Delta p}{L} \\ v(x,r) = \dfrac{ru(x,r)}{R(x)}\dfrac{dR}{dx} \end{cases}, \tag{52}$$

where $R(x)$ is nozzle radius at the distance of x from nozzle inlet, L is nozzle length, μ is gas viscosity, and Δp is pressure difference between inlet and outlet of the nozzle.

A semi-analytical expression for the gas velocity field at any point (x,r) was given in our recent paper [17]:

$$\begin{cases} u = U_{in}\cdot u_0(\bar{x},\bar{r}) + U_{in}\cdot\varepsilon\cdot u_1(\bar{x},\bar{r}) \\ v = \left(\dfrac{R_{in}U_{in}}{L}\right)\cdot v_0(\bar{x},\bar{r}) + \left(\dfrac{R_{in}U_{in}}{L}\right)\cdot\varepsilon\cdot v_1(\bar{x},\bar{r}) \end{cases}, \tag{53}$$

where R_{in} is the nozzle inlet radius, U_{in} is the maximum gas velocity at the nozzle inlet, $\mathrm{Re} = \rho U_{in} R_{in}/\mu$ is the flow Reynolds number in the nozzle inlet, $\varepsilon = R_{in}/L$, and

$$\bar{x} = x/L,\ \bar{r} = r/R_{in},\ \bar{R} = R(x)/R_{in}$$

$$\begin{cases} u_0(\bar{x},\bar{r}) = \dfrac{1}{\bar{R}^2(\bar{x})}\left[1-\dfrac{\bar{r}^2}{\bar{R}^2(\bar{x})}\right] \\ v_0(\bar{x},\bar{r}) = \dfrac{\bar{r}u_0(\bar{x},\bar{r})}{\bar{R}(\bar{x})}\dfrac{d\bar{R}}{d\bar{x}} \end{cases}, \text{ and} \tag{54}$$

$$\begin{cases} u_1(\bar{x},\bar{r}) = \dfrac{\mathrm{Re}}{18\bar{R}^3(\bar{x})}\left[1-\dfrac{9\bar{r}^2}{2\bar{R}^2(\bar{x})}+\dfrac{9\bar{r}^4}{2\bar{R}^4(\bar{x})}-\dfrac{\bar{r}^6}{\bar{R}^6(\bar{x})}\right]\dfrac{d\bar{R}}{d\bar{x}} \\ v_1(\bar{x},\bar{r}) = \dfrac{\mathrm{Re}}{18\bar{R}^3(\bar{x})}\left[\dfrac{3}{2}-\dfrac{45\bar{r}^2}{8\bar{R}^2(\bar{x})}+\dfrac{21\bar{r}^4}{4\bar{R}^4(\bar{x})}-\dfrac{9\bar{r}^6}{8\bar{R}^6(\bar{x})}\right]\dfrac{\bar{r}}{\bar{R}(\bar{x})}\left(\dfrac{d\bar{R}}{d\bar{x}}\right)^2 - \\ -\dfrac{\mathrm{Re}}{18\bar{R}^3(\bar{x})}\left[\dfrac{1}{2}-\dfrac{9\bar{r}^2}{8\bar{R}^2(\bar{x})}+\dfrac{3\bar{r}^4}{4\bar{R}^4(\bar{x})}-\dfrac{\bar{r}^6}{8\bar{R}^6(\bar{x})}\right]\bar{r}\dfrac{d^2\bar{R}}{d\bar{x}^2} \end{cases} \quad \textbf{(55)}$$

Detailed derivations of these semi-analytical equations (53)-(55) are presented in sub-section 3.1.3. Note that these expressions for the gas velocity components are valid only with the assumption that gas is incompressible, while ANSYS simulations can provide results for both cases: incompressible or compressible gas.

Figure 60 and Figure 61 are devoted to axial and radial components of velocity at one fourth of the nozzle length. Figure 62 and Figure 63 are devoted to axial and radial components of velocity at two fourths of the nozzle length. Figure 64 and Figure 65 are devoted to axial and radial components of velocity at three fourths of the nozzle length. Figure 66 and Figure 67 are devoted to axial and radial components of velocity at the outlet of the nozzle. In all Figure 60-Figure 67, red lines correspond to CFX results, blue lines correspond to semi-analytical approximation, green lines correspond to Poiseuille flow.

Based on the results plotted in Figure 60-Figure 67, one can conclude that the CFX axial velocity component is in between the Poiseuille profile and the semi-analytical solution everywhere inside of the nozzle. The Poiseuille profile of velocity cannot be reached in the CFX model because a convergent nozzle is considered rather than a constant diameter section. At the same time, the semi-analytical approach gives underestimated axial component of gas velocity.

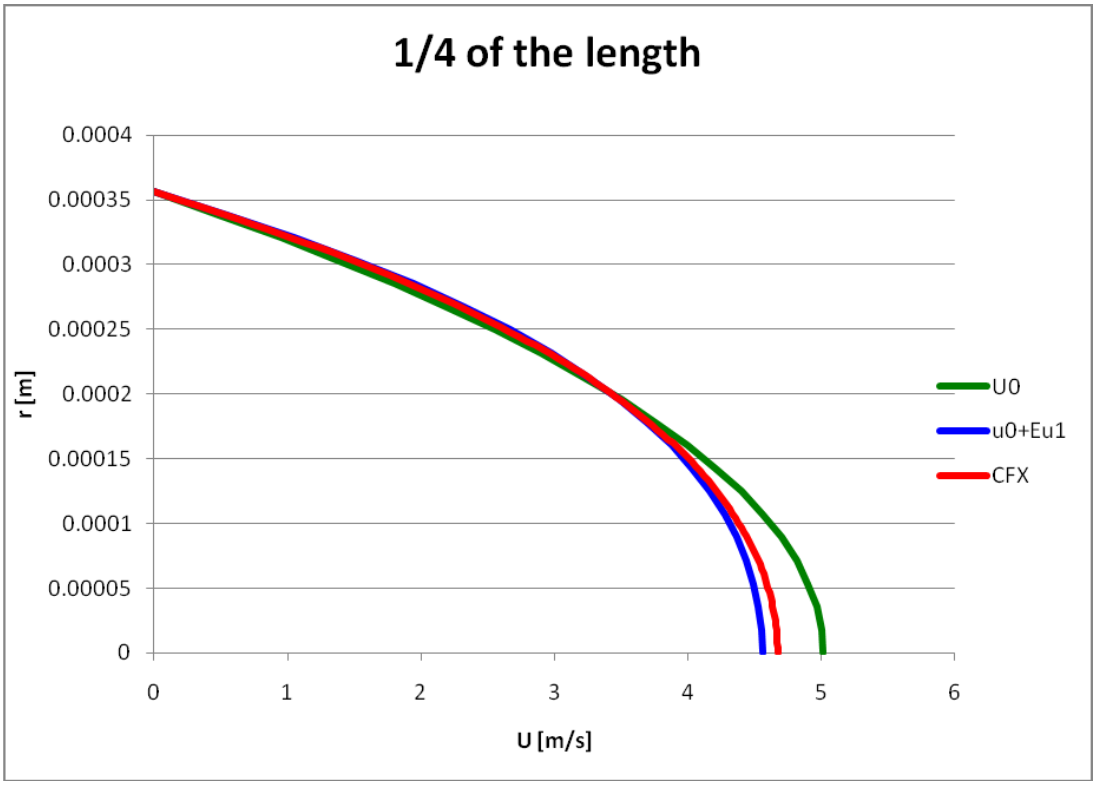

Figure 60. Comparison of axial component of velocity at 1/4 of the nozzle length.

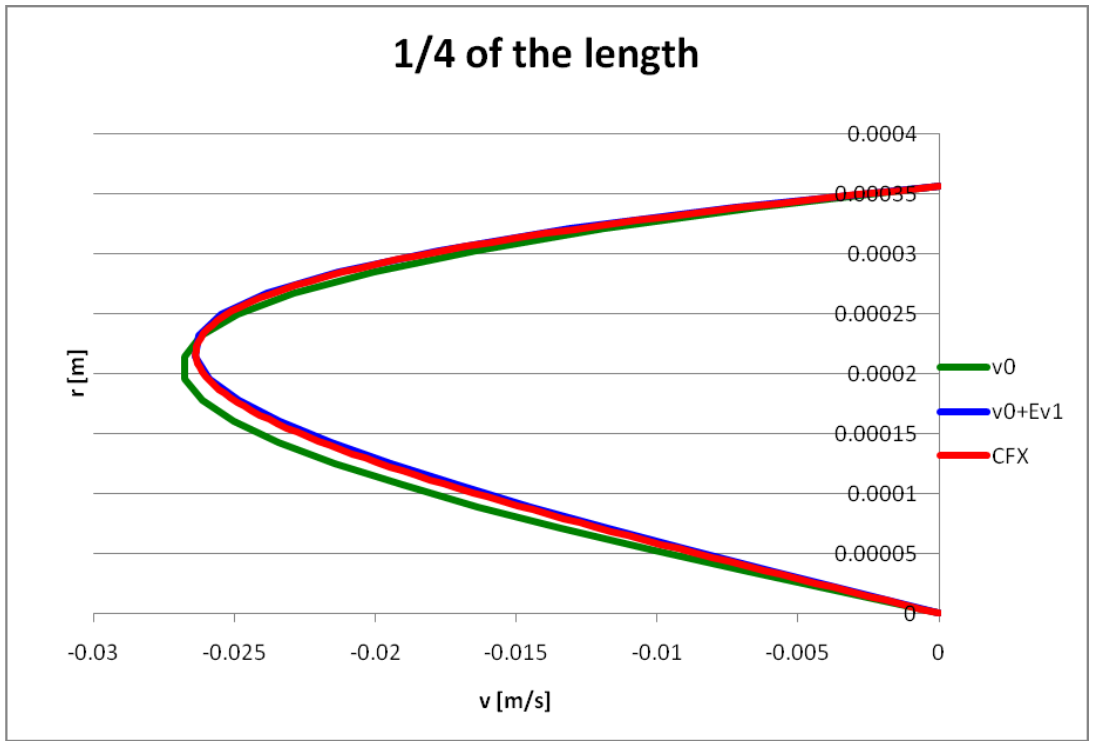

Figure 61. Comparison of radial component of velocity at 1/4 of the nozzle length.

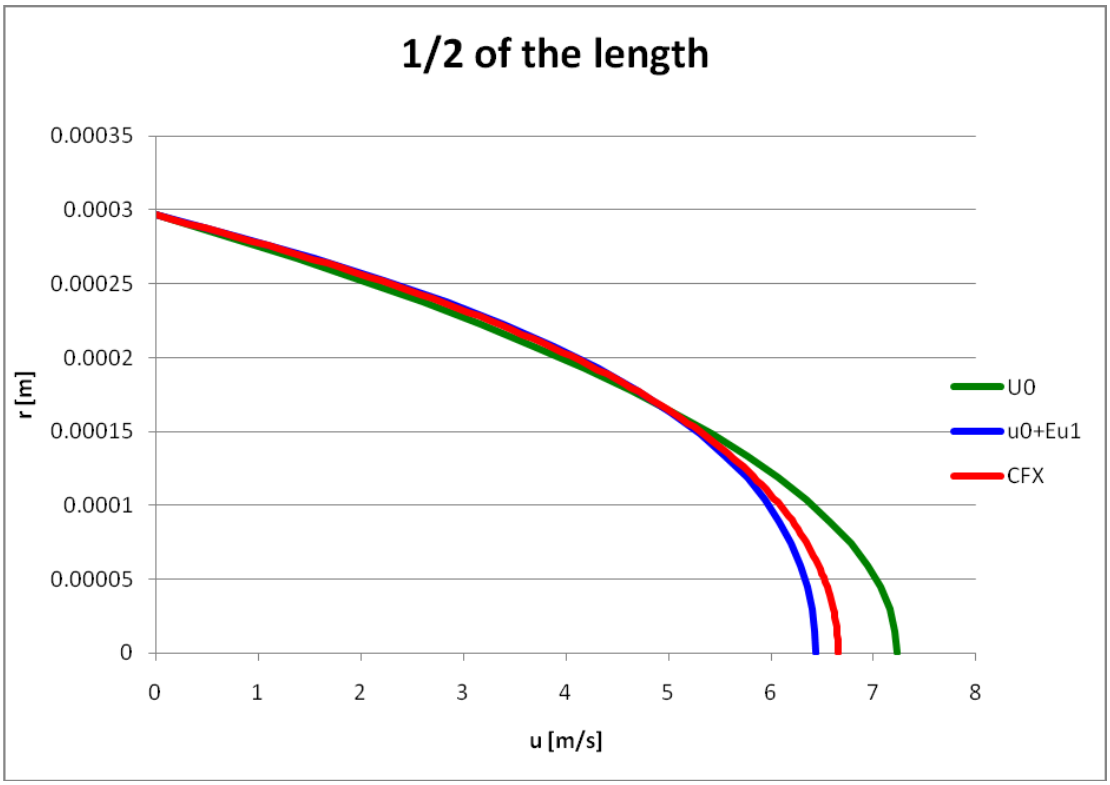

Figure 62. Comparison of axial component of velocity at 1/2 of the nozzle length.

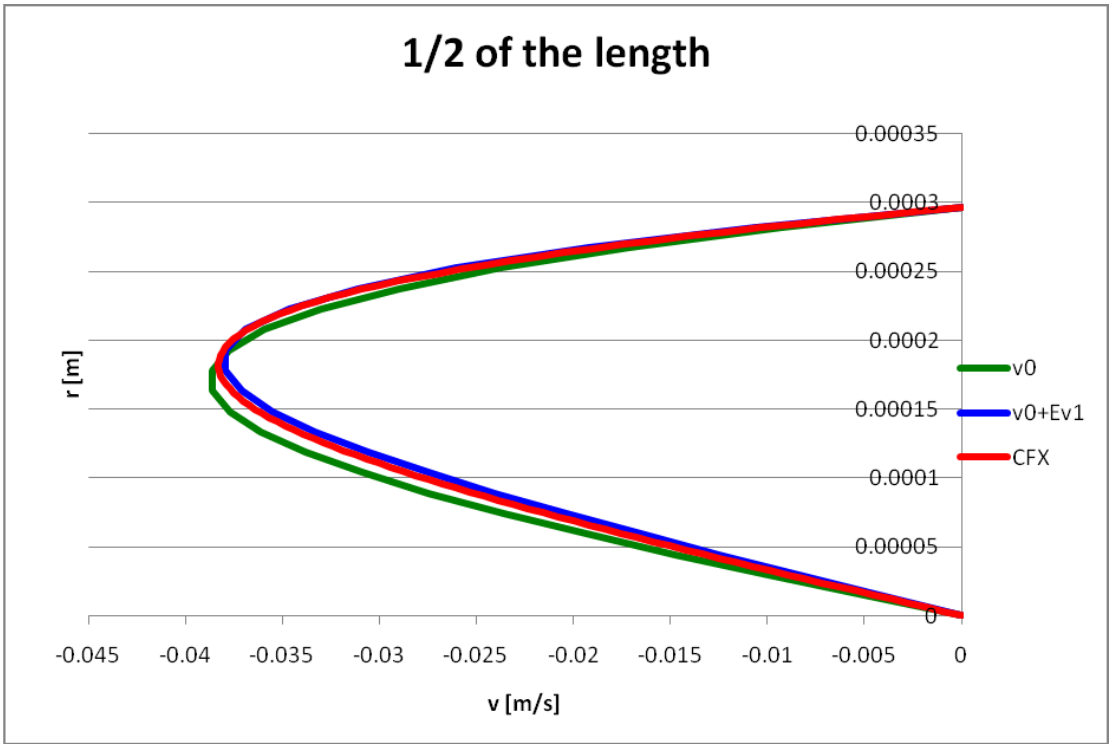

Figure 63. Comparison of radial component of velocity at 1/2 of the nozzle length.

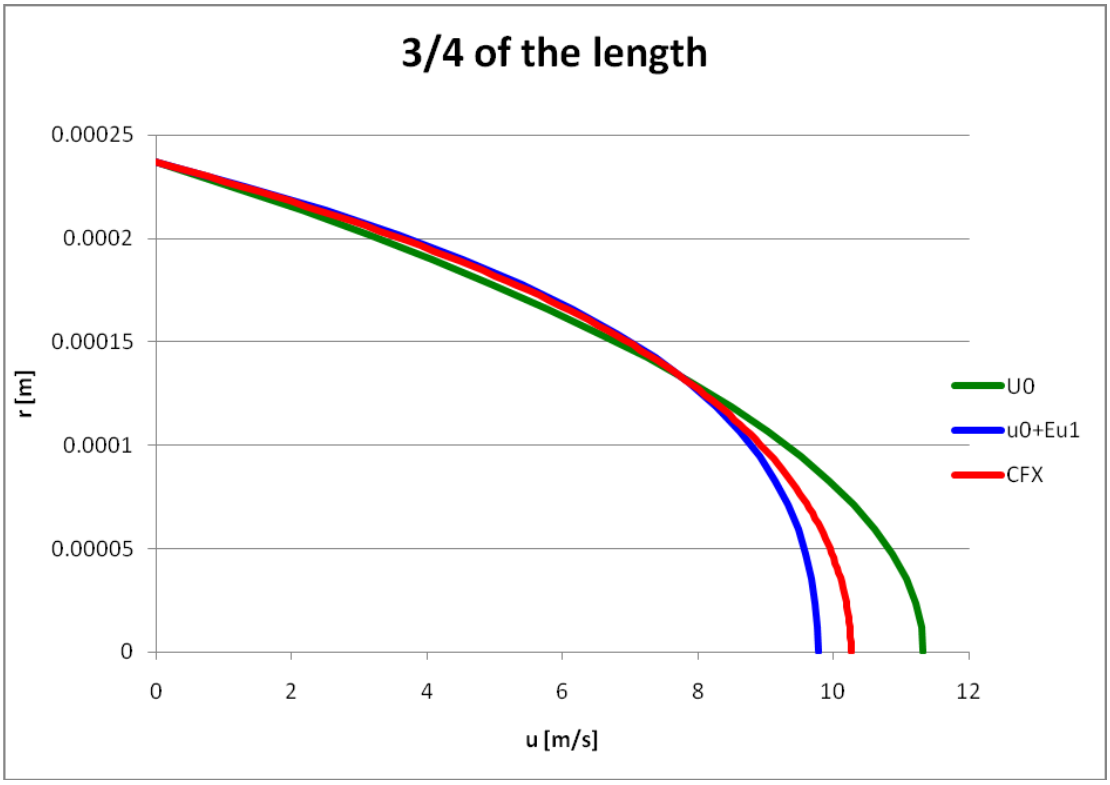

Figure 64. Comparison of axial component of velocity at 3/4 of the nozzle length.

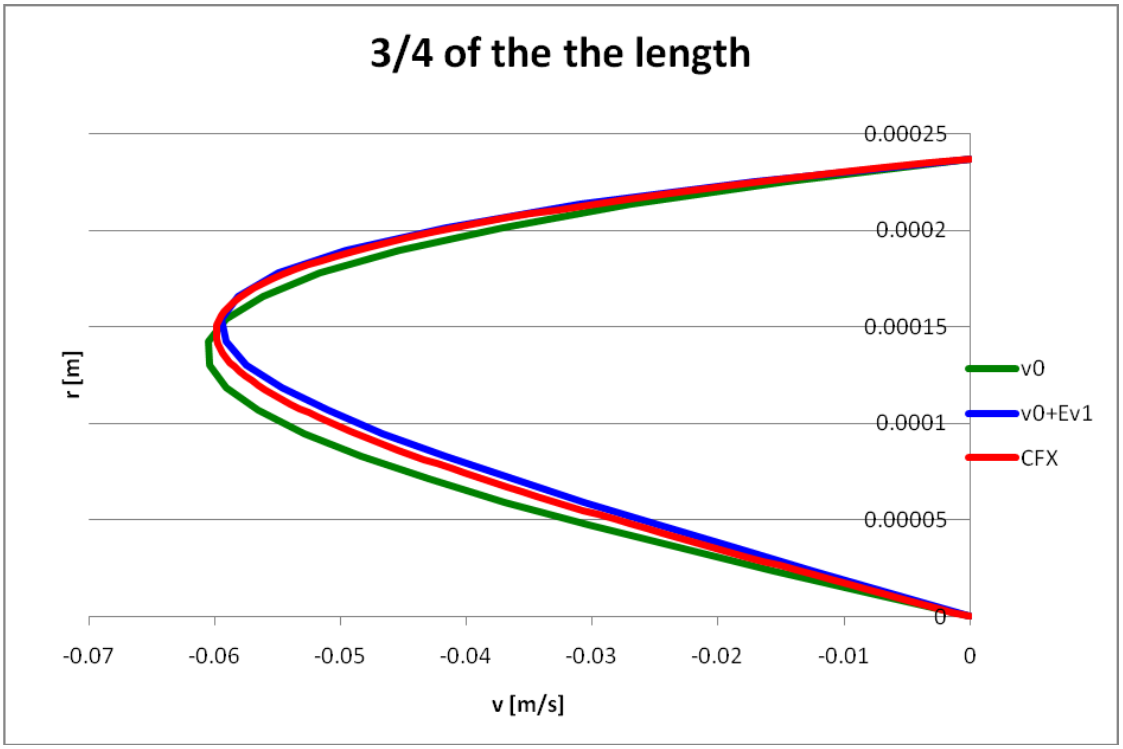

Figure 65. Comparison of radial component of velocity at 3/4 of the nozzle length.

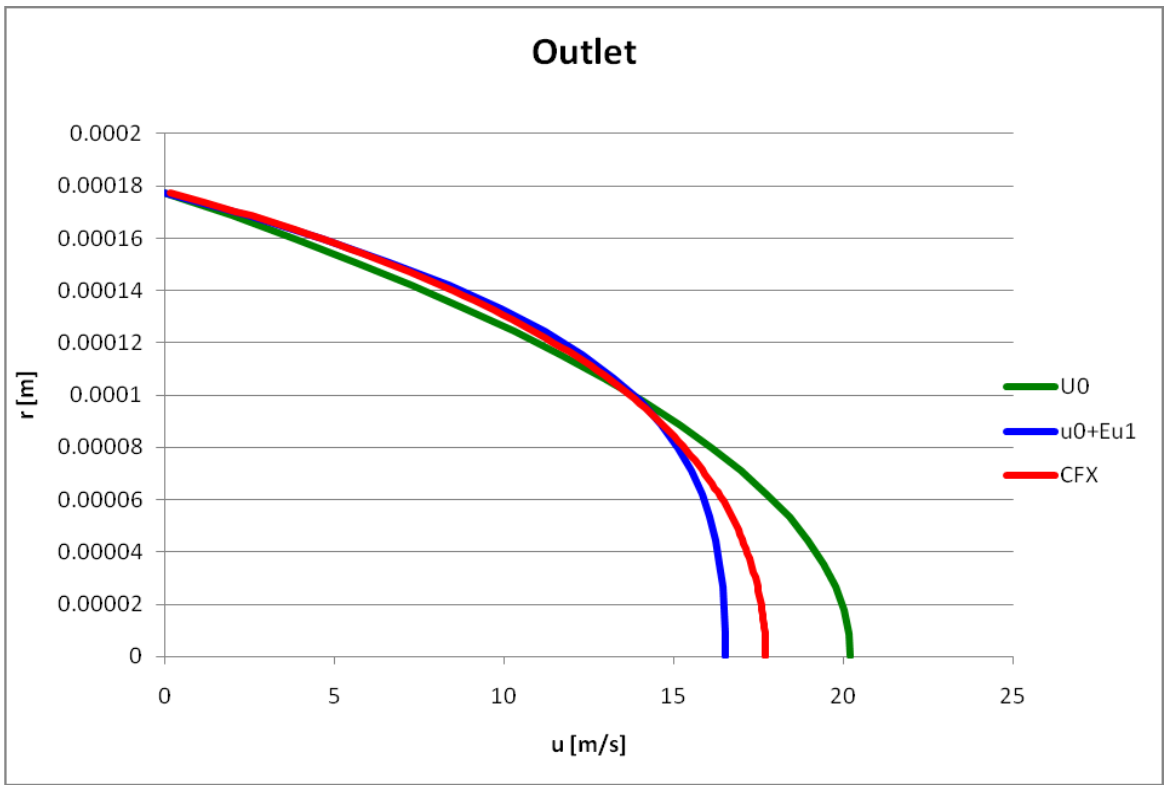

Figure 66. Comparison of axial component of velocity at outlet of the nozzle.

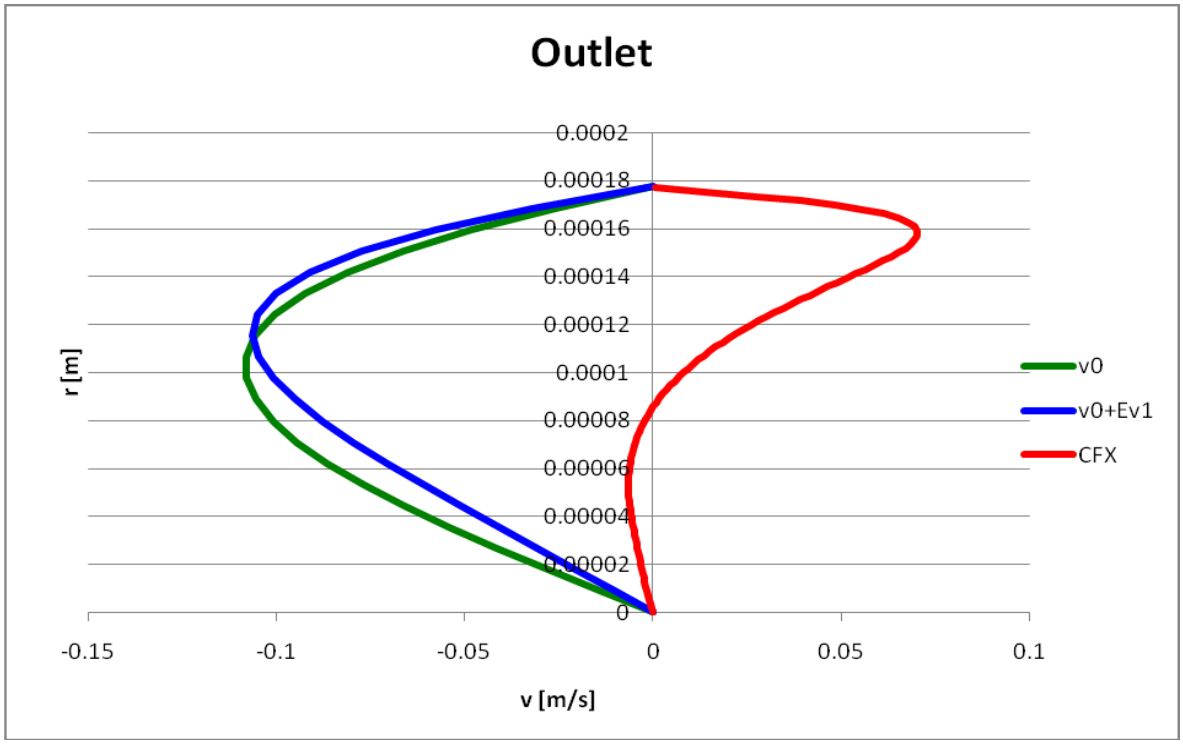

Figure 67. Comparison of radial component of velocity at outlet of the nozzle.

Regarding the radial component of velocity, it is observed that CFX results coincide with semi-analytical results better than with Poiseuille's profiles. Therefore, if one wants to minimize calculation time (or avoid ANSYS CFX modeling), semi-analytical equations can be used to replace CFX results as a first approximation to the gas flow field. However, this is true only for a simple geometry nozzle: linearly convergent nozzle. In the case of variable diameter nozzles, one has to rely on CFX modeling results.

Note that this comparison between the ANSYS gas flow field and semi-analytical model results is valid only for fixed geometry nozzle (linearly-convergent nozzle) and fixed flow rate of 60 ccm. If a higher flow rate or complex geometry nozzle is considered, then the semi-analytical approach may not be applicable. One of the reasons for these phenomena is that the smaller terms, $\varepsilon u_1(\bar{x},\bar{r})$ and $\varepsilon v_1(\bar{x},\bar{r})$, become comparable with the larger terms, $u_0(\bar{x},\bar{r})$ and $v_0(\bar{x},\bar{r})$, if the ratio $\frac{\varepsilon \,\mathrm{Re}}{18\bar{R}(\bar{x})}$ approaches one. This can happen if any of the following conditions is satisfied:

- Higher flow rate is employed, which leads to higher Reynolds number,
- Normalized nozzle radius, $\bar{R}(\bar{x})$, is close to zero, or
- Ratio of the inlet radius to the nozzle length, $\varepsilon = R_{in} / L$, is not a small number. This can be done by considering the nozzle with the length higher than the inlet radius.

It should be noted that, for the linearly-convergent nozzle, the normalized nozzle radius approaches zero while $\bar{x} \to 1$ if the nozzle outlet radius is much smaller than the nozzle inlet radius (in the semi-analytical model, the nozzle radius is normalized to the inlet radius, $\bar{R} = R(x)/R_{in}$). So, semi-analytical equations cannot be used in this case.

Figure 68 is devoted to the case when the same linearly-convergent nozzle is considered with the higher flow rate of 180 ccm employed. We can see that the semi-analytical approach fails by giving the low gas velocity at the nozzle centerline (gas velocity at the nozzle centerline is less than 11 m/s, while the gas velocity at distance of 125 microns from the centerline is higher than 11 m/s). This behavior of the gas velocity is not physical due to the non-slip boundary conditions set at the nozzle wall.

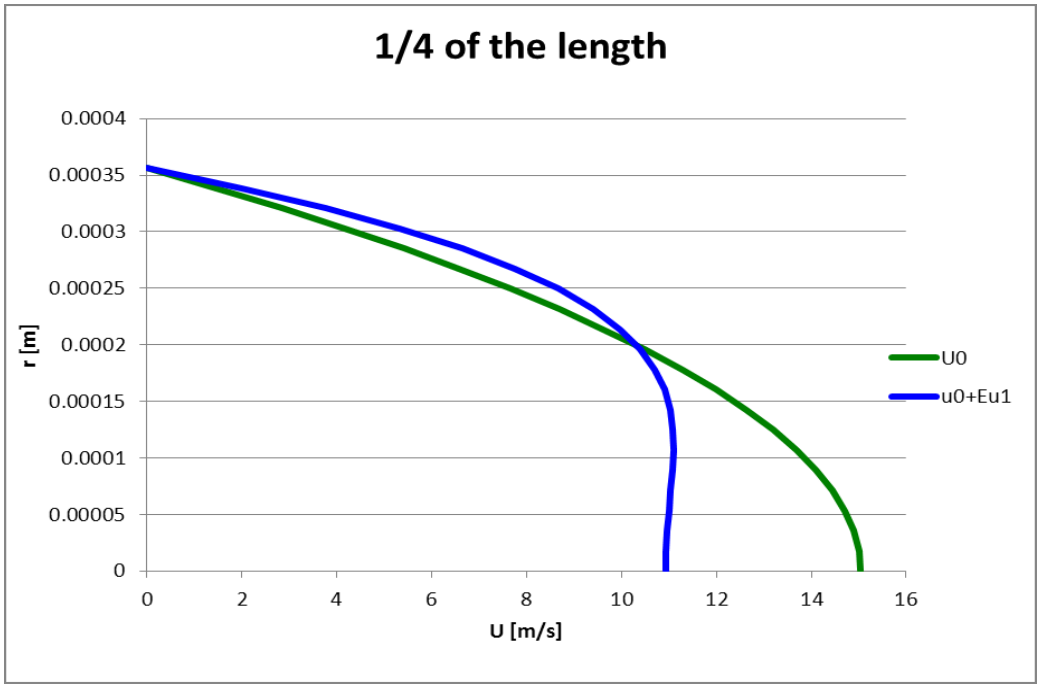

Figure 68. Comparison of axial component of velocity at 1/4 of the nozzle length for the flow rate of 180 ccm.

To check the gas flow data obtained from ANSYS CFX simulations, we can also compare the pressure required to push the gas through the nozzle. Table 12 shows the results obtained from the ANSYS modeling and from direct pressure measurements in real experiments. We can observe that the experimental results are slightly higher than the modeling results. This can be explained by the fact that measurements were taken not at the

nozzle inlet, but at some distance upstream. Therefore, extra pressure is required to move the gas from this upstream point to the deposition head and then to push the gas through the deposition head. Based on this data analysis, we see that the modeling results for the applied pressure are in good agreement with experimental ones.

Table 12. Comparison of results between the ANSYS CFX simulations and experimental measurements.

Volumetric Flow Rate	ANSYS CFX Results	Experimental Results
60 ccm	1880 Pa	2172 Pa ± 150 Pa
80 ccm	2900 Pa	3310 Pa ± 150 Pa
100 ccm	4060 Pa	4620 Pa ± 150 Pa
120 ccm	5420 Pa	5930 Pa ± 150 Pa
180 ccm	10500 Pa	10136 Pa ± 150 Pa

3.1.3. Semi-Analytical Equation for the Gas Flow

Based on Ref. [17], the dimensionless continuity and momentum equations for viscous and incompressible gas in steady motion look as follows:

$$\frac{\partial(\bar{r}\bar{u})}{\partial\bar{x}}+\frac{\partial(\bar{r}\bar{v})}{\partial\bar{r}}=0, \tag{56}$$

$$\varepsilon\,\mathrm{Re}\left(\bar{u}\frac{\partial\bar{u}}{\partial\bar{x}}+\bar{v}\frac{\partial\bar{u}}{\partial\bar{r}}\right)=-\frac{\partial\bar{p}}{\partial\bar{x}}+\varepsilon^{2}\frac{\partial^{2}\bar{u}}{\partial\bar{x}^{2}}+\frac{\partial^{2}\bar{u}}{\partial\bar{r}^{2}}+\frac{1}{\bar{r}}\frac{\partial\bar{u}}{\partial\bar{r}}, \tag{57}$$

$$\varepsilon^{3}\,\mathrm{Re}\left(\bar{u}\frac{\partial\bar{v}}{\partial\bar{x}}+\bar{v}\frac{\partial\bar{v}}{\partial\bar{r}}\right)=-\frac{\partial\bar{p}}{\partial\bar{r}}+\varepsilon^{4}\frac{\partial^{2}\bar{v}}{\partial\bar{x}^{2}}+\varepsilon^{2}\left(\frac{\partial^{2}\bar{v}}{\partial\bar{r}^{2}}+\frac{1}{\bar{r}}\frac{\partial\bar{v}}{\partial\bar{r}}-\frac{\bar{v}}{\bar{r}^{2}}\right), \tag{58}$$

Assuming that $\bar{u}=\bar{u}_0+\varepsilon\bar{u}_1$, $\bar{v}=\bar{v}_0+\varepsilon\bar{v}_1$, and $\bar{p}=\bar{p}_0+\varepsilon\bar{p}_1$ and neglecting the small terms of order higher than $\varepsilon\,\mathrm{Re}$ and ε, Equations (56)-(58) will be modified to:

$$\frac{\partial(\bar{r}\bar{u}_0)}{\partial\bar{x}} + \frac{\partial(\bar{r}\bar{v}_0)}{\partial\bar{r}} + \varepsilon\left[\frac{\partial(\bar{r}\bar{u}_1)}{\partial\bar{x}} + \frac{\partial(\bar{r}\bar{v}_1)}{\partial\bar{r}}\right] = 0, \tag{59}$$

$$\varepsilon \mathrm{Re}\left(\bar{u}_0 \frac{\partial\bar{u}_0}{\partial\bar{x}} + \bar{v}_0 \frac{\partial\bar{u}_0}{\partial\bar{r}}\right) = -\frac{\partial\bar{p}_0}{\partial\bar{x}} - \varepsilon\frac{\partial\bar{p}_1}{\partial\bar{x}} + \frac{1}{\bar{r}}\frac{\partial}{\partial\bar{r}}\left(\bar{r}\frac{\partial\bar{u}_0}{\partial\bar{r}}\right) + \varepsilon\frac{1}{\bar{r}}\frac{\partial}{\partial\bar{r}}\left(\bar{r}\frac{\partial\bar{u}_1}{\partial\bar{r}}\right), \tag{60}$$

$$\frac{\partial\bar{p}_0}{\partial\bar{r}} + \varepsilon\frac{\partial\bar{p}_1}{\partial\bar{r}} = 0, \tag{61}$$

Considering Eqs. (59)-(61), first, let us separate equations with zeroth order terms, ε^0:

$$\frac{\partial(\bar{r}\bar{u}_0)}{\partial\bar{x}} + \frac{\partial(\bar{r}\bar{v}_0)}{\partial\bar{r}} = 0, \tag{62}$$

$$\frac{\partial\bar{p}_0}{\partial\bar{x}} = \frac{1}{\bar{r}}\frac{\partial}{\partial\bar{r}}\left(\bar{r}\frac{\partial\bar{u}_0}{\partial\bar{r}}\right), \tag{63}$$

$$\frac{\partial\bar{p}_0}{\partial\bar{r}} = 0, \tag{64}$$

and then remaining equations with the first order terms, ε^1, look as follows:

$$\frac{\partial(\bar{r}\bar{u}_1)}{\partial\bar{x}} + \frac{\partial(\bar{r}\bar{v}_1)}{\partial\bar{r}} = 0, \tag{65}$$

$$\mathrm{Re}\left(\bar{u}_0 \frac{\partial\bar{u}_0}{\partial\bar{x}} + \bar{v}_0 \frac{\partial\bar{u}_0}{\partial\bar{r}}\right) = -\frac{\partial\bar{p}_1}{\partial\bar{x}} + \frac{1}{\bar{r}}\frac{\partial}{\partial\bar{r}}\left(\bar{r}\frac{\partial\bar{u}_1}{\partial\bar{r}}\right), \tag{66}$$

$$\frac{\partial\bar{p}_1}{\partial\bar{r}} = 0, \tag{67}$$

Eqs. (64) and (67) assume that zeroth and first order terms for pressure do not depend on r, and they are a function of x only. Therefore, based on Eq. (63), we can conclude that the zeroth order axial gas velocity has parabolic shape:

$$\bar{u}_0(\bar{x},\bar{r}) = u_0^{\max}(\bar{x})\left(1-\frac{\bar{r}^2}{\bar{R}^2(\bar{x})}\right), \tag{68}$$

Using Eqs. (63) and (68), the pressure derivative of zeroth order is calculated by:

$$\frac{d\bar{p}_0}{d\bar{x}} = \frac{-4u_0^{\max}(\bar{x})}{\bar{R}^2(\bar{x})}, \tag{69}$$

Volumetric flow can be found by integration:

$$Q = \int_0^{R(x)} 2\pi r u_0(x,r)dr = \pi R_{in}^2 \frac{U_{in}}{2} \times 4 \times \int_0^{\bar{R}(x)} \bar{r}\bar{u}_0(\bar{x},\bar{r})d\bar{r} = Q \times 4 \times \int_0^{\bar{R}(x)} \bar{r}\bar{u}_0(\bar{x},\bar{r})d\bar{r}, \tag{70}$$

Therefore

$$\int_0^{\bar{R}(x)} \bar{r}\bar{u}_0(\bar{x},\bar{r})d\bar{r} = 1/4 \text{ which leads to the fact that } u_0^{\max}(\bar{x}) = \frac{1}{\bar{R}^2(\bar{x})} \tag{71}$$

Using Eqs. (68), (69), and (71), we obtain that

$$\bar{u}_0(\bar{x},\bar{r}) = \frac{1}{\bar{R}^2(\bar{x})}\left(1-\frac{\bar{r}^2}{\bar{R}^2(\bar{x})}\right), \text{ and} \tag{72}$$

$$\frac{d\bar{p}_0}{d\bar{x}} = -\frac{4}{\bar{R}^4(\bar{x})} \tag{73}$$

From continuity equation, Eq. (62), we can conclude that

$$\frac{\partial(\bar{r}\bar{v}_0)}{\partial\bar{r}} = -\frac{\partial(\bar{r}\bar{u}_0)}{\partial\bar{x}} = \left[\frac{2\bar{r}}{\bar{R}^3(\bar{x})} - \frac{4\bar{r}^3}{\bar{R}^5(\bar{x})}\right]\frac{d\bar{R}}{d\bar{x}} \tag{74}$$

Integration of Eq. (74) will lead to the following equation:

$$\bar{v}_0(\bar{x},\bar{r}) = -\frac{1}{\bar{r}}\int_0^{\bar{r}} \frac{\partial}{\partial\bar{x}}(\bar{r}\bar{u}_0(\bar{x},\bar{r}))d\bar{r}\,, \tag{75}$$

Therefore, the following expression for radial velocity component of zeroth order can be obtained combining Eqs. (74) and (75):

$$\bar{v}_0(\bar{x},\bar{r}) = \frac{\bar{r}\bar{u}_0(\bar{x},\bar{r})}{\bar{R}(\bar{x})}\frac{d\bar{R}}{d\bar{x}}\,. \tag{76}$$

Considering Eq. (66) for the first order terms and using Eqs. (72) and (76), we see that:

$$\frac{1}{\bar{r}}\frac{\partial}{\partial \bar{r}}\left(\bar{r}\frac{\partial \bar{u}_1}{\partial \bar{r}}\right)=\frac{\partial \bar{p}_1}{\partial \bar{x}}+\mathrm{Re}\left(\bar{u}_0\frac{\partial \bar{u}_0}{\partial \bar{x}}+\bar{v}_0\frac{\partial \bar{u}_0}{\partial \bar{r}}\right)=$$
$$\frac{\partial \bar{p}_1}{\partial \bar{x}}+\mathrm{Re}\left[\frac{-2}{\bar{R}^5(\bar{x})}+\frac{4\bar{r}^2}{\bar{R}^7(\bar{x})}-\frac{2\bar{r}^4}{\bar{R}^9(\bar{x})}\right]\frac{d\bar{R}}{d\bar{x}}= \quad , \tag{77}$$
$$\frac{d\bar{p}_1}{d\bar{x}}+\mathrm{Re}\left[\frac{-2}{\bar{R}^5(\bar{x})}+\frac{4\bar{r}^2}{\bar{R}^7(\bar{x})}-\frac{2\bar{r}^4}{\bar{R}^9(\bar{x})}\right]\frac{d\bar{R}}{d\bar{x}}=f(\bar{x},\bar{r})$$

where

$$f(\bar{x},\bar{r})=\frac{d\bar{p}_1}{d\bar{x}}+\mathrm{Re}\left[\frac{-2}{\bar{R}^5(\bar{x})}+\frac{4\bar{r}^2}{\bar{R}^7(\bar{x})}-\frac{2\bar{r}^4}{\bar{R}^9(\bar{x})}\right]\frac{d\bar{R}}{d\bar{x}}. \tag{78}$$

Therefore

$$\frac{\partial}{\partial \bar{r}}\left(\bar{r}\frac{\partial \bar{u}_1}{\partial \bar{r}}\right)=\bar{r}f(\bar{x},\bar{r}),\ \bar{r}\frac{\partial \bar{u}_1}{\partial \bar{r}}=\int_0^{\bar{r}}\eta f(\bar{x},\eta)d\eta\text{, and}$$
$$\bar{u}_1(\bar{x},\bar{r})=\int_{\bar{R}(\bar{x})}^{\bar{r}}\frac{1}{\xi}\left[\int_0^{\xi}\eta f(\xi,\eta)d\eta\right]d\xi. \tag{79}$$

Substitution of Eq. (78) into Eq. (79) leads to the following expression for the axial velocity component of first order:

$$\bar{u}_1(\bar{x},\bar{r})=-\frac{1}{4}\left[\bar{R}^2(\bar{x})-\bar{r}^2\right]\frac{d\bar{p}_1}{d\bar{x}}+\mathrm{Re}\left[\frac{11}{36\bar{R}^3(\bar{x})}-\frac{\bar{r}^2}{2\bar{R}^5(\bar{x})}+\frac{\bar{r}^4}{4\bar{R}^7(\bar{x})}-\frac{\bar{r}^6}{18\bar{R}^9(\bar{x})}\right]\frac{d\bar{R}}{d\bar{x}} \tag{80}$$

By using Eq. (80) we obtain that

$$
\begin{aligned}
&0 \equiv \int_0^{\bar{R}(\bar{x})} \bar{r}\bar{u}_1(\bar{x},\bar{r})d\bar{r} = \\
&\int_0^{\bar{R}(\bar{x})} \left\{ \frac{1}{4}\left[r\bar{R}^2(\bar{x}) - \bar{r}^3 \right] \frac{d\bar{p}_1}{d\bar{x}} + \mathrm{Re}\left[\frac{11\bar{r}}{36\bar{R}^3(\bar{x})} - \frac{\bar{r}^3}{2\bar{R}^5(\bar{x})} + \frac{\bar{r}^5}{4\bar{R}^7(\bar{x})} - \frac{\bar{r}^7}{18\bar{R}^9(\bar{x})} \right] \frac{d\bar{R}}{d\bar{x}} \right\} d\bar{r} = \\
&\frac{1}{4}\left[\bar{R}^2(\bar{x}) - \bar{r}^2 \right] \frac{d\bar{p}_1}{d\bar{x}} + \mathrm{Re}\left[\frac{11}{36\bar{R}^3(\bar{x})} - \frac{\bar{r}^2}{2\bar{R}^5(\bar{x})} + \frac{2\bar{r}^4}{4\bar{R}^7(\bar{x})} - \frac{\bar{r}^6}{18\bar{R}^9(\bar{x})} \right] \frac{d\bar{R}}{d\bar{x}} = \\
&\frac{1}{16}\left[-\bar{R}^4(\bar{x}) \frac{d\bar{p}_1}{d\bar{x}} + \frac{\mathrm{Re}}{\bar{R}(\bar{x})} \frac{d\bar{R}}{d\bar{x}} \right]
\end{aligned}
, \qquad \textbf{(81)}
$$

which means that the pressure derivative of first order can be found by:

$$
\frac{d\bar{p}_1}{d\bar{x}} = \frac{\mathrm{Re}}{\bar{R}^5(\bar{x})} \frac{d\bar{R}}{d\bar{x}} . \qquad \textbf{(82)}
$$

Combining Eqs. (80) and (82), the formula for the first order axial velocity will be modified to:

$$
\bar{u}_1(\bar{x},\bar{r}) = \frac{\mathrm{Re}}{18\bar{R}^3(\bar{x})} \left[1 - \frac{9\bar{r}^2}{2\bar{R}^2(\bar{x})} + \frac{9\bar{r}^4}{2\bar{R}^4(\bar{x})} - \frac{\bar{r}^6}{\bar{R}^6(\bar{x})} \right] \frac{d\bar{R}}{d\bar{x}} \qquad \textbf{(83)}
$$

Based on the continuity equation, the first order radial velocity component is calculated as follows:

$$\bar{v}_1(\bar{x},\bar{r}) = -\frac{1}{\bar{r}}\int_0^{\bar{r}} \frac{\partial}{\partial \bar{x}}\left(\bar{r}\bar{u}_1(\bar{x},\bar{r})\right)d\bar{r}\ . \tag{84}$$

Using Eq. (83), we see that

$$\bar{r}\bar{u}_1(\bar{x},\bar{r}) = \frac{\mathrm{Re}}{18\bar{R}^3(\bar{x})}\left[r - \frac{9\bar{r}^3}{2\bar{R}^2(\bar{x})} + \frac{9\bar{r}^5}{2\bar{R}^4(\bar{x})} - \frac{\bar{r}^7}{\bar{R}^6(\bar{x})}\right]\frac{d\bar{R}}{d\bar{x}} \text{ and} \tag{85}$$

$$\frac{\partial}{\partial x}\left(\bar{r}\bar{u}_1(\bar{x},\bar{r})\right) = \frac{\mathrm{Re}}{18}\left[-\frac{3\bar{r}}{\bar{R}^4(\bar{x})} + \frac{45\bar{r}^3}{2\bar{R}^6(\bar{x})} - \frac{63\bar{r}^5}{2\bar{R}^8(\bar{x})} + \frac{9\bar{r}^7}{\bar{R}^{10}(\bar{x})}\right]\left(\frac{d\bar{R}}{d\bar{x}}\right)^2 + \frac{\mathrm{Re}}{18}\left[\frac{\bar{r}}{\bar{R}^3(\bar{x})} - \frac{9\bar{r}^3}{2\bar{R}^5(\bar{x})} + \frac{9\bar{r}^5}{2\bar{R}^7(\bar{x})} - \frac{\bar{r}^7}{\bar{R}^9(\bar{x})}\right]\frac{d^2\bar{R}}{d\bar{x}^2}\ . \tag{86}$$

Combining Eqs. (84) and (86), finally we get:

$$\bar{v}_1(\bar{x},\bar{r}) = \frac{\mathrm{Re}}{18}\left[\frac{3\bar{r}}{2\bar{R}^4(\bar{x})} - \frac{45\bar{r}^3}{8\bar{R}^6(\bar{x})} + \frac{63\bar{r}^5}{12\bar{R}^8(\bar{x})} - \frac{9\bar{r}^7}{8\bar{R}^{10}(\bar{x})}\right]\left(\frac{d\bar{R}}{d\bar{x}}\right)^2 + \frac{\mathrm{Re}}{18}\left[-\frac{\bar{r}}{\bar{R}^3(\bar{x})} + \frac{9\bar{r}^3}{8\bar{R}^5(\bar{x})} - \frac{9\bar{r}^5}{12\bar{R}^7(\bar{x})} + \frac{\bar{r}^7}{8\bar{R}^9(\bar{x})}\right]\frac{d^2\bar{R}}{d\bar{x}^2}\ . \tag{87}$$

3.1.4. Gas-Particle Interaction

If the gas flow field is known, all forces acting on an aerosol particle due to interaction with the gas flow can be computed and then the particles' trajectories can be found. Each particle's velocity and trajectory are calculated based on Newton's Second Law:

$$\frac{4}{3}\pi a^3 \rho_p \frac{d\mathbf{v}_p}{dt} = \sum \mathbf{F}, \tag{88}$$

where a is the particle radius, ρ_p is the particle density, $\mathbf{v}_p$ is the velocity vector of the particle, and $\sum \mathbf{F}$ is sum of all forces acting on the aerosol particle. In general, there are seven main forces due to the gas-particle interaction:

$$\sum \mathbf{F} = \mathbf{F}_{St} + \mathbf{F}_{Sa} + \mathbf{F}_{Gr} + \mathbf{F}_{Vm} + \mathbf{F}_{Ma} + \mathbf{F}_{Ba} + \mathbf{F}_{Ps}, \tag{89}$$

where $\mathbf{F}_{St}$ is the Stokes force or a steady viscous drag force, $\mathbf{F}_{Sa}$ is the Saffman force or a lift force acting on particle, $\mathbf{F}_{Gr}$ is the buoyancy force due to gravity, $\mathbf{F}_{Vm}$ is the virtual mass force or the force to accelerate the virtual mass of the fluid in the volume occupied by the particle, $\mathbf{F}_{Ma}$ is the Magnus force due to domain rotation, $\mathbf{F}_{Ba}$ is the Basset force or history term which accounts for the deviation in flow pattern from a steady state, and $\mathbf{F}_{Ps}$ is the pressure gradient force or the force applied on the particle due to the pressure gradient in the fluid surrounding the particle caused by fluid acceleration [75-83].

The Stokes force, $\mathbf{F}_{St}$, acting on a spherical particle due to the gas flow in the case of low particle Reynolds number flow, $\mathrm{Re}_p << 1$, can be calculated by the following equation:

$$\mathbf{F}_{St} = 6\pi a \mu \left(\mathbf{v} - \mathbf{v}_p\right), \tag{90}$$

where μ is the gas viscosity, $\mathbf{v}$ is the velocity vector of the carrier gas, and the particle Reynolds number is defined as follows:

$$\mathrm{Re}_p \equiv \frac{2a\rho_f \left|\mathbf{v} - \mathbf{v}_p\right|}{\mu}. \tag{91}$$

Considering a high Reynolds number flow motion, the Stokes force formula, Eq. (90), must be corrected:

$$\mathbf{F}_{St} = \frac{\pi}{2} C_D a^2 \rho_f \left|\mathbf{v} - \mathbf{v}_p\right| \left(\mathbf{v} - \mathbf{v}_p\right), \tag{92}$$

where C_D is a Stokes force correction factor which mostly depends on the particle Reynolds number and the particle shape. Detailed analysis of how this correction factor is dependent on the particle shape, different Reynolds number range, the particle rotation, the turbulence, etc. is given by Clift et al. [84]. In the current paper, the correction for the Stokes force is a function not only of the particle Reynolds number, but also of the Mach and Knudsen numbers:

$$G = \frac{\left(1 + \frac{1}{6}\mathrm{Re}_p^{2/3}\right)\left(1 + e^{-\frac{0.427}{M_p^{4.63}} - \frac{3}{\mathrm{Re}_p^{0.88}}}\right)}{1 + Kn_p\left(2.57 + 0.68e^{-\frac{1.86}{Kn_p}}\right)}, \tag{93}$$

where the Stokes force is finally calculated by:

$$\mathbf{F}_{St} = 6\pi G a \mu \left(\mathbf{v} - \mathbf{v}_p \right). \tag{94}$$

Mach and Knudsen numbers are defined as follows:

$$M_p = \frac{\left| \mathbf{v} - \mathbf{v}_p \right|}{C_g}, \tag{95}$$

$$Kn_p = \frac{\lambda}{2a}, \tag{96}$$

here C_g is the carrier gas sonic velocity (353 m/s for nitrogen at STP), and λ is the mean free path. According to the kinetic theory of gases, the mean free path is defined by the following expression [85]:

$$\lambda = \frac{1}{\sqrt{2} n_g \pi \sigma_m^2}, \tag{97}$$

where n_g is the number concentration of gas molecules per unit volume, $n_g = \frac{N_A \rho_f}{m_m}$,

$N_A = 6.02 \times 10^{23}$ atoms/mole is Avogadro number, m_m is molar mass, (for nitrogen

m_m =0.028 kg/mole [85]), and σ_m is the collision diameter of a molecule (for nitrogen σ_m =0.375 nm in the code [85], 0.368 nm [86]).

The buoyancy force, $\mathbf{F}_{Gr}$, is the force on a particle submerged in a fluid. This gravitational force is equal to:

$$\mathbf{F}_{Gr} = m(1-\chi)\mathbf{g}, \tag{98}$$

where m is the particle mass, $\chi = \rho_f / \rho_p$ is fluid-to-particle density ratio, and $\mathbf{g}$ is the gravitational acceleration vector. The ratio of the buoyancy force to the Stokes force can be expressed as follows:

$$\varepsilon_{Gr} = \frac{2}{9}\frac{a^2(\rho_p - \rho_f)}{\mu(\mathbf{v} - \mathbf{v}_p)}. \tag{99}$$

The aerosol particle sizes considered in the paper are small (0.5-5 microns), and their densities (~10^3 kg/m^3) are much higher than the carrier gas density (~1 kg/m^3). The aerosol particles move due the nitrogen flow with viscosity of 1.76×10^{-5} Pa·s and average relative speed of 50 m/s. Therefore, the gravity force can be neglected in further consideration, because the ratio of the buoyancy to the Stokes force is about $\varepsilon_{Gr} = 2.5\times10^{-7}$.

The pressure gradient force, $\mathbf{F}_{Ps}$, due to the acceleration of the external flow past the particle, is calculated by the following equation [77]:

$$\mathbf{F}_{Ps} = \chi m \frac{D\mathbf{v}}{Dt}, \text{ or } \mathbf{F}_{Ps} = -\frac{4}{3}\pi a^3 \frac{\partial p}{\partial x}\mathbf{e}_x \quad \textbf{(100)}$$

where D/Dt denotes the rate of change with time following a fluid particle, such that

$$\frac{D\mathbf{v}}{Dt} = \frac{d\mathbf{v}}{dt} - \left[\left(\mathbf{v}_p - \mathbf{v}\right)\cdot\nabla\right]\mathbf{v}, \quad \textbf{(101)}$$

and $\partial p/\partial x$ is the pressure gradient. The pressure gradient force is significant where the pressure gradient of the carrier gas is high, for an example, when a shock wave propagates through a gas-solid suspension. In this paper, laminar subsonic flow is considered, so this force is negligibly small and ignored.

The virtual or added mass force $\mathbf{F}_{Vm}$ is given by [77]:

$$\mathbf{F}_{Vm} = -c_M \chi m\left(\frac{d\mathbf{v}}{dt} - \frac{d\mathbf{v}_p}{dt}\right), \quad \textbf{(102)}$$

where the added mass coefficient for a sphere is equal to $c_M = 1/2$. Carlos F.M. Coimbra and Marcelo H. Kobayashi mentioned that the ratio of virtual force to the Stokes force is order of $O\left(\mathrm{Re}_p\right)$[87]. Detailed expression for the ratio of the virtual mass force to the Stokes force looks as follows:

$$\varepsilon_{Vm} = \frac{2}{9}\frac{c_M a^2 \rho_f \left| d\mathbf{v}/dt - d\mathbf{v}_p/dt \right|}{\mu \left| \mathbf{v} - \mathbf{v}_p \right|} \approx \frac{2}{9}\frac{c_M a^2 \rho_f}{\mu \tau_\mu} = \left| \tau_\mu = \frac{2a^2 \rho_p}{9\mu_f} \right| = \frac{c_M \rho_f}{\rho_p} = 5 \times 10^{-4}. \quad \textbf{(103)}$$

here $\tau_\mu = \frac{2a^2 \rho_p}{9\mu_f}$ is a characteristic time or viscous response time. Marshall also estimated the ratio of the pressure gradient and the virtual mass forces with respect to the Stokes force: $\mathbf{F}_{Ps}\,(or\,\mathbf{F}_{Vm})/\mathbf{F}_{St} \approx O(\chi)$ [77]. Therefore, these two forces: pressure gradient and the virtual mass force can be ignored in the modeling of the aerosol particles motion.

The Basset force is defined as follows [78-80]:

$$\mathbf{F}_{Ba} = 6a^2 \sqrt{\pi \mu \rho_f} \int_0^t \left(\frac{d\mathbf{v}/dt - d\mathbf{v}_p/dt}{\sqrt{t-\tau}} \right) d\tau, \quad \textbf{(104)}$$

Assuming a simple model with constant acceleration, Chao Zhu and Liang-Shih Fan in the CRC Handbook of Fluid Dynamics mentioned that the ratio of the Basset force to the Stokes force can be estimated as follows [83]:

$$\varepsilon_{Ba} = \frac{\left| \mathbf{F}_{Ba} \right|}{\left| \mathbf{F}_{St} \right|} = \sqrt{\frac{18}{\pi}\frac{\rho_f}{\rho_p}\frac{\tau_\mu}{t}} \quad \textbf{(105)}$$

where τ_μ is the Stokes relaxation time: $\tau_\mu = \frac{2a^2 \rho_p}{9\mu_f}$.

Another expression for the ratio of the Basset force to the drag force was given by Marshall where this ratio is presented in terms of the particle Reynolds number.

$$\varepsilon_{Ba} = \frac{|\mathbf{F}_{Ba}|}{|\mathbf{F}_{St}|} \cong \mathrm{Re}_p^{0.5} << 1 \tag{106}$$

where

$$\mathrm{Re}_p \equiv \frac{2a\rho_f |\mathbf{v} - \mathbf{v}_p|}{\mu} \tag{107}$$

Crowe in [80] mentioned that for gas-particle flows, the pressure force, the virtual mass force, and the Basset force can be neglected, when the ratio of continuous phase density to the particle density is very small (~10^{-3}). So we assumed that the Basset force does not play any role.

If the particle rotates differently than the surrounding fluid, an additional force called Magnus force is initiated, given by [77]:

$$\mathbf{F}_{Ma} = -\frac{3}{4}\chi m\left(\frac{1}{2}\boldsymbol{\omega} - \boldsymbol{\Omega}\right)\times\left(\mathbf{v}_p - \mathbf{v}\right), \tag{108}$$

where $\boldsymbol{\omega}$ is fluid vorticity at the particle location, $\boldsymbol{\omega} = \nabla \times \mathbf{v}$, and $\boldsymbol{\Omega}$ is angular rotation rate of particle. Based on the analysis given in [77], it can be noted that the ratio of the Magnus force to the Stokes force is equal to:

$$\varepsilon_{Ma} = \frac{\left|\mathbf{F}_{Ma}\right|}{\left|\mathbf{F}_{St}\right|} = O(\varepsilon S\, St), \tag{109}$$

where it was assumed that: $\left|\mathbf{v} - \mathbf{v}_p\right| / U = O(St)$. Here U is the mean velocity of the fluid flow through the capillary, $\varepsilon = a / L$ is the dimensionless particle radius, L is the fluid characteristic length scale, $S = \omega L^2 \rho / \mu$ is the dimensionless shear parameter, and $St = 2\rho_p a^2 U / 9\mu L$ is Stokes number.

Chao Zhu and Liang-Shih Fan showed that the ratio of the Magnus force to the Stokes force can be presented by

$$\varepsilon_{Ma} = \frac{\left|\mathbf{F}_{Ma}\right|}{\left|\mathbf{F}_{St}\right|} = \frac{a^2}{6}\frac{\rho_f}{\mu}\left|\frac{1}{2}\boldsymbol{\omega} - \boldsymbol{\Omega}\right|. \tag{110}$$

Therefore, assuming that the fluid flow is non-rotational and the aerosol particle rotates due to local shear of the carrier flow, $\left|\frac{1}{2}\boldsymbol{\omega} - \boldsymbol{\Omega}\right| \approx \left|\frac{\partial u}{\partial y}\right| \approx \frac{U}{R}$, this ratio of the Magnus force to the Stokes force can be further simplified to

$$\varepsilon_{Ma} = \frac{\left|\mathbf{F}_{Ma}\right|}{\left|\mathbf{F}_{St}\right|} \approx \frac{a^2}{6}\frac{\rho_f}{\mu}\frac{U}{R}. \tag{111}$$

where u is the gas axial velocity component, U is the mean velocity of the fluid flow through the capillary, and R is the radius of the capillary. Therefore, the ratio ε_{Ma} is about

10^{-3}, assuming aerosol particles of 1 μm diameter moving in nitrogen at standard conditions with mean velocity of 50 m/s through a capillary of 100 μm in radius.

It was shown by Saffman that if a solid spherical particle moves along the x-axis with the velocity vector $\mathbf{v}_p = (u_p, 0, 0)$ due to the gas motion with the velocity vector of $\mathbf{v} = (u, 0, 0)$, then the Saffman force is equal to [82]:

$$\mathbf{F}_{Sa} = 6.46a^2 (u - u_p) \sqrt{\rho\mu \left|\frac{\partial u}{\partial y}\right|} Sign\left(\frac{\partial u}{\partial y}\right) \mathbf{e}_y, \tag{112}$$

where ρ is the gas density, u is the axial component of gas velocity, u_p is the axial component of particle velocity, $\mathbf{e}_x$ and $\mathbf{e}_y$ are unit vectors along x and y axis, respectively. In the derivation of Eq. (112), Saffman assumed that the particle Reynolds number, Re_p, the shear Reynolds number, Re_f, and the rotational Reynolds number, Re_Ω, are much less than one:

$$\mathrm{Re}_p = \frac{2a\rho_f \left|\mathbf{v} - \mathbf{v}_p\right|}{\mu} << 1, \ \mathrm{Re}_f = \frac{(2a)^2 \rho_f}{\mu} \left|\frac{du}{dy}\right| << 1, \ \mathrm{Re}_\Omega = \frac{(2a)^2 \rho_f}{\mu} |\Omega| << 1, \tag{113}$$

and the particle Reynolds number is much less than the square root of the shear Reynolds number:

$$\mathrm{Re}_p << \mathrm{Re}_f^{1/2} \text{ , or } \varepsilon = \frac{\mathrm{Re}_f^{1/2}}{\mathrm{Re}_p} >> 1. \tag{114}$$

Later Dandy and Dwyer along with McLaughlin extended Saffman's analysis for broad ranges of the particle and the shear Reynolds numbers. Dandy and Dwyer [88] considered the case when the particle Reynolds number is in range of $0.1 \le \mathrm{Re}_p \le 100$ and dimensionless shear rate is in range of $\alpha = \frac{a}{|\mathbf{v} - \mathbf{v}_p|}\left|\frac{du}{dy}\right| \in [0.005, 0.4]$, while McLaughlin in [89] investigated the scenario when the particle Reynolds number is not small compared to square root of the shear Reynolds number, $\mathrm{Re}_f^{1/2}$, even though both Reynolds number are much smaller than one: $\mathrm{Re}_p << 1$, $\mathrm{Re}_f << 1, \varepsilon = \mathrm{Re}_f^{1/2} / \mathrm{Re}_p$ is arbitrary. Mei in his paper first summarized Dandy and Dwyer's results giving the following correction for the Saffman lift force [90]:

$$C_{Sa} = \begin{cases} 0.2343\left[1 - e^{-0.1\mathrm{Re}_p}\right]\sqrt{\frac{\mathrm{Re}_f}{\mathrm{Re}_p}} + e^{-0.1\mathrm{Re}_p}, & 0.1 \le \mathrm{Re}_p \le 40 \\ 0.0371\sqrt{\mathrm{Re}_f}, & 40 < \mathrm{Re}_p \le 100 \end{cases} \text{, so that} \tag{115}$$

the corrected Saffman lift force looks as follows:

$$\mathbf{F}_{Sa} = 6.46a^2\left(u - u_p\right)\sqrt{\rho\mu\left|\frac{\partial u}{\partial y}\right|}\,Sign\left(\frac{\partial u}{\partial y}\right)C_{Sa}\mathbf{e}_y. \tag{116}$$

Additionally, analyzing McLaughlin's tabular data for the Saffman force correction, Mei constructed the following correction function which depends only on ε to fit the tabular data:

$$C_{Sa} = 0.3\{1+\tanh[2.5\log_{10}\varepsilon + 0.191]\}\{0.667+\tanh[6(\varepsilon-0.32)]\}, \quad \mathrm{Re}_p << 1,\ \mathrm{Re}_f << 1, \forall\varepsilon \qquad \textbf{(117)}$$

Saffman force correction given in Eq. (117) should be employed only in the case when both the particle and shear Reynolds numbers are much less than one without paying attention to the restriction giving in Eq. (114).

Detailed estimation of the ratio between the Saffman force and the Stokes force was given in [17] by Akhatov et al.:

$$\varepsilon_{Sa} = \frac{|\mathbf{F}_{Sa}|}{|\mathbf{F}_{St}|} \approx 0.3\frac{a}{R}\sqrt{\mathrm{Re}_c}\ ,\ \mathrm{Re}_c = \frac{2RU\rho_f}{\mu} \qquad \textbf{(118)}$$

where R is the radius of the capillary, and U is the mean velocity of the fluid flow through the capillary. Based on their analysis, it was found that $\varepsilon_{Sa} = \frac{|F_{Sa}|}{|F_{St}|} \approx 0.05$. An analogous result for the ratio of the Saffman force to the Stokes drag force is presented by Chao Zhu and Liang-Shih Fan in the Handbook of Fluid Dynamics:

$$\varepsilon_{Sa} = \frac{|\mathbf{F}_{Sa}|}{|\mathbf{F}_{St}|} = \frac{6.46\, a}{6\pi} \sqrt{\frac{\rho_f}{\mu} \left| \frac{\partial (u - u_p)}{\partial u} \right|}, \tag{119}$$

where the simplified form of the Saffman to the Stokes force ratio can be presented by the equation below assuming simple shear flow:

$$\varepsilon_{Sa} = \frac{|\mathbf{F}_{Sa}|}{|\mathbf{F}_{St}|} = \frac{6.46}{12\pi} \sqrt{\mathrm{Re}_p} \,. \tag{120}$$

Using Eq. (108) and (122), the ratio of the Magnus force to the Saffman force is equal to:

$$\frac{\varepsilon_{Ma}}{\varepsilon_{Sa}} = \frac{|\mathbf{F}_{Ma}|}{|\mathbf{F}_{Sa}|} = \frac{\pi a}{6.46} \sqrt{\frac{\rho_f}{\mu} |\nabla \times \mathbf{v}|} \approx \frac{\pi}{6.46} \sqrt{\frac{a \rho_f |\mathbf{v} - \mathbf{v}_p|}{\mu}} = \frac{\pi}{6.46} \sqrt{\mathrm{Re}_p} << 1 . \tag{121}$$

Eq. (121) shows that the Magnus force is much less than the Saffman force which in turn is smaller than the Stokes force, so this is another proof of the fact that the Magnus force can be omitted in further consideration.

3.1.5. Generalization of Saffman Force in 2D Flow

As one can see, the Saffman lift force, Eq. (112), is derived only for the case, when the gas and particle have zero velocity components (1D case). The one dimensional expression for the Saffman force is generalized by Crowe et al. for the case of three dimensional flow [80]:

$$\mathbf{F}_{Sa} = 6.46a^2 \sqrt{\frac{\mu\rho_f}{|\nabla \times \mathbf{v}|}} \left[\left(\mathbf{v} - \mathbf{v}_p \right) \times \left(\nabla \times \mathbf{v} \right) \right]. \quad \textbf{(122)}$$

The same equation to express the Saffman force in 3D is given in the manual of the ANSYS CFX software, but there is no reference showing how this generalized expression is obtained. That is why in this sub-section, the generalized equation for Saffman force in 2D flow will be derived.

In general, the particle does not have zero components in the velocity vector, so let us define a local coordinate system (ξ, η), which moves along with particle and at the same time the direction of ξ coincides with direction of the vector $\tilde{\mathbf{v}} = \mathbf{v} - \mathbf{v}_p$, where $\mathbf{v}_p$ is the particle velocity vector and $\mathbf{v}$ is gas velocity vector at the particle coordinate (see Figure 69). Here we assume that x component of vector $\tilde{\mathbf{v}} = \mathbf{v} - \mathbf{v}_p$ is positive, e.g. $u - u_p > 0$. Angle α is the angle between vector $\tilde{\mathbf{v}} = \mathbf{v} - \mathbf{v}_p$ and x-axis. This angle is positive, if the direction from x-axis to vector $\tilde{\mathbf{v}} = \mathbf{v} - \mathbf{v}_p$ is counterclockwise, and it is negative, if the direction from the x-axis to vector $\tilde{\mathbf{v}} = \mathbf{v} - \mathbf{v}_p$ is clockwise. This depends on the sign of the difference $v - v_p$.

The coordinate system, (ξ, η), which moves along with particle, can be described in the global coordinate system by the following expressions:

$$\begin{cases} \xi = \left(x - x_p \right) \cos\alpha + \left(y - y_p \right) \sin\alpha \\ \eta = -\left(x - x_p \right) \sin\alpha + \left(y - y_p \right) \cos\alpha \end{cases}, \quad \textbf{(123)}$$

where (x_p, y_p) are x and y coordinates of the particle in the global coordinate system, (x, y) are the x- and y-coordinates of any point in the vicinity of point (x_p, y_p) in the global coordinate system, $\alpha = \arctan\left(\frac{v - v_p}{u - u_p}\right)$.

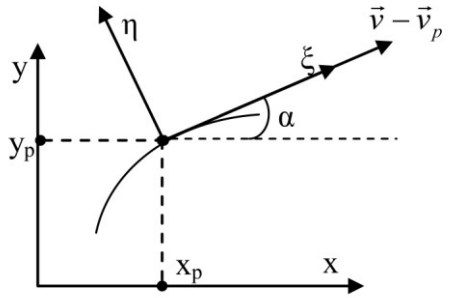

Figure 69. Transformation of global coordinate system to local coordinate system, which is moving along with particle.

Let us define the differences in x and y by tildes

$$\begin{cases} \tilde{x} = x - x_p \\ \tilde{y} = y - y_p \end{cases}. \tag{124}$$

Therefore:

$$\begin{cases} \xi = \tilde{x}\cos\alpha + \tilde{y}\sin\alpha \\ \eta = -\tilde{x}\sin\alpha + \tilde{y}\cos\alpha \end{cases}. \tag{125}$$

Inversely, the difference in global coordinates can be expressed by local coordinates:

$$\begin{cases} \widetilde{x} = \xi \cos\alpha - \eta \sin\alpha \\ \widetilde{y} = \xi \sin\alpha + \eta \cos\alpha \end{cases}. \tag{126}$$

Therefore

$$\begin{cases} \mathbf{e}_x = \mathbf{e}_\xi \cos\alpha - \mathbf{e}_\eta \sin\alpha \\ \mathbf{e}_y = \mathbf{e}_\xi \sin\alpha + \mathbf{e}_\eta \cos\alpha \end{cases} \text{and} \begin{cases} \mathbf{e}_\xi = \mathbf{e}_x \cos\alpha + \mathbf{e}_y \sin\alpha \\ \mathbf{e}_\eta = -\mathbf{e}_x \sin\alpha + \mathbf{e}_y \cos\alpha \end{cases}, \tag{127}$$

where $\mathbf{e}_\xi$ and $\mathbf{e}_\eta$ are unit vectors along ξ and η axis.

The gas velocity field at any point has two components:

$$\mathbf{v}(x, y) = u(x, y)\mathbf{e}_x + v(x, y)\mathbf{e}_y \tag{128}$$

If we assume that we are moving along with aerosol particle, then the gas velocity vector in vicinity of point (x_p, y_p) is equal to:

$$\widetilde{\mathbf{v}} = \mathbf{v} - \mathbf{v}_p . \tag{129}$$

Therefore, let us express this gas velocity vector, $\widetilde{\mathbf{v}} = \mathbf{v} - \mathbf{v}_p$, by using Taylor's series approximation:

$$\tilde{\mathbf{v}}(x,y)=\left[u(x,y)-u_p(x,y)\right]\mathbf{e}_x+\left[v(x,y)-v_p(x,y)\right]\mathbf{e}_y=\tilde{u}(x,y)\mathbf{e}_x+\tilde{v}(x,y)\mathbf{e}_x\cong$$
$$\cong\tilde{\mathbf{v}}(\tilde{x},\tilde{y})=\left[\tilde{u}(0,0)+\left.\frac{\partial u}{\partial x}\right|_p\tilde{x}+\left.\frac{\partial u}{\partial y}\right|_p\tilde{y}\right]\mathbf{e}_x+\left[\tilde{v}(0,0)+\left.\frac{\partial v}{\partial x}\right|_p\tilde{x}+\left.\frac{\partial v}{\partial y}\right|_p\tilde{y}\right]\mathbf{e}_y \quad . \qquad \textbf{(130)}$$

Applying Eqs. (126) and (127), the approximation for the velocity field (130) will be rewritten by:

$$\tilde{\mathbf{v}}(x,y)\cong\tilde{\mathbf{v}}(\tilde{x},\tilde{y})=\tilde{\mathbf{v}}(\xi,\eta)=$$
$$\left[\begin{array}{l}\tilde{u}(0,0)\cos\alpha+\left.\frac{\partial u}{\partial x}\right|_p\left(\xi\cos^2\alpha-\eta\cos\alpha\sin\alpha\right)+\left.\frac{\partial u}{\partial y}\right|_p\left(\xi\sin\alpha\cos\alpha+\eta\cos^2\alpha\right)+\\ \tilde{v}(0,0)\sin\alpha+\left.\frac{\partial v}{\partial x}\right|_p\left(\xi\sin\alpha\cos\alpha-\eta\sin^2\alpha\right)+\left.\frac{\partial v}{\partial y}\right|_p\left(\xi\sin^2\alpha+\eta\cos\alpha\sin\alpha\right)\end{array}\right]\mathbf{e}_\xi+$$
$$\left[\begin{array}{l}-\tilde{u}(0,0)\sin\alpha+\left.\frac{\partial u}{\partial x}\right|_p\left(-\xi\sin\alpha\cos\alpha+\eta\sin^2\alpha\right)+\left.\frac{\partial u}{\partial y}\right|_p\left(-\xi\sin^2\alpha-\eta\sin\alpha\cos\alpha\right)+\\ \tilde{v}(0,0)\cos\alpha+\left.\frac{\partial v}{\partial x}\right|_p\left(\xi\cos^2\alpha-\eta\sin\alpha\cos\alpha\right)+\left.\frac{\partial v}{\partial y}\right|_p\left(\xi\sin\alpha\cos\alpha+\eta\cos^2\alpha\right)\end{array}\right]\mathbf{e}_\eta \qquad \textbf{(131)}$$

Since $\alpha=\arctan\left(\dfrac{v-v_p}{u-u_p}\right)$, we have:

$$\tan\alpha=\frac{v-v_p}{u-u_p}=\frac{\tilde{v}(0,0)}{\tilde{u}(0,0)}=\frac{\sin\alpha}{\cos\alpha}\,. \qquad \textbf{(132)}$$

Therefore:

$$\widetilde{u}(0,0)\sin\alpha = \widetilde{v}(0,0)\cos\alpha\,. \tag{133}$$

At the same time:

$$\begin{aligned}
&\widetilde{u}(0,0)\cos\alpha + \widetilde{v}(0,0)\sin\alpha = \frac{\widetilde{u}(0,0)}{\sqrt{1+\tan^2\alpha}} + \frac{\widetilde{v}(0,0)\tan\alpha}{\sqrt{1+\tan^2\alpha}} = \\
&= \frac{\widetilde{v}(0,0)}{\sqrt{1+\tan^2\alpha}}\left(\frac{1}{\tan\alpha} + \tan\alpha\right) = \frac{\widetilde{v}(0,0)}{\sqrt{1+\tan^2\alpha}}\left(\frac{1+\tan^2\alpha}{\tan\alpha}\right) = \\
&= \frac{\widetilde{v}(0,0)}{\tan\alpha}\sqrt{1+\tan^2\alpha} = \widetilde{u}(0,0)\sqrt{1+\frac{\widetilde{v}^2(0,0)}{\widetilde{u}^2(0,0)}} = \sqrt{\widetilde{u}^2(0,0)+\widetilde{v}^2(0,0)}
\end{aligned} \tag{134}$$

Using Eqs. (133) and (134), Eq. (131) will be simplified to:

$$\begin{aligned}
&\widetilde{\mathbf{v}}(x,y) \cong \widetilde{\mathbf{v}}(\widetilde{x},\widetilde{y}) = \widetilde{\mathbf{v}}(\xi,\eta) = \\
&= \left[\begin{array}{l}
\sqrt{\widetilde{u}^2(0,0)+\widetilde{v}^2(0,0)} + \\
+\xi\left(\left.\frac{\partial u}{\partial x}\right|_p \cos^2\alpha + \left.\frac{\partial u}{\partial y}\right|_p \sin\alpha\cos\alpha + \left.\frac{\partial v}{\partial x}\right|_p \sin\alpha\cos\alpha + \left.\frac{\partial v}{\partial y}\right|_p \sin^2\alpha\right) + \\
+\eta\left(-\left.\frac{\partial u}{\partial x}\right|_p \sin\alpha\cos\alpha + \left.\frac{\partial u}{\partial y}\right|_p \cos^2\alpha - \left.\frac{\partial v}{\partial x}\right|_p \sin^2\alpha + \left.\frac{\partial v}{\partial y}\right|_p \sin\alpha\cos\alpha\right)
\end{array}\right]\mathbf{e}_\xi + \\
&+ \left[\begin{array}{l}
\xi\left(-\left.\frac{\partial u}{\partial x}\right|_p \sin\alpha\cos\alpha - \left.\frac{\partial u}{\partial y}\right|_p \sin^2\alpha + \left.\frac{\partial v}{\partial x}\right|_p \cos^2\alpha + \left.\frac{\partial v}{\partial y}\right|_p \sin\alpha\cos\alpha\right) + \\
+\eta\left(\left.\frac{\partial u}{\partial x}\right|_p \sin^2\alpha - \left.\frac{\partial u}{\partial y}\right|_p \sin\alpha\cos\alpha - \left.\frac{\partial v}{\partial x}\right|_p \sin\alpha\cos\alpha + \left.\frac{\partial v}{\partial y}\right|_p \cos^2\alpha\right)
\end{array}\right]\mathbf{e}_\eta\,.
\end{aligned} \tag{135}$$

Therefore, denoting U as

$$
\begin{aligned}
U(\xi,\eta) &= \sqrt{\tilde{u}^2(0,0)+\tilde{v}^2(0,0)}+ \\
&+\xi\left(\left.\frac{\partial u}{\partial x}\right|_p \cos^2\alpha+\left.\frac{\partial u}{\partial y}\right|_p \sin\alpha\cos\alpha+\left.\frac{\partial v}{\partial x}\right|_p \sin\alpha\cos\alpha+\left.\frac{\partial v}{\partial y}\right|_p \sin^2\alpha\right)+, \\
&+\eta\left(-\left.\frac{\partial u}{\partial x}\right|_p \sin\alpha\cos\alpha+\left.\frac{\partial u}{\partial y}\right|_p \cos^2\alpha-\left.\frac{\partial v}{\partial x}\right|_p \sin^2\alpha+\left.\frac{\partial v}{\partial y}\right|_p \sin\alpha\cos\alpha\right)
\end{aligned}
\tag{136}
$$

and V as

$$
\begin{aligned}
V(\xi,\eta) &= \xi\left(-\left.\frac{\partial u}{\partial x}\right|_p \sin\alpha\cos\alpha-\left.\frac{\partial u}{\partial y}\right|_p \sin^2\alpha+\left.\frac{\partial v}{\partial x}\right|_p \cos^2\alpha+\left.\frac{\partial v}{\partial y}\right|_p \sin\alpha\cos\alpha\right)+ \\
&+\eta\left(\left.\frac{\partial u}{\partial x}\right|_p \sin^2\alpha-\left.\frac{\partial u}{\partial y}\right|_p \sin\alpha\cos\alpha-\left.\frac{\partial v}{\partial x}\right|_p \sin\alpha\cos\alpha+\left.\frac{\partial v}{\partial y}\right|_p \cos^2\alpha\right)
\end{aligned}
, \tag{137}
$$

we get that:

$$
\tilde{\mathbf{v}}(x,y) \cong \tilde{\mathbf{v}}(\tilde{x},\tilde{y}) = \tilde{\mathbf{v}}(\xi,\eta) = U(\xi,\eta)\mathbf{e}_\xi + V(\xi,\eta)\mathbf{e}_\eta, \tag{138}
$$

In the local coordinate system, all velocity components for the particle are equal to zero, and the gas field is described by Eq. (135).

Based on Eq. (135), we see that if ξ and η go to zero (we are coming close to the particle), then

$$
\tilde{\mathbf{v}}(x,y) \cong \tilde{\mathbf{v}}(\tilde{x},\tilde{y}) = \tilde{\mathbf{v}}(\xi,\eta) = U(\xi,\eta)\mathbf{e}_\xi = \left\lfloor\sqrt{\tilde{u}^2(0,0)+\tilde{v}^2(0,0)}\right\rfloor\mathbf{e}_\xi, \tag{139}
$$

So the V component of the gas around the particle is equal to zero, and we can apply Eq. (112):

$$\mathbf{F}_{Sa} = 6.46a^2\sqrt{\left(u-u_p\right)^2+\left(v-v_p\right)^2}\sqrt{\rho\mu\left|\frac{\partial U}{\partial\eta}\right|}Sign\left(\frac{\partial U}{\partial\eta}\right)\mathbf{e}_\eta, \tag{140}$$

where

$$\frac{\partial U}{\partial\eta} = -\left.\frac{\partial u}{\partial x}\right|_p \sin\alpha\cos\alpha + \left.\frac{\partial u}{\partial y}\right|_p \cos^2\alpha - \left.\frac{\partial v}{\partial x}\right|_p \sin^2\alpha + \left.\frac{\partial v}{\partial y}\right|_p \sin\alpha\cos\alpha, \tag{141}$$

$$\alpha = \arctan\left(\frac{v-v_p}{u-u_p}\right). \tag{142}$$

Using Eq. (127), we finally obtain that

$$\mathbf{F}_{Sa} = 6.46a^2\sqrt{\left(u-u_p\right)^2+\left(v-v_p\right)^2}\sqrt{\rho\mu\left|\frac{\partial U}{\partial\eta}\right|}Sign\left(\frac{\partial U}{\partial\eta}\right)\left[-\sin\alpha\cdot\mathbf{e}_x+\cos\alpha\cdot\mathbf{e}_y\right], \tag{143}$$

Employing Eq. (142), the Saffman force equation can be rewritten as follows:

$$\mathbf{F}_{Sa} = 6.46a^2\sqrt{\rho\mu\left|\frac{\partial U}{\partial\eta}\right|}Sign\left(\frac{\partial U}{\partial\eta}\right)\left[-\left(v-v_p\right)\mathbf{e}_x+\left(u-u_p\right)\mathbf{e}_y\right]. \tag{144}$$

Substitution of the expression for $\frac{\partial U}{\partial \eta}$, Eq. (141), into the Saffman force equation, Eq.(144), leads to:

$$\begin{aligned}
&\mathbf{F}_{Sa} = 6.46a^2\sqrt{\rho\mu}\times \\
&\sqrt{\left|-\frac{\partial u}{\partial x}\sin\alpha\cos\alpha+\frac{\partial u}{\partial y}\cos^2\alpha-\frac{\partial v}{\partial x}\sin^2\alpha+\frac{\partial v}{\partial y}\sin\alpha\cos\alpha\right|}\times \\
&Sign\left(-\frac{\partial u}{\partial x}\sin\alpha\cos\alpha+\frac{\partial u}{\partial y}\cos^2\alpha-\frac{\partial v}{\partial x}\sin^2\alpha+\frac{\partial v}{\partial y}\sin\alpha\cos\alpha\right)\times \\
&\left[-\left(v-v_p\right)\mathbf{e}_x+\left(u-u_p\right)\mathbf{e}_y\right]
\end{aligned}. \qquad \textbf{(145)}$$

To compare this final Eq. (145) with the generalized 3D formula, Eq. (122), two-dimensional case can be considered where the velocity vectors have only 2 components that depend on x and y:

$$\mathbf{v}(x,y)=u(x,y)\mathbf{e}_x+v(x,y)\mathbf{e}_y, \qquad \textbf{(146)}$$

Therefore:

$$\nabla\times\mathbf{v}=\left(\frac{\partial v}{\partial x}-\frac{\partial u}{\partial y}\right)\mathbf{e}_z, \text{ and} \qquad \textbf{(147)}$$

$$\left(\mathbf{v}-\mathbf{v}_p\right)\times\left(\nabla\times\mathbf{v}\right)=\left(v-v_p\right)\left(\frac{\partial v}{\partial x}-\frac{\partial u}{\partial y}\right)\mathbf{e}_x+\left(u-u_p\right)\left(\frac{\partial u}{\partial y}-\frac{\partial v}{\partial x}\right)\mathbf{e}_y. \qquad \textbf{(148)}$$

So, Eq. (122) can be presented as follows:

$$\mathbf{F}_{Sa} = 6.46a^2\sqrt{\rho\mu\left|\frac{\partial u}{\partial y}-\frac{\partial v}{\partial x}\right|}\times Sign\left(\frac{\partial u}{\partial y}-\frac{\partial v}{\partial x}\right)\left[-\left(v-v_p\right)\mathbf{e}_x+\left(u-u_p\right)\mathbf{e}_y\right], \quad \textbf{(149)}$$

As one can see Eq. (145) is similar to Eq. (149), but there is a difference between the equation derived in the paper and the equation given in literature for the Saffman force: instead of the expression $\sqrt{\left|\frac{\partial u}{\partial y}-\frac{\partial v}{\partial x}\right|}\times Sign\left(\frac{\partial u}{\partial y}-\frac{\partial v}{\partial x}\right)$ in Eq. (149), the following term is used in the Eq. (145): $\sqrt{\left|-\frac{\partial u}{\partial x}\sin\alpha\cos\alpha+\frac{\partial u}{\partial y}\cos^2\alpha-\frac{\partial v}{\partial x}\sin^2\alpha+\frac{\partial v}{\partial y}\sin\alpha\cos\alpha\right|}\times Sign\left(-\frac{\partial u}{\partial x}\sin\alpha\cos\alpha+\frac{\partial u}{\partial y}\cos^2\alpha-\frac{\partial v}{\partial x}\sin^2\alpha+\frac{\partial v}{\partial y}\sin\alpha\cos\alpha\right)$.

Note that the equation for the Saffman force derived in the paper, Eq. (145), is identical to the equation given in the literature, Eq. (149), only when two conditions are satisfied:

- both the angle α and $\frac{\partial v}{\partial x}$ are equal to zero; or,
- the angle α is equal to 90° and $\frac{\partial u}{\partial x}$ is equal to zero.

Eq. (143) is correct for any u and u_p which satisfy the condition: $u-u_p>0$. The sign of $v-v_p$ is taken into account, because $\alpha=\arctan\left(\frac{v-v_p}{u-u_p}\right)$. Therefore, if the difference $v-v_p>0$, then angle α will be positive over the range [0, π/2]. And if the difference $v-v_p<0$, then angle α will be negative over the range [-π/2, 0]. The

condition: $u-u_p>0$, means that the gas is dragging the particle. In other words, the particle is moving slow in comparison with gas. The condition: $u-u_p<0$, means that the particle velocity is higher in comparison with gas velocity.

If $u-u_p<0$, then Eq. (143) also can be used with correction for angle α:

$$\alpha=\pi+\arctan\left(\frac{v-v_p}{u-u_p}\right), \tag{150}$$

The detailed explanation for this particular case is presented further down.

First, let us consider the case when $u-u_p<0$ and $v-v_p<0$. If $u-u_p<0$ and $v-v_p<0$, then $\alpha_1=\arctan\left(\frac{v-v_p}{u-u_p}\right)>0$ (see Figure 70). Therefore,

$$\alpha=\pi+\alpha_1=\pi+\arctan\left(\frac{v-v_p}{u-u_p}\right).$$

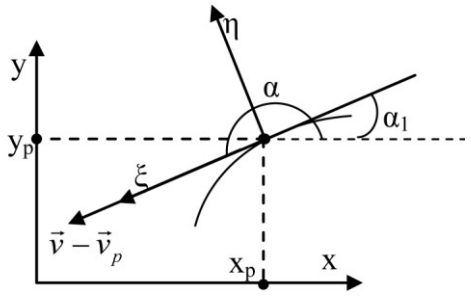

Figure 70. Transformation of global coordinate system to local coordinate system, which is moving along with particle. The case when $u-u_p<0$ and $v-v_p<0$ is considered.

Second, let us consider the case when $u-u_p<0$ and $v-v_p>0$. If $u-u_p<0$ and $v-v_p>0$, then $a_1=\arctan\left(\frac{v-v_p}{u-u_p}\right)<0$ (see Figure 71). Therefore,

$$\alpha=\pi+a_1=\pi+\arctan\left(\frac{v-v_p}{u-u_p}\right).$$

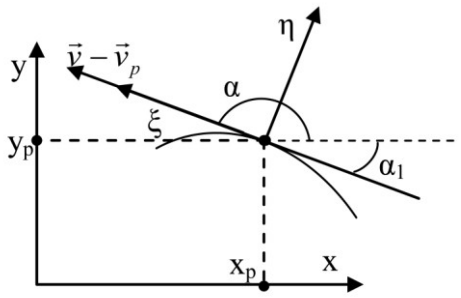

Figure 71. Transformation of global coordinate system to local coordinate system, which is moving along with particle. The case when $u-u_p<0$ and $v-v_p>0$, is considered.

Finally the equation for the angle α looks as follows:

$$\alpha=\begin{cases}\arctan\left(\frac{v-v_p}{u-u_p}\right), \text{if } u-u_p>0\\ \pi+\arctan\left(\frac{v-v_p}{u-u_p}\right), \text{if } u-u_p<0\end{cases}, \quad \textbf{(151)}$$

where $\arctan(x)\in\left[-\frac{\pi}{2},\frac{\pi}{2}\right]$.

To summarize, knowing the gas velocity field and the gas density from ANSYS CFX, the gas-particle interaction forces can be calculated by using Eqs. (90) and (143). In order to

calculate aerosol particles' trajectories and velocities, a home-made Matlab code was developed. The detailed algorithm of this code is presented in the next sub-section.

3.1.6. Calculation Algorithm

In this section the calculation algorithm of aerosol particles' trajectories and velocities is presented. Initially any aerosol particle with given radius, density, and radial position should be placed in the nozzle inlet, where the x position of the particle is equal to zero. The axial particle velocity component is assigned to be 90% of the gas velocity in the case of Poiseuille flow. The radial component of particle velocity is assumed to be zero. Then 4 nodes containing this aerosol particle must be found in the gas data file. To do this, first, the file has to be opened and 9 arrays are created: x and y coordinates of node, gas density, axial and radial components of velocity, and their derivatives with respect to x and y. By knowing the distance between nodes in x and y direction, the search function is initialized to get nodes which have aerosol particle inside. Since a sector of five degrees is considered, there will be not 4 nodes, but 8 nodes due to the symmetry boundary condition. That is why duplicates of nodes should be deleted, and the rest 4 of the nodes are rearranged in a counterclockwise way. To get gas velocity components and gas density in the particle current position, (x, y), the following four shape functions have been used:

$$\begin{cases} \psi_1 = \dfrac{x - x_2}{x_1 - x_2}\dfrac{y - y_4}{y_1 - y_4} \\ \psi_2 = \dfrac{x - x_1}{x_2 - x_1}\dfrac{y - y_3}{y_2 - y_3} \\ \psi_3 = \dfrac{x - x_1}{x_3 - x_1}\dfrac{y - y_2}{y_3 - y_2} \\ \psi_4 = \dfrac{x - x_2}{x_4 - x_2}\dfrac{y - y_1}{y_4 - y_1} \end{cases}, \tag{152}$$

where x_1, x_2, x_3, and x_4 are x coordinates of 4 nodes, and y_1, y_2, y_3, and y_4 are y coordinates of 4 nodes. Therefore gas velocity at position (x, y) looks as follows:

$$\begin{cases} u = \psi_1 u_1 + \psi_2 u_2 + \psi_3 u_3 + \psi_4 u_4 \\ v = \psi_1 v_1 + \psi_2 v_2 + \psi_3 v_3 + \psi_4 v_4 \end{cases}, \tag{153}$$

where (u_1, v_1), (u_2, v_2), (u_3, v_3), and (u_4, v_4) are axial and radial components of gas velocity at 4 nodes. Similar result is obtained for gas density:

$$\rho = \psi_1 \rho_1 + \psi_2 \rho_2 + \psi_3 \rho_3 + \psi_4 \rho_4, \tag{154}$$

where ρ_1, ρ_2, ρ_3, and ρ_4 are gas densities at four nodes.

Derivatives of velocity components with respect to x and y can be found from:

$$\begin{cases} \dfrac{\partial u}{\partial x} = \psi_1 \left.\dfrac{\partial u}{\partial x}\right|_1 + \psi_2 \left.\dfrac{\partial u}{\partial x}\right|_2 + \psi_3 \left.\dfrac{\partial u}{\partial x}\right|_3 + \psi_4 \left.\dfrac{\partial u}{\partial x}\right|_4 \\ \dfrac{\partial u}{\partial y} = \psi_1 \left.\dfrac{\partial u}{\partial y}\right|_1 + \psi_2 \left.\dfrac{\partial u}{\partial y}\right|_2 + \psi_3 \left.\dfrac{\partial u}{\partial y}\right|_3 + \psi_4 \left.\dfrac{\partial u}{\partial y}\right|_4 \\ \dfrac{\partial v}{\partial x} = \psi_1 \left.\dfrac{\partial v}{\partial x}\right|_1 + \psi_2 \left.\dfrac{\partial v}{\partial x}\right|_2 + \psi_3 \left.\dfrac{\partial v}{\partial x}\right|_3 + \psi_4 \left.\dfrac{\partial v}{\partial x}\right|_4 \\ \dfrac{\partial v}{\partial y} = \psi_1 \left.\dfrac{\partial v}{\partial y}\right|_1 + \psi_2 \left.\dfrac{\partial v}{\partial y}\right|_2 + \psi_3 \left.\dfrac{\partial v}{\partial y}\right|_3 + \psi_4 \left.\dfrac{\partial v}{\partial y}\right|_4 \end{cases} \quad \textbf{(155)}$$

where $\left.\dfrac{\partial u}{\partial x}\right|_1$, $\left.\dfrac{\partial u}{\partial x}\right|_2$, $\left.\dfrac{\partial u}{\partial x}\right|_3$, and $\left.\dfrac{\partial u}{\partial x}\right|_4$ are derivatives of axial components of gas velocity with respect to x at 4 nodes; $\left.\dfrac{\partial u}{\partial y}\right|_1$, $\left.\dfrac{\partial u}{\partial y}\right|_2$, $\left.\dfrac{\partial u}{\partial y}\right|_3$, and $\left.\dfrac{\partial u}{\partial y}\right|_4$ are derivatives of axial components of gas velocity with respect to y at 4 nodes, $\left.\dfrac{\partial v}{\partial x}\right|_1$, $\left.\dfrac{\partial v}{\partial x}\right|_2$, $\left.\dfrac{\partial v}{\partial x}\right|_3$, and $\left.\dfrac{\partial v}{\partial x}\right|_4$ are derivatives of radial components of gas velocity with respect to x at 4 nodes; $\left.\dfrac{\partial v}{\partial y}\right|_1$, $\left.\dfrac{\partial v}{\partial y}\right|_2$, $\left.\dfrac{\partial v}{\partial y}\right|_3$, and $\left.\dfrac{\partial v}{\partial y}\right|_4$ are derivatives of radial components of gas velocity with respect to y at 4 nodes.

As soon as gas velocity components, their derivatives, and gas density are known at the current particle position (see Eqs. (153),(154), and (155)), Stokes and Saffman forces acting on the particle can be calculated, see Eqs. (90) and (143). Therefore the equation of motion, Eq. (89), can be solved for a small time step (an order of microsecond). Here a Runge-Kutta fourth order method is employed to solve the second order differential equations. This will lead to a new particle position and velocity. All calculations are repeated while the particle is moving inside of the nozzle or in the plenum part. Then

another particle with given density, diameter and radial position should be introduced at the nozzle inlet until the trajectories of all particles are found.

After the calculation part, the visualization part of the code follows. There are five figures at the end. In the first figure, all particles' trajectories are shown (an example is in Figure 72). The second and third figures are devoted to axial and radial components of velocities: their dependencies on x position are shown (Figure 73).

Fourth and fifth figures show axial and radial velocity components of all particles at the distance of 100 microns from the nozzle exit (Figure 74). This is done to compare modeling results with experimental ones. The modeling results are obtained not at the nozzle outlet, because experimental values cannot be gained right at the nozzle outlet. It is possible to get experimental data at the distance of 100 micron from the nozzle outlet.

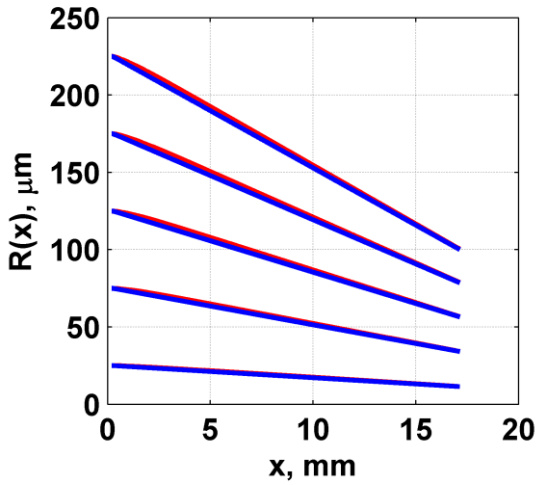

Figure 72. Five particles' trajectories.

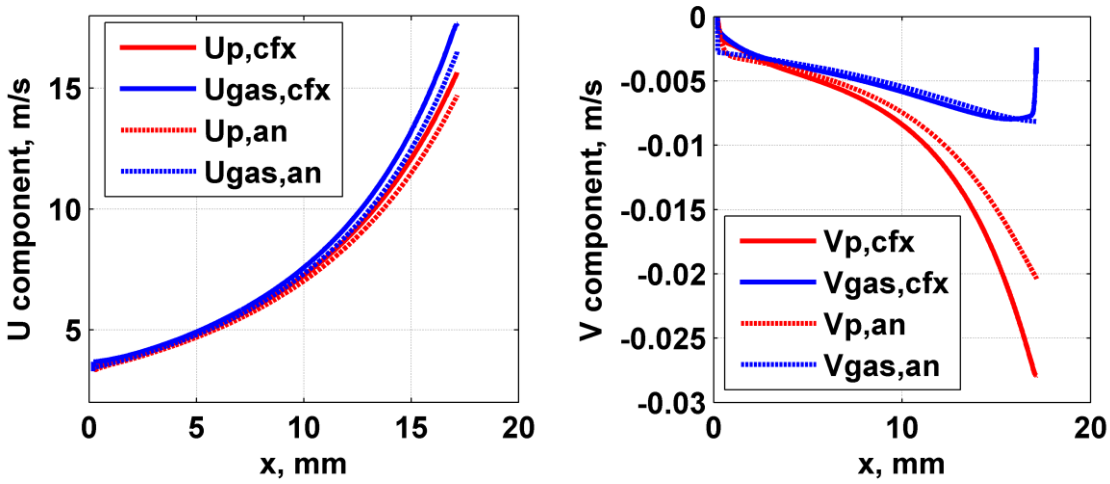

(a) (b)

Figure 73. Axial velocity component (a) and radial velocity component (b) for one of the aerosol particle versus x-position.

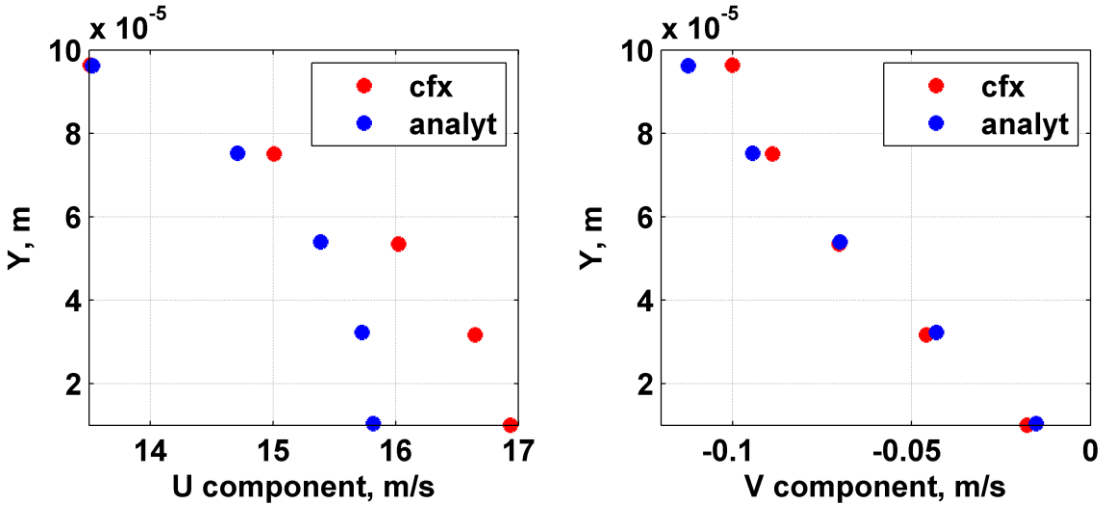

(a) (b)

Figure 74. Axial velocity components (a) and radial velocity components (b) for five aerosol particles at the nozzle exit.

The Matlab code and comments to the code can be found in Appendix.

3.1.7. Model Validation with Experiments

In this section the modeling results are compared with experimental ones. To collect experimental data, a shadowgraphy system installed in our laboratory is used. This system consists of the following (see Figure 75):

- a pair of Nd:YAG pulsed lasers pumping fluorescent dye, a liquid fiber guide, and a Fresnel lens to illuminate aerosol particles;
- a high speed camera along with magnification lenses;
- a CW laser for alignment and collection of beam width results; and,
- three stages in XYZ assembly to move the deposition head to the focal plane.

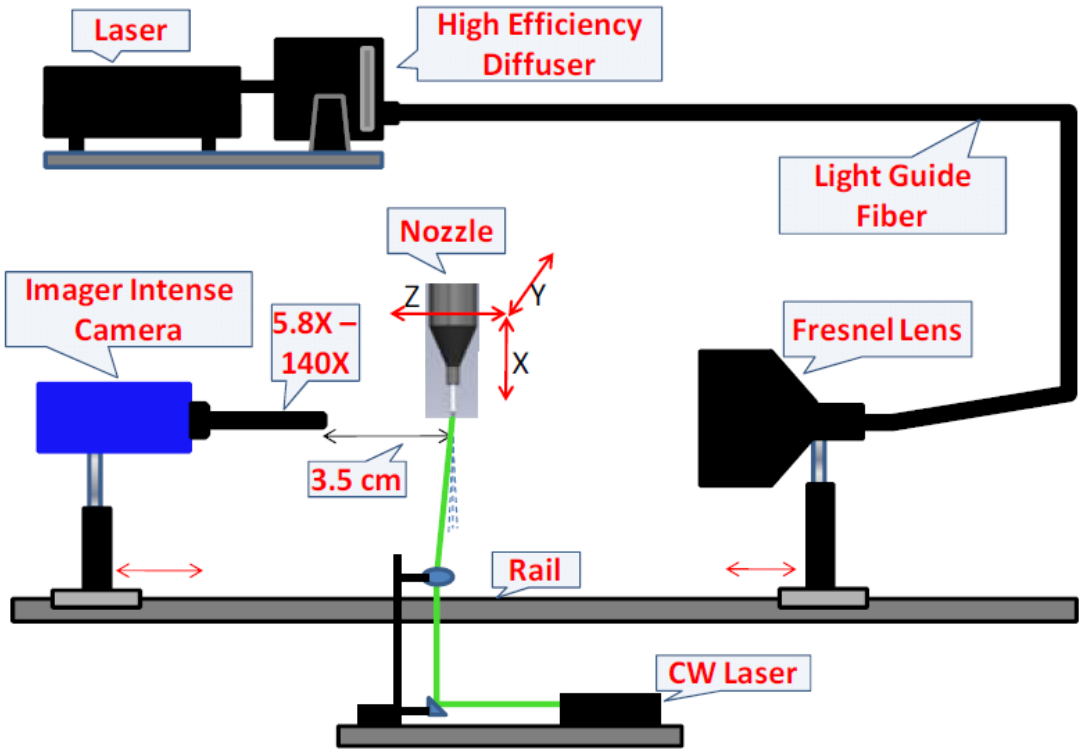

Figure 75. Schematic of the shadowgraphy system from Mahmud et al., "Experimental Characterization of Aerosol Flow through a Micro-Capillary," Proceedings of ASME 2010 3rd Joint US-European Fluids Engineering Summer Meeting and 8th International Conference on Nanochannels, Microchannels, and Minichannels, Copyright 2010 [91]. Reproduced with permission from ASME.

Only a few experimental results will be shown to validate the model. Detailed descriptions of the experimental setups and explanations of how experimental results were collected can be found in Michael Robinson's master thesis titled "Experimental Characterization of Aerosol Flows through Micro-Capillaries" [92].

Model/experiment comparison is done using simple nozzle geometries: linearly-convergent nozzle and linearly-convergent nozzle attached to straight part. First the linearly-convergent nozzle is considered with inlet diameter of 820 micron, outlet diameter of 216 microns, and length of 19.05 mm. Mono-dispersed, solid, and spherical silica particles are entrained by nitrogen flow both in the model and experiments. The diameter of these silica spheres is about 3.8 microns +/- 0.4 microns: SEM picture of these particles is shown in Figure 76.

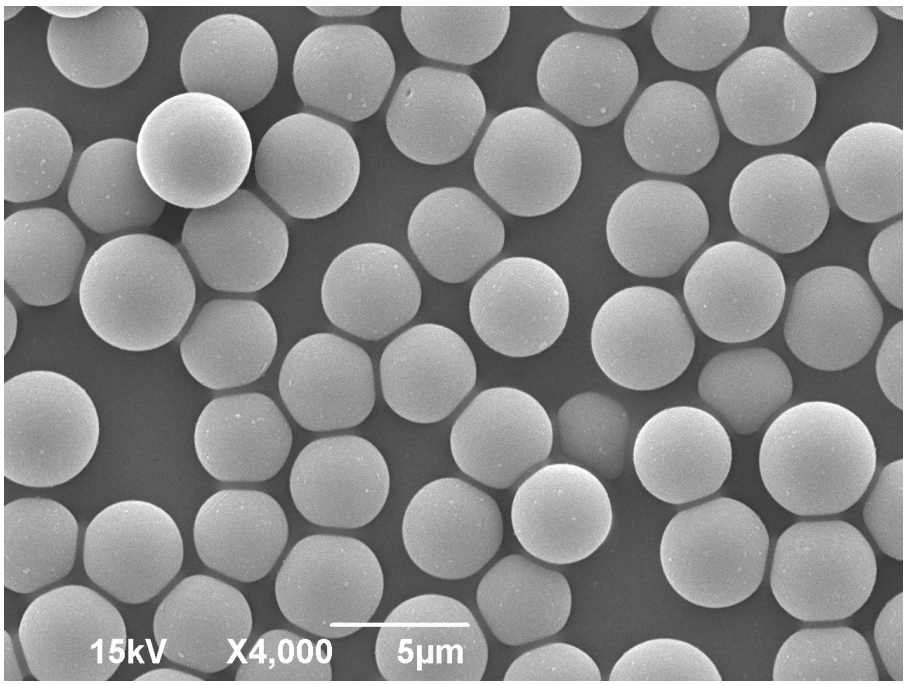

Figure 76. SEM picture of mono-dispersed silica particles.

The density of particles taken from the manufacturer's catalog is 1800 kg/m^3. Two different flow rates (120 ccm and 180 ccm) are set both in the model and experiments. Note that these flow rates are gas volumetric flows which come out of the nozzle outlet. Due to compressibility of the nitrogen, the inlet flow rates are equal to 115 and 167 ccm. From experiments for the flow rate of 180 ccm, it is known that initially silica particles occupy part of the inlet area due to the sheath gas usage: the distance between radial components of solid spheres entering the nozzle and the nozzle centerline is less than 32% of the inlet radius. This fact is employed as an initial boundary condition in the model. Since the nozzle is made from tungsten carbide, it is impossible to visualize particles inside the nozzle. Therefore, experimentally we can measure particles' velocities only when they exit the nozzle outlet. In addition, we can experimentally identify particles' locations to calculate the aerosol beam width only when the particles are out of the nozzle. In contrast, in the model we calculate any particle velocity at any location. Also, we track the particle while it moves inside the nozzle and in the plenum.

Figure 77 shows a comparison between simulations and experiments for the aerosol beam width when the flow rate is equal to 180 ccm. Dashed lines are devoted to the modeling results: red represents results where only Stokes force is used; green represents results where both Stokes and Saffman forces are used in model. Experimental results are shown by using solid lines: the blue line with the diamond symbol shows results found by the shadowgraphy system; the brown line with the square symbol illustrates results obtained by the aerosol beam illumination with CW laser. It is clear that experimental results cannot be described by the model while both Stokes and Saffman forces are used.

The addition of the Saffman force to the model leads to smaller beam width which is not noticed during the experiments.

Considering beam width results, we see a good match between the model and the shadowgraphy system experiment when Stokes force is employed in the model and when the distance from the nozzle exit is less than 4 mm (x<4 mm). It is also noted that initially the CW beam width diverges from the modeling results because of the laser light scattering out of the nozzle outer wall. Starting from the distance of about 2 mm out of the nozzle exit, CW beam width gets closer to the modeling results (where only Stokes force is employed). Another finding is that after the distance of about 6-7 mm, modeling results cannot explain experimental ones: aerosol beam width starts to diverge rapidly. Therefore, the comparison between model and experiments for the beam width does not answer open question if Saffman force plays a role in the gas-particle interaction or not.

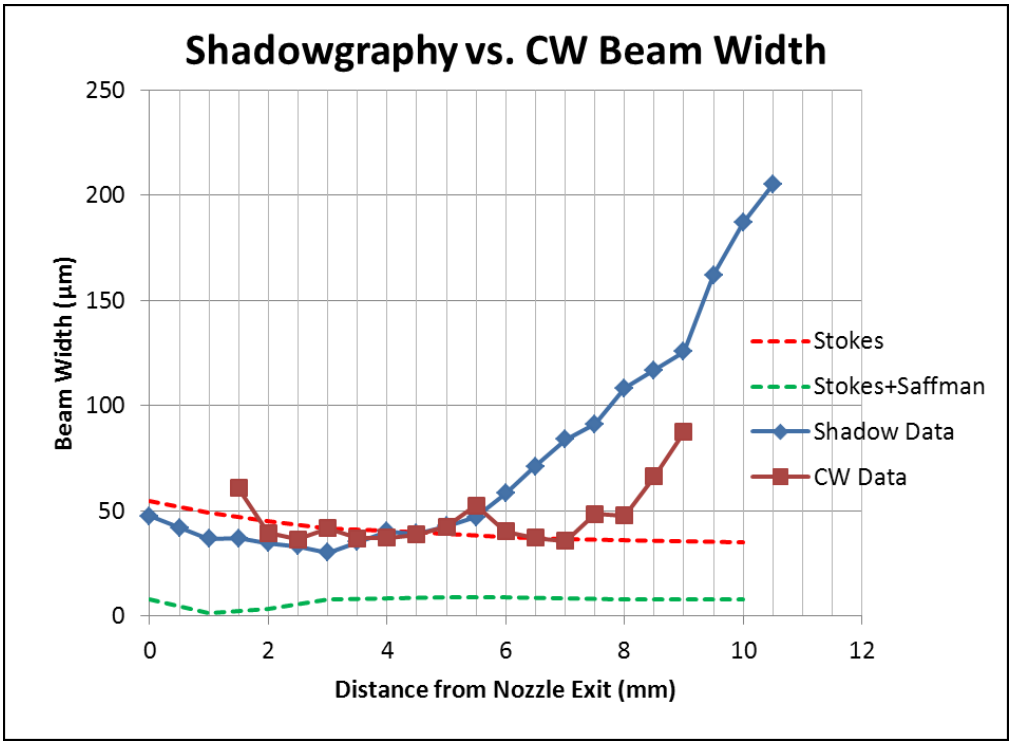

Figure 77. Aerosol beam width results: model versus experiment.

Figure 78 displays a comparison between simulations and experiments for the silica particle axial velocities at different distances out of the nozzle outlet, where (a), (b), (c), and (d) are devoted to the model/experiment comparison right after the nozzle outlet, at the distance of 1 mm from the nozzle outlet, at the distance of 3 mm from the nozzle outlet, and at the distance of 5 mm from the nozzle outlet, respectively. Note that here only Stokes force is utilized for the calculation of the particle axial velocities. Relying on model/experiments data for particles' velocities, we see that modeling results are in high agreement with experimental velocities.

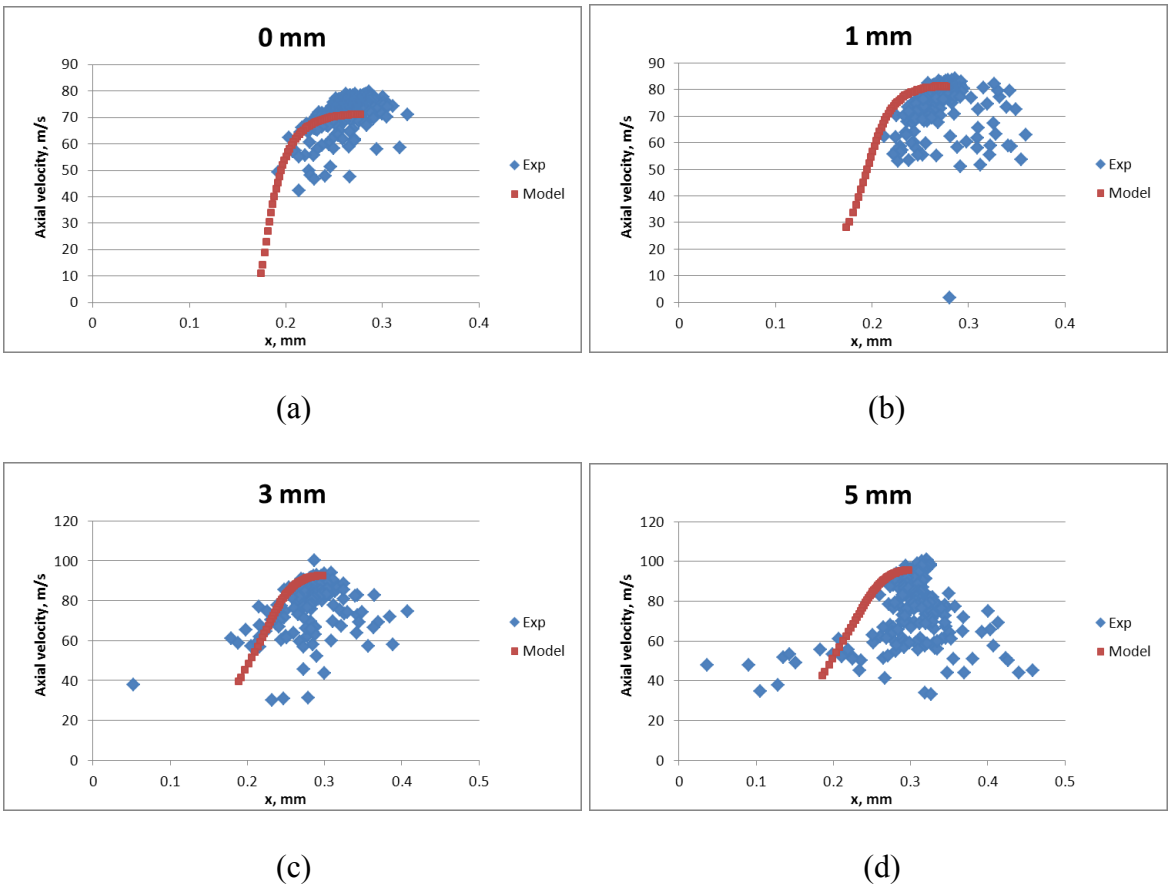

Figure 78. Silica particle axial velocities at different distances from the nozzle outlet. Model versus experiment comparison: (a) is right after the nozzle outlet, (b) is at 1 mm from the nozzle outlet, (c) is at 3 mm from the nozzle outlet, and (d) is at 5 mm from the nozzle outlet.

Based on the comparison between model and experiments both for the beam width and for the particle axial velocity, it seems like Saffman force has to be neglected in the model, but this conclusion is hard to make due to model/experiment mismatch for the beam width when the distance from the nozzle exit is more than 7 mm.

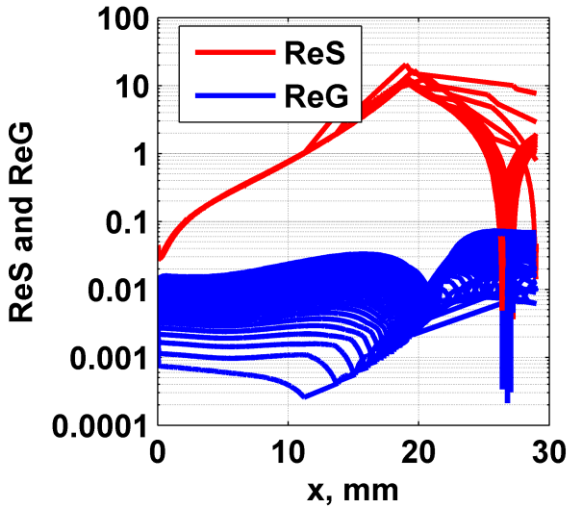

Figure 79. Particle (ReS) and shear (ReG) Reynolds numbers as function of x (distance from the nozzle inlet).

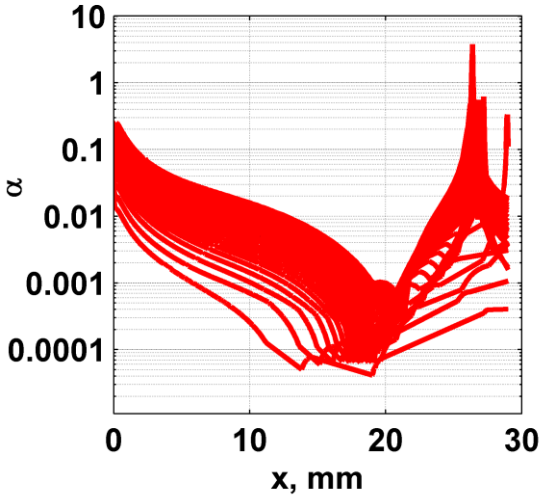

Figure 80. Dimensionless shear rate, α, as function of x (distance from the nozzle inlet).

It should be noted that both original 1D and generalized 2D flow equations for Saffman force are not applicable because in the parameters range of our aerosol flow, Saffman's assumptions, Eqs. (113) and (114), are not valid: the particle Reynolds number is higher than one, and moreover it is higher than the square root of the shear Reynolds number (see Figure 79). Therefore, the Saffman force correction, Eq. (115), proposed by Dandy and Dwyer should be utilized, but this equation can be used only when dimensionless shear rate, α, is in the range of $0.005<\alpha<0.4$, which is not true in our case (see Figure 80). At some distances from the nozzle inlet, the dimensionless shear rate is less than 0.005 or higher than 0.4. This result leads to the conclusion that the Saffman force equation should be further corrected when the shear rate is out of the applicability range.

Since the linearly-convergent nozzle does not show the influence of the Saffman force, the second nozzle geometry was considered: the same linearly-convergent nozzle attached to a straight capillary with diameter and length of 264 microns and 30 mm, respectively (see Figure 81). In this figure, the black line represents the nozzle wall; blue lines are silica particle trajectories when only Stokes force is applied; red lines are silica particle trajectories when both Stokes and Saffman forces are used; green lines are silica particle trajectories calculated using the following force to the particle: Stokes force plus 0.19 multiplied by Saffman force. The modeling results show that an addition of the straight section does not change the aerosol beam width when only Stokes force is applied. On the other hand, a very thin beam should be observed while both Stokes and Saffman forces are used. Doing experiments with this nozzle, the beam width of about 7 microns is observed (the yellow line in Figure 82). The model predicts the beam width of about 55 microns, when only Stokes force is applied (the blue line in Figure 82). Using both Stokes

and Saffman force, the beam width should be about1-2 microns (the brown line in Figure 82). This model/experiment comparison shows that not only should Stokes force be used: Saffman force has to be included in the model. Furthermore, it is observed that the magnitude of Saffman force should be decreased by a factor of 0.19 in order to have a match with experimental results (see the green line in Figure 82).

Since this correction factor of 0.19 is applicable only for the fixed geometry, the fixed flow rate of 120 ccm, and the fixed particle size of 3.8 μm, one has to change all possible factors in order to get the correction factor based of the flow characteristics. Therefore, the following parameters may be changed: the length and diameter of the straight section, the length and diameters of the linearly-convergent part, the flow rate, and the particle size.

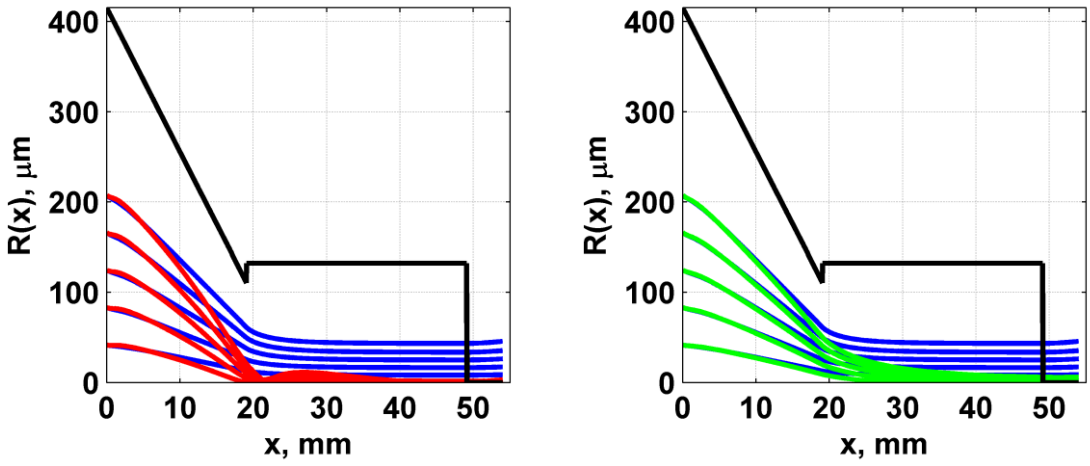

Figure 81. Silica particle trajectories through the linearly-convergent nozzle attached to the straight capillary. The black line is the nozzle wall. Blue lines are simulation results when only Stokes force is applied. Red lines are simulation results when both Stokes and Saffman forces are used. Green lines are simulation results when the following force is applied to the silica particle: Stokes+0.19*Saffman.

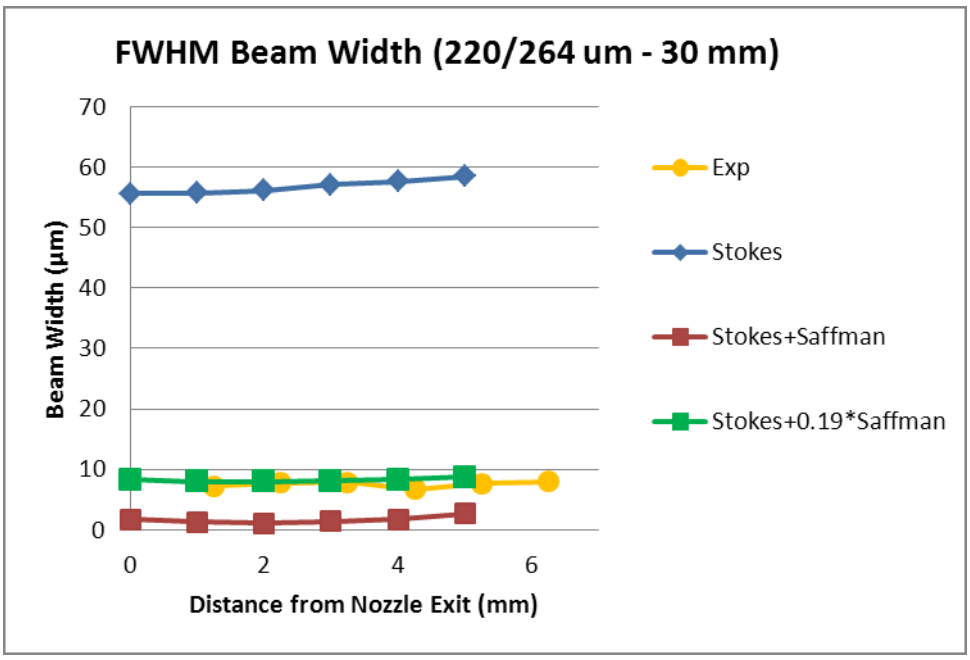

Figure 82. Beam width results for the linearly-convergent nozzle attached to the straight capillary.

To check the model assumption of neglecting the Magnus force, the pressure gradient force, the virtual mass force, and the buoyancy force, we evaluated these forces while the particles are in flight through the nozzle. The magnitude of all forces in axial and radial directions is presented in Figure 83, where (a) is devoted to the radial components of all forces acting on the aerosol particles in flight, (b) is devoted to the axial components of all forces, (c) is (b) without the Stokes force, and (d) is (c) but without the pressure gradient force (note that in the calculations of the Magnus force, we assume that the particle rotates with a speed proportional to the gas velocity gradient: $\boldsymbol{\Omega} = \frac{\partial u}{\partial y}\mathbf{e}_z$). Based on this plot, we see that the magnitude of the Magnus force in the radial direction is much lower than the Saffman force, which confirms the model assumption of neglecting the Magnus force. In addition, the comparison of all forces in the axial direction shows that the Stokes force is

much stronger than all other forces: it is about 100 times stronger than the pressure gradient force and at least 1000 times stronger than the Saffman force, the virtual mass force, the Magnus force, and the gravity force. Thus, these results illustrate that all forces except Stokes and Saffman can be ignored.

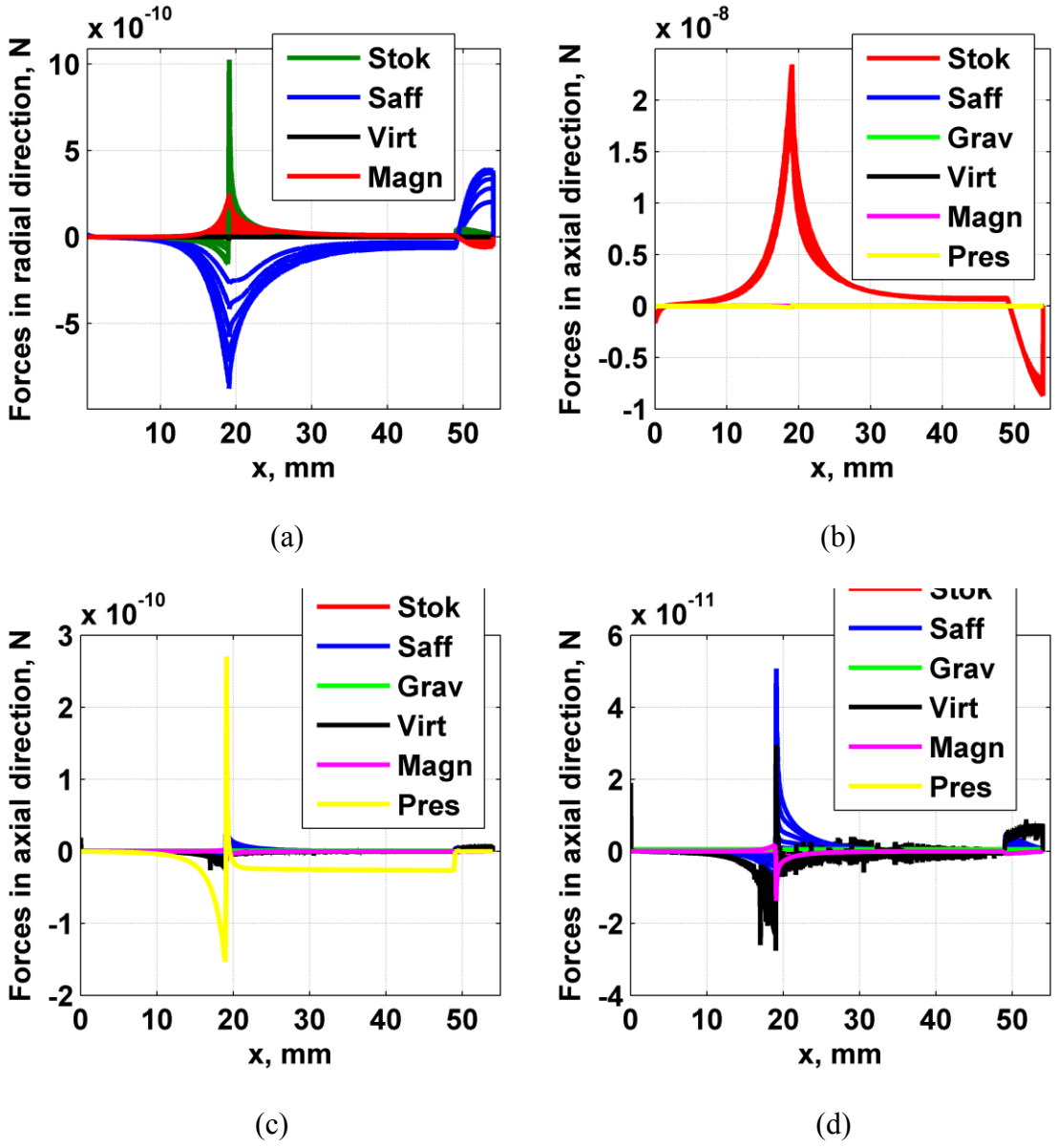

Figure 83. Axial and radial components of all forces acting on aerosol particles moving through linearly-convergent nozzle attached to the straight capillary.

3.2. Nozzle Design to Collimate Aerosol Particles

3.2.1. Scenario When Both Stokes and Saffman Forces are Used in the Model

Several different nozzle geometries were investigated by using the model described above. The goal of this research was to find the nozzle geometry which leads to collimation of all particles toward the centerline. It was desired to collimate all particles with diameters from one micron to five microns. Assuming that both Stokes and Saffman forces are acting on aerosol particle, it was found that the best nozzle design should have two sections: a linearly-convergent part and a straight part. The linearly convergent part serves as a tool for initial collimation of all particles, especially if their diameter is more than three microns. Bigger particles start to focus inside the nozzle, and then they defocus and focus again. That is why there is a need for the linear section. The linear part has two functions. First, it minimizes oscillations of the bigger particles with diameters of 2.5-3.5 μm along the nozzle centerline. Second, it still collimates smaller particles with diameters of 1-1.5 μm toward the centerline even if they are not collimated yet.

An example of aerosol particles' trajectories in the proposed nozzle design with gas flow rate of 192 ccm is shown in Figure 84. One can see that only 1 micron in diameter particles do not collimate toward the nozzle centerline. To enhance the process of particles' collimation, one can increase the flow rate: Figure 85 represents the difference between aerosol particles' trajectories for two different flow rates: 192 and 240 ccm.

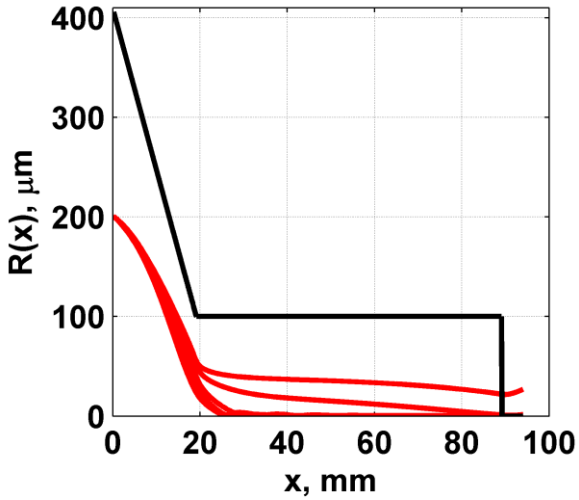

Figure 84. The proposed nozzle design is shown by the black line. Red lines represent aerosol particles' trajectories where particles' diameters are 1, 1.5, 2.5, 3.5, and 4.5 microns.

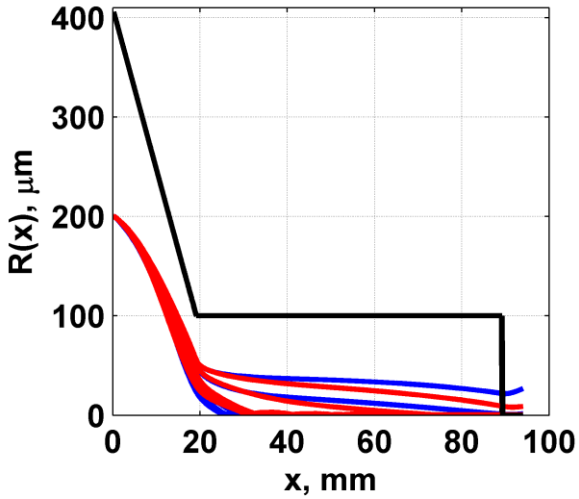

Figure 85. The proposed nozzle design is shown by the black line. Red and blue lines represent aerosol particles' trajectories where particles' diameters are 1, 1.5, 2.5, 3.5, and 4.5 microns. Blue lines correspond to a flow rate of 192 ccm, and red lines correspond to a flow rate of 240 ccm.

Increase of the flow rate from 192 ccm to 240 ccm leads to the decrease of the distance between 1 micron particle and the centerline from 25 microns to 10 microns. Another way to collimate particles is to introduce heavier particles. An example of solid particles'

trajectories is presented in Figure 86, where silver particles instead of aerosol particles were used. One can see that all particles are collimated in this case. This happens because silver particle density is ten times higher than aerosol particle density.

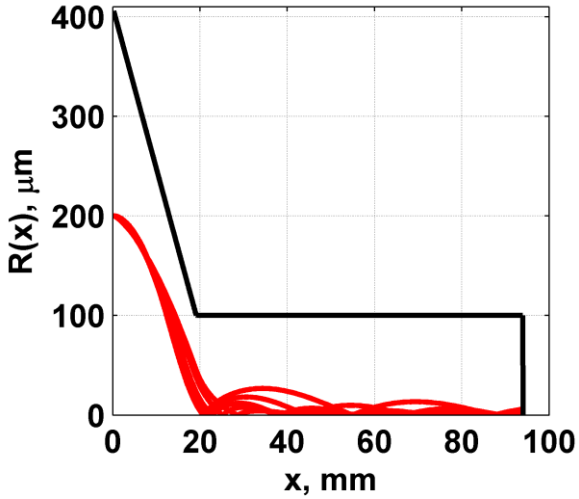

Figure 86. The proposed nozzle design is shown by the black line. Red lines represent silver particles' trajectories where particles' diameters are 1, 1.5, 2.5, 3.5, and 4.5 microns.

3.2.2. Scenario When Only Stokes Force is Used in the Model

In sub-section 3.2.1, the case was considered when both Stokes and Saffman forces are used. This was done in order to show what happens in the situation when both forces are acting on aerosol particle. The current sub-section is devoted to a more realistic case where only Stokes force is employed in the model.

Based on a trial and error approach, the nozzle geometry presented in Figure 87 is proposed for use if only Stokes force is acting on aerosol particle. As shown in this figure, the nozzle should have three sections:

- A linearly-convergent part with slow convergence;
- A linearly-convergent part with higher convergence; and,

- A straight part.

In addition, Figure 87 shows that liquid aerosol particles (of diameters 1.5 microns and density 1100 kg/m^3) along with silica particles (of diameters 1.0 micron and density 1800 kg/m^3) are collimated toward the nozzle centerline. Note that larger size particle cannot be collimated by using this nozzle design.

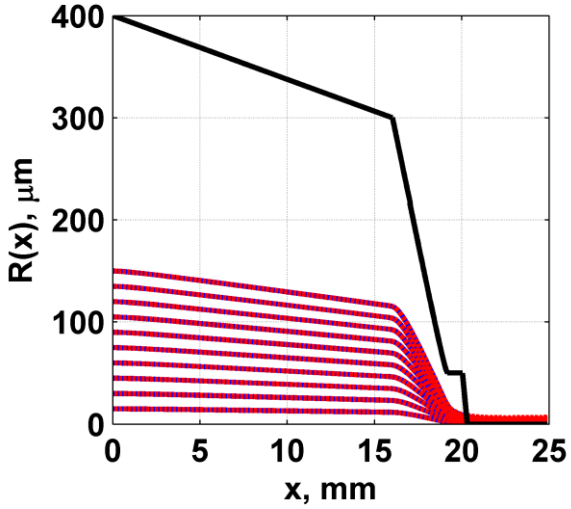

Figure 87. The proposed nozzle design is shown by the black line. Red lines represent silica particles' trajectories where particles' diameters are 1 micron (density of particles are 1800 kg/m^3). Blue lines represent liquid aerosol particles' trajectories where particles' diameters are 1.5 micron (density of particles are 1100 kg/m^3).

In order to focus and collimate aerosol particles from 2 to 4 microns in diameters, the nozzle geometry of the CAB-DW system must be used (see Figure 88 - Figure 91). Here liquid aerosol droplets are tracked with different particle diameters from 1 to 4 microns at a constant flow rate of 40 ccm. We see that Stokes force is enough to collimate particles with diameters from 2 to 4 microns, but particles with diameter of 1 micron are not focused. Insertion of Saffman force in the model leads to fast focusing first, but then fast defocusing is noticed.

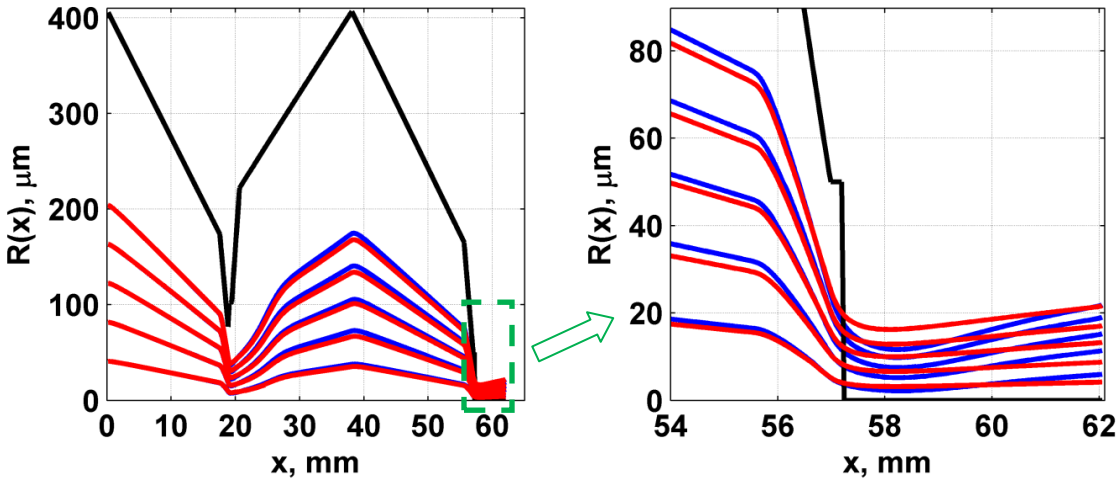

Figure 88. Aerosol particle trajectories. Particle diameters are 1 micron (blue lines – all forces, red lines – Stokes only). Q=40 ccm.

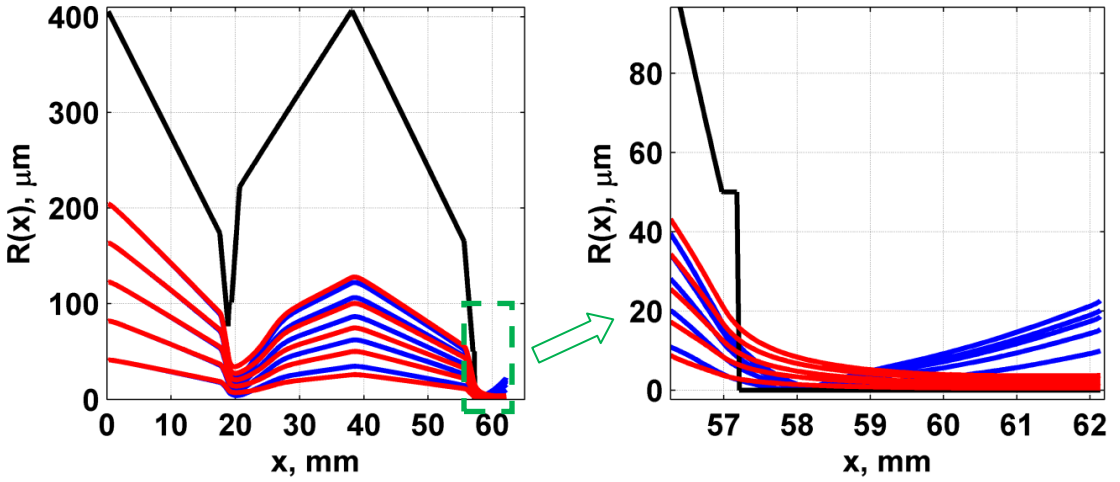

Figure 89. Aerosol particle trajectories. Particle diameters are 2 microns (blue lines – all forces, red lines – Stokes only). Q=40 ccm.

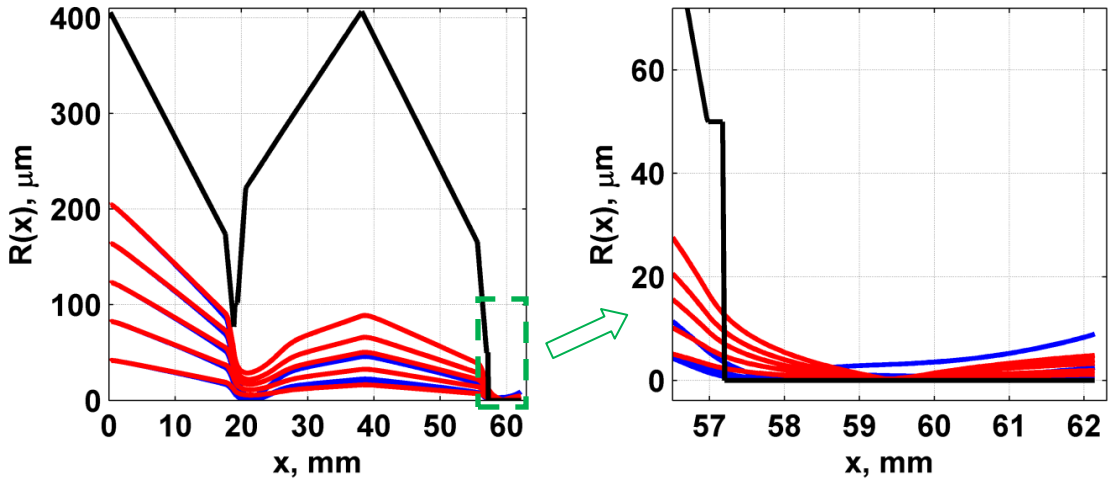

Figure 90. Aerosol particle trajectories. Particle diameters are 3 microns (blue lines – all forces, red lines – Stokes only). Q=40 ccm.

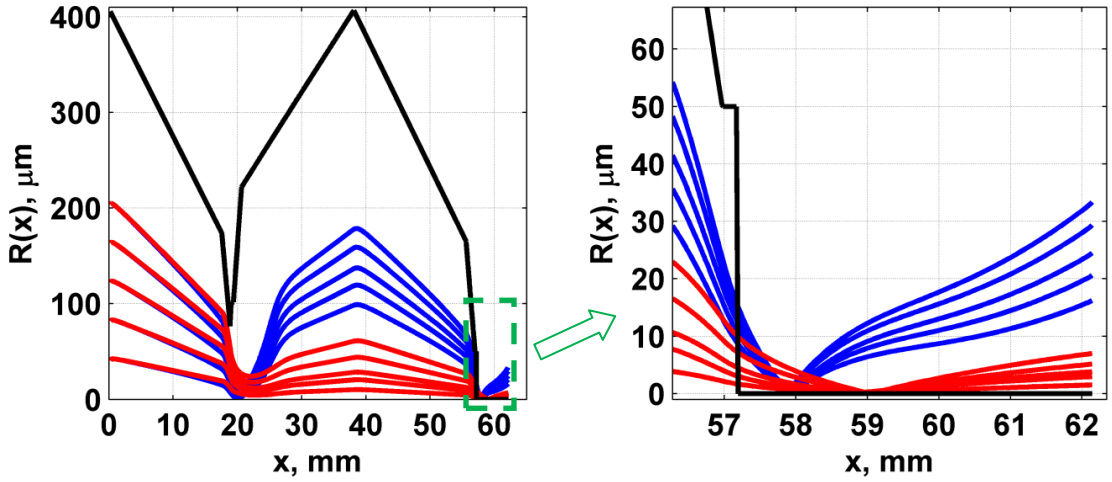

Figure 91. Aerosol particle trajectories. Particle diameters are 4 microns (blue lines – all forces, red lines – Stokes only). Q=40 ccm.

3.2.3. Different Nozzle Geometries under Different Conditions

This sub-section is devoted to consideration of different nozzle geometries while the following parameters are modified:

1. The particle diameter is decreased or increased;

2. The particle density is set to the liquid droplet density (1100 kg/m^3) or to the solid silver sphere density (11000 kg/m^3);
3. Saffman force is turned on or off.

First, the nozzle design proposed in 3.3.1 is investigated using the Saffman force (see Figure 92 and Figure 93). On the other hand, Figure 94 and Figure 95 correspond to the case when only Stokes force is included in the model. We can see that particles start to diverge in the straight section of the nozzle. Introducing silver particles (Figure 96) helps to converge them, but it is not enough. Therefore, proper evaluation of Saffman force by using experiments is needed. Figure 97 is also devoted to the simulation with silver particles where both forces are employed. Based on this figure, we see that only particles with diameters higher than 0.8 micron will be collimated.

Note that the collimation parameter is defined as:

$$S = \frac{1}{2NL}\sum_{i=1}^{N}\sqrt{\int_0^L \left\{\left[\frac{V_i(x)}{U_i(x)}\right]^2 + \left[\frac{R_i(x)}{R_c}\right]^2\right\}dx} \qquad \textbf{(156)}$$

where S is collimation parameter, L is distance between nozzle outlet and substrate, $V_i(x)$ is radial component of velocity of particle #i, $U_i(x)$ is axial component of velocity of particle #i, $R_i(x)$ is radial position of particle #i, R_c is nozzle outlet radius, N is number of particles. If S goes to zero, than all particles are collimated.

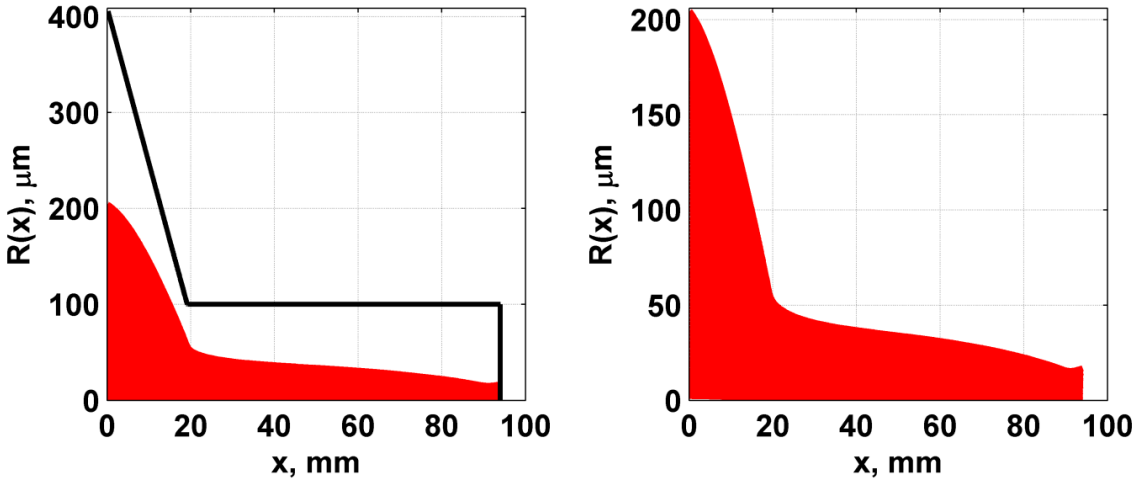

(a) (b) is (a) without the wall

Figure 92. Aerosol particle trajectories. Q=240 ccm, the black line is the wall, red lines are particles' trajectories. Particles' diameters are 1 micron. Stokes and Saffman forces are used. Collimation parameter is equal to $S=2.00\times10^{-3}$.

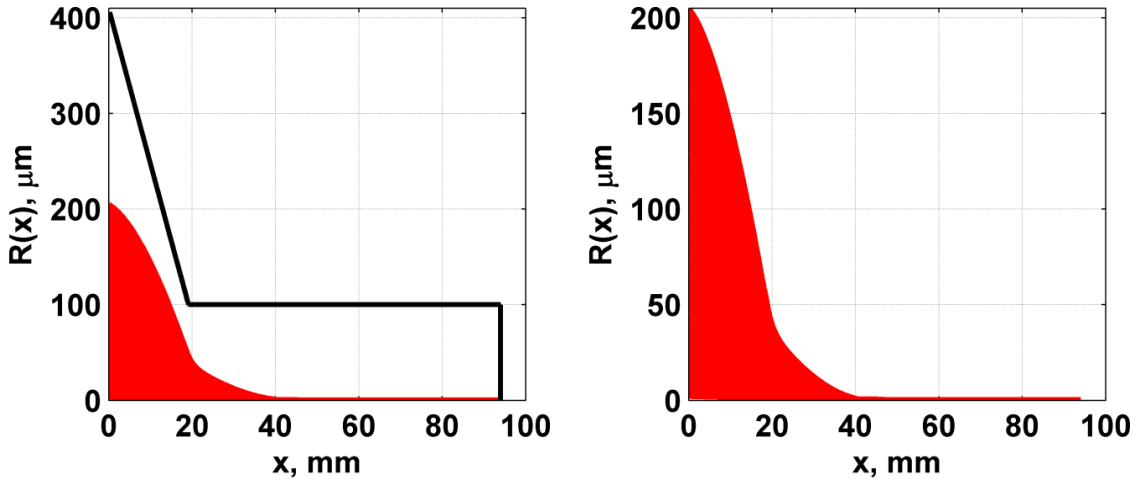

(a) (b) is (a) without the wall

Figure 93. Aerosol particle trajectories. Q=240 ccm, the black line is the wall, red lines are particles' trajectories. Particles' diameters are 2 microns. Stokes and Saffman forces are used. Collimation parameter is equal to $S=1.27\times10^{-4}$.

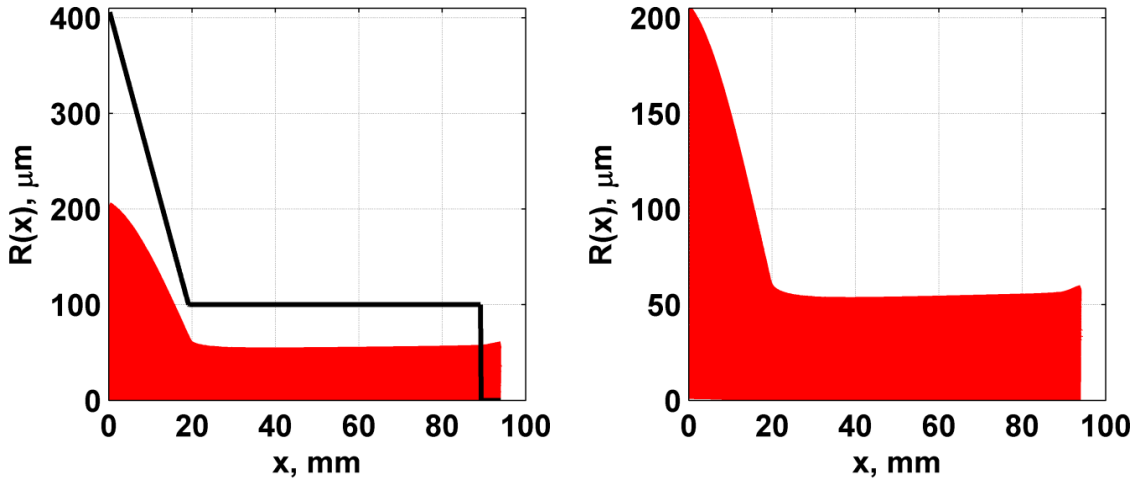

(a) (b) is (a) without the wall

Figure 94. Aerosol particle trajectories. Q=240 ccm, the black line is the wall, red lines are particles' trajectories. All particles' diameters are 1 micron. Saffman force is ignored. Collimation parameter is equal to $S=7.5\times10^{-3}$.

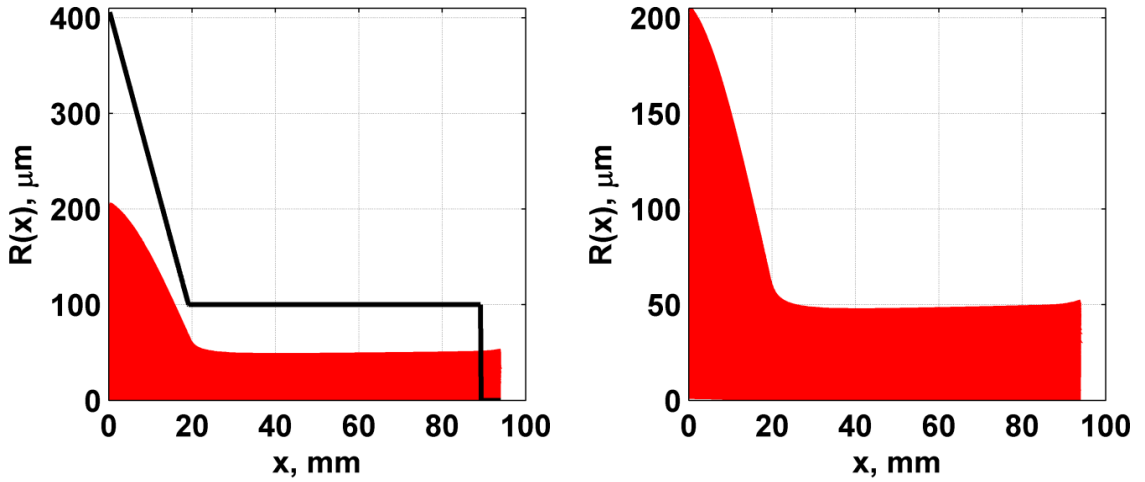

(a) (b) is (a) without the wall

Figure 95. Aerosol particle trajectories. Q=240 ccm, the black line is the wall, red lines are particles' trajectories. All particles' diameters are 2 microns. Saffman force is ignored. Collimation parameter is equal to $S=6.5\times10^{-3}$.

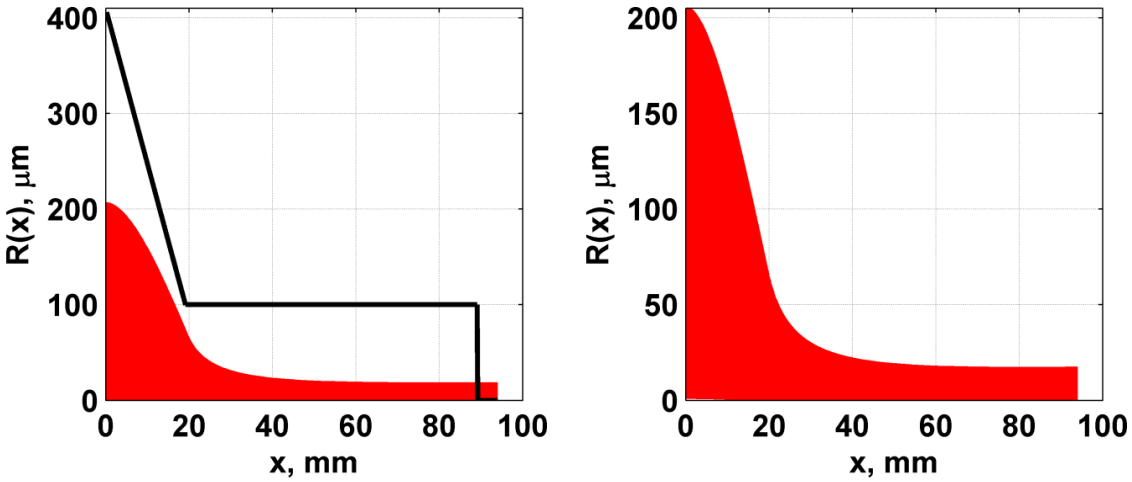

(a) (b) is (a) without the wall

Figure 96. Silver particle trajectories. Q=240 ccm, the black line is the wall, red lines are particles' trajectories. All particles' diameters are 2 microns. Saffman force is ignored. Collimation parameter is equal to $S=1.8\times10^{-3}$.

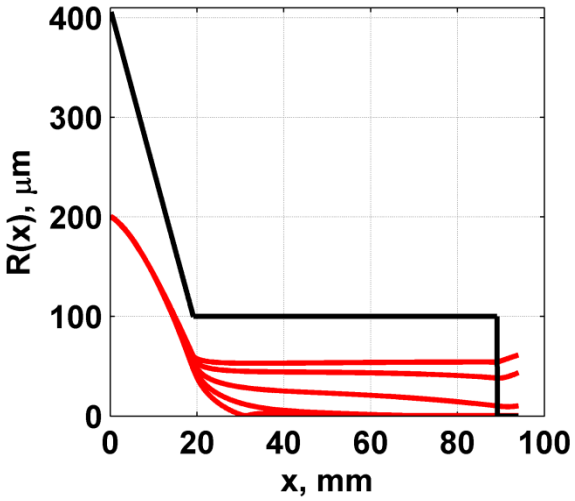

Figure 97. Silver particle trajectories. Q=192 ccm, the black line is the wall, red lines are particles' trajectories. Particle diameters are 0.2, 0.4, 0.6, 0.8, and 1.0 microns. Stokes and Saffman forces are used.

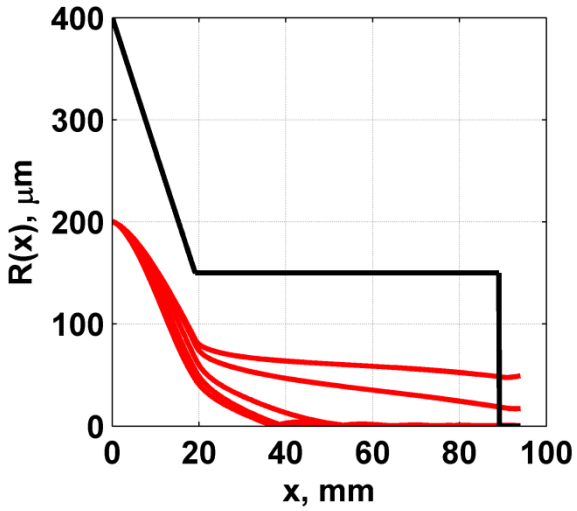

Figure 98. Aerosol particle trajectories. Q=432 ccm, the black line represents the wall, red lines represent particles' trajectories calculated using both Stokes and Saffman forces.

Figure 98 illustrates the case when the straight section has a larger diameter of 300 microns instead of the 200 microns shown in Figure 84. This diameter increase causes poor collimation of particles: particles with diameters of 2.5 microns and higher will be collimated.

Figure 99 shows the influence of the straight section: (a) and (b) are devoted to the simulations of the particle trajectories when we have only the convergent part; (c) and (d) depict the trajectories when the straight section is added to the convergent part. In Figure 100 the length of the straight section was increased from 70 mm to 100 mm, but this does not affect the collimation of particles with diameters of 1 micron.

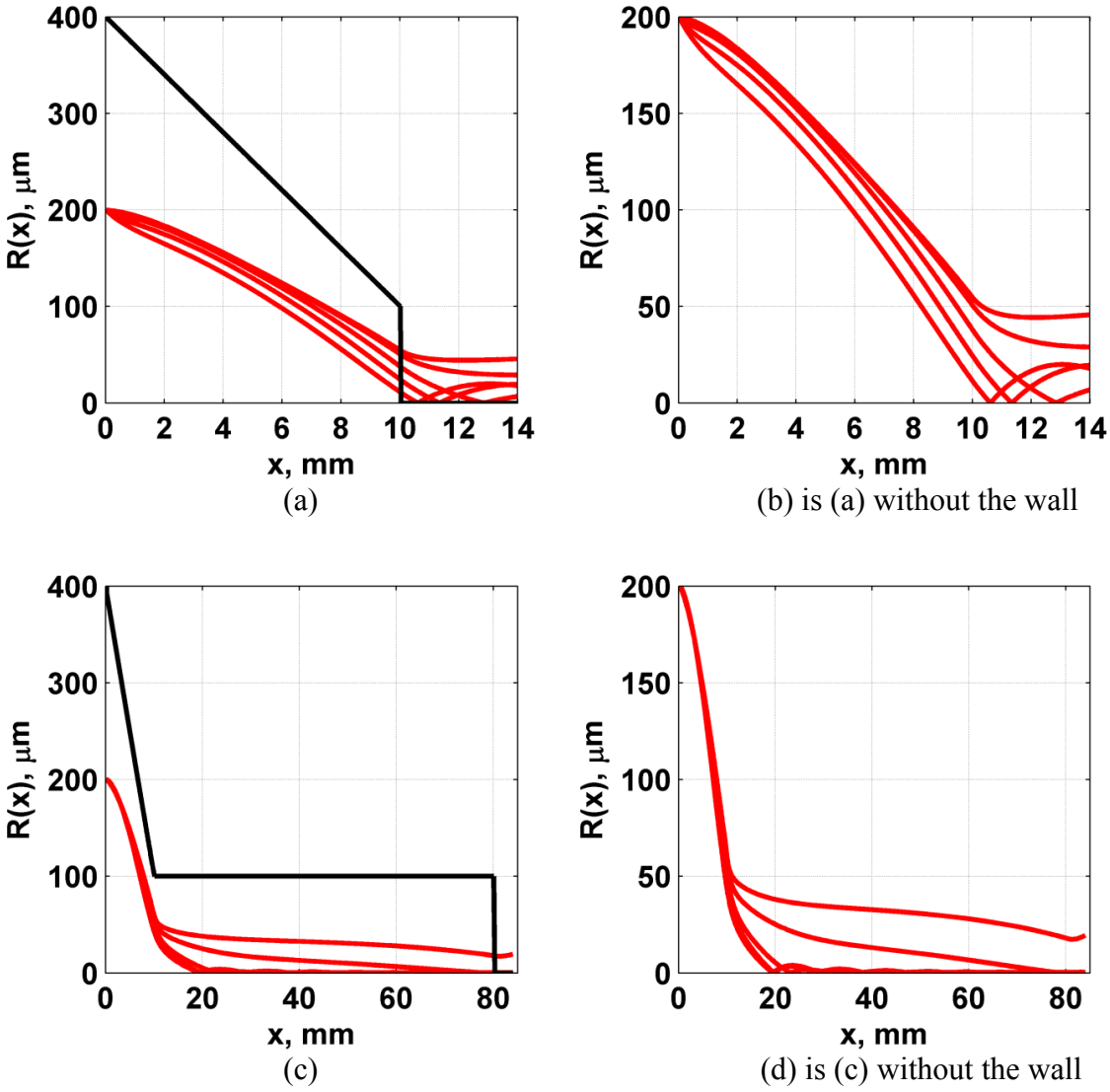

(a) (b) is (a) without the wall

(c) (d) is (c) without the wall

Figure 99. Aerosol particle trajectories. Q=192 ccm, the black line represents the wall, red lines represent particles' trajectories calculated using both Stokes and Saffman forces.

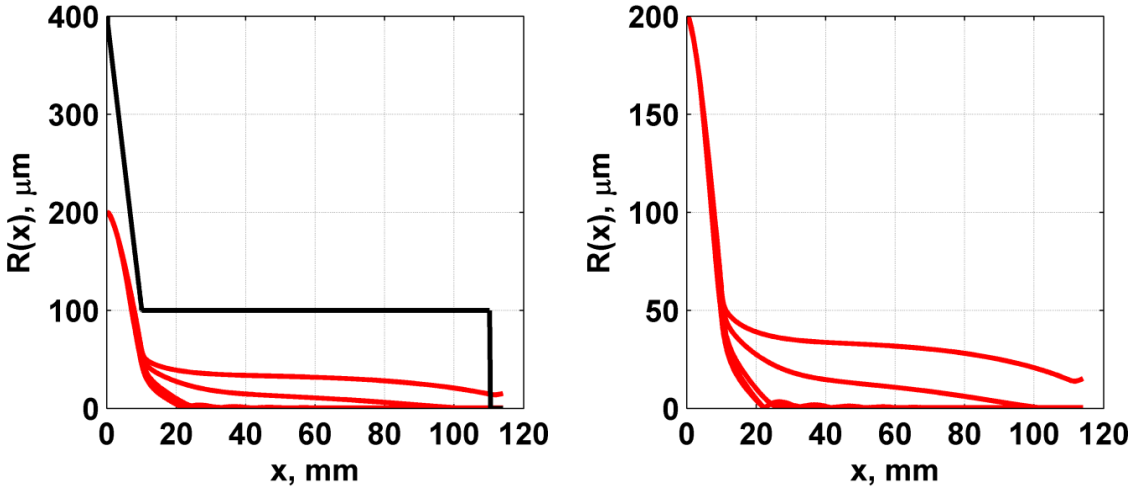

(a) (b) is (a) without the wall

Figure 100. Aerosol particle trajectories. Q=192 ccm, the black line represents the wall, red lines represent particles' trajectories calculated using both Stokes and Saffman forces.

Figure 101-Figure 103 present the results for the linearly-convergent nozzle by using silver particles with diameters ranging from 1 to 2 microns. Based on this simulation with the assumption that both forces (Stokes and Saffman) are acting on the particle, we see that particles with diameters of about 1.2 micron will be nicely collimated.

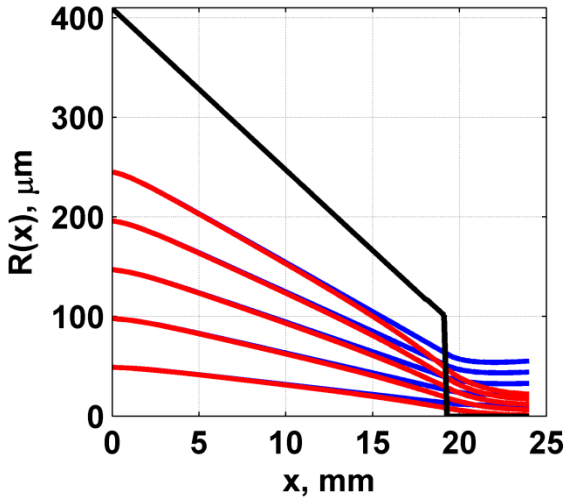

Figure 101. Silver particles' trajectories. D=1 micron. Blue lines correspond to calculations without Saffman force, red lines correspond to calculations when both forces are applied. Q=80 ccm.

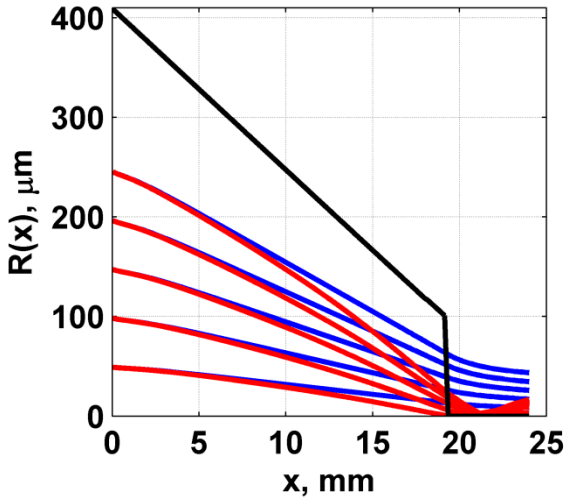

Figure 102. Silver particles' trajectories. D=2 microns. Blue lines correspond to calculations without Saffman force, red lines correspond to calculations when both forces are applied. Q=80 ccm.

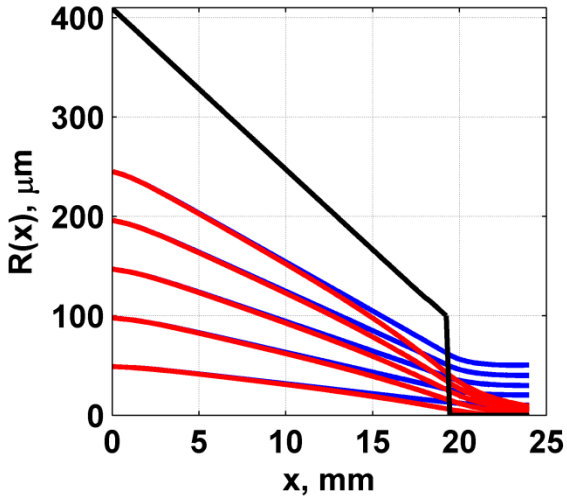

Figure 103. Silver particles' trajectories. D=1.2 micron. Blue lines correspond to calculations without Saffman force, red lines correspond to calculations when both forces are applied. Q=80 ccm.

4. SUMMARY AND RECOMMENDATIONS

A review of the existing direct-write techniques is presented in the first chapter of the dissertation. In this review, tip-based direct-write methods (e.g dip-pen nano-lithography and fountain pen nano-lithography) along with droplet-based direct-write techniques (e.g. ink-jet direct-write and aerosol-jet direct-write) are discussed in details. The advantages and disadvantages of available printing methods are identified. Based on this literature review, it is concluded that the main drawbacks of tip-based methods are the tip wearing and the substrate modification. To resolve these problems, a new Capillary-Based Droplet Deposition method is proposed that allows deposition of tiny amount of liquid on a substrate without any damage to the substrate and the tip. In addition, it is found that the difficulties associated with droplet-based direct-write techniques include the line width minimization and the ink overspray. Therefore, the need to improve the aerosol-based direct-write technique for particle better focusing and collimation is introduced.

In the second chapter of this work, the proposed Capillary-Based Droplet Deposition method is theoretically justified and experimentally verified. The theoretical model identifies the crucial parameters affecting the size of the deposited droplet: the applied pressure, the inner diameter and the wall thickness of the capillary, and the liquid-capillary and the liquid-substrate equilibrium contact angles. Liquid bridge stability diagrams for different liquid-capillary and liquid-substrate equilibrium contact angles are calculated. By varying the applied liquid pressure, three deposition scenarios are theoretically revealed. The comparison of the droplet deposition by using the hollow capillary and the solid rod is discussed. From the liquid bridge model, it is concluded that the liquid bridges can serve as manipulators of small objects laying on the substrate due to

capillary forces. The developed model for the liquid bridge between the capillary and substrate is then tested in micro-scale experiments where water/glycerol solutions of different viscosities are used as the deposition liquid and capillaries of different sizes are employed as dispensing tools. Experimental observations conform well to theoretical predictions. To scale this capillary-based droplet deposition method to the nano-scale, the scanning tunneling microscope is modified by replacing the standard STM tip with the gold-coated nano-capillary. Detailed steps of the nano-capillary fabrication, the liquid insertion into the capillary, and the capillary integration into the STM are shown. While successful nano-scale deposition was not achieved, a detailed discussion of possible reasons is presented.

The third chapter of the dissertation is devoted to the modeling of aerosol flow through a micro-nozzle. Aerosol motion is simulated by using Eulerian-Lagrangian approach: first, the gas flow is modeled separately in ANSYS CFX, and then the Matlab code is written to calculate particles' trajectories and velocities based on given gas flow field. Considering all forces acting on the aerosol particles due to the gas-particle interaction, only Stokes and Saffman forces are found to be valuable; other forces (e.g. Magnus force, Basset force, buoyancy force, pressure gradient force, and virtual mass force) are negligibly small. Since the Saffman force was originally derived for 1D case, the generalization of this force to 2D flow is proposed. The developed model is compared with experiments with simple geometry nozzles: a) linearly-convergent nozzle and b) convergent segment with straight section. The comparison of the simulation results with experimental observations shows that Saffman force should be used in the model with some corrections for the range of parameters used. Based on the established model, two

new nozzle designs are proposed in order to focus and collimate all aerosol particles with size from 1.5 to 5 microns in diameters. One design is created assuming that only Stokes force is acting on aerosol particle; the second design is devoted to the case when both Stokes and Saffman forces are acting on the aerosol particle. Furthermore, it is shown that higher flow rate and high particle density lead to better collimation. Therefore, it would be better to use solid particles for smaller line printing. Collimation of particles with diameters smaller than 1 micron cannot be done, because these particles follow the gas streamlines.

REFERENCES

1. K. K. B. Hon, L. Li and I. M. Hutchings, "Direct writing technology - Advances and developments," CIRP Annals - Manufacturing Technology, Vol. 57, 2008, pp. 601-620.
2. Qian Tang, San-Qiang Shi, “Preparations of gas sensors via dip-pen nanolithography,” Sensors and Actuators B, Vol. 131, 2008, pp. 379-383.
3. Stephan Kramer, Ryan R. Fuierer, and Christopher B. Gorman, “Scanning Probe Lithography Using Self-Assembled Monolayers,” Chem. Rev., Vol. 103, 2003, pp. 4367-4418.
4. Sheehan, P.E. and Whitman L.J., “Thiol diffusion and the role of humidity in “Dip Pen Nanolithography”,” Physical Review Letters, Vol. 88, 2002, pp. 156104-1 - 156104-4.
5. Jason Haaheim, Ray Ebi, Mike Nelson, Joe Fragala, Bjoern Rosner, Hua Zhang, Greg Atas, “Dip Pen Nanolithography (DPN): process and instrument performance with NanoInk’s Nscriptor system,” Ultramicroscopy, Vol. 103, 2005, pp. 117-132.
6. Richard D. Piner, Jin Zhu, Feng Xu, Seunghun Hong, Chad A. Mirkin, “”Dip-Pen” Nanolithography,” Science, Vol. 283, 1999, pp. 661-663.
7. Horacio D. Espinosa, Nicolaie Moldovan, K.-H. Kim, “Novel AFM Nanoprobes,” Chapter from Applied Scanning Probe Methods, Vol. 7: Biomimetics and Industrial Applications, Edited by B. Bhushan and H. Fuchs. Springer-Verlag, Heidelberg 2007.

8. Isabel Nocedal, Horacio Espinosa, Keun-Ho Kim, “Ink Diffusion in Dip-Pen Nanolithography: A Study in the Development of Nano Fountain Probes,” Nanoscape, Vol. 2(1), 2005, pp. 105-111.
9. Keun-Ho Kim, Raymond G. Sanedrin, Andrea M. Ho, Seung W. Lee, Nicolaie Moldovan, Chad A. Mirkin, and Horacio D. Espinosa, “Direct Delivery and Submicrometer Patterning of DNA by a Nanofountain Probe,” Adv. Mater., Vol. 20, 2008, pp. 330-334.
10. Keun-Ho Kim, Nicolaie Moldovan, and Horacio D. Espinosa, “A Nanofountain Probe with Sub-100 nm Molecular Writing Resolution,” Small, Vol. 1(6), 2005, pp. 632-635.
11. Miki Onoue, Hirobumi Ushijima, “Fabrication for metal photomask pattern by using fountain-pen nanolithography,” Microelectronic Engineering, Vol. 87(5-8), 2010, pp. 910-913.
12. Alberto Pique and Douglas B. Chrisey, “Direct-Write Technologies for Rapid Prototyping Applications: Sensors, Electronics, and Integrated Power Sources,” Academic Press, San Diego, CA, USA, 2002.
13. Yan Zhang, Changqing Liu, and David Whalley, “Direct-write Techniques for Maskless Production of Microelectronics: A Review of Current State-of-the-art Technologies,” International Conference on Electronic Packaging Technology & High Density Packaging, 2009, pp. 497-503.
14. http://www.optomec.com/Additive-Manufacturing-Technology/Printed-Electronics, Accessed 10-25-12.

15. J.M. Hoey, A. Lutfurakhmanov, D.L. Schulz, and I.S. Akhatov, "A Review on Aerosol-Based Direct-Write and Its Applications for Microelectronics," Journal of Nanotechnology, Vol. 2012, 2012.

16. I.S. Akhatov, J.M. Hoey, O.F. Swenson, D.L. Schulz, "Aerosol flow through a long micro-capillary: collimated aerosol beam," Microfluid and Nanofluid, Vol. 5, 2008, pp. 215-224.

17. I.S. Akhatov, J.M. Hoey, D. Thompson, A. Lutfurakhmanov, Z. Mahmud, O.F. Swenson, D.L. Schulz, "Aerosol Flow through a Micro-Nozzle," Proc. of ASME 2009 2nd Micro/Nanoscale Heat & Mass Transfer International Conference, December 18-22, 2009.

18. Artur Lutfurakhmanov, "Capillary-based nanolithography: modeling and experiment," Master thesis, 2009.

19. Robert Allan Sailer, "STM-controlled capillary based non-contact material deposition nanolithography", Master thesis, 2007.

20. I. Martinez and A. Eyer, Liquid bridge analysis of silicon crystal growth experiments under microgravity, Journal of Crystal Growth, Vol. 75, 1986, pp. 535-544.

21. L.M. Witkowski and J.S. Walker, Solutocapillary instabilities in liquid bridges, Physics of Fluids, Vol. 14, number 8, 2002, pp. 2647-2656.

22. K. Curran, S. Colin, and L. Baldas, Liquid bridge instability applied to microfluidics, Microfluid Nanofluid, Vol. 1, 2005, pp. 336-345.

23. A. Resnick and J. I. D. Alexander, Plateau tank apparatus for the study of liquid bridges, Rev. Sci. Instrum., Vol. 68(3), 1997, pp. 1495-1500.

24. M.A. Erle, D.C. Dyson, and N.R. Morrow, “Liquid Bridges Between Cylinders, in a Torus, and Between Spheres,” AIChE Journal, Vol. 17(1), 1971, pp. 115-121.

25. David R. Otis, J.R. Ferenc Petac, Zoltan Hantos, Jeffrey J. Fredberg, and Roger D. Kamm, Airway closure and reopening assessed by the alveolar capsule oscillation technique, J. Appl. Physiol., Vol. 80(6), 1996, pp. 2077-2084.

26. M. Johnson, R.G. Kamm, L.W. Ho, A. Shapiro, and T.J. Pedley, The nonlinear growth of surface-tension-driven instabilities of a thin annular film, J. Fluid Mech., Vol. 233, 1991, pp. 141-156.

27. D. Langbein, Fluid static and dynamics in microgravity, J. Phys. Condens. Matter, Vol. 2, 1990, pp. SA491-SA498.

28. J. Plateau, Experimental and theoretical researches on the figures of equilibrium of a liquid mass withdrawn from the action of gravity, Annual Report of the Board of Regents of the Smithsonian Institution, 1863, p. 207.

29. W.B. Haines, Studies in the Physical Properties of Soils. II. A note on the cohesion developed by capillary forces in an ideal soil, J. Agric. Sci., Vol. 15, 1925, pp. 529-535.

30. R.A. Fisher, On the capillary forces in an ideal soil; correction of formulae given by W.B. Haines, J. Agric. Sci., Vol. 16, 1926, pp. 492-505.

31. G. Mason and W.C. Clark, Liquid bridges between spheres, Chemical Engineering Science, Vol. 20, 1965, pp. 859-866.

32. F.M. Orr, L.E. Scriven, and A.P. Rivas, Pendular rings between solids: meniscus properties and capillary force, J. Fluid. Mech., Vol. 67(4), 1975, pp. 723-742.

33. W.C. Clark, J.M. Haynes, and G. Mason, Liquid bridges between a sphere and a plane, Chemical Engineering Science, Vol. 23, 1968, pp. 810-812.

34. I. Martinez, Stability of axisymmetric liquid bridges, Proceeding of the 4th European Symposium on Material Sciences under Microgravity, Madrid, Spain, 1983, pp. 267-273.

35. I. Martinez and J.M. Perales, Liquid bridge stability data, Journal of Crystal Growth, Vol. 78, 1986, pp. 369-378.

36. L.A. Slobozhanin and J.M. Perales, Stability of liquid bridges between equal disks in an axial gravity field, Phys. Fluids A, Vol. 5, 1993, pp. 1305-1314.

37. Lev A. Slobozhanin, J. Iwan D. Alexander, and Andrew H. Resnick, Bifurcation of the equilibrium states of a weightless liquid bridge, Phys. Fluids, Vol. 9(7), 1993, pp. 1893-1905.

38. J. Meseguer, L.A. Slobozhanin, J.M. Perales, A review on the stability of liquid bridges, Adv. Space Res., Vol. 16(5), 1995, pp. 5-14.

39. B. Qian, M. Loureiro, D.A. Gagnon, A. Tripathi, and K.S. Breuer, Micron-Scale Droplet Deposition on a Hydrophobic Surface Using a Retreating Syringe, Physical Review Letters, Vol. 102, 164502, 2009.

40. B. Qian and K.S. Breuer, The motion, stability and breakup of a stretching liquid bridge with a receding contact line, J. Fluid Mech., Vol. 666, 2011, pp. 554-572.

41. S. Cai and B. Bhushan, Meniscus and viscous forces during separation of hydrophilic and hydrophobic smooth/rough surfaces with symmetric and asymmetric contact angles, Phil. Trans. R. Soc. A, Vol. 366, 2010, pp. 1627-1647.

42. Frederick M. Fowkes, “Dispersion Force Contributions to Surface and Interfacial Tensions, Contact Angles, and Heat of Immersion,” Advances in Chemistry Series, 1964, pp. 99-111.

43. Kwok D.Y., Li D., Neumann A.W. “Fowkes’ surface tension component approach revisited,” Colloids and Surfaces A: Physicochemical and Engineering Aspects, Vol. 89, 1994, pp. 181-191.

44. Zisman W.A., “Relation of the Equilibrium Contact Angle to Liquid and Solid Constitution,” Advances in Chemistry Series, 1964, pp. 1-51.

45. Kwok D.Y., Neumann A.W., “Contact angle interpretation in terms of solid surface tension,” Colloids and Surfaces A: Physicochemical and Engineering Aspects, Vol. 161, 2000, pp. 31-48.

46. Janczuk B., Zdziennicka A., “A study on the components of surface free energy of quartz from contact angle measurements,” Journal of Material Science, Vol. 29, 1994, pp. 3559-3564.

47. Natalia T. Correia, Joaquim J. Moura Ramos, Benilde J.V. Saramago, and Jorge C.G. Calado, “Estimation of the surface tension of a solid: application to a liquid crystalline polymer,” Journal of Colloid and Interface Science, Vol. 189, 1997, pp. 361-369.

48. Owens D.K., Wendt R.C., “Estimation of the Surface Free Energy of Polymers,” Journal of Applied Polymer Science, Vol. 13, 1969, pp. 1741-1747.

49. Fowkes F.M., “Attractive forces at interface,” Industrial and Engineering Chemistry, Vol. 56 (12), 1964, pp. 40-52.

50. Li D., and Neumann A.W., "Contact Angles on Hydrophobic Solid Surfaces and Their Interpretation," Journal of Colloid and Interface Science, Vol. 148 (1), 1992, pp. 190-200.

51. Kwok D.Y., "The usefulness of the Lifshitz-van der Waals/acid-base approach for surface tension components and interfacial tensions," Colloids and Surfaces A: Physicochemical and Engineering Aspects, Vol. 156, 1999, pp. 191-200.

52. John C. Berg, "Wettability," New York-Basel-Hong Kong, 1993.

53. J.B. Segur and H.E. Oberstar, Viscosity of Glycerol and Its Aqueous Solutions, Industrial and Engineering Chemistry, Vol. 43(9), 1951, pp. 2117-2120.

54. C. Tropea, A. Yarin, and J.F. Foss, Springer Handbook of Experimental Fluid Mechanics, 2007.

55. Y. Wang, A. Lutfurakhmanov, and I.S. Akhatov, Spectral boundary element method for liquid bridge dynamics between capillary and substrate, Proceedings of ASME 2011 International Mechanical Engineering Congress & Exposition, November 11-17, 2011.

56. Y. Wang, A. Lutfurakhmanov, and D.L. Schulz, Bridge dynamics for the capillary-based deposition, Proceedings of ASME 2012 International Mechanical Engineering Congress & Exposition, November 9-15, 2012.

57. A. Lutfurakhmanov, R. Sailer, G. Loken, A. Kohut, Y. Wang, A. Voronov, D.L. Schulz, and I.S. Akhatov, Liquid Deposition at Micro and Nanoscale, Proceedings of ASME 2010 3rd Joint US-European Fluids Engineering Summer Meeting and 8th International Conference on Nanochannels, Microchannels, and Minichannels, August 2-4, 2010.

58. A. Lutfurakhmanov, G. Loken, D.L. Schulz, and I.S. Akhatov, Capillary-Based Liquid Microdroplet Deposition, Applied Physics Letters, Vol. 97, 124107, 2010.

59. Krastanka G. Marinova, Diana Christova, Slavka Tcholakova, Evtim Efremov, and Nikolai D. Denkov, "Hydrophobization of Glass Surface by Adsorption of Poly(dimethylsiloxane)," Langmuir, Vol. 21, 2005, pp. 11729-11737.

60. Peng Jiang, Shun-Yu Li, Hiroyuki Sugimura, Osamu Takai, "Pattern design in large area using octadecyltrichlorosilane self-assembled monolayers as resist material," Applied Surface Science, Vol. 252, 2006, pp. 4230-4235.

61. Lutfurakhmanov A., Sailer R., Akhatov I., Schulz D.L., "Quick "easy?!" determination of the diameter of nanocapillaries", Nanotech 2007 Conference Proceedings, Vol. 3, 2007, pp. 344-347.

62. Hofer W.A., Foster A.S., Shluger A.L., Rev. Mod. Phys., Vol. 75, 2003, pp. 1287.

63. He J., Sankey O., Lee M., Tao N., Li X., Lindsay S., Faraday Discuss., Vol. 131, 2006, pp. 145.

64. http://www.ntmdt.com/data/media/files/spm_basics/observed_physical_quantities_in_stm.pdf, "Observed" Physical Quantities in STM, Accessed 10-25-12.

65. Simmons J.G., "Generalized Formula for the Electric Tunnel Effect between Similar Electrodes Separated by a Thin Insulating Film," J. Appl. Phys., Vol. 34(6), 1963, pp. 1793-1803.

66. Sridhar Hari, Yassin A. Hassan, Andrew R. McFarland, "Aerodynamic Focusing Effect in a Rectangular Slit Real Impactor at Different Reynolds Numbers," Part. Part. Syst. Charact., Vol. 23, 2006, pp. 457-467.

67. Cheng-Hsiung Huang and Chuen-Jinn Tsai, “Influence of Impaction Plate Diameter and Particle Density on the Collection Efficiency of Round-Nozzle Inertial Impactors,” Aerosol Science and Technology, Vol. 36, 2002, pp. 714-720.

68. Sridhar Hari, Y.A. Hassan, A.R. McFarland, “Computational Fluid Dynamics Simulation of a Rectangular Slit Real Impactor’s Performance,” Nuclear Engineering and Design, Vol. 235, 2005, pp. 1015-1028.

69. Virgil A. Marple and Benjamin Y. H. Liu, “Characteristics of Laminar Jet Impactors,” Environmental Science and Technology, Vol. 8(7), 1974, pp. 648-654.

70. Daniel J. Rader and Virgil A. Marple, “Effect of Ultra-Stokesian Drag and Particle Interception on Impaction Characteristics,” Aerosol Science and Technology, Vol. 4, 1985, pp. 141-156.

71. Matt Frain, David P. Schmidt, Yong-Le Pan, and Richard K. Chang, “Selective Deflection and Localization of Flowing Aerosols onto a Substrate,” Aerosol Science and Technology, Vol. 40, 2006, pp. 218-225.

72. Rensheng Deng, Xuefeng Zhang, Kenneth A. Smith, Joda Wormhoudt, David K. Lewis, and Andrew Freedman, “Focusing Particles with Diameters of 1 to 10 Microns into Beams at Atmospheric Pressure,” Aerosol Science and Technology, Vol. 42, 2008, pp. 899-915.

73. Yong-Le Pan, John Bowersett, Steven C. Hill, Ronald G. Pinnick, and Richard K. Chang, “Nozzles for Focusing Aerosol Particles,” Army Research Laboratory, 2009, pp. 1-14.

74. Yong-Le Pan, Patrick J. Cobler, Scott A. Rhodes, Justin Halverson, and Richard K. Chang, “Separating hazardous aerosols from ambient aerosol: role of fluorescence-

spectral determination, aerodynamic deflector and pulse aerodynamic localizer (PAL)," Proc. of SPIE, Vol. 5990, pp. 5990Y-1-5990Y-6, 2005.

75. ANSYS CFX-Solver Theory Guide.

76. Sukbeom You and Mansoo Choi, "Numerical simulation of microscopic motion and deposition of nanoparticles via electrodynamic focusing," Aerosol Science, Vol. 38, 2007, pp. 1140-1149.

77. J.S. Marshall, "Discrete-element modeling of particulate aerosol flow," Journal of Computational Physics, Vol. 228, 2009, pp. 1541-1561.

78. Odar, F. and Hamilton, W. S., "Forces on a Sphere Accelerating in a Viscous Fluid," J. Fluid Mech., Vol. 18, 1964, pp. 302-314.

79. Kim, I., Elghobashi, S., and Sirignano, W. A., "On the Equation for Spherical-Particle Motion: Effect of Reynolds and Acceleration Numbers," J. Fluid Mech., Vol. 367, 1998, pp. 221-253.

80. C. Crowe, M. Sommerfield, and Y. Tsuji, "Multiphase flows with droplets and particles," CRC Press, 1998.

81. Jingyu Ran, Li Zhang, Qiang Tang, Mingdao Xin, "Numerical Simulation of the Particle Motion Characteristics in Boundary Layer of Gas-Solid Rotary Flow," Journal of Fluids Engineering, Vol. 128, 2006, pp. 596-601.

82. P.G. Saffman, The Lift on a Small Sphere in a Slow Shear Flow, Journal of Fluid Mechanics, Vol. 22, 1965, pp. 385-400; Corrigendum, Journal of Fluid Mechanics, Vol. 31, 1968, p. 624.

83. R. W. Johnson, "The handbook of fluid dynamics," Washington D.C., CRC Press, 1998.

84. R. Clift, J.R. Grace, and M.E. Weber, “Bubbles, Drops, and Particles,” Vol. 3, Academic Press, New York, NY, USA, 1978.

85. E.H. Kennard, “Kinetic theory of gases, with an introduction to statistical mechanics,” McGraw-Hill Book Company, Inc., 1938.

86. R.C. Read and T.K. Sherwood, “The properties of gases and liquids,” McGraw-Hill Book Company, Inc., 1958.

87. Carlos F.M. Coimbra and Marcelo H. Kobayashi, On the viscous motion of a small particle in a rotating cylinder, Journal of Fluid Mechanics, Vol. 469, 2002, pp. 257-286.

88. D.S. Dandy and H.A. Dwyer, “A sphere in shear flow at finite Reynolds number: effect of shear on particle lift, drag, and heat transfer,” J. Fluid Mech., Vol. 216, 1990, pp. 381-410.

89. J.B. McLaughlin, “Inertial migration of a small sphere in linear shear flows,” J. Fluid Mech., Vol. 224, 1991, pp. 261-274.

90. R. Mei, “An approximate expression for the shear lift force on a spherical particle at finite Reynolds number,” Int. J. Multiphase Flow, Vol. 18(1), 1992, pp. 145-147.

91. Z. Mahmud, J.M. Hoey, A. Lutfurakhmanov, J. Daugs, O.F. Swenson, D.L. Schulz, and I.S. Akhatov, “Experimental Characterization of Aerosol Flow Through a Micro Capillary,” Proceedings of ASME 2010 3rd Joint US-European Fluids Engineering Summer Meeting and 8th International Conference on Nanochannels, Microchannels, and Minichannels, August 2-4, 2010.

92. Michael Robinson, “Experimental Characterization of Aerosol Flow through Micro-Capillaries,” Master thesis, 2012.

APPENDIX. ANSYS CFX PARAMETERS AND MATLAB CODE TO CALCULATE VELOCITIES AND TRAJECTORIES OF AEROSOL PARTICLES

1. Geometry and Mesh Creation in ANSYS CFX

The following steps are needed in order to create the nozzle geometry and mesh using ANSYS CFX:

- Create points: Geometry → Create Point → Explicit coordinates
    - (0.0; 0.0; 0.0)
    - (0.0; 0.00041; 0.0)
    - (0.01905; 0.0; 0.0)
    - (0.01905; 0.00011; 0.0)
    - (0.01905; 0.00075; 0.0)
    - (0.01905; 0.00100; 0.0)
    - (0.02405; 0.0; 0.0)
    - (0.02405; 0.00011; 0.0)
    - (0.02405; 0.00075; 0.0)
    - (0.02405; 0.00100; 0.0)
- Create edges: Geometry → Create/Modify Curve → From Points (choose appropriate points)
- Create surfaces: Geometry → Create/Modify Surface → Surface of revolution (choose appropriate lines)
- Create surfaces: Geometry → Create/Modify Surface → Simple surface (choose appropriate 4 lines, tolerance=10^{-7})

- Make parts of POINTS, CURVES, INLET, WALL, WALL2, OPEN1, OPEN2, OPEN3, SYM1, SYM2: Part → Create Part
- Blocking → Create Block
- Blocking → Split Block into parts (converging, exit area, etc.)
- Blocking → Merge Vertices → Check only **Merge to averag**e and choose the vertices close to rotation axis
- Blocking → Associate → Associate Edge to Curve (choose appropriate edges and curves)
- Blocking → Move vertices
- Blocking → Pre-mesh Params → Edge Params: (set number on nodes)
- Blocking → Pre-mesh Params → Update Sizes
- Pre-Mesh → Convert to Unstruct Mesh
- Output → Select Solver → Output Solver: ANSYS CFX
- Output → Select Solver → Common structural solver: ANSYS
- Output → Write input.

2. ANSYS CFX Modeling Parameters

To calculate the gas velocity and density inside and outside of the nozzle using ANSYS CFX, the following parameters should be set:

- Simulation
  - Simulation Type Option: Steady state
  - Domain Type: Fluid Domain
  - Fluid list: N2 ideal gas

- Domain Models → Pressure → Reference Pressure: 1 [atm]
- Domain Models → Buoyancy Option: Non Buoyant
- Domain Models → Domain Motion Option: Stationary
- Domain Models → Mesh Deformation Option: None
- Fluid models → Heat Transfer Option: Total Energy
- Fluid models → Turbulence Option: None (Laminar)

➢ Boundary conditions

- Inlet → Flow Regime Option → Subsonic
- Inlet → Mass and Momentum Option →
    - Velocity field: U=3.6787[m/s]*(1-y*y/(0.000416[m]*0.000416[m]))
    - Mass flow rate: 1.5909722×10^{-8} kg/s=10^{-6} m^3/s*1.145 kg/m^3*5°/360°
- Inlet → Heat Transfer Option → Static temperature: 25 C
- Open → Flow Regime Option → Subsonic
- Open → Mass and Momentum Option → Static Pres. (Entrain): 0 Pa
- Open → Heat Transfer Option → Static temperature: 25 C
- Symmetry → Choose Two symmetry planes
- Wall → Wall Influence On Flow Option: No slip
- Wall → Heat Transfer Option → Temperature: 25 C

➢ Run parameters

- Convergence criteria: 10^{-6}
- Max iteration: 500.

3. Data Export from ANSYS CFX

The following steps are required in order to export the gas flow data from ANSYS CFX into Matlab:

- Open the results file (*.res) in CFX-Post
- Go to File→Export: the export window will show up
- Give a file name in File field
- Select only the following variables:
    - Density
    - Pressure.Gradient X
    - Velocity u
    - Velocity u.Gradient X
    - Velocity u.Gradient Y
    - Velocity v
    - Velocity v.Gradient X
    - Velocity v.Gradient Y
- Click on Formatting tab
    - Choose proper precision (5)
    - Space should be selected as separator
- Click: Save.

4. Matlab Code

To calculate particles' velocities and trajectories, the following Matlab code should be used:

```
clear all;
clc
global FstU FstV FsaffU FsaffV a rop

%fid = fopen('415_110_132_132_L_12_Q_60.csv'); %
%fid = fopen('415_110_132_132_L_12_Q_120.csv'); %
fid = fopen('415_110_132_132_L_12_Q_180.csv'); %
C = textscan(fid, '%f %f %f %f %f %f %f %f %f %f %f %f %f %f');    % data
file reading
X =    C{1};           % X coordinate
Y =    C{2};           % Y coordinate
ZZ =   C{3};           % X coordinate
rho =  C{4};         % density
pr_grX=C{5};
U =    C{6};         % U component of velocity
dUdX = C{7};         % dU/dx
dUdY = C{8};         % dU/dy
V =    C{9};         % V component of velocity
dVdX = C{10};         % dV/dx
dVdY = C{11};        % dV/dy
fclose(fid);         % data file closing
[M,N] = size(X);     % define the size of arrays

%$$$$$$$$$$$$$$$$$$$$$$$$$$$$$$$$$$$$$$$$$$$$$$$
%$$$$$$$$$$$$$$$$$$$$$$$$$$$$$$$$$$$$$$$$$$$$$$$
% geometry of the nozzle and particle size should be revised each time
Rin = 0.000415;   % inlet radius of converging nozzle
Rout = 0.000110;  % outlet radius of converging nozzle
L1   = 0.01905;   % length of converging part

Rout2 = 0.000132;   % radius of straight capillary
L2   = 0.01214;       % length of straight part

Lend = 0.03619;          % total length of the nozzle
(Lconv+Lcapillary+Lplenum)
Lstop = 0.03617;           % length where calculation will stop
thresh = Rout/300;
Lexit = 0.03119;         % length where the nozzle exit results will be
shown

tanl1 = (Rin-Rout)/(L1);  % tangent
alfa1 = atan(tanl1);      % alfa

mu = 1.77*10^(-5);       % viscosity of gas
a = 3.8*10^(-6)/2;       % particle radius
a = 1.88*10^(-6)/2;       % particle radius
%a = 2.5*10^(-6)/2;
```

```
RHOgiven=1.14;          % gas density to initiate calculation
rop = 10000;
%rop = 2648;
rop = 1800; % rop is particle density
%rop = 1100;
Qgas  = 115.0*10^(-6)/60.0; % Q is inlet flow rate to initiate
Qgas  = 50.0*10^(-6)/60.0;
%Qgas  = 115.0*10^(-6)/60.0;
Ureal = 2*Qgas/(pi()*Rin^2);
%$$$$$$$$$$$$$$$$$$$$$$$$$$$$$$$$$$$$$$$$$$$$$$$$$$$$$$$$
%$$$$$$$$$$$$$$$$$$$$$$$$$$$$$$$$$$$$$$$$$$$$$$$$

%%%%%%%%%%%%%%%%%%%%%%%%%%%%%%%%%%%%%%%%
ndensity = 6.02*10^23*RHOgiven/(28*10^(-3));
sigma = 0.375*10^(-9);
meanfreepath = 1/(2^0.5*3.14*ndensity*sigma^2);
cpeed = 353;
Knp = meanfreepath/(2*a);
%%%%%%%%%%%%%%%%%%%%%%%%%%%%%%%%%%%%%%%%

nparticle = 50; % number of particles

Xar = zeros(nparticle,9000);
Yar = zeros(nparticle,9000);
Uar = zeros(nparticle,9000);
Var = zeros(nparticle,9000);

Ugas = zeros(nparticle,9000);
Vgas = zeros(nparticle,9000);

Fstok = zeros(nparticle,9000);
FstokU = zeros(nparticle,9000);
FstokV = zeros(nparticle,9000);

Fsaff = zeros(nparticle,9000);
FsaffUU = zeros(nparticle,9000);
FsaffVV = zeros(nparticle,9000);

Fgrav = zeros(nparticle,9000);
Fbass = zeros(nparticle,9000);

Fmagn = zeros(nparticle,9000);
FmagnU = zeros(nparticle,9000);
FmagnV = zeros(nparticle,9000);

Fpres = zeros(nparticle,9000);

Fvirt = zeros(nparticle,9000);
FvirtU = zeros(nparticle,9000);
FvirtV = zeros(nparticle,9000);
```

```
Rwall = zeros(nparticle,9000);
ReS = zeros(nparticle,9000);
ReG = zeros(nparticle,9000);
ALF = zeros(nparticle,9000);
Cor = zeros(nparticle,9000);
CS_EPS = zeros(nparticle,9000);
COR_MC = zeros(nparticle,9000);


njp = zeros(1,nparticle);
PYAR = zeros(nparticle,17);
NDAR = zeros(nparticle,17);
OLDNDAR = zeros(nparticle,17);
OLDPYAR = zeros(nparticle,17);
YYAR = zeros(nparticle,17);
UUAR = zeros(nparticle,17);
VVAR = zeros(nparticle,17);
RPOSITION = zeros(1,nparticle);
RDIAMETER = zeros(1,nparticle);
% RPOSITION = [25*10^(-6);25*10^(-6);25*10^(-6);25*10^(-6);25*10^(-6);...
%              75*10^(-6);75*10^(-6);75*10^(-6);75*10^(-6);75*10^(-6);
...
%              125*10^(-6);125*10^(-6);125*10^(-6);125*10^(-6);125*10^(-
6);...
%              175*10^(-6);175*10^(-6);175*10^(-6);175*10^(-6);175*10^(-
6);...
%              225*10^(-6);225*10^(-6);225*10^(-6);225*10^(-6);225*10^(-
6)];
% RDIAMETER = [2.25*10^(-6); 1.75*10^(-6); 1.25*10^(-6); 0.75*10^(-6);
0.55*10^(-6);...
%              2.25*10^(-6); 1.75*10^(-6); 1.25*10^(-6); 0.75*10^(-6);
0.55*10^(-6);...
%              2.25*10^(-6); 1.75*10^(-6); 1.25*10^(-6); 0.75*10^(-6);
0.55*10^(-6);...
%              2.25*10^(-6); 1.75*10^(-6); 1.25*10^(-6); 0.75*10^(-6);
0.55*10^(-6);...
%              2.25*10^(-6); 1.75*10^(-6); 1.25*10^(-6); 0.75*10^(-6);
0.55*10^(-6)];

%RPOSITION = [25*10^(-6); 75*10^(-6); 125*10^(-6); 175*10^(-6); 225*10^(-
6)];
%RDIAMETER = [2.25*10^(-6); 1.75*10^(-6); 1.25*10^(-6); 0.75*10^(-6);
0.55*10^(-6)];
NDENSITY = [100; 80; 70; 40; 10];



for iparticle = 1:nparticle
    xgiven = 2*10^(-5); %0.009525;  % set the current position of x
    %xgiven = 6.86*10^(-3); % Q = 115 ccm new IC
    %xgiven = 0.01905; %   #2 Q = 87.5 ccm

    %$$$$$$$$$$$$$$$$$$$$$$$$$$$$$$$$$$$$$$$$$$$$
    % y given is initial particle location based on the inlet condition
```

```
    ygiven = (Rin*0.3125)*iparticle/nparticle; % Q = 164 ccm
    ygiven = (Rin*0.4000)*iparticle/nparticle; % Q = 115 ccm
    ygiven = (Rin*0.5000)*iparticle/nparticle; % Q = 115 ccm
    %ygiven = (Rin*0.3750)*iparticle/nparticle; % Q = 55 ccm
    %ygiven = (0.000617*0.3750/2)*iparticle/nparticle; % Q = 115 ccm new
IC
    %ygiven = (Rin*0.99)*iparticle/nparticle; % Q = 164 ccm
    %ygiven = (Rin*0.63)*iparticle/nparticle; % Q = 115 ccm
    %ygiven = (Rin*0.5)*iparticle/nparticle; % Q = 164 ccm
%     if (iparticle == 1)
%         ygiven = (Rin*0.99)*1/70; % Q = 164 ccm
%     end;
%      if (iparticle == 10)
%         ygiven = (Rin*0.99)*100/100; % Q = 164 ccm
%     end;
    %ygiven = Rin*0.6+Rin*0.3*(iparticle-1)/(nparticle-1); % Q = 164 ccm

    %ygiven = Rin*0.50; % Q = 55 ccm
    %a = RDIAMETER(iparticle);
    RDIAMETER(iparticle)=a*2.0*10^6;
    RPOSITION(iparticle)=ygiven*10^6;

    YYAR(iparticle,1)=ygiven;
    PYAR(iparticle,1)=ygiven;
    % parabolic intensity profile is introduced here
    NDAR(iparticle,1:17)=-6.091*10^7*ygiven*ygiven+1.0; % Q = 164 ccm
    NDAR(iparticle,1:17)=-3.718*10^7*ygiven*ygiven+1.0; % Q = 115 ccm
    NDAR(iparticle,1:17)=-2.323*10^7*ygiven*ygiven+1.0; % Q = 115 ccm
    %NDAR(iparticle,1:17)=-4.444*10^7*ygiven*ygiven+1.0; % Q = 55 ccm
    %NDAR(iparticle,1:17)=-7.471*10^7*ygiven*ygiven+1.0; % Q = 115 ccm
new IC
    %NDAR(iparticle,1:17)=-6.069*10^6*ygiven*ygiven+1.0; % Q = 164 ccm
    %NDAR(iparticle,1:17)=-1.498*10^7*ygiven*ygiven+1.0; % Q = 115 ccm
    %NDAR(iparticle,1:17)=-2.379*10^7*ygiven*ygiven+1.0; % Q = 164 ccm
    %NDAR(iparticle,1:17)=-2.65*10^8*(ygiven-0.75*Rin)^2+1.0; % Q = 164
ccm

    xfocus = Rin*L1/(Rin-Rout);
    cos1 = xfocus/sqrt(ygiven^2.0+xfocus^2.0);
    sin1 = ygiven/sqrt(ygiven^2.0+xfocus^2.0);

    Upart =  0.99*Ureal*(1-ygiven^2/Rin^2)*cos1;
    Vpart = -0.99*Ureal*(1-ygiven^2/Rin^2)*sin1;
    UUAR(iparticle,1)=Upart;
    VVAR(iparticle,1)=Vpart;
    %Upart =  72*(1-ygiven^2/Rout^2);        % #2 Q = 87.5 ccm
    %Vpart = -72*(1-ygiven^2/Rout^2)*0.0;    % #2 Q = 87.5 ccm

    %Upart = 0.0;
    %Vpart = 0.0;

    Ugiven = Ureal*(1-ygiven^2/Rin^2);
    Vgiven = 0;
```

```
    Xar(iparticle,1)=xgiven;
    Yar(iparticle,1)=ygiven;
    Uar(iparticle,1)=Upart;
    Var(iparticle,1)=Vpart;
    Ugas(iparticle,1)=Upart;
    Vgas(iparticle,1)=Vpart;
    Rwall(iparticle,1)=0.000409;

    j=1;
    flag = 0;
    flagend = 0;

    while ((j < 9000) && (flag == 0))
        %tic;
        number = 0;         % number of points close to
Point(xgiven,ygiven)
        kl = 0;
        clear nxy nxyorg norg final myindexX myindexY;
        Ugivenold = Ugiven;
        Vgivenold = Vgiven;

        %$$$$$$$$$$$$$$$$$$$$$
        %$$$$$$$$$$$$$$$$$$$$$
        % mesh size should be properly inserted here
        % delta x is the x distance between neighbor nodes
        % delta y is the y distance between neighbor nodes
        if (xgiven>(L1+L2))
            deltax = L1/570;
            deltay = Rout2/132;
            Rwall(iparticle,j+1) = 0;
        end;

        if (xgiven>L1)&&(xgiven<=(L1+L2))      % set the x and y
distances between  nodes
            deltax = L1/570;
            deltay = Rout2/132;
            Rwall(iparticle,j+1) = Rout2;
        end;

        if (xgiven<=L1)      % set the x and y distances between  nodes
            deltax = L1/570; %500/1.2;
            deltay = (Rout+(L1-xgiven)*tanl1)/132;%200/1.2
            Rwall(iparticle,j+1) = (Rout+(L1-xgiven)*tanl1);
        end;
        %$$$$$$$$$$$$$$$$$$$$$$$$$$

        % find 8 nodes where Point(xgiven,ygiven) is placed
        % we have 8 points due to symmerty (4*2 = 8)
        %     for k = 1:M
        %         if ((abs(X(k)-xgiven)<deltax)&&(abs(Y(k)-
ygiven)<deltay))%0.0000005)%0.0000381)
        %           number = number+1;
        %           nxy(number) = k;
        %         end;
        %     end;
```

```
        %time1(j)=toc;
        %tic;

        MATX = abs(X-xgiven);
        MATY = abs(Y-ygiven);
        myindexX = find(MATX<=deltax);
        myindexY = find(MATY<=deltay);
        [ninX,minX] = size(myindexX);
        [ninY,minY] = size(myindexY);
        kl = 0;
        for k1 = 1:ninX
            for k2 = 1:ninY
                if (myindexX(k1,1)==myindexY(k2,1))
                    kl=kl+1;
                    final(kl)=myindexX(k1,1);
                end;
            end;
        end;
        number = kl;
        nxy = final;

        % remove 4 points from 8 which repeat due to symmetry
        nxyorg(1) = nxy(1);
        norg(1) = nxy(1);
        numberorg = 1;
        for i = 1:number-1
            if (X(nxy(i))==X(nxy(i+1)))&&(Y(nxy(i))==Y(nxy(i+1)))
                nxyorg(i+1) = 0;
            else
                numberorg = numberorg + 1;
                norg(numberorg) = nxy(i+1);
                nxyorg(i+1) = nxy(i+1);
            end;
        end;
        % reorganize 4 last points counterclockwise for interpolation
        [MORG,NORG] = size(norg);
        if (NORG==4)
            NX(1) = X(norg(2));
            NX(2) = X(norg(4));
            NX(3) = X(norg(3));
            NX(4) = X(norg(1));
            NY(1) = Y(norg(2));
            NY(2) = Y(norg(4));
            NY(3) = Y(norg(3));
            NY(4) = Y(norg(1));

            %if ((NX(1)~=NX(2))&(NY(1)~=NY(4))&(NY(2)~=NY(3)))
            if ((abs(NX(1)-NX(2))>10^(-5))&(abs(NX(1)-NX(3))>10^(-
5))&(abs(NX(2)-NX(4))>10^(-5))&(abs(NY(1)-NY(4))>10^(-7))&(abs(NY(2)-
NY(3))>10^(-7)))
                % shape functions are calculated
                psi1 = (xgiven-NX(2))*(ygiven-NY(4))/((NX(1)-
NX(2))*(NY(1)-NY(4)));
                psi2 = (xgiven-NX(1))*(ygiven-NY(3))/((NX(2)-
NX(1))*(NY(2)-NY(3)));
```

```
                psi3 = (xgiven-NX(1))*(ygiven-NY(2))/((NX(3)-
NX(1))*(NY(3)-NY(2)));
                psi4 = (xgiven-NX(2))*(ygiven-NY(1))/((NX(4)-
NX(2))*(NY(4)-NY(1)));
            else
                psi1 = 1;
                psi2 = 0;
                psi3 = 0;
                psi4 = 0;

            end;

                % U,V,dU/dx,dU/dy,dV/dx/dV/dy are calculated in point
(xgiven,yviven)
            RHOgiven =
rho(norg(2))*psi1+rho(norg(4))*psi2+rho(norg(3))*psi3+rho(norg(1))*psi4;
            Ugiven =
U(norg(2))*psi1+U(norg(4))*psi2+U(norg(3))*psi3+U(norg(1))*psi4;
            Vgiven =
V(norg(2))*psi1+V(norg(4))*psi2+V(norg(3))*psi3+V(norg(1))*psi4;
            dUdXgiven =
dUdX(norg(2))*psi1+dUdX(norg(4))*psi2+dUdX(norg(3))*psi3+dUdX(norg(1))*ps
i4;
            dUdYgiven =
dUdY(norg(2))*psi1+dUdY(norg(4))*psi2+dUdY(norg(3))*psi3+dUdY(norg(1))*ps
i4;
            dVdXgiven =
dVdX(norg(2))*psi1+dVdX(norg(4))*psi2+dVdX(norg(3))*psi3+dVdX(norg(1))*ps
i4;
            dVdYgiven =
dVdY(norg(2))*psi1+dVdY(norg(4))*psi2+dVdY(norg(3))*psi3+dVdY(norg(1))*ps
i4;
            PrGrX   =
pr_grX(norg(2))*psi1+pr_grX(norg(4))*psi2+pr_grX(norg(3))*psi3+pr_grX(nor
g(1))*psi4;
        end;

        if (NORG==3)
            NX(1) = X(norg(1));
            NX(2) = X(norg(2));
            NX(3) = X(norg(3));
            NY(1) = Y(norg(1));
            NY(2) = Y(norg(2));
            NY(3) = Y(norg(3));

            % shape functions are calculated
             %if ((NY(1)~=NY(2))&(NY(1)~=NY(3))&(NY(2)~=NY(3)))
             if ((abs(NY(1)-NY(2))>10^(-7))&(abs(NY(1)-NY(3))>10^(-
7))&(abs(NY(2)-NY(3))>10^(-7)))
                psi1 = (ygiven-NY(2))*(ygiven-NY(3))/((NY(1)-
NY(2))*(NY(1)-NY(3)));
                psi2 = (ygiven-NY(1))*(ygiven-NY(3))/((NY(2)-
NY(1))*(NY(2)-NY(3)));
                psi3 = (ygiven-NY(1))*(ygiven-NY(2))/((NY(3)-
NY(1))*(NY(3)-NY(2)));
```

```
             else
                 psi1=1;
                 psi2=0;
                 psi3=0;
             end

            % U,V,dU/dx,dU/dy,dV/dx/dV/dy are calculated in point
(xgiven,yviven)
            RHOgiven =
rho(norg(1))*psi1+rho(norg(2))*psi2+rho(norg(3))*psi3;
            Ugiven = U(norg(1))*psi1+U(norg(2))*psi2+U(norg(3))*psi3;
            Vgiven = V(norg(1))*psi1+V(norg(2))*psi2+V(norg(3))*psi3;
            dUdXgiven =
dUdX(norg(1))*psi1+dUdX(norg(2))*psi2+dUdX(norg(3))*psi3;
            dUdYgiven =
dUdY(norg(1))*psi1+dUdY(norg(2))*psi2+dUdY(norg(3))*psi3;
            dVdXgiven =
dVdX(norg(1))*psi1+dVdX(norg(2))*psi2+dVdX(norg(3))*psi3;
            dVdYgiven =
dVdY(norg(1))*psi1+dVdY(norg(2))*psi2+dVdY(norg(3))*psi3;
            PrGrX   =
pr_grX(norg(1))*psi1+pr_grX(norg(2))*psi2+pr_grX(norg(3))*psi3;
        end;

        if (NORG>=5)
            NX(1) = X(norg(1));
            NX(2) = X(norg(2));
            NY(1) = Y(norg(1));
            NY(2) = Y(norg(2));

            % shape functions are calculated
            %if (NY(1)~=NY(2))
            if (abs(NY(1)-NY(2))>10^(-7))
                psi1 = (ygiven-NY(2))/(NY(1)-NY(2));
                psi2 = (ygiven-NY(1))/(NY(2)-NY(1));
            else
                psi1 = 1;
                psi2 = 0;
            end;

            % U,V,dU/dx,dU/dy,dV/dx/dV/dy are calculated in point
(xgiven,yviven)
            RHOgiven = rho(norg(1))*psi1+rho(norg(2))*psi2;
            Ugiven = U(norg(1))*psi1+U(norg(2))*psi2;
            Vgiven = V(norg(1))*psi1+V(norg(2))*psi2;
            dUdXgiven = dUdX(norg(1))*psi1+dUdX(norg(2))*psi2;
            dUdYgiven = dUdY(norg(1))*psi1+dUdY(norg(2))*psi2;
            dVdXgiven = dVdX(norg(1))*psi1+dVdX(norg(2))*psi2;
            dVdYgiven = dVdY(norg(1))*psi1+dVdY(norg(2))*psi2;
            PrGrX   = pr_grX(norg(1))*psi1+pr_grX(norg(2))*psi2;
        end;

        if (NORG==2)
            NX(1) = X(norg(1));
            NX(2) = X(norg(2));
```

```
            NY(1) = Y(norg(1));
            NY(2) = Y(norg(2));

            % shape functions are calculated
            %if (NY(1)~=NY(2))
            if (abs(NY(1)-NY(2))>10^(-7))
                psi1 = (ygiven-NY(2))/(NY(1)-NY(2));
                psi2 = (ygiven-NY(1))/(NY(2)-NY(1));
            else
                psi1 = 1;
                psi2 = 0;
            end;
            % U,V,dU/dx,dU/dy,dV/dx/dV/dy are calculated in point
(xgiven,yviven)
            RHOgiven = rho(norg(1))*psi1+rho(norg(2))*psi2;
            Ugiven = U(norg(1))*psi1+U(norg(2))*psi2;
            Vgiven = V(norg(1))*psi1+V(norg(2))*psi2;
            dUdXgiven = dUdX(norg(1))*psi1+dUdX(norg(2))*psi2;
            dUdYgiven = dUdY(norg(1))*psi1+dUdY(norg(2))*psi2;
            dVdXgiven = dVdX(norg(1))*psi1+dVdX(norg(2))*psi2;
            dVdYgiven = dVdY(norg(1))*psi1+dVdY(norg(2))*psi2;
            PrGrX   = pr_grX(norg(1))*psi1+pr_grX(norg(2))*psi2;
        end;


        Ugas(iparticle,j+1)=Ugiven;
        Vgas(iparticle,j+1)=Vgiven;

        if (Ugiven~=Upart)
            al = atan((Vgiven-Vpart)/(Ugiven-Upart));
        else
            al = 0;
        end;

        if (Ugiven<Upart)
            al = al+pi;
        end;

        B = -dUdXgiven*sin(al)*cos(al)+dUdYgiven*cos(al)*cos(al)-
dVdXgiven*sin(al)*sin(al)+dVdYgiven*sin(al)*cos(al);

        %%%%%%%%%%%%%%%%%%%%%%
        %%%%%%%%%%%%%%%%%%%%
        Rep = 2*a*RHOgiven*sqrt((Ugiven-Upart)^2+(Vgiven-Vpart)^2)/mu;
        maxp = sqrt((Ugiven-Upart)^2+(Vgiven-Vpart)^2)/cpeed;
        Ref = a^2*RHOgiven*abs(B)/(mu);
        Cor_St = 1;
        Cor_Kn = 1;
        Cor_Sa = 1;
        if (Rep~=0)
           Cor_St = (1+Rep^(2/3)/6)*(1+exp(-0.427/maxp^4.63-3/Rep^0.88));
        end;
        Cor_Kn = 1+Knp*(2.57+0.68*exp(-1.86/Knp));
        %Cor_Sa = (Cor_St/Cor_Kn)^2;
```

```
        if ((Rep>=0.1)&&(Rep<=40))
           Cor_Sa = 0.23434*(1-exp(-0.1*Rep))*(Ref/Rep)^0.5+exp(-
0.1*Rep);
        end;
        if ((Rep>40)&&(Rep<=100))
           Cor_Sa = 0.0371*Ref^0.5;
        end;
        %%%%%%%%%%%%%%%%%%%%%%%
        %%%%%%%%%%%%%%%%%%%%%%%

        % Stokes formula in Akhatov's paper
        FstU = 1.0*(Cor_St/Cor_Kn)*6.0*pi*a*mu*(Ugiven-Upart);
        FstV = 1.0*(Cor_St/Cor_Kn)*6.0*pi*a*mu*(Vgiven-Vpart);

        % Stokes correction by Schiller and Nauman
        %FstU = (1.0+0.15*Rep^0.687)*6.0*pi*a*mu*(Ugiven-Upart);
        %FstV = (1.0+0.15*Rep^0.687)*6.0*pi*a*mu*(Vgiven-Vpart);

        FsaffU = 0; %6.46*a*a*sqrt((Ugiven-Upart)^2+(Vgiven-
Vpart)^2)*sqrt(RHOgiven*mu*abs(B))*sign(B)*sin(al);
        FsaffV = 0; %6.46*a*a*sqrt((Ugiven-Upart)^2+(Vgiven-
Vpart)^2)*sqrt(RHOgiven*mu*abs(B))*sign(B)*cos(al);


        ReS(iparticle,j) = 2.0*a*sqrt((Ugiven-Upart)^2+(Vgiven-
Vpart)^2)*RHOgiven/mu;
        ReG(iparticle,j) = abs(B)*4.0*a*a*RHOgiven/mu;
        ALF(iparticle,j) = abs(B)*a/sqrt((Ugiven-Upart)^2+(Vgiven-
Vpart)^2);

        if
((ReS(iparticle,j)<0.1)||(ALF(iparticle,j)<0.005)||(ALF(iparticle,j)>0.4)
)
          %Cor_Sa = 0.0;
          %FsaffU = 1.0*(-6.46)*a*a*sqrt((Ugiven-Upart)^2+(Vgiven-
Vpart)^2)*sqrt(RHOgiven*mu*abs(B))*sign(B)*sin(al);
          %FsaffV = 1.0*(6.46)*a*a*sqrt((Ugiven-Upart)^2+(Vgiven-
Vpart)^2)*sqrt(RHOgiven*mu*abs(B))*sign(B)*cos(al);
        end;
        %FsaffU = 0.22*(Cor_Sa)*(-6.46)*a*a*sqrt((Ugiven-
Upart)^2+(Vgiven-Vpart)^2)*sqrt(RHOgiven*mu*abs(B))*sign(B)*sin(al);
        %FsaffV = 0.22*(Cor_Sa)*(6.46)*a*a*sqrt((Ugiven-Upart)^2+(Vgiven-
Vpart)^2)*sqrt(RHOgiven*mu*abs(B))*sign(B)*cos(al);

        %FsaffU = 0.12*(Cor_Sa)*(-6.46)*a*a*sqrt((Ugiven-
Upart)^2+(Vgiven-Vpart)^2)*sqrt(RHOgiven*mu*abs(B))*sign(B)*sin(al);
        %FsaffV = 0.12*(Cor_Sa)*(6.46)*a*a*sqrt((Ugiven-Upart)^2+(Vgiven-
Vpart)^2)*sqrt(RHOgiven*mu*abs(B))*sign(B)*cos(al);

        %FsaffU = 0.19*(Cor_Sa)*(-6.46)*a*a*sqrt((Ugiven-
Upart)^2+(Vgiven-Vpart)^2)*sqrt(RHOgiven*mu*abs(B))*sign(B)*sin(al);
        %FsaffV = 0.19*(Cor_Sa)*(6.46)*a*a*sqrt((Ugiven-Upart)^2+(Vgiven-
Vpart)^2)*sqrt(RHOgiven*mu*abs(B))*sign(B)*cos(al);
```

```
        FsaffU = 1.0*(Cor_Sa)*(-6.46)*a*a*sqrt((Ugiven-Upart)^2+(Vgiven-
Vpart)^2)*sqrt(RHOgiven*mu*abs(B))*sign(B)*sin(al);
        FsaffV = 1.0*(Cor_Sa)*(6.46)*a*a*sqrt((Ugiven-Upart)^2+(Vgiven-
Vpart)^2)*sqrt(RHOgiven*mu*abs(B))*sign(B)*cos(al);

        %FsaffU = 1.0*(Cor_Sa)*(-6.46)*a*a*sqrt((Ugiven-Upart)^2+(Vgiven-
Vpart)^2)*sqrt(RHOgiven*mu*abs(B))*sign(B)*sin(al);
        %FsaffV = 1.0*(Cor_Sa)*(6.46)*a*a*sqrt((Ugiven-Upart)^2+(Vgiven-
Vpart)^2)*sqrt(RHOgiven*mu*abs(B))*sign(B)*cos(al);

        % Crowe equation
        % FsaffU = 1.0*(Cor_Sa)*6.46*a*a*sqrt(abs(dUdYgiven-
dVdXgiven))*sqrt(RHOgiven*mu)*sign(dUdYgiven-dVdXgiven)*(Vpart-Vgiven);
        % FsaffV = 1.0*(Cor_Sa)*6.46*a*a*sqrt(abs(dUdYgiven-
dVdXgiven))*sqrt(RHOgiven*mu)*sign(dUdYgiven-dVdXgiven)*(Ugiven-Upart);

        eps = sqrt(Ref)/Rep;
        if ((Rep<0.1)&&(Ref<0.1))
            Cor_McLaughlin =
0.443*0.6765*(1+tanh(2.5*log10(eps)+0.191))*(0.667+tanh(6*(eps-0.32)));
            %FsaffU = 1.0*(Cor_McLaughlin)*(-6.46)*a*a*sqrt((Ugiven-
Upart)^2+(Vgiven-Vpart)^2)*sqrt(RHOgiven*mu*abs(B))*sign(B)*sin(al);
            %FsaffV = 1.0*(Cor_McLaughlin)*(6.46)*a*a*sqrt((Ugiven-
Upart)^2+(Vgiven-Vpart)^2)*sqrt(RHOgiven*mu*abs(B))*sign(B)*cos(al);
        else
            Cor_McLaughlin = 0.0;
        end;
%         FsaffU = Cor_McLaughlin*FsaffU;
%         FsaffV = Cor_McLaughlin*FsaffV;



        Cor(iparticle,j) = Cor_Sa;
        CS_EPS(iparticle,j) = eps;
        COR_MC(iparticle,j) = Cor_McLaughlin;


        clear  TODE YODE;

%         if (xgiven<0.018)
%             deltat = 0.75*10^(-6);
%         else
%             deltat = 0.35*10^(-6);
%         end;
% %
% %         if (xgiven<0.018)
% %             deltat = 2.25*10^(-6);
% %         else
% %             deltat = 1.05*10^(-6);
% %         end;

        %flow rate of 78 ccm
%         if (xgiven<0.018)
%             deltat = 4.5*10^(-6);
```

```
%         else
%             deltat = 0.75*10^(-6);
%         end;

        %flow rate of 164 ccm
        if (xgiven<0.017)
            deltat = 2.5*10^(-6);
        else
            deltat = 0.75*10^(-6);
        end;

%         if (iparticle > (nparticle-2))
%             if (xgiven<0.017)
%                 deltat = 8.5*10^(-6);
%             else
%                 deltat = 3.5*10^(-6);
%             end;
%         end;


        tspan = [0 deltat];
        y0 = [xgiven Upart ygiven Vpart];
        [TODE,YODE] = ode45(@f,tspan,y0);
        [MYode,NYode] = size(YODE);

        FsaffU = 1.0*(Cor_Sa)*(-6.46)*a*a*sqrt((Ugiven-Upart)^2+(Vgiven-
Vpart)^2)*sqrt(RHOgiven*mu*abs(B))*sign(B)*sin(al);
        FsaffV = 1.0*(Cor_Sa)*(6.46)*a*a*sqrt((Ugiven-Upart)^2+(Vgiven-
Vpart)^2)*sqrt(RHOgiven*mu*abs(B))*sign(B)*cos(al);

        Fstok(iparticle,j) = sqrt(FstU^2+FstV^2);
        FstokU(iparticle,j) = FstU;
        FstokV(iparticle,j) = FstV;

        Fsaff(iparticle,j) = sqrt(FsaffU^2+FsaffV^2);
        FsaffUU(iparticle,j) = FsaffU;
        FsaffVV(iparticle,j) = FsaffV;

        Fgrav(iparticle,j) = 4.0*pi*a^3*rop*(1-RHOgiven/rop)*9.8/3.0;

        FvirtU(iparticle,j) = (2.0/3.0)*pi*a^3*RHOgiven*(Upart-
YODE(MYode,2)-Ugiven+Ugivenold)/deltat;
        FvirtV(iparticle,j) = (2.0/3.0)*pi*a^3*RHOgiven*(Vpart-
YODE(MYode,4)-Vgiven+Vgivenold)/deltat;
        Fvirt(iparticle,j) =
sqrt(FvirtU(iparticle,j)^2+FvirtV(iparticle,j)^2);
        %Fvirt(iparticle,j) = (2.0/3.0)*pi*a^3*RHOgiven*sqrt((Upart-
YODE(MYode,2))^2+(Vpart-YODE(MYode,4))^2+(Ugiven-Ugivenold)^2+(Vgiven-
Vgivenold)^2)/deltat;

        FmagnU(iparticle,j) =
pi*a^3*RHOgiven*sqrt(dUdXgiven^2+dUdYgiven^2+dVdXgiven^2+dVdYgiven^2)*(-
Vgiven+Vpart);
```

```
        FmagnV(iparticle,j) =
pi*a^3*RHOgiven*sqrt(dUdXgiven^2+dUdYgiven^2+dVdXgiven^2+dVdYgiven^2)*(
Ugiven-Upart);
        Fmagn(iparticle,j) =
sqrt(FmagnU(iparticle,j)^2+FmagnV(iparticle,j)^2);
        %Fmagn(iparticle,j) =
pi*a^3*RHOgiven*sqrt(dUdXgiven^2+dUdYgiven^2+dVdXgiven^2+dVdYgiven^2)*sqr
t((Ugiven-Upart)^2+(Vgiven-Vpart)^2);

        Fpres(iparticle,j) = 4.0*pi*a^3*(PrGrX);




        xgiven = YODE(MYode,1);
        ygiven = YODE(MYode,3);
        Upart = YODE(MYode,2);
        Vpart = YODE(MYode,4);

        if ((xgiven>Lexit)&(flagend == 0))
            for iode = 1:MYode
                if (abs(YODE(iode,1)-Lexit)<0.000003)
                    flagend=1;
                    UUAR(iparticle,2) = YODE(iode,2);
                    VVAR(iparticle,2) = YODE(iode,4);
                    YYAR(iparticle,2) = YODE(iode,3);
                    PYAR(iparticle,2) = YODE(iode,3);%YYAR(iparticle);

                end;
            end;
        end;

        if ((xgiven>Lexit)&(flagend == 1))
            for iode = 1:MYode
                if (abs(YODE(iode,1)-Lexit)<0.0000015)
                    flagend=2;
                    UUAR(iparticle,2) = YODE(iode,2);
                    VVAR(iparticle,2) = YODE(iode,4);
                    YYAR(iparticle,2) = YODE(iode,3);
                    PYAR(iparticle,2) = YODE(iode,3);%YYAR(iparticle);
                end;
            end;
        end;



        if (abs(xgiven-Lexit-0.001)<0.000075)
            UUAR(iparticle,3) = Upart;
            VVAR(iparticle,3) = Vpart;
            YYAR(iparticle,3) = ygiven;
            PYAR(iparticle,3) = ygiven;
        end;
        if (abs(xgiven-Lexit-0.002)<0.000095)
            UUAR(iparticle,4) = Upart;
```

```
    VVAR(iparticle,4) = Vpart;
    YYAR(iparticle,4) = ygiven;
    PYAR(iparticle,4) = ygiven;
end;
if (abs(xgiven-Lexit-0.003)<0.0005)
    UUAR(iparticle,5) = Upart;
    VVAR(iparticle,5) = Vpart;
    YYAR(iparticle,5) = ygiven;
    PYAR(iparticle,5) = ygiven;
end;
if (abs(xgiven-Lexit-0.004)<0.00015)
    UUAR(iparticle,6) = Upart;
    VVAR(iparticle,6) = Vpart;
    YYAR(iparticle,6) = ygiven;
    PYAR(iparticle,6) = ygiven;
end;
if (abs(xgiven-Lexit-0.005)<0.00015)
    UUAR(iparticle,7) = Upart;
    VVAR(iparticle,7) = Vpart;
    YYAR(iparticle,7) = ygiven;
    PYAR(iparticle,7) = ygiven;
end;
if (abs(xgiven-Lexit-0.006)<0.00015)
    UUAR(iparticle,8) = Upart;
    VVAR(iparticle,8) = Vpart;
    YYAR(iparticle,8) = ygiven;
    PYAR(iparticle,8) = ygiven;
end;
if (abs(xgiven-Lexit-0.007)<0.00015)
    UUAR(iparticle,9) = Upart;
    VVAR(iparticle,9) = Vpart;
    YYAR(iparticle,9) = ygiven;
    PYAR(iparticle,9) = ygiven;
end;
if (abs(xgiven-Lexit-0.008)<0.00015)
    UUAR(iparticle,10) = Upart;
    VVAR(iparticle,10) = Vpart;
    YYAR(iparticle,10) = ygiven;
    PYAR(iparticle,10) = ygiven;
end;
if (abs(xgiven-Lexit-0.009)<0.00015)
    UUAR(iparticle,11) = Upart;
    VVAR(iparticle,11) = Vpart;
    YYAR(iparticle,11) = ygiven;
    PYAR(iparticle,11) = ygiven;
end;
if (abs(xgiven-Lexit-0.010)<0.00025)
    UUAR(iparticle,12) = Upart;
    VVAR(iparticle,12) = Vpart;
    YYAR(iparticle,12) = ygiven;
    PYAR(iparticle,12)=ygiven;
end;
if (abs(xgiven-Lexit-0.011)<0.00015)
    UUAR(iparticle,13) = Upart;
    VVAR(iparticle,13) = Vpart;
    YYAR(iparticle,13) = ygiven;
```

```
            PYAR(iparticle,13) = ygiven;
        end;
        if (abs(xgiven-Lexit-0.012)<0.00015)
            UUAR(iparticle,14) = Upart;
            VVAR(iparticle,14) = Vpart;
            YYAR(iparticle,14) = ygiven;
            PYAR(iparticle,14) = ygiven;
        end;
        if (abs(xgiven-Lexit-0.013)<0.00015)
            UUAR(iparticle,15) = Upart;
            VVAR(iparticle,15) = Vpart;
            YYAR(iparticle,15) = ygiven;
            PYAR(iparticle,15) = ygiven;
        end;
        if (abs(xgiven-Lexit-0.014)<0.00015)
            UUAR(iparticle,16) = Upart;
            VVAR(iparticle,16) = Vpart;
            YYAR(iparticle,16) = ygiven;
            PYAR(iparticle,16) = ygiven;
        end;
        if (abs(xgiven-Lexit-0.015)<0.0005)
            UUAR(iparticle,17) = Upart;
            VVAR(iparticle,17) = Vpart;
            YYAR(iparticle,17) = ygiven;
            PYAR(iparticle,17) = ygiven;
        end;


%         if (abs(xgiven-L2)<=0.00009)
%             UUAR(iparticle) = Upart;
%             VVAR(iparticle) = Vpart;
%             YYAR(iparticle) = ygiven;
%         end;
        %%%%%%%%%%%%%%%%%%%%%%
        if (xgiven==Lstop)
            flag = 1;
        end;
        if (xgiven>Lstop)
            flag = 2;
            xgiven = Lstop;
            for iode = 1:MYode
                if (abs(YODE(iode,1)-Lstop)<0.000003)
                    ygiven = YODE(iode,3);
                    Upart = YODE(iode,2);
                    Vpart = YODE(iode,4);
                end;
            end;
        end;

        if (ygiven<thresh)%deltay)

           tangent = abs(Yar(iparticle,j)-ygiven)/abs(xgiven-
Xar(iparticle,j));
           dx = thresh/tangent;
```

```
            Xar(iparticle,j) = Xar(iparticle,j)+(Yar(iparticle,j)-
thresh)/tangent;
            Yar(iparticle,j) = thresh;

            xgiven = Xar(iparticle,j)+2*dx;
            ygiven = thresh;
            Upart =  Uar(iparticle,j);
            Vpart = -Var(iparticle,j);



            if (xgiven>Lstop)
                xgiven = Lstop;
            end;
        end;
        %%%%%%%%%%%%%%%%%%%%%
        j=j+1;
        Xar(iparticle,j)=xgiven;
        Yar(iparticle,j)=ygiven;
        Uar(iparticle,j)=Upart;
        Var(iparticle,j)=Vpart;

        njp(iparticle) = j;
        %
    end;

end;

OLDPYAR = PYAR;
OLDNDAR = NDAR;
%PYARNEW = PYAR;
%NDARNEW = NDAR;

for i = 1:17
    NP(i) = nparticle;
end;

% for m = 1:17
%     dxbin = abs(max(PYAR(:,m))/nparticle);
%     maxbin(m) = 0;
%     for Nnew = 1:nparticle
%         NDARNEW(Nnew,m) = 0;
%         PYARNEW(Nnew,m) = dxbin*(Nnew-0.5);
%         for i = 1:nparticle
%             if (abs(PYAR(i,m)-dxbin*(Nnew-0.5))<=0.5*dxbin)
%                 NDARNEW(Nnew,m)= NDARNEW(Nnew,m)+NDAR(i,m);
%                 PYARNEW(Nnew,m)= dxbin*(Nnew-0.5);
%             end;
%         end;
%
%         if (NDARNEW(Nnew,m)>maxbin(m))
%             maxbin(m) = NDARNEW(Nnew,m);
%         end;
%
```

```
%     end;
% end;
% dnbin = maxbin/nparticle;

NDARNEW = zeros(105,17);
PYARNEW = zeros(105,17);
numberbin = 1.2*nparticle;


for m = 1:17
    dxbin = abs(max(PYAR(:,m)))/numberbin;
    counter(m) = 0;
    for Nnew = 1:numberbin+1 %bin number
        flag = 0;
        for i = 1:nparticle
            if (((PYAR(i,m)-dxbin*(Nnew-0.5))>=(-
0.5*dxbin))&&((PYAR(i,m)-dxbin*(Nnew-0.5))<0.5*dxbin))
                if (flag==0)
                    counter(m) = counter(m)+1;
                    flag =1;
                end;
                NDARNEW(counter(m),m)= NDARNEW(counter(m),m)+NDAR(i,m);
                PYARNEW(counter(m),m)= dxbin*(Nnew-0.5);
            end;
        end;

    end;
end;

for m = 1:17
    maxbin(m) = 0;
    for j = 1:counter(m)
        if (NDARNEW(j,m)>maxbin(m))
            maxbin(m) = NDARNEW(j,m);
        end;
    end;
end;
for m = 1:17
  dnbin(m) = maxbin(m)/counter(m);
end;



for m = 1:17
    RMIN(m) = 0.7*max(PYAR(:,m))/nparticle;
    for i = 1:NP(m)
        for j = i+1:NP(m)
            if (abs(PYAR(i,m)-PYAR(j,m))<RMIN(m))
                NDAR(i,m)= NDAR(i,m)+NDAR(j,m);
                PYAR(i,m)= (PYAR(i,m)+PYAR(j,m))/2.0;
                for k = j:NP(m)-1
                    NDAR(k,m)= NDAR(k+1,m);
                    PYAR(k,m)= PYAR(k+1,m);
                end;
```

```
                NP(m) = NP(m)-1;
            end;
        end;
    end;
end;
%
% for m = 1:17
%     width1(m) = 0;
%     width2(m) = 0;
%     width3(m) = 0;
%     for i = 1:NP(m)
%         if (abs(NDAR(i,m)-1/exp(1)^2)<=5/nparticle)
%             width1(m) = PYAR(i,m);
%         end;
%
%         if (abs(NDAR(i,m)-1/exp(1))<3/nparticle)
%             width2(m) = PYAR(i,m);
%         end;
%
%         if (abs(NDAR(i,m)-0.5)<1/nparticle)
%             width3(m) = PYAR(i,m);
%         end;
%     end;
% end;

for m = 1:17
    width1(m) = 0;
    width2(m) = 0;
    width3(m) = 0;
    flagW1 = 0;
    flagW2 = 0;
    flagW3 = 0;
    XW1_1 = 0;
    XW2_1 = 0;
    XW3_1 = 0;
    XW1_2 = 0;
    XW2_2 = 0;
    XW3_2 = 0;
    for i = 1:counter(m)
        if (((NDARNEW(i,m)-1/exp(1)^2)>-0.1)&&((NDARNEW(i,m)-
1/exp(1)^2)<0.1)&&(flagW1==0))
            XW1_1 = PYARNEW(i,m);
            flagW1 = 1;
            NWflag1 = i;
        end;
        if (((NDARNEW(i,m)-1/exp(1))>-0.07)&&((NDARNEW(i,m)-
1/exp(1))<0.07)&&(flagW2==0))
            XW2_1 = PYARNEW(i,m);
            flagW2 = 1;
            NWflag2 = i;
        end;
        if (((NDARNEW(i,m)-0.5)>-0.05)&&((NDARNEW(i,m)-
0.5)<0.05)&&(flagW3==0))
            XW3_1 = PYARNEW(i,m);
            flagW3 = 1;
            NWflag3 = i;
```

```
        end;
    end;

%     for i = (NWflag1+4):counter(m)
%         if (((NDARNEW(i,m)-1/exp(1)^2)>-0.1)&&((NDARNEW(i,m)-
1/exp(1)^2)<0.1)&&(flagW1==1))
%             XW1_2 = PYARNEW(i,m);
%             flagW1 = 2;
%         end;
%     end;
%     for i = (NWflag2+4):counter(m)
%         if (((NDARNEW(i,m)-1/exp(1))>-0.07)&&((NDARNEW(i,m)-
1/exp(1))<0.07)&&(flagW2==1))
%             XW2_2 = PYARNEW(i,m);
%             flagW2 = 2;
%         end;
%     end;
%     for i = (NWflag3+3):counter(m)
%         if (((NDARNEW(i,m)-0.5)>-0.05)&&((NDARNEW(i,m)-
0.5)<0.05)&&(flagW3==1))
%             XW3_2 = PYARNEW(i,m);
%             flagW3 = 2;
%         end;
%     end;
    %width1(m) = abs(XW1_1-XW1_2);
    %width2(m) = abs(XW2_1-XW2_2);
    %width3(m) = abs(XW3_1-XW3_2);

    width1(m) = 2*XW1_1;
    width2(m) = 2*XW2_1;
    width3(m) = 2*XW3_1;
% %     for i = 1:counter(m)
% %         if (abs(NDARNEW(i,m)-maxbin(m)/exp(1)^2)<=4*dnbin(m))
% %             width1(m) = PYARNEW(i,m);
% %         end;
% %
% %         if (abs(NDARNEW(i,m)-maxbin(m)/exp(1))<=6*dnbin(m))
% %             width2(m) = PYARNEW(i,m);
% %         end;
% %
% %         if (abs(NDARNEW(i,m)-0.5*maxbin(m))<=7*dnbin(m))
% %             width3(m) = PYARNEW(i,m);
% %         end;
% %     end;
end;

for m = 1:17
    width1f(m) = 0;
    width2f(m) = 0;
    width3f(m) = 0;
    flagF1 = 0;
    flagF2 = 0;
    flagF3 = 0;
    XF1_1 = 0;
    XF2_1 = 0;
```

```
    XF3_1 = 0;
    XF1_2 = 0;
    XF2_2 = 0;
    XF3_2 = 0;
    for i = 1:nparticle
        if (((OLDNDAR(i,m)-1/exp(1)^2)>-0.1)&&((OLDNDAR(i,m)-
1/exp(1)^2)<0.1)&&(flagF1==0))
           XF1_1 = OLDPYAR(i,m);
           flagF1 = 1;
           Nflag1 = i;
        end;
        if (((OLDNDAR(i,m)-1/exp(1))>-0.07)&&((OLDNDAR(i,m)-
1/exp(1))<0.07)&&(flagF2==0))
           XF2_1 = OLDPYAR(i,m);
           flagF2 = 1;
           Nflag2 = i;
        end;
        if (((OLDNDAR(i,m)-0.5)>-0.05)&&((OLDNDAR(i,m)-
0.5)<0.05)&&(flagF3==0))
           XF3_1 = OLDPYAR(i,m);
           flagF3 = 1;
           Nflag3 = i;
        end;
    end;

%     for i = (Nflag1+6):nparticle
%         if (((OLDNDAR(i,m)-1/exp(1)^2)>-0.1)&&((OLDNDAR(i,m)-
1/exp(1)^2)<0.1)&&(flagF1==1))
%            XF1_2 = OLDPYAR(i,m);
%            flagF1 = 2;
%         end;
%     end;
%     for i = (Nflag2+5):nparticle
%         if (((OLDNDAR(i,m)-1/exp(1))>-0.07)&&((OLDNDAR(i,m)-
1/exp(1))<0.07)&&(flagF2==1))
%            XF2_2 = OLDPYAR(i,m);
%            flagF2 = 2;
%         end;
%     end;
%     for i = (Nflag3+4):nparticle
%         if (((OLDNDAR(i,m)-0.3)>-0.05)&&((OLDNDAR(i,m)-
0.3)<0.05)&&(flagF3==1))
%            XF3_2 = OLDPYAR(i,m);
%            flagF3 = 2;
%         end;
%     end;
    width1f(m) = abs(XF1_1-XF1_2);
    width2f(m) = abs(XF2_1-XF2_2);
    width3f(m) = abs(XF3_1-XF3_2);

    width1f(m) = 2*XF1_1;
    width2f(m) = 2*XF2_1;
    width3f(m) = 2*XF3_1;
end;
```

```
figure (1)
hold on
xlabel('x, mm');
ylabel('R(x), \mum');
for iparticle = 1:nparticle
    plot(Xar(iparticle,1:njp(iparticle))/10^-
3,Yar(iparticle,1:njp(iparticle))/10^-6,'r','LineWidth',2);
end;
plot(Xar(nparticle,1:njp(nparticle))/10^-
3,Rwall(nparticle,1:njp(nparticle))/10^-6,'k','LineWidth',2);
grid;
hold off;

figure (2)
hold on
xlabel('x, mm');
ylabel('U component, m/s');
for iparticle = 1:nparticle
    plot(Xar(iparticle,1:njp(iparticle))/10^-
3,Uar(iparticle,1:njp(iparticle)),'r',Xar(iparticle,1:njp(iparticle))/10^
-3,Ugas(iparticle,1:njp(iparticle)),'b','LineWidth',2);
end;
grid;
hold off;


figure (3)
hold on
xlabel('x, mm');
ylabel('V component, m/s');
for iparticle = 1:nparticle
    plot(Xar(iparticle,1:njp(iparticle))/10^-
3,Var(iparticle,1:njp(iparticle)),'r',Xar(iparticle,1:njp(iparticle))/10^
-3,Vgas(iparticle,1:njp(iparticle)),'b','LineWidth',2);
end;
grid;
hold off;


figure (4)
hold on
xlabel('U component, m/s');
ylabel('Y, m');
plot(UUAR(:,1), YYAR(:,1),'r*', UUAR(:,2), YYAR(:,2),'b*',  UUAR(:,3),
YYAR(:,3),'g*',...
     UUAR(:,5), YYAR(:,5),'y*', UUAR(:,7), YYAR(:,7),'k*',...
     UUAR(:,9), YYAR(:,9),'ro', UUAR(:,11),YYAR(:,11),'bo',
UUAR(:,13),YYAR(:,13),'go',...

UUAR(:,15),YYAR(:,15),'yo',UUAR(:,17),YYAR(:,17),'co','LineWidth',2);
legend('inl','out','1 mm','3 mm','5 mm','7 mm','9 mm','11 mm','13 mm','15
mm');
grid;
hold off;
```

```
figure (5)
hold on
xlabel('V component, m/s');
ylabel('Y, m');
plot(VVAR(:,1), YYAR(:,1),'r*', VVAR(:,2), YYAR(:,2),'b*',  VVAR(:,3),
YYAR(:,3),'g*',...
     VVAR(:,5), YYAR(:,5),'y*', VVAR(:,7), YYAR(:,7),'k*',...
     VVAR(:,9), YYAR(:,9),'ro', VVAR(:,11),YYAR(:,11),'bo',
VVAR(:,13),YYAR(:,13),'go',...

VVAR(:,15),YYAR(:,15),'yo',VVAR(:,17),YYAR(:,17),'co','LineWidth',2);
legend('inl','out','1 mm','3 mm','5 mm','7 mm','9 mm','11 mm','13 mm','15
mm');
%plot(VVAR(:,2),YYAR(:,2),'r*','LineWidth',2);
grid;
hold off;

PYAR=PYAR*10^6;
PYARNEW=PYARNEW*10^6;
OLDPYAR = OLDPYAR*10^6;
width1 = width1*10^6;
width2 = width2*10^6;
width3 = width3*10^6;
width1f = width1f*10^6;
width2f = width2f*10^6;
width3f = width3f*10^6;

figure (6)
hold on
xlabel('Y, \mum');
ylabel('Number density');
plot(PYAR(1:NP(1),1),NDAR(1:NP(1),1),'r*',PYAR(1:NP(2),2),NDAR(1:NP(2),2)
,'b*',PYAR(1:NP(3),3),NDAR(1:NP(3),3),'g*',PYAR(1:NP(4),4),NDAR(1:NP(4),4
),'m*',...

PYAR(1:NP(5),5),NDAR(1:NP(5),5),'y*',PYAR(1:NP(6),6),NDAR(1:NP(6),6),'c*'
,PYAR(1:NP(7),7),NDAR(1:NP(7),7),'k*','LineWidth',2);
%plot(PYAR(:,1),NDAR,'r*','LineWidth',2);
legend('inl','out','1 mm','2 mm','3 mm','4 mm','5 mm');
grid;
hold off;

figure (7)
hold on
xlabel('Y, \mum');
ylabel('Number density');
plot(OLDPYAR(:,1),OLDNDAR(:,1),'r*',...
     PYARNEW(1:counter(2),2),  NDARNEW(1:counter(2),2),'b*',
PYARNEW(1:counter(3),3),  NDARNEW(1:counter(3),3),'g*',
PYARNEW(1:counter(4),4),  NDARNEW(1:counter(4),4),'m*',...
     PYARNEW(1:counter(5),5),  NDARNEW(1:counter(5),5),'y*',
PYARNEW(1:counter(6),6),  NDARNEW(1:counter(6),6),'c*',
PYARNEW(1:counter(7),7),  NDARNEW(1:counter(7),7),'k*',...
```

```
     PYARNEW(1:counter(9),9),  NDARNEW(1:counter(9),9),'ro',
PYARNEW(1:counter(11),11),NDARNEW(1:counter(11),11),'bo',
PYARNEW(1:counter(13),13),NDARNEW(1:counter(13),13),'go',...

PYARNEW(1:counter(15),15),NDARNEW(1:counter(15),15),'yo',PYARNEW(1:counte
r(17),17),NDARNEW(1:counter(17),17),'co','LineWidth',2);
%plot(PYAR(:,1),NDAR,'r*','LineWidth',2);
legend('inl','out','1 mm','2 mm','3 mm','4 mm','5 mm','7 mm','9 mm','11
mm','13 mm','15 mm');
grid;
hold off;

% figure (7)
% hold on
% xlabel('Y, \mum');
% ylabel('Number density');
%
plot(PYARNEW(:,1),NDARNEW(:,1),'r*',PYARNEW(:,2),NDARNEW(:,2),'b*',PYARNE
W(:,3),NDARNEW(:,3),'g*',PYARNEW(:,4),NDARNEW(:,4),'m*',...
%
PYARNEW(:,5),NDARNEW(:,5),'y*',PYARNEW(:,6),NDARNEW(:,6),'c*',PYARNEW(:,7
),NDARNEW(:,7),'k*','LineWidth',2);
% %plot(PYAR(:,1),NDAR,'r*','LineWidth',2);
% legend('inl','out','1 mm','2 mm','3 mm','4 mm','5 mm');
% grid;
% hold off;

figure (8)
hold on
xlabel('Y, \mum');
ylabel('Number density');
plot(OLDPYAR(:,1), OLDNDAR(:,1),'r*', OLDPYAR(:,2),OLDNDAR(:,2),'b*',
OLDPYAR(:,3),OLDNDAR(:,3),'g*',OLDPYAR(:,4),OLDNDAR(:,4),'m*',...
     OLDPYAR(:,5), OLDNDAR(:,5),'y*', OLDPYAR(:,6),OLDNDAR(:,6),'c*',
OLDPYAR(:,7),OLDNDAR(:,7),'k*',...
     OLDPYAR(:,9), OLDNDAR(:,9),'ro',
OLDPYAR(:,11),OLDNDAR(:,11),'bo',OLDPYAR(:,13),OLDNDAR(:,13),'go',...

OLDPYAR(:,15),OLDNDAR(:,15),'yo',OLDPYAR(:,17),OLDNDAR(:,17),'co','LineWi
dth',2);
%plot(PYAR(:,1),NDAR,'r*','LineWidth',2);
legend('inl','out','1 mm','2 mm','3 mm','4 mm','5 mm','7 mm','9 mm','11
mm','13 mm','15 mm');
grid;
hold off;


figure (9)
hold on
xlabel('x, mm');
ylabel('beam diameter, \mum');
plot([0,1,2,3,4,5,6,7,8,9,10,11,12,13,14,15],width1(2:17),'r',[0,1,2,3,4,
5,6,7,8,9,10,11,12,13,14,15],width2(2:17),'b',[0,1,2,3,4,5,6,7,8,9,10,11,
12,13,14,15],width3(2:17),'g','LineWidth',2);
legend('1/e^2','1/e','0.5');
```

```
grid;
hold off;

figure (10)
hold on
xlabel('x, mm');
ylabel('beam diameter, \mum');
plot([0,1,2,3,4,5,6,7,8,9,10,11,12,13,14,15],width1f(2:17),'r',[0,1,2,3,4
,5,6,7,8,9,10,11,12,13,14,15],width2f(2:17),'b',[0,1,2,3,4,5,6,7,8,9,10,1
1,12,13,14,15],width3f(2:17),'g','LineWidth',2);
legend('1/e^2','1/e','0.5');
grid;
hold off;



figure (11)
hold on
xlabel('x, mm');
ylabel('Cor_S_a_f_f_m_a_n');
for iparticle = 1:nparticle
    plot(Xar(iparticle,1:njp(iparticle))/10^-
3,Cor(iparticle,1:njp(iparticle)),'r','LineWidth',2);
end;
grid;
hold off;

figure (12)
hold on
xlabel('x, mm');
ylabel('ReS and ReG');
for iparticle = 1:nparticle
    plot(Xar(iparticle,1:njp(iparticle))/10^-
3,ReS(iparticle,1:njp(iparticle)),'r',Xar(iparticle,1:njp(iparticle))/10^
-3,ReG(iparticle,1:njp(iparticle)),'b','LineWidth',2);
end;
%legend('ReS','ReG','ReS','ReG','ReS','ReG','ReS','ReG','ReS','ReG');
legend('ReS','ReG');
grid;
hold off;

% figure (13)
% hold on
% xlabel('x, mm');
% ylabel('ReS and ReG');
% for iparticle = 1:nparticle
%     plot(Xar(iparticle,1:njp(iparticle))/10^-
3,ReS(iparticle,1:njp(iparticle)),'r',Xar(iparticle,1:njp(iparticle))/10^
-3,sqrt(ReG(iparticle,1:njp(iparticle))),'b','LineWidth',2);
% end;
%
legend('ReS','(ReG)^0^.^5','ReS','(ReG)^0^.^5','ReS','(ReG)^0^.^5','ReS',
'(ReG)^0^.^5','ReS','(ReG)^0^.^5');
% grid;
% hold off;
```

```
figure (14)
hold on
xlabel('x, mm');
ylabel('\alpha');
for iparticle = 1:nparticle
    plot(Xar(iparticle,1:njp(iparticle))/10^-
3,ALF(iparticle,1:njp(iparticle)),'r','LineWidth',2);
end;
grid;
hold off;


figure (15)
hold on
xlabel('x, mm');
ylabel('\epsilon');
for iparticle = 1:nparticle
    plot(Xar(iparticle,1:njp(iparticle))/10^-
3,CS_EPS(iparticle,1:njp(iparticle)),'r','LineWidth',2);
end;
grid;
hold off;


figure (16)
hold on
xlabel('x, mm');
ylabel('Cor_M_C');
for iparticle = 1:nparticle
    plot(Xar(iparticle,1:njp(iparticle))/10^-
3,COR_MC(iparticle,1:njp(iparticle)),'r','LineWidth',2);
end;
grid;
hold off;

figure (17)
hold on
xlabel('x, mm');
ylabel('Cor_S_a_f_f_m_a_n and Cor_M_c');
for iparticle = 1:nparticle
    plot(Xar(iparticle,1:njp(iparticle))/10^-
3,Cor(iparticle,1:njp(iparticle)),'r','LineWidth',2);
    plot(Xar(iparticle,1:njp(iparticle))/10^-
3,COR_MC(iparticle,1:njp(iparticle)),'b','LineWidth',2);
end;
legend('Cor_S','Cor_M');
grid;
hold off;


figure (18)
hold on
xlabel('x, mm');
```

```
ylabel('Forces, N');
for iparticle = 1:nparticle
    plot(Xar(iparticle,1:njp(iparticle))/10^-
3,Fstok(iparticle,1:njp(iparticle)),'r',...
         Xar(iparticle,1:njp(iparticle))/10^-
3,Fsaff(iparticle,1:njp(iparticle)),'b',...
         Xar(iparticle,1:njp(iparticle))/10^-
3,Fgrav(iparticle,1:njp(iparticle)),'g',...
         Xar(iparticle,1:njp(iparticle))/10^-
3,Fvirt(iparticle,1:njp(iparticle)),'k',...
         Xar(iparticle,1:njp(iparticle))/10^-
3,Fmagn(iparticle,1:njp(iparticle)),'m',...
         Xar(iparticle,1:njp(iparticle))/10^-
3,abs(Fpres(iparticle,1:njp(iparticle))),'y','LineWidth',2);
         %Xar(iparticle,1:njp(iparticle))/10^-
3,Fsaff(iparticle,1:njp(iparticle)),'b','LineWidth',2);
end;
legend('Stok','Saff','Grav','Virt','Magn','Pres');
grid;
hold off;

figure (19)
hold on
xlabel('x, mm');
ylabel('Forces in axial direction, N');
for iparticle = 1:nparticle
    plot(Xar(iparticle,1:njp(iparticle))/10^-
3,FstokU(iparticle,1:njp(iparticle)),'r',...
         Xar(iparticle,1:njp(iparticle))/10^-
3,FsaffUU(iparticle,1:njp(iparticle)),'b',...
         Xar(iparticle,1:njp(iparticle))/10^-
3,Fgrav(iparticle,1:njp(iparticle)),'g',...
         Xar(iparticle,1:njp(iparticle))/10^-
3,FvirtU(iparticle,1:njp(iparticle)),'k',...
         Xar(iparticle,1:njp(iparticle))/10^-
3,FmagnU(iparticle,1:njp(iparticle)),'m',...
         Xar(iparticle,1:njp(iparticle))/10^-
3,Fpres(iparticle,1:njp(iparticle)),'y','LineWidth',2);
         %Xar(iparticle,1:njp(iparticle))/10^-
3,Fsaff(iparticle,1:njp(iparticle)),'b','LineWidth',2);
end;
legend('Stok','Saff','Grav','Virt','Magn','Pres');
grid;
hold off;

figure (20)
hold on
xlabel('x, mm');
ylabel('Forces in radial direction, N');
for iparticle = 1:nparticle
    plot(Xar(iparticle,1:njp(iparticle))/10^-
3,FstokV(iparticle,1:njp(iparticle)),'r',...
         Xar(iparticle,1:njp(iparticle))/10^-
3,FsaffVV(iparticle,1:njp(iparticle)),'b',...
```

```
        Xar(iparticle,1:njp(iparticle))/10^-
3,FvirtV(iparticle,1:njp(iparticle)),'k',...
        Xar(iparticle,1:njp(iparticle))/10^-
3,FmagnV(iparticle,1:njp(iparticle)),'m','LineWidth',2);
        %Xar(iparticle,1:njp(iparticle))/10^-
3,Fsaff(iparticle,1:njp(iparticle)),'b','LineWidth',2);
end;
legend('Stok','Saff','Virt','Magn');
grid;
hold off;

Xar=Xar';
Yar=Yar';
Uar=Uar';
Var=Var';
Ugas=Ugas';
Vgas=Vgas';

%YYAR=YYAR';
%UUAR=UUAR';
%VVAR=VVAR';
```